# Dense inorganic membranes

## Studies on transport properties, defect chemistry and catalytic behaviour

Elshof, Johan Evert ten

Dense inorganic membranes : Studies on transport properties, defect chemistry and catalytic behaviour / Johan Evert ten Elshof. - [S.1. : s.n.]. - Ill.
Thesis Enschede. - With ref. - With summary in Dutch.
ISBN 90-3650930-0
Subject headings: ceramic membranes / oxygen separation / mixed conducting oxides.


Printing and binding: PrintPartners Ipskamp, Enschede

# DENSE INORGANIC MEMBRANES

## STUDIES ON TRANSPORT PROPERTIES, DEFECT CHEMISTRY AND CATALYTIC BEHAVIOUR

PROEFSCHRIFT

ter verkrijging van
de graad van doctor aan de Universiteit Twente,
op gezag van de rector magnificus,
prof. dr. F.A. van Vught,
volgens besluit van het College voor Promoties
in het openbaar te verdedigen
op vrijdag 4 april 1997 te 15.00 uur.

door

Johan Evert ten Elshof

geboren op 13 november 1968
te Groenlo

Dit proefschrift is goedgekeurd door de promotor

prof. dr. ir. H. Verweij

en de assistent promotor

dr. H.J.M. Bouwmeester

*Aan mijn ouders*

Part of the investigations described in this thesis was supported financially by the Commission of the European Communities in the framework of the Joule programme.

# Summary

Oxygen separation with dense oxide membranes may be an attractive method for the production of oxygen from air. Another possible application is the direct supply of oxygen in membrane reactors for the (partial) oxidation of hydrocarbons. The driving force for oxygen permeation through dense mixed ionic-electronic conducting membranes is an oxygen partial pressure gradient, which causes selective transport of $O^{2-}$ from the high to the low oxygen partial pressure side. The oxygen diffusion process is facilitated by a large concentration of vacant crystallographic sites in the oxygen sublattice of the oxide. Overall charge neutrality in the membrane is maintained by a counterbalancing flux of electrons or electron holes. This thesis describes a number of studies on the oxygen transport and catalytic properties of several dense inorganic membranes. The relationship with the defect chemistry of the metal oxide is investigated.

The concepts of oxygen permeation with dense membranes and the scope of this thesis are discussed in Chapter 1. Steady state oxygen permeation experiments on dense $La_{1-x}Sr_xFeO_{3-\delta}$ ($x$=0.1-0.4) membranes at high temperature (1123-1323 K) are described in Chapters 2 and 3. $La_{1-x}Sr_xFeO_{3-\delta}$ exhibits reasonably high oxygen fluxes, while it is chemically stable under reducing conditions. The combination of these two factors makes it a candidate material for membrane reactor applications. Chapter 2 reports on the steady state permeation properties in small pressure gradients, i.e., the difference between the oxygen partial pressures at opposite sides of the membrane is about one to three orders of magnitude. The permeation behaviour of the same membranes in large gradients (10-14 orders of magnitude) is discussed in Chapter 3.

It is demonstrated in Chapter 2 that *in situ* treatment of the permeate side membrane surface for several hours in a CO-containing atmosphere at 1273 K leads to significantly higher oxygen fluxes in small gradients afterwards. Hence, prior to treatment the oxygen fluxes are rate-determined by the surface exchange process at the low partial pressure side. Analysis of this surface shows that the perovskite structure remains intact upon extended exposure to CO, albeit that an enrichment of strontium, present in the form of SrO and/or $SrCO_3$, is observed on the surface. The level of enrichment depends on the pretreatment. Surface profile measurements show that the specific surface area is enlarged upon exposure to CO. It is therefore likely that the increased oxygen fluxes are caused by a larger surface area on which the exchange of oxygen can take place.

After exposure to CO the oxygen fluxes in small gradients (0.1-4.5 mmol $O_2$ $m^{-2}$ $s^{-1}$ at 1273 K) are diffusion-limited. The experimental data are compared with results from model calculations based on data of oxygen nonstoichiometry ($\delta$) from literature. The predicted trends, which are based on the assumption of ionic diffusion

by randomly distributed, non-interacting oxygen vacancies and electron holes, show good agreement with the experimental values. Fitting of the theoretical curves to the experimental data yield oxygen vacancy diffusion coefficients in the range $5.3\text{-}9.3\cdot10^{-6}$ $cm^2$ $s^{-1}$.

The presence of a $CO,CO_2$,He gas mixture at the permeate side of the membrane, while air is supplied to the feed side, causes a large oxygen activity gradient, since all permeated oxygen is directly consumed by carbon monoxide: $CO+½O_2\rightarrow CO_2$. Chapter 3 describes the results of oxygen permeation experiments under these conditions. Surface exchange-limited $O_2$ fluxes up to 25 mmol $m^{-2}$ $s^{-1}$ are reached at 1273 K. The oxygen flux is linearly proportional to the CO partial pressure and the strontium content of the oxide. To account for this behaviour, two models are proposed for the rate-determining step of the oxygen exchange reaction in the presence of CO. Oxygen vacancies at the perovskite interface play a role in both models.

Steady state measurements in a partial pressure gradient do not provide detailed information about the two individual processes that determine the overall rate of transport, i.e., chemical diffusion in the bulk (characterized by the chemical diffusion coefficient), and oxygen exchange at the gas/solid interfaces (characterized by the surface exchange coefficient). Transient response experiments are more suitable for that purpose. Chapter 4 presents data of conductivity relaxation experiments on $La_{1-x}Sr_xFeO_{3-\delta}$ ($x$=0.1, 0.4) at 923-1223 K. Thin specimens (350-460 μm) are utilized to maximize the contribution of interfacial exchange on the overall re-equilibration process. The response curve of the electrical conductivity is measured after a sudden change of the ambient oxygen pressure and analyzed in the frequency domain. Diffusion-controlled kinetics are encountered at oxygen partial pressures above 0.03 bar. The chemical diffusion coefficients show reasonable agreement with the permeation data in Chapter 2. A slow surface exchange process governs the re-equilibration process at oxygen partial pressures below 0.01 bar. The magnitude of the surface exchange coefficient is shown to depend strongly on the oxygen pressure. A model is proposed for the rate-determining step of the surface reaction, which involves an oxygen molecule and a surface oxygen vacancy.

Chapters 5-7 report on cobalt-containing perovskites $La_{0.6}Sr_{0.4}Co_{1-y}Fe_yO_{3-\delta}$. These compounds are less stable than $La_{0.6}Sr_{0.4}FeO_{3-\delta}$ but they exhibit higher fluxes. In Chapter 5 the partial thermodynamic quantities of oxygen in $La_{0.6}Sr_{0.4}Co_{1-y}Fe_yO_{3-\delta}$ ($y$=0-0.6), determined by means of oxygen coulometric titration as a function of nonstoichiometry and temperature (923-1223 K), are described. The oxygen coulometric titration technique is based on measurement of the oxygen chemical potential of a perovskite sample enclosed in a compartment in which the total amount of oxygen can be varied. Changes of nonstoichiometry and thermodynamic quantities like the energy and entropy of oxygen can be determined with this method. Although the defect structures of $La_{1-x}Sr_xFeO_{3-\delta}$ and $La_{1-x}Sr_xCoO_{3-\delta}$ at high temperature are rather well known, detailed information on $La_{1-x}Sr_xCo_{1-y}Fe_yO_{3-\delta}$ is

scarce. The electrical conductivity of $La_{1-x}Sr_xCoO_{3-\delta}$ is metallic-like, while $La_{1-x}Sr_xFeO_{3-\delta}$ is a p-type semiconductor at sufficiently high oxygen pressures, i.e., the band structures of these two classes of materials are different. The partial thermodynamic quantities of $La_{0.6}Sr_{0.4}Co_{1-y}Fe_yO_{3-\delta}$ presented in Chapter 5 can be interpreted in terms of an electronic structure with localized states on iron and a partially filled conduction band of which the density of states at the Fermi level is proportional to the cobalt concentration. The data indicate that the oxygen vacancies are randomly distributed and non-interacting. The energy of the Fe 3*d* states is close to the energy at the Fermi level in the conduction band. The random distribution of oxygen vacancies is probably facilitated by the presence of iron.

Besides determining equilibrium data like the oxygen chemical potential and nonstoichiometry, the coulometric titration technique can also be used for step-response measurements to study chemical diffusion. Chapter 6 reports on the transport parameters of $La_{0.6}Sr_{0.4}Co_{0.6}Fe_{0.4}O_{3-\delta}$ determined with both electrical conductivity relaxation and oxygen coulometric titration, covering the temperature range 923-1285 K. The values for the chemical diffusion coefficients ($10^{-6}$-$5\cdot10^{-5}$ $cm^2\ s^{-1}$) obtained by the two methods are in reasonable agreement. Conductivity relaxation experiments performed down to pressures of $10^{-4}$ bar $O_2$ demonstrate that the re-equilibration process is governed by slow interfacial exchange at low oxygen partial pressures. The exchange coefficients are almost proportional to the oxygen pressure. The exchange rate increases up to a factor of five after treatment of the surface in a nitric acid solution for several hours.

A study of oxidative methane coupling on $La_{0.6}Sr_{0.4}Co_{0.8}Fe_{0.2}O_{3-\delta}$ membranes is presented in Chapter 7. The steady state fluxes in air/helium gradients at 1073-1273 K indicate surface exchange-controlled permeation kinetics occurring at the low oxygen partial pressure side of the membrane. The oxygen flux increases slightly upon admixing of methane with helium. Although methane is converted to ethane and ethene with selectivities up to 70%, the conversion is low, typically 1-3% at 1073-1173 K. The selectivities are considerably lower (30-35%) when oxygen is admixed with methane and helium and the membrane is used as a conventional catalyst. This may indicate that permeated oxygen reacts more selectively with methane than molecular oxygen. Surface analysis indicates segregation of strontium. The level of segregation possibly depends on the magnitude of the gradient across the membrane.

In general, perovskite-type membranes do not show high oxygen fluxes at temperatures below about 1000 K. The fluorite-type oxide erbia-stabilized bismuth oxide ($Bi_{1.5}Er_{0.5}O_3$) is a good oxygen ion conductor at lower temperatures, but the electronic conductivity of the material is small, so that its performance as an oxygen separation membrane is limited by the (charge-balancing) diffusion of electrons. However, a cermet membrane made of $Bi_{1.5}Er_{0.5}O_3$ and 10-40 vol% silver, as described in Chapter 8, may exhibit oxygen fluxes up to 0.25 mmol $m^{-2}\ s^{-1}$ at 873 K. The electron transport in these composites takes place mainly through the silver

phase, provided that there is enough metal in the cermet material to form a percolative silver network. The highest steady state permeation rates in the temperature range 848-1003 K are observed on composites containing 40 vol% silver. It is shown that charge-coupled diffusion of oxygen ions and electrons in the bulk of the latter type of membrane is so fast that the overall flux in air/helium gradients is determined by a relatively slow interfacial exchange process. Steady state oxygen permeation and $^{18}O/^{16}O$ isotopic exchange experiments both indicate that the kinetic order in oxygen of the oxygen exchange reaction is ¼, suggesting that the rate-determining step is fundamentally different from that on pure $Bi_{1.5}Er_{0.5}O_3$.

An evaluation of the main results of this thesis is given in Chapter 9.

# Samenvatting

Het scheiden van zuurstof met behulp van dichte anorganische membranen is een aantrekkelijke methode voor de productie van zuurstof uit lucht. Dezelfde membranen kunnen mogelijk ook toegepast worden in membraanreactoren voor de (partiële) oxidatie van koolwaterstoffen. De drijvende kracht voor de permeatie van zuurstof door deze ionen- en electronengeleidende dichte membranen is een zuurstofpartiaalspanningsgradiënt over het membraan, waardoor $O^{2-}$ selectief van de hoge drukzijde naar de lage drukzijde getransporteerd wordt. De diffusie van zuurstofanionen wordt versneld door een relatief hoge concentratie van vacante kristallografische plaatsen in het zuurstofsubrooster. Een flux van electronen of electronengaten zorgt ervoor dat ladingsneutraliteit in het membraan behouden blijft tijdens het transport van de negatief geladen anionen. In dit proefschrift worden een aantal studies naar het zuurstoftransport en de katalytische eigenschappen van dichte anorganische membranen beschreven. Tevens wordt de relatie met de defectchemie van het metaaloxide onderzocht.

Hoofdstuk 1 bevat een introductie over zuurstofscheidende dichte membranen en enkele definities met betrekking tot bulkdiffusie en zuurstofuitwisseling aan de grensvlakken van het membraan. De resultaten van zuurstofpermeatiemetingen aan $La_{1-x}Sr_xFeO_{3-\delta}$ ($x$=0.1-0.4) membranen in stationaire toestand bij hoge temperatuur (1123-1323 K) worden beschreven in hoofdstukken 2 en 3. Dit materiaal vertoont relatief hoge zuurstoffluxen, terwijl het chemisch stabiel is in reducerende milieus. De combinatie van deze twee factoren maakt dat $La_{1-x}Sr_xFeO_{3-\delta}$ potentieel geschikt is voor toepassing in membraanreactoren. Hoofdstuk 2 behandelt het permeatie-gedrag in kleine drukgradiënten, d.w.z. het verschil tussen de zuurstofpartiaal-spanningen aan weerszijden van het membraan bedraagt ongeveer 1-3 orden van grootte. Het permeatiegedrag in grote gradiënten (10-14 orden van grootte) wordt beschreven in hoofdstuk 3.

In hoofdstuk 2 wordt aangetoond dat *in situ* behandeling van het oppervlak aan de lage drukzijde van het membraan in een CO-houdende atmosfeer bij 1273 K leidt tot significant hogere zuurstoffluxen in kleine gradiënten ná de behandeling. Dit impliceert dat de grootte van de zuurstofflux vóór behandeling bepaald wordt door het zuurstofuitwisselingsproces aan de lage drukzijde van het membraan. Uit analyses van dit oppervlak blijkt dat de perovskietstructuur behouden blijft na langdurige blootstelling aan CO, hoewel er sprake is van oppervlakteverrijking van strontium in de vorm van SrO en/of $SrCO_3$. De mate van verrijking hangt af van de wijze van voorbehandelen. Het membraanoppervlak blijkt bij behandeling vergroot te worden. Het is daarom aannemelijk dat de verhoogde zuurstoffluxen veroorzaakt worden door een groter oppervlak waarop zuurstofuitwisseling kan plaatsvinden.

Na behandeling in CO zijn de zuurstoffluxen in kleine gradiënten door membranen van 0.5-2 mm dikte diffusiegelimiteerd (0.1-4.5 mmol $O_2$ $m^{-2}$ $s^{-1}$ bij 1273 K). De experimentele waarden worden in hoofdstuk 2 vergeleken met modelberekeningen op basis van nonstoechiometriedata uit de literatuur. De berekende trends, die gebaseerd zijn op de aanname van willekeurig verdeelde en elkaar niet beïnvloedende zuurstofvacatures en electronengaten, komen goed overeen met de experimentele gegevens. De diffusiecoëfficiënten van de zuurstofvacatures bij 1273 K kunnen door vergelijking van de theoretische curven en de experimentele data geschat worden op 5.3-9.3·$10^{-6}$ $cm^2$ $s^{-1}$.

De aanwezigheid van een CO,$CO_2$,He gasmengsel aan de lage drukzijde van het membraan, terwijl met lucht wordt gevoed aan de hoge drukzijde, veroorzaakt een grote gradiënt, omdat al het gepermeëerde zuurstof direct geconsumeerd wordt door koolmonoxide: $CO+½O_2 \rightarrow CO_2$. De resultaten van permeatieëxperimenten onder deze omstandigheden zijn beschreven in hoofdstuk 3. Bij 1273 K worden zuurstoffluxen tot 25 mmol $O_2$ $m^{-2}$ $s^{-1}$ bereikt. De zuurstofflux is lineair afhankelijk van de CO partiaaldruk en van het strontiumgehalte in het perovskietmateriaal. Ter verklaring van dit gedrag worden eenvoudige modellen voor de snelheidsbepalende stap van de uitwisselingsreactie voorgesteld. In beide modellen spelen zuurstofvacatures aan het grensvlak een rol.

Metingen in stationaire toestand, zoals de in hoofdstuk 2 beschreven permeatiemetingen, geven slechts beperkt inzicht in de twee afzonderlijke processen die de uiteindelijke netto snelheid van zuurstoftransport bepalen, namelijk chemische diffusie (gekarakteriseerd door de chemische diffusiecoëfficiënt), en oppervlaktereactie (beschreven met de zuurstofuitwisselingscoëfficiënt). In hoofdstuk 4 worden resultaten gepresenteerd van geleidingsrelaxatiemetingen aan $La_{1-x}Sr_xFeO_{3-\delta}$ ($x$=0.1, 0.4) bij 923-1223 K. In dit onderzoek zijn dunne monsters (350-460 μm) gebruikt om het aandeel van de grensvlakuitwisselingsreactie in het totale equilibratieproces te maximaliseren. De methode is gebaseerd op het meten van de electrische geleiding na een stapsgewijze verandering van de zuurstofpartiaalspanning in de omringende atmosfeer. De aldus verkregen responscurve wordt in het frequentiedomein geanalyseerd. Diffusiegelimiteerde reëquilibratie blijkt op te treden bij zuurstofpartiaaldrukken boven 0.03 bar. De chemische diffusiecoëfficiënten in dit druk-interval komen redelijk overeen met de resultaten in hoofdstuk 2. Bij zuurstofpartiaaldrukken lager dan 0.01 bar wordt het equilibratieproces beheerst door een relatief langzame uitwisseling van zuurstof. De grootte van de zuurstofuitwisselingscoëfficiënt hangt sterk af van de zuurstofdruk. Op basis van de experimentele gegevens wordt een model voorgesteld voor de snelheidsbepalende stap waarin een zuurstofmolecuul en een zuurstofvacature aan het oppervlak deelnemen.

Hoofdstukken 5-7 betreffen studies naar de kobalthoudende perovskieten $La_{0.6}Sr_{0.4}Co_{1-y}Fe_yO_{3-\delta}$. Hoewel deze verbindingen minder stabiel zijn dan $La_{0.6}Sr_{0.4}FeO_{3-\delta}$ zijn er hogere fluxen mee te bereiken. Hoofdstuk 5 beschrijft de partiële thermodynamische grootheden van zuurstof in $La_{0.6}Sr_{0.4}Co_{1-y}Fe_yO_{3-\delta}$ ($y$=0-0.6)

die door middel van coulometrische titratie bepaald zijn als functie van temperatuur (923-1223 K) en nonstoechiometrie. Het principe van de coulometrische titratietechniek betreft het meten van de chemische potentiaal van $O_2$ van een perovskietmonster dat geplaatst is in een compartiment waarin de totale hoeveelheid zuurstof gevarieerd kan worden. Veranderingen van nonstoechiometrie en thermodynamische grootheden als de energie en entropie van zuurstof kunnen met deze methode bepaald worden.

Hoewel de defectstructuren van $La_{1-x}Sr_xFeO_{3-\delta}$ and $La_{1-x}Sr_xCoO_{3-\delta}$ bij hoge temperatuur redelijk bekend zijn is de structuur van $La_{1-x}Sr_xCo_{1-y}Fe_yO_{3-\delta}$ nagenoeg onbekend. De electrische geleiding van $La_{1-x}Sr_xCoO_{3-\delta}$ is metallisch; $La_{1-x}Sr_xFeO_{3-\delta}$ daarentegen is een p-type halfgeleider bij voldoende hoge zuurstofdrukken. De bandenstructuren van beide klassen van materialen zijn dus verschillend. De partiële thermodynamische grootheden in hoofdstuk 5 kunnen worden geïnterpreteerd door aan te nemen dat de electronische structuur van $La_{0.6}Sr_{0.4}Co_{1-y}Fe_yO_{3-\delta}$ gelokaliseerde toestanden op ijzer kent, alsmede een partieel gevulde geleidingsband waarvan de *density of states* van het Ferminiveau evenredig is met de kobaltconcentratie. Uit de data kan bovendien worden afgeleid dat de zuurstofvacatures willekeurig verdeeld zijn over het kristalrooster en elkaar niet beïnvloeden. De energie van het Fe 3*d* niveau ligt dicht bij de energie aan het Ferminiveau in de geleidingsband. Er zijn aanwijzingen dat de aanwezigheid van ijzer leidt tot behoud van een willekeurige verdeling van vacatures tot hogere waarden van $\delta$.

Naast het bepalen van de nonstoechiometrie en de thermodynamische grootheden kan de coulometrische titratietechniek ook gebruikt worden voor stap-respons-metingen ter bepaling van de chemische diffusiecoëfficiënt. In hoofdstuk 6 worden zowel electrische geleidingsrelaxatie- als coulometrische titratiemetingen beschreven die bij temperaturen van 923-1285 K zijn uitgevoerd aan $La_{0.6}Sr_{0.4}Co_{0.6}Fe_{0.4}O_{3-\delta}$. Toepassing van beide methoden levert waarden op voor de chemische diffusiecoëfficiënt ($10^{-6}$-$5\cdot10^{-5}$ $cm^2\ s^{-1}$) die redelijk met elkaar overeenkomen. De geleidingsmetingen, die zijn uitgevoerd tot zuurstofpartiaaldrukken van $10^{-4}$ bar $O_2$, tonen aan dat het equilibratieproces oppervlaktegelimiteerd is bij lage zuurstofdrukken, en dat de uitwisselingscoëfficiënten bijna evenredig zijn aan de zuurstofdruk. Tenslotte wordt in dit hoofdstuk aangetoond dat de snelheid van uitwisseling verhoogd kan worden met een factor vijf als de membraanoppervlakken enige tijd behandeld worden in een salpeterzuuroplossing.

De oxidatieve koppeling van methaan op $La_{0.6}Sr_{0.4}Co_{0.8}Fe_{0.2}O_{3-\delta}$ membranen wordt beschreven in hoofdstuk 7. Zuurstofpermeatiemetingen aan dit materiaal bij 1073-1273 K wijzen erop dat de snelheidsbepalende stap aan het lage drukgrensvlak optreedt. De zuurstofflux wordt een weinig groter zodra methaan aan de heliumstroom wordt toegevoegd. Hoewel methaan met selectiviteiten tot 70% wordt omgezet naar ethaan en etheen is de conversie laag (1-3% bij temperaturen van 1073-1173 K). Beduidend lagere selectiviteiten (30-35%) worden echter bereikt na

bijmenging van zuurstof aan het $CH_4$,He mengsel en gebruik van het membraan als conventionele katalysator. Gepermeëerd zuurstof reageert dus mogelijk selectiever met methaan dan moleculair zuurstof. Analyse van het membraanoppervlak toont segregatie van strontium aan. De mate van segregatie blijkt te worden bepaald door de zuurstofdrukgradiënt over het membraan.

In het algemeen zijn de zuurstoffluxen door perovskietmembranen beneden temperaturen van ongeveer 1000 K erg klein. Het fluoriet-type oxide erbium-gestabiliseerd bismutoxide ($Bi_{1.5}Er_{0.5}O_3$) is nog een goede ionogene geleider bij lagere temperaturen, maar de electronische geleiding is klein, zodat de maximaal haalbare fluxen begrensd worden door de laatstgenoemde component van de totale geleiding. Hogere zuurstoffluxen (tot 0.25 mmol $O_2$ $m^{-2}$ $s^{-1}$ bij 873 K) kunnen echter worden bereikt worden met een composietmembraan gemaakt van $Bi_{1.5}Er_{0.5}O_3$ en 10-40 vol% zilver, zoals beschreven in hoofdstuk 8. Het electronentransport vindt voornamelijk plaats door de metaalfase indien er voldoende zilver in het composiet aanwezig is om een percolatief zilvernetwerk te vormen. De hoogste permeatiesnelheden worden bereikt met membranen met 40 vol% zilver. De ladingsgekoppelde diffusie van ionen en electronen in de bulk van dit composiet is dermate snel dat het grensvlakproces de snelheidsbepalende stap is. Zuurstofpermeatiemetingen en $^{18}O/^{16}O$ isotoopuit-wisselingsexperimenten tonen aan dat de kinetische orde in zuurstof van de snelheidsbepalende stap ¼ is. Dit impliceert een fundamenteel andere snelheids-bepalende stap dan op puur $Bi_{1.5}Er_{0.5}O_3$.

Hoofdstuk 9 bevat een evaluatie van de belangrijkste resultaten van dit proefschrift.

# Contents

The following chapters are modified versions of papers already published or submitted to journals:

**Chapter 2:** J.E. ten Elshof, H.J.M. Bouwmeester and H. Verweij, "Oxygen transport through $La_{1-x}Sr_xFeO_{3-\delta}$ membranes. I. Permeation in air/He gradients," *Solid State Ionics*, **81** (1995) 97-109.

**Chapter 3:** J.E. ten Elshof, H.J.M. Bouwmeester and H. Verweij, "Oxygen transport through $La_{1-x}Sr_xFeO_{3-\delta}$ membranes. II. Permeation in air/CO,$CO_2$ gradients," *Solid State Ionics*, **89** (1996) 81-92.

**Chapter 4:** J.E. ten Elshof, M.H.R. Lankhorst and H.J.M. Bouwmeester, "Oxygen exchange and diffusion coefficients of strontium-doped lanthanum ferrites by electrical conductivity relaxation," *J. Electrochem. Soc.*, **144** (1997) 1060-1067.

**Chapter 5:** M.H.R. Lankhorst and J.E. ten Elshof, "Thermodynamic quantities and defect structure of $La_{0.6}Sr_{0.4}Co_{1-y}Fe_yO_{3-\delta}$ ($y$=0-0.6) from high-temperature coulometric titration experiments," *J. Solid State Chem.*, **130** (1997) 302-310.

**Chapter 6:** J.E. ten Elshof, M.H.R. Lankhorst and H.J.M. Bouwmeester, "Chemical diffusion and oxygen exchange of the perovskite-type oxide $La_{0.6}Sr_{0.4}Co_{0.6}Fe_{0.4}O_{3-\delta}$," *Solid State Ionics*, **99** (1997) 15-22.

**Chapter 7:** J.E. ten Elshof, H.J.M. Bouwmeester and H. Verweij, "Oxidative coupling of methane in a mixed-conducting perovskite membrane reactor," *Appl. Catal. A*, **130** (1995) 195-212.

**Chapter 8:** J.E. ten Elshof, N.Q. Nguyen, M.W. den Otter and H.J.M. Bouwmeester, "Oxygen permeation properties of dense $Bi_{1.5}Er_{0.5}O_3$/Ag cermet membranes," *J. Electrochem. Soc.*, **144** (1997) 4361-4366.

**Appendix B:** J.E. ten Elshof and J. Boeijsma, "Influence of iron content on cell parameters of rhombohedral $La_{0.6}Sr_{0.4}Co_{1-y}Fe_yO_3$," *Powder Diff.*, **11** (1996) 240-245.

# 1

# Introduction

## 1.1. Oxygen separation methods

At present oxygen is produced on industrial scale mainly by cryogenic distillation of air. This is a very energy intensive process and economic operation is possible only on a large scale. An alternative method is pressure swing adsorption, where nitrogen from compressed air at high pressure is adsorbed preferentially on active carbon or a zeolite. After removal of the oxygen-enriched air, the pressure is reduced to desorb the nitrogen. Pressure swing adsorption can be operated economically at smaller scale but has the disadvantage of being a discontinuous process. A method for the continuous production of oxygen on a small scale would be advantageous in view of the important role of oxygen in industrial processes.

A relatively new development are dense ceramic membranes which can exclusively separate oxygen from air at high temperature [1]. In future these membranes may possibly be applied in small scale units for the production of pure oxygen. Another important application is to be found in the field of chemical processing, such as the partial oxidation of hydrocarbons.

The ability for separation is based in general on the existence of a considerable concentration of vacant crystallographic sites in the oxygen sublattice of the oxide material from which the membrane is made. At elevated temperatures the oxygen anions become mobile, and considerable diffusion of oxygen occurs due to hopping of oxygen ions to neighbouring vacant crystallographic sites (so-called 'oxygen vacancies'). In a number of cases the crystal structure contains sufficient internal space to allow oxygen anions to occupy interstitial sites, which may contribute further to the oxygen ion conductivity of the material. Two types of dense membranes can be distinguished, the *solid oxide electrolytes* and the *mixed ionic-electronic conductors*. The latter type of membrane is the subject of research of this thesis and is discussed in more detail in the following section.

The solid electrolytes are pure oxygen ion conducting materials. In order to operate as an oxygen separation membrane, electrodes are deposited on both sides, and external wiring is attached. At the triple phase boundary line between solid

oxide, electrode and gas phase, oxygen may be incorporated into or released from the lattice following the net exchange reaction $O_2 + 4e^- \rightleftharpoons 2O^{2-}$.

A solid electrolyte membrane can be operated in two different modes, as depicted schematically in Figure 1.1. Both modes have been applied in oxidation processes, covering a wide range of reactions [2,3]. Figure 1.1a illustrates the solid oxide fuel cell mode. In general the primary purpose of this mode of operation is the generation of electrical energy. The cathode is exposed to air. An oxygen-consuming chemical reaction takes place in the anode compartment, thus causing a local decrease in the thermodynamic potential of oxygen. The driving force for oxygen transport is the oxygen pressure gradient across the membrane. In principle, useful chemicals can be co-generated next to electricity if a proper choice is made for the oxidation reaction in the anode compartment.

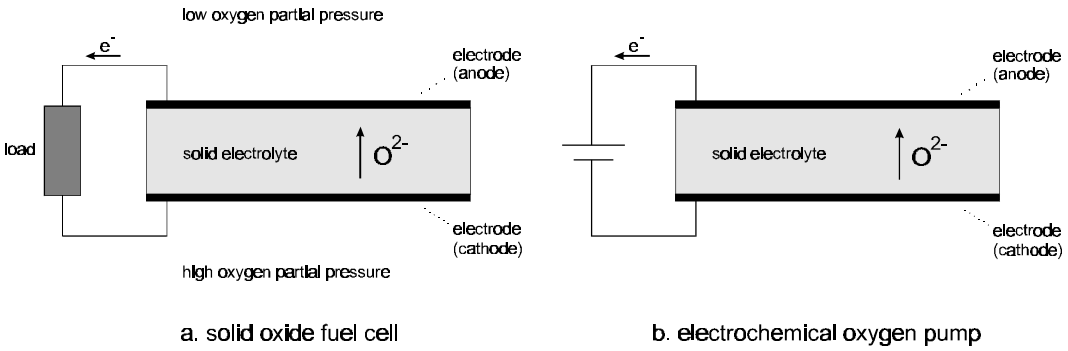


Figure 1.1. Modes of operation of solid electrolytes for the separation of oxygen.

Figure 1.1b shows the electrical oxygen pumping mode. The driving force for $O^{2-}$ transport through the electrolyte is an externally imposed electrical potential difference between the anode and cathode. In most cases a chemical reaction, of which the rate is affected directly by the supply or removal of oxygen, is carried out in one of the compartments. In a number of cases it has been observed that the catalytic activity of the electrode itself is altered strongly upon electrochemical pumping of oxygen [4].

Commonly known solid electrolytes are $\delta$-$Bi_2O_3$ and yttria-stabilized zirconia (YSZ). The cubic $\delta$-phase of $Bi_2O_3$ is the best oxygen ion conductor known. 25% of the crystallographic sites in the oxygen sublattice is vacant. The high mobility of oxygen is due to the nature of bismuth [5]. The stabilized zirconias are the most commonly used solid electrolytes. The occurrence of oxygen vacancies in these materials is due to the partial substitution of $Zr^{4+}$ in $ZrO_2$ by cations with a lower valency, e.g., $Y^{3+}$, $Ca^{2+}$ or $Mg^{2+}$. These dopants occupy normal crystallographic sites in the zirconium sublattice. In order to compensate for the lack of positive charge caused by substitution, the doped oxide contains a fixed concentration of oxygen vacancies. For instance, the general formulas for YSZ and calcia-stabilized zirconia are $Zr_{1-x}Y_xO_{2-½x}$ and $Zr_{1-x}Ca_xO_{2-x}$. Stabilized zirconia membranes are thermally, mechanically and chemically stable.

## 1.2. Mixed ionic-electronic conducting membranes for oxygen separation

An alternative to solid electrolytes are the mixed ionic-electronic conductors. Next to ionic conductivity these materials exhibit significant electronic conductivity, which acts as an internal short-circuit. For this reason mixed conducting membranes do not need electrodes and an external circuit in order to be capable of separating oxygen, which is a significant advantage from a technical and safety point of view if they are to be realized on large scale. If a mixed conducting membrane is placed in an oxygen partial pressure gradient, oxygen anions permeate from the high to the low partial pressure side, while overall charge neutrality is maintained by a counterbalancing flux of electrons (and/or electron holes), as depicted schematically in Figure 1.2a.

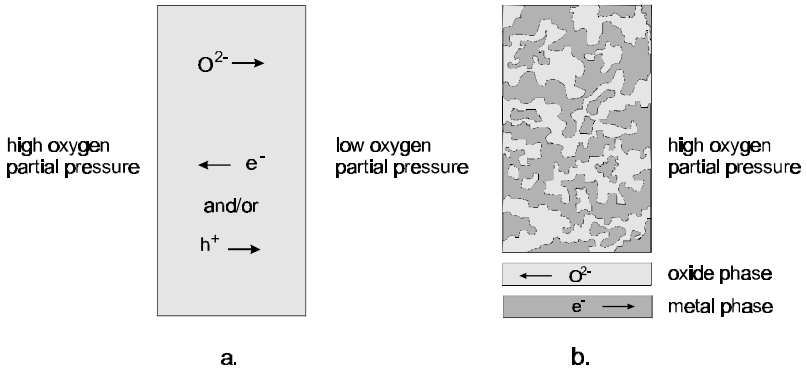


Figure 1.2. Types of mixed ionic-electronic conducting dense membranes. a. single phase membrane; b. dual phase composite membrane.

Most solid electrolytes also exhibit some electronic conductivity. Hence, the division between solid electrolyte and mixed conductor is somewhat arbitrary, being based solely on the magnitude of the electronic conductivity. Both calcia-stabilized zirconia [6] and erbia-stabilized bismuth oxide ($Bi_{1.5}Er_{0.5}O_3$) [7] have been applied as mixed conducting membranes in oxygen pressure gradients, but it was demonstrated for both materials that the chemical diffusion of $O^{2-}$ was limited by the electronic conductivity. Attempts have been made to increase the concentration of electronic charge carriers in YSZ and bismuth oxide by partial doping with multivalent elements, e.g., cerium ($Ce^{4+}+e^- \rightleftharpoons Ce^{3+}$) [8] and terbium ($Tb^{4+}+e^- \rightleftharpoons Tb^{3+}$) [9,10], which may influence the concentration of oxygen vacancies as well. Although the oxygen semipermeability could be enhanced by these dopants, the observed fluxes remained relatively low.

The first work on oxygen semipermeable dense membranes with high ionic and electronic conductivities was reported by Teraoka et al. [11]. A perovskite-type oxide $LaMO_3$, with Co and/or Fe on the M-site, was doped partially with $Sr^{2+}$ on the $La^{3+}$-site, yielding a solid oxide solution with the general formula $La_{1-x}Sr_xCo_{1-y}Fe_yO_{3-\delta}$ ($x$=0-1, $y$=0-1), where $\delta$ denotes the average number of vacant oxygen sites per unit cell. $\delta$ is called the level of nonstoichiometry. In this class of materials the

mechanism of charge compensation for the introduced aliovalent Sr-cations involves not only the creation of oxygen vacancies, but also the oxidation of a fraction of $M^{3+}$ to $M^{4+}$, which leads to high concentrations of mobile ionic and electronic charge carriers at elevated temperatures (>700°C) [12,13]. It was shown that the oxygen semipermeability increased with increasing strontium content. In later studies the influence of cation substitution in compounds $La_{0.6}A_{0.4}Co_{0.8}Fe_{0.2}O_{3-\delta}$ (A=La, Na, Ca, Ba, Sr) and $La_{0.6}Sr_{0.4}Co_{0.8}M_{0.2}O_{3-\delta}$ (M=Fe, Co, Ni, Cu) was reported [14,15]. Apart from fast oxygen diffusion in the bulk of the material, mixed-conducting perovskite-type oxides also exhibit a significant rate of oxygen exchange with the surrounding atmosphere [16,17], which contributes further to the high oxygen fluxes through these materials.

Since the pioneering work of Teraoka et al. many perovskite-type oxides have been studied. For the purpose of oxygen separation from air, cobalt-rich compounds with high concentrations of aliovalent dopants appear to be most promising, since they combine high oxygen semipermeability with reasonable chemical stability in atmospheres with reduced oxygen pressures at elevated temperatures. Reported studies include $SrCo_{0.8}M_{0.2}O_{3-\delta}$ (M=Cr, Fe, Co, Cu) [18,19], $SrCo_{1-x}M_xO_{3-\delta}$ ($x$=0-0.5, M=Ti, Cr, Mn, Fe, Ni, Cu) [20,21], $SrCo_{1-x-y}Fe_xCu_yO_{3-\delta}$ ($x$=0-0.5, y=0-0.3) [21], $Ln_{1-x}M_xCoO_{3-\delta}$ ($x$=0-0.9, Ln=La, Pr, Nd; M=Sr, Ca, Bi, Pb) [21-24], $Y_{0.05}BaCo_{0.95}O_{3-\delta}$ [25], $Y_{0.10}Ba_{0.90}CoO_{3-\delta}$ [25] and $La_{1-x}M_xCo_{1-y}Fe_yO_{3-\delta}$ (M=Sr, Ba, Ca) [26,27]. A number of oxyen permeation studies on compounds containing no cobalt are also known, e.g., $La_{1-x}Sr_xFeO_{3-\delta}$ (x=0.1, 0.2) [28], $La_{1-x}Ca_xCrO_{3-\delta}$ [29,30] and $CaTi_{1-x}M_xO_{3-\delta}$ (M=Fe, Co, Ni) [31]. In general, their oxygen semipermeabilities are significantly lower than for the Co-containing perovskites.

Another dense membrane concept, depicted schematically in Figure 1.2b, was first proposed by Mazanec et al. [32]. It consists of two percolative phases with ionic and electronic conductivity, respectively. The transport of oxygen occurs through the ionic conducting phase, while the counter flux of electrons occurs through the electronic conducting phase. Mazanec et al. demonstrated the applicability of the principle with dual phase membranes consisting of YSZ and a dispersed metallic phase (Pd, Pt, $In_{0.9}Pr_{0.1}$, $In_{0.95}Pr_{0.025}Zr_{0.025}$) [32]. More recently, successful operation of cermet membranes based on bismuth oxide, i.e., $Bi_{1.5}Y_{0.5}O_3$-$Ag_{0.7}Pd_{0.3}$, $Bi_{1.5}Y_{0.5}O_3$-Ag,[33], $Bi_{1.5}Er_{0.5}O_3$-Ag and $Bi_{1.5}Er_{0.5}O_3$-Au [34] was also reported.

For more detailed information regarding dense ceramic membranes for oxygen separation the reader is referred to Ref. [35].

## 1.3. Dense mixed-conducting membrane reactors

Besides oxygen production, dense membranes may be applied in membrane reactors for the supply of oxygen in oxidation processes. The major advantage of membrane reactors over conventional reactors is their ability to perform reaction and separation in a single step and supply oxygen in a controlled manner. For instance, for the

direct partial oxidation of methane to syngas, $CH_4+½O_2 \rightarrow CO+2H_2$, it is necessary that pure oxygen is used as the oxidant, since nitrogen and methane are difficult to separate downstream. The most capital intensive part of a process unit for syngas production is the oxygen plant, so the use of mixed conducting membrane reactors, in which both air separation and methane conversion may be achieved in one single step, is attractive (Figure 1.3). An additional advantage of the membrane reactor approach appears to be that lattice oxygen may be a more selective form of oxygen in several partial oxidation reactions. It has been demonstrated for several reactions that electrochemically supplied $O^{2-}$ showed better performance in terms of selectivities or conversions than molecular $O_2$ [36].

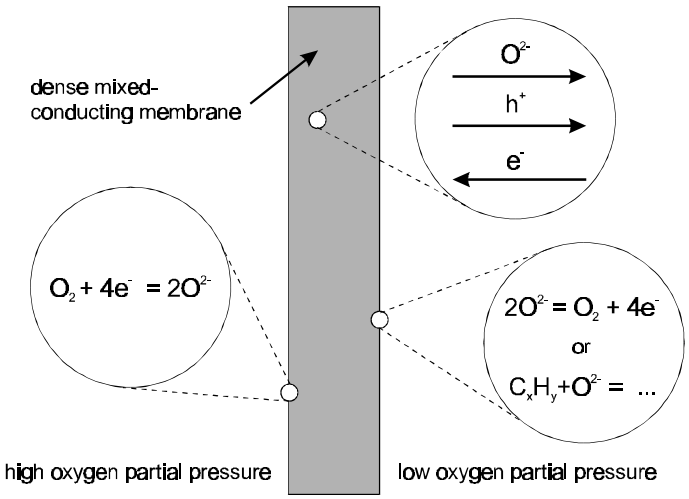


Figure 1.3. Schematic survey of fluxes and reactions in mixed-conducting membrane reactors.

The first membrane reactor studies concerned the thermal splitting of water using calcia-stabilized zirconia (CSZ) [37,38]: $H_2OWH_2+½O_2$. This reaction has a small equilibrium conversion (<4% below 2000°C at normal pressures) which is reached quickly, so preventing recombination reactions occurring at lower temperatures is quite difficult. Both drawbacks may be eliminated by selective removal of $O_2$ from the reaction compartment.

$H_2O$ was fed to the high oxygen pressure (feed) side at 1400-1800°C. In order to maximize the oxygen flux a low oxygen activity was imposed at the lower pressure (permeate) side by feeding a $CO,CO_2$ mixture, thus enlarging the gradient across the membrane. Although the conversion increased in comparison with the reaction without separation membrane, it was clearly demonstrated that the performance was limited by the low permeability of CSZ, which is in turn due to the small electronic conductivity of the solid electrolyte. Similar studies were performed on the thermal decomposition of carbon dioxide $CO_2WCO+½O_2$, [39,40] which also has a small equilibrium conversion that is easily reached.

$Bi_2O_3$-based membranes have been applied in the oxidative dehydrodimerization of propylene to 1,5-hadiene and benzene [41]. Upon feeding propene, He and air separately at 600°C, the selectivity to $C_6$ hydrocarbons was 77%. Alternatively, when $O_2$ was cofed with propene, while using the membrane as a catalyst, the main product was $CO_2$.

More recently, perovskite-type oxides have also been applied in membrane reactor studies. Since many hydrocarbon oxidation processes take place between 200°C and 600°C, temperatures at which dense mixed-conducting membranes show little or no oxygen permeation, the most significant area of current research concerns the conversion of natural gas, which takes place at high temperatures. Oxidative coupling of methane to $C_2$ hydrocarbons (ethane, ethene) has been reported on $BaCe_{0.8}Gd_{0.2}O_{3-\delta}$ membranes at 900°C [42]. At the same levels of methane conversion the $C_2$ selectivities for permeated oxygen ($O^{2-}$) and oxygen cofed with methane ($O_2$) were 70-25% and 30-10%, respectively, which may indicate that $O^{2-}$ is a more selective oxidant.

The production of syngas has been reported using tubes made of $SrCo_{0.8}Fe_{0.2}O_{3-\delta}$ [43] and $La_{0.2}Sr_{0.8}Fe_{0.6}Co_{0.4}O_{3-\delta}$ [44] operated at 900°C. The membranes showed a high catalytic activity to total combustion of methane. Upon introducing a Rh-based catalyst in the reaction compartment, syngas was produced with 90% selectivity to CO and $H_2$ at a methane conversion of 97%. Direct conversion of methane to syngas with 100% selectivity to CO was reported in a tubular $CaCo_{0.8}Fe_{0.2}O_{3-\delta}$ membrane reactor at 750°C [45].

After modification of the surface with $PbO$-$K_2O$, a $C_2$ selectivity of 55% was reported, albeit that the activity of the membrane had decreased.

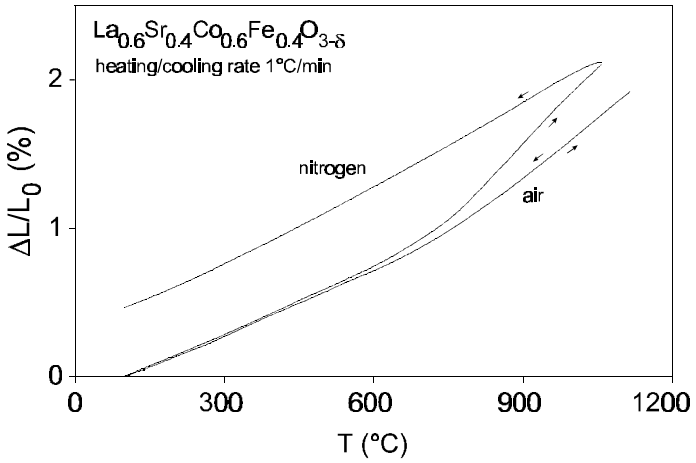


Figure 1.4. Relative thermal expansion of $La_{0.6}Sr_{0.4}Co_{0.6}Fe_{0.4}O_{3-\delta}$ upon heating and cooling in atmospheres with different oxygen partial pressures.

Under operating conditions the mechanical stability of perovskite-type membranes is affected by the expansion of the crystal lattice with decreasing oxygen content

[43,44], which causes the low oxygen pressure side to expand with respect to the high pressure side. This leads to significant mechanical stresses in the membrane along the direction of the oxygen partial pressure gradient. Figure 1.4 illustrates the thermal expansion of a $La_{0.6}Sr_{0.4}Co_{0.6}Fe_{0.4}O_{3-\delta}$ cylinder ($L$=17 mm, diameter 6.5 mm), which was previously equilibrated in air, in two different gas atmospheres [46].

A technologically important advantage of membrane reactors is the control of temperature. Two-dimensional model calculations of syngas production in $SrCo_{0.8}Fe_{0.2}O_{3-\delta}$ tubes [47] showed that the heat generation per unit reactor volume remained low due to the gradual supply of oxygen along the length of the reactor, thus preventing thermal runaway.

## 1.4. Oxygen permeation transport parameters

In this section the two basic oxygen transport processes occurring in a single-phase ceramic membrane in an oxygen partial pressure gradient at steady state are discussed. In the bulk, coupled diffusion of oxygen ions and electrons takes place, while exchange reactions of oxygen from the lattice with molecular oxygen in the gas phase occurs at both interfaces of the membrane.

### *1.4.1. Coupled diffusion of ionic and electronic species*

When the oxygen transport in a membrane is at steady state, there is no net charge current. This relates the fluxes $\mathbf{j}_i$ of species i with electrical charge $z_i$ by

$$\sum_{i=1}^{n} z_i \mathbf{j}_i = 0 . \tag{1.1}$$

Limiting the discussion to one-dimensional diffusion in direction $x$, the flux of a species can be described [48] by

$$j_i = -\frac{\sigma_i}{z_i^2 F^2} \cdot \frac{\partial \eta_i}{\partial x}, \tag{1.2}$$

where $\sigma_i$ is the conductivity of the species, $F$ the Faraday constant, and $\eta_i$ the electrochemical potential, defined by $\eta_i = \mu_i + z_i F\phi$, where $\mu_i$ indicates the chemical potential of species i, and $\phi$ is the electrical potential.

If assume the charge-carrying species in the oxide to be oxygen anions $O^{2-}$, electron holes $h^+$ and electrons $e^-$, we may assume the chemical quasi-equilibria

$$\tfrac{1}{2}O_2 + 2e^- \rightleftharpoons O^{2-}, \tag{1.3}$$

$$e^- + h^+ \rightleftharpoons \text{nil}, \tag{1.4}$$

between lattice oxygen, electrons, electron holes and molecular oxygen. Combination of Eqs. (1.1) and (1.2), applied to these species, yields for the flux of $O^{2-}$

$$j_{O^{2-}} = -\frac{\sigma_{O^{2-}}(\sigma_{e^-}+\sigma_{h^+})}{(\sigma_{O^{2-}}+\sigma_{e^-}+\sigma_{h^+})z_{O^{2-}}^2 F^2}\left(\frac{\partial \mu_{O^{2-}}}{\partial x}-\frac{z_{O^{2-}}}{z_{e^-}}\frac{\sigma_{e^-}}{\sigma_{e^-}+\sigma_{h^+}}\frac{\partial \mu_{e^-}}{\partial x}-\frac{z_{O^{2-}}}{z_{h^+}}\frac{\sigma_{h^+}}{\sigma_{e^-}+\sigma_{h^+}}\frac{\partial \mu_{h^+}}{\partial x}\right). \quad (1.5)$$

It follows from the quasi-equilibria (1.3) and (1.4) that

$$\tfrac{1}{2}\frac{\partial \mu_{O_2}}{\partial x} = \frac{\partial \mu_{O^{2-}}}{\partial x} - 2\frac{\partial \mu_{e^-}}{\partial x}, \quad (1.6)$$

$$\frac{\partial \mu_{e^-}}{\partial x} = -\frac{\partial \mu_{h^+}}{\partial x}. \quad (1.7)$$

Taking into account that $z_{O^{2-}}$=-2, $z_{e^-}$=-1 and $z_{h^+}$=+1, Eqs. (1.5)-(1.7) can be combined to

$$j_{O^{2-}} = -\frac{\sigma_{O^{2-}}(\sigma_{e^-}+\sigma_{h^+})}{8(\sigma_{O^{2-}}+\sigma_{e^-}+\sigma_{h^+})F^2}\frac{\partial \mu_{O_2}}{\partial x}. \quad (1.8)$$

The thickness of the membrane is $L$ and its interfaces are exposed at the higher and lower oxygen partial pressure side to atmospheres with partial pressures $p'_{O_2}$ and $p''_{O_2}$, respectively. With the definition of the oxygen chemical potential, $\mu_{O_2} = \mu^0_{O_2} + RT \ln p_{O_2}$ (where $\mu^0_{O_2}$ is the reference chemical potential at temperature $T$, and $R$ the gas constant), while taking into account that $j_{O_2} = \tfrac{1}{2} j_{O^{2-}}$, it follows for the oxygen flux that

$$j_{O_2} = \frac{1}{16F^2L}\int_{\ln p''_{O_2}}^{\ln p'_{O_2}} \frac{\sigma_{O^{2-}}(\sigma_{e^-}+\sigma_{h^+})}{\sigma_{O^{2-}}+\sigma_{e^-}+\sigma_{h^+}}\, d\ln p_{O_2}. \quad (1.9)$$

This is the Wagner equation [49]. It was derived originally to describe the oxide film growth on metals. A similar equation can be derived for dual phase composite membranes [50], although the condition of local charge neutrality does not hold there. In many of the perovskite-type oxides that have been investigated till now, the total electronic conductivity $\sigma_{e^-}+\sigma_{h^+}$ is several orders of magnitude larger than the ionic conductivity $\sigma_{O^{2-}}$. This simplifies the above expression to

$$j_{O_2} = \frac{1}{16F^2L}\int_{\ln p''_{O_2}}^{\ln p'_{O_2}} \sigma_{O^{2-}}\, d\ln p_{O_2}. \quad (1.10)$$

The ionic conductivity of a species $O^{2-}$ can be described [48] by

$$\sigma_{O^{2-}} = \frac{z_{O^{2-}}^2 F^2 D_O c_O}{RT}, \tag{1.11}$$

where $D_O$ is the self-diffusion coefficient of i, and $c_O$ the concentration of charge carriers. Physically the transport of oxygen anions is the same as the transport of oxygen vacancies V in the opposite direction. Hence the oxygen anion and oxygen vacancy conductivities are the same. In view of Eq. (1.11), this implies that $D_O c_O = D_V c_V$, where $D_V$ and $c_V$ are the oxygen vacancy diffusion coefficient and concentration of mobile oxygen vacancies, respectively. The diffusional flux can then be expressed as

$$j_{O_2} = \frac{D_V}{4RTV_m L} \int_{\ln p''_{O_2}}^{\ln p'_{O_2}} \delta \, d \ln p_{O_2}, \tag{1.12}$$

where it was assumed for simplicity that all oxygen vacancies are mobile and contribute equally to oxygen transport, so that $c_V = \delta / V_m$, with $V_m$ the unit cell volume of perovskite.

### *1.4.2. Surface exchange of oxygen*

The reaction of oxygen between oxide surfaces and the gas phase involves a series of reaction steps, each of which may be rate determining [51,52]. Possible steps involve the adsorption $O_2 W O_{2,ads}$ on the surface, dissociation $O_{2,ads} W 2O_{ads}$, diffusion of intermediate species on the surface, charge transfer $O_{ads} W O_{ads}^- + h^+ W O_{ads}^{2-} + 2h^+$, and incorporation of $O_{ads}^{2-}$ into the lattice. In general it is assumed that reduction of $O_2$ and oxidation of $O^{2-}$ follow the same sequence of steps in reverse directions [35].

The prevailing mechanism of oxygen exchange may be different when reactive gases such as CO or hydrocarbons are present. A detailed expression for the interfacial flux can therefore be established only when the rate-determining step of the surface exchange reaction is known.

The transport parameter used to describe the rate of surface exchange is the surface exchange coefficient $k_O$, which is directly accessible from $^{18}O/^{16}O$ isotopic exchange data [16]. The rate of $O_2$ exchange at the surface in chemical equilibrium $j_{O_2}^{ex}$ is related to the surface exchange coefficient by [35]

$$j_{O_2}^{ex} = \tfrac{1}{4} k_O c_O. \tag{1.13}$$

Here $c_O$ is the concentration of oxygen anions in the oxide at equilibrium.

## 1.5. Scope of this thesis

A number of studies on dense ceramic membranes is described in this thesis. Emphasis is put on the oxygen transport properties, but considerable attention is also paid to the defect chemistry of the oxides and the application of dense membranes in catalytic processes.

The single-phase perovskite-type oxides $La_{1-x}Sr_xFeO_{3-\delta}$ ($x$=0.1-0.4) are the subject of investigation in Chapters 2-4. Iron-based perovskites are potentially attractive materials for membrane reactor applications because they exhibit reasonable oxygen conductivity at elevated temperatures, and may be chemically stable under strongly reducing conditions. In Chapter 2 the oxygen permeation properties of $La_{1-x}Sr_xFeO_{3-\delta}$ membranes in small oxygen partial pressure gradients, i.e., air/helium, are reported. In Chapter 3 the model reaction $CO+O_2 \rightarrow CO_2$ on $La_{1-x}Sr_xFeO_{3-\delta}$ membranes is treated. The determination of the chemical diffusion coefficients and surface exchange coefficients of $La_{1-x}Sr_xFeO_{3-\delta}$ by oxygen pressure step measurements are described in Chapter 4.

A study of the compounds $La_{0.6}Sr_{0.4}Co_{1-y}Fe_yO_{3-\delta}$ in the range $y$=0-0.6 are reported in Chapters 5-7. The rate and mechanism of chemical diffusion of oxygen depends on the defect chemistry of the oxide. Although the nonstoichiometry behaviour of $La_{1-x}Sr_xFeO_{3-\delta}$ and $La_{1-x}Sr_xCoO_{3-\delta}$ are rather well known, information is scarce on $La_{1-x}Sr_xCo_{1-y}Fe_yO_{3-\delta}$. In Chapter 5, the nonstoichiometry and thermodynamic quantities of $La_{0.6}Sr_{0.4}Co_{1-y}Fe_yO_{3-\delta}$ ($y$=0-0.6) are determined from oxygen coulometric voltage step measurements.

In Chapter 6, pressure step experiments as discussed in Chapter 4 are reported on $La_{0.6}Sr_{0.4}Co_{0.6}Fe_{0.4}O_{3-\delta}$. Chapter 7 describes a membrane reactor study of methane coupling on $La_{0.6}Sr_{0.4}Co_{0.8}Fe_{0.2}O_{3-\delta}$. A comparison is made with results from experiments in which the membrane is placed in a single-chamber reactor and oxygen is admixed with the methane feed stream.

In general, perovskite-type oxides are not good oxygen ion conductors at temperatures below 750°C, while stabilized bismuth oxides may exhibit significant oxygen ion conductivity at significantly lower temperatures. In Chapter 8, a study of the oxygen permeation characteristics of $Bi_{1.5}Er_{0.5}O_3$-Ag composite membranes are reported.

A brief evaluation of the results obtained in Chapters 2-8 is given in Chapter 9.

## References

1. J. Zaman and A. Chakma, “Inorganic membrane reactors,” *J. Membr. Sci.*, **92** (1994) 1-28.
2. G. Saracco and V. Specchia, “Catalytic inorganic-membrane reactors: Present experience and future opportunities,” *Catal. Rev.-Sci. Eng.*, **36** (1994) 305-384.
3. D. Eng and M. Stoukides, "Catalytic and electrocatalytic methane oxidation with solid oxide membranes," *Catal. Rev.-Sci. Eng.*, **33** (1991) 375-412.

4. C.G. Vayenas, S. Bebelis, I.V. Yentekakis and H.G. Luntz, "Non-faradaic electrochemical modification of catalytic activity," *Catal. Today*, **11** (1992) 303-442.
5. P. Shuk, H.-D. Wiemhöfer, U. Guth, W. Göpel and M. Greenblatt, "Oxide ion conducting solid electrolytes based on $Bi_2O_3$," *Solid State Ionics*, **89** (1996) 179-196.
6. S. Dou, C.R. Masson and P.D. Pacey, "Mechanism of oxygen permeation through lime-stabilized zirconia," *J. Electrochem. Soc.*, **132** (1985) 1843-1849.
7. H.J.M. Bouwmeester, H. Kruidhof, A.J. Burggraaf and P.J. Gellings, "Oxygen semipermeability of erbia-stabilized bismuth oxide," *Solid State Ionics*, **53-56** (1992) 460-468.
8. B. Calès and J.F. Baumard, "Mixed conduction and defect structure of $ZrO_2$-$CeO_2$-$Y_2O_3$ solid solutions," *J. Electrochem. Soc.*, **131** (1984) 2407-2413.
9. G.Z. Cao, X.Q. Liu, H.W. Brinkman, K.J. de Vries and A.J. Burggraaf, "Mixed conduction and oxygen permeation of $ZrO_2$-$Tb_2O_{3.5}$-$Y_2O_3$ solid solutions," in: *Science and Technology of Zirconia V*, ed. S.P.S. Badwal, M.J. Bannister and R.H.J. Bannink, Technomic Publishing, Lancaster, 1993, p. 576-583.
10. I.C. Vinke, B.A. Boukamp, K.J. de Vries and A.J. Burggraaf, "Mixed conductivity in terbia-stabilized bismuth oxide," *Solid State Ionics*, **57** (1992) 91-98.
11. Y. Teraoka, H.-M. Zhang, S. Furukawa and N. Yamazoe, "Oxygen permeation through perovskite-type oxides," *Chem. Let.*, (1985) 1743-1746.
12. J. Mizusaki, "Nonstoichiometry, diffusion, and electrical properties of perovskite-type oxide electrode materials," *Solid State Ionics*, **52** (1992) 79-91.
13. H.U. Anderson, "Review of p-type doped perovskite materials for SOFC and other applications," *Solid State Ionics*, **52** (1992) 33-41.
14. Y. Teraoka, T. Nobunaga and N. Yamazoe, "Effect of cation substitution on the oxygen semipermeability of perovskite-type oxides," *Chem. Let.*, (1988) 503-506.
15. Y. Teraoka, T. Nobunaga, K. Okamoto, N. Miura and N. Yamazoe, "Influence of constituent metal cations in substituted $LaCoO_3$ on mixed conductivity and oxygen permeability," *Solid State Ionics*, **48** (1991) 207-212.
16. S. Carter, A. Selcuk, R.J. Chater, J. Kajda, J.A. Kilner and B.C.H. Steele, "Oxygen transport in selected nonstoichiometric perovskite-type oxides," *Solid State Ionics*, **53-56** (1992) 597-605.
17. T. Ishigaki, S. Yamauchi, K. Kishio, J. Mizusaki and K. Fueki, "Diffusion of oxide ion vacancies in perovskite-type oxides," *J. Solid State Chem.*, **73** (1988) 179-187.
18. L. Qiu, T.H. Lee, L.-M. Liu, Y.L. Yang and A.J. Jacobson, "Oxygen permeation studies of $SrCo_{0.8}Fe_{0.2}O_{3-\delta}$," *Solid State Ionics*, **76** (1995) 321-329.
19. H. Kruidhof, H.J.M. Bouwmeester, R.H.E. van Doorn and A.J. Burggraaf, "Influence of order-disorder transitions on oxygen permeability through selected nonstoichiometric perovskite-type oxides," *Solid State Ionics*, **63-65** (1993) 816-822.
20. V.V. Kharton, E.N. Naumovich and A.V. Nikolaev, "Oxide ion and electron conjugate diffusion in perovskite-like $SrCo_{1-x}M_xO_{3-\delta}$ (M=Cr..Cu; $x$=0..0.5)," *Solid State Phenom.*, **39-40** (1994) 147-152.
21. V.V. Kharton, E.N. Naumovich, A.V. Nikolaev and V.V. Samokhval, "Development of mixed conductive materials for high-temperature electrochemical oxygen membranes," in: Proc. 17th Risø Intl. Symp. on Mat. Sci.: *High Temperature Electrochemistry: Ceramics and Metals*, ed. F.W. Poulsen, N. Bonanos, S. Linderoth, M. Mogensen and B. Zachau-Christiansen, Risø National Laboratory, Roskilde, Denmark, 1996, p. 301-306.
22. N. Itoh, T. Kato, K. Uchida and K. Haraya, "Preparation of pore-free disks of $La_{1-x}Sr_xCoO_3$ mixed conductors and its oxygen permeability," *J. Membr. Sci.*, **92** (1994) 239-246.

23. R.H.E. van Doorn, H. Kruidhof, H.J.M. Bouwmeester and A.J. Burggraaf, "Oxygen permeability of strontium-doped $LaCoO_{3-\delta}$," in: *Materials Research Society Symposium Proceedings, Vol. 369, Solid State Ionics IV*, ed. G.-A. Nazri, J.-M. Taracson and M.S. Schreiber, Materials Research Society, Pittsburgh, PA, 1995, p. 373-382.
24. V.V. Kharton, E.N. Naumovich, A.A. Vecher and A.V. Nikolaev, "Oxide ion conduction in solid solutions $Ln_{1-x}Sr_xCoO_{3-\delta}$ (Ln=La, Pr, Nd)," *J. Solid State Chem.*, **120** (1995) 128-136.
25. H.W. Brinkman, H. Kruidhof and A.J. Burggraaf, "Mixed conducting yttrium-barium-cobalt-oxide for high oxygen permeation," *Solid State Ionics*, **68** (1994) 173-176.
26. J.W. Stevenson, T.R. Armstrong, R.D. Carneim, L.R. Pederson and W.J. Weber, "Electrochemical properties of mixed conducting perovskites $La_{1-x}M_xCo_{1-y}Fe_yO_3$ (M=Sr, Ba, Ca)," *J. Electrochem. Soc.*, **143** (1996) 2722-2729.
27. N. Miura, Y. Okamoto, J. Tamaki, K. Morinaga and N. Yamazoe, "Oxygen semipermeability of mixed-conductive oxide thick-film prepared by slip casting," *Solid State Ionics*, **79** (1995) 195-200.
28. B.A. van Hassel, J.E. ten Elshof and H.J.M. Bouwmeester, "Oxygen permeation flux through $La_{1-y}Sr_yO_3$ limited by carbon monoxide oxidation rate," *Appl. Cat. A*, **119** (1994) 279-291.
29. N. Sakai, T. Horita, H. Yokokawa, M. Dokiya and T. Kawada, "Oxygen permeation measurement of $La_{1-x}Ca_xCrO_{3-\delta}$ by using an electrochemical method," *Solid State Ionics*, **86-88** (1996) 1273-1278.
30. T. Kawada, T. Horita, N. Sakai, H. Yokokawa and M. Dokiya, "Experimental determination of oxygen permeation flux through bulk and grain boundary of $La_{0.7}Ca_{0.3}CrO_3$," *Solid State Ionics*, **79** (1995) 201-207.
31. H. Iwahara, T. Esaka and T. Mangahara, "Mixed conduction and oxygen permeation in the substituted oxides for $CaTiO_3$," *J. Appl. Electrochem.*, **18** (1988) 173-177.
32. T.J. Mazanec, T.L. Cable and J.G. Frye, jr., "Electrocatalytic cells for chemical reaction," *Solid State Ionics*, **53-56** (1992) 111-118.
33. Y. Shen, M. Liu, D. Taylor, S. Bolagopal, A. Joshi and K. Krist, "Mixed ionic-electronic conductors based on Bi-Y-O-Ag metal-ceramic system," Proc. 2nd Intl. Symp. on *Ionic and mixed conducting ceramics*, ed. T.A. Ramanarayanan, W.L. Worrell and H.L. Tuller, Proc. vol. 94-12, The Electrochemical Society, Pennington, NJ, 1994, p. 574-597.
34. C.S. Chen, H. Kruidhof, H.J.M. Bouwmeester, H. Verweij and A.J. Burggraaf, "Oxygen permeation through oxygen ion oxide-noble metal dual phase composites," *Solid State Ionics*, **86-88** (1996) 569-572.
35. H.J.M. Bouwmeester, "Dense ceramic membranes for oxygen separation," in: *CRC Handbook Solid State Chemistry*, ed. P.J. Gellings and H.J.M. Bouwmeester, CRC Press, Boca Raton, 1996, p. 481-553.
36. H. Nagamoto, K. Hayashi and H. Inoue, "Methane oxidation by oxygen transported through solid electrolyte," *J. Catal.*, **126** (1990) 671-673.
37. J. Lede, F. Lapicque, J. Villermaux, B. Cales, A. Ounalli, J.F. Baumard and A.M. Anthony, "Production of hydrogen by direct thermal decomposition of water: preliminary investigations," *Int. J. Hydrogen Energy*, **7** (1982) 939-950.
38. B. Calès and J.F. Baumard, "Production of hydrogen by direct thermal decomposition of water with the aid of a semipermeable membrane," *High Temperatures-High Pressures*, **14** (1982) 681-686.
39. Y. Nigara and B. Cales, "Production of carbon monoxide by direct thermal splitting of carbon dioxide at high temperature," *Bull. Chem. Soc. Jpn.*, **59** (1986) 1997-2002.

40. N. Itoh, M.A. Sanchez C., W.-C. Xu, K. Haraya and M. Hongo, "Application of a membrane reactor system to thermal decomposition of $CO_2$," *J. Membr. Sci.*, **77** (1993) 245-253.
41. R. Di Cosimo, J.D. Burrington and R.K. Graselli, "Oxidative dehydrodimerization of propylene over a $Bi_2O_3$-$La_2O_3$ oxide ion-conductive catalyst," *J. Catal.*, **102** (1986) 234-239.
42. T. Hibino, T. Sato, K. Ushiki and Y. Kuwahara, "Membrane reactor for oxidative coupling of $CH_4$ with an oxide ion-electron hole conductor," *J. Chem. Soc. Faraday Trans.*, **91** (1995) 4419-4422.
43. S. Pei, M.S. Kleefisch, T.P. Kobylinski, J. Faber, C. Udovich, V. Zhang-McCoy, B. Dabrowski, U. Balachandran, R.L. Mieville and R.B. Poeppel, "Failure mechanisms of ceramic membrane reactors in partial oxidation of methane to synthesis gas," *Catal. Let.*, **30** (1995) 201-212.
44. U. Balachandran, J.T. Dusek, S.M. Sweeney, R.B. Poeppel, R.L. Mieville, P.S. Maiya, M.S. Kleefisch, S. Pei, T.P. Kobylinski, C. Udovich and A.C. Bose, "Methane to syngas via ceramic membranes," *Am. Cer. Soc. Bull.*, **74** (1995) 71-75.
45. T. Nozaki, O. Yamazaki, K. Omata and K. Fujimoto, "Selective oxidative coupling of methane with membrane reactor," *Chem. Eng. Sci.*, **47** (1992) 2945-2950.
46. J.E. ten Elshof, unpublished work.
47. C.-Y. Tsai, Y.H. Ma, W.R. Moser and A.G. Dixon, "Modeling and simulation of a nonisothermal catalytic membrane reactor," *Chem. Eng. Commun.*, **134** (1995) 107-132.
48. H. Schmalzried, *Solid state reactions*, 2nd ed., Verlag Chemie, Weinheim-Deerfield Beach-Basel, 1981.
49. C. Wagner, "Beitrag zur Theorie des Anlaufvorgangs," *Z. Phys. Chem.*, **21** (1933) 25-41.
50. C.S. Chen, Chapter 2 in *Fine grained zirconia-metal dual phase composites*, Thesis, University of Twente, Enschede, the Netherlands, 1994.
51. J. Nowotny and J.B. Wagner, jr., "Influence of the surface on the equilibration kinetics of nonstoichiometric oxides," *Oxid. Met.*, **15** (1981) 169-190.
52. Z. Adamczyk and J. Nowotny, "Effect of the surface on gas/solid equilibration kinetics on nonstoichiometric compounds," *Solid State Phenom. - Diffusion and Defect Data*, **15&16** (1991) 285-336.

# 2

# Oxygen transport through $La_{1-x}Sr_xFeO_{3-\delta}$ membranes

## Part I. Permeation in air/helium gradients


### Abstract

Oxygen permeation measurements in air/He gradients were performed on dense $La_{1-x}Sr_xFeO_{3-\delta}$ membranes in the composition range $x$=0.1-0.4 and temperature range 1123-1323 K. Pretreatment of the lower oxygen partial pressure side of the membranes in a CO-containing atmosphere for several hours at 1273 K led to higher oxygen fluxes, which were in the range of 0.1-4.5 mmol $m^{-2}$ $s^{-1}$. After treatment, the observed oxygen fluxes could be described in terms of bulk diffusion-limited permeation behaviour. Experimental evidence for a bulk-diffusion controlled flux was found from thickness dependence measurements on membranes with thicknesses between 0.5 mm and 2.0 mm. Model calculations were performed, based on Wagner theory in conjunction with data of oxygen nonstoichiometry and vacancy diffusion coefficients from literature. The experimental flux values deviated from the model calculations with factors up to 2.5. Adjustment of the value of the vacancy diffusion coefficient led to good agreement between the experimental data and the model calculations. The calculated vacancy diffusion coefficients $D_V^0$ were virtually independent of $x$ and were found to be in the range 5.3-9.3·$10^{-6}$ $cm^2$ $s^{-1}$.

## 2.1. Introduction

Doping of oxygen-conducting ceramics with multivalent cations can lead to the simultaneous occurrence of ionic and electronic conductivity. In recent years the study of such mixed conductors has received considerable attention, since they hold promise for use as membranes for air separation or as a combined oxygen supplying membrane and catalyst in membrane reactors [1-3]. Provided that the membrane is fully dense, it is impermeable to all gases except oxygen. Attention was initially paid to yttria- and calcia-stabilized zirconia (YSZ and CSZ, respectively) based systems [4-6]. More recently, other mixed ionic-electronic conducting oxides of the fluorite and perovskite structure have drawn interest [7-10].

Oxygen fluxes through perovskite membranes were first reported by Teraoka et al. [8,11], who showed preliminary results for $La_{1-x}A_xCo_{1-y}M_yO_{3-\delta}$ membranes (A=Ca, Sr, Ba; M=Co, Fe, Cu, Ni). The oxygen flux was found to be roughly proportional to the ionic conductivity [11]. The results suggest a relationship between the oxygen semi-permeability and the reducibility of the perovskite [12]. Currently the research efforts mainly focus on alkaline earth-doped cobaltites $La_{1-x}A_xCoO_{3-\delta}$ (A=Ca, Sr, Ba) which combine high oxygen semipermeability [9-11] in the temperature range of 1000-1200 K, and chemical stability above $10^{-4}$ bar $O_2$ at elevated temperatures [13]. The oxygen activity in a membrane of thickness $L$, placed in an oxygen partial

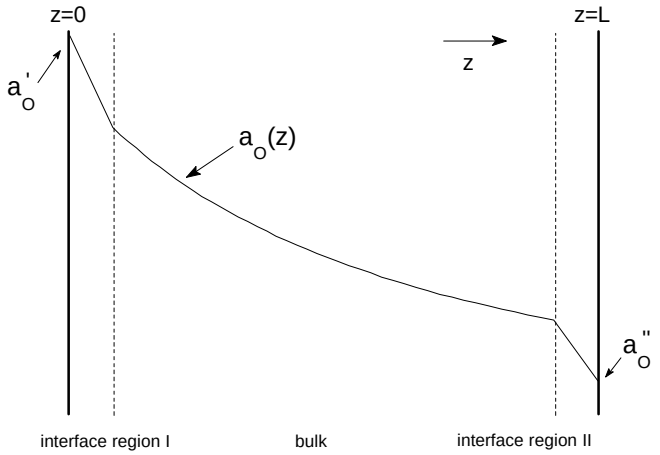


Figure 2.1. Schematic oxygen activity profile inside a membrane placed in a gradient. The gas phase activities are denoted with $a_O^{'}$ and $a_O^{''}$.

pressure gradient, is schematically shown in Figure 2.1 as a function of $z$ ($0 \le z \le L$). Oxygen activity drops generally occur in both interface regions and the bulk of the material. It is therefore of particular interest for practical applications to know whether the oxygen flux is limited by bulk diffusion or by a surface exchange process for a certain compound. In the former case, the oxygen flux is inversely proportional to the membrane thickness. Higher permeation rates can then be achieved by

reducing the thickness. In the latter case beneficial effects can only be expected from surface enlargement and modification. A characteristic thickness $L_c$ indicating the membrane thickness at which the oxygen flux is equally limited by bulk diffusion and surface exchange kinetics has been derived on theoretical grounds [14], provided that the electronic transference number is close to unity:

$$L_c = \frac{D_O^*}{k_O}. \tag{2.1}$$

Here $D_O^*$ is the tracer diffusion coefficient ($cm^2\ s^{-1}$) and $k_O$ the surface exchange coefficient ($cm\ s^{-1}$). If $L<L_c$, the oxygen flux is limited predominantly by the surface exchange kinetics. It should be noted that the characteristic thickness is not an intrinsic material property, but depends on oxygen partial pressure and temperature.

Oxygen diffusion through the bulk may be modeled using Wagner theory [15], provided that sufficient data are available on the defect chemistry or conductivity parameters of the material under consideration. The $La_{1-x}Sr_xFeO_{3-\delta}$ solid solution system ($0\leq x\leq 1$) has been studied extensively, which makes it an attractive material for modeling purposes. Dissolution of SrO in $LaFeO_{3-\delta}$ increases the concentration of oxygen vacancies. The oxygen nonstoichiometry parameter $\delta$ depends on oxygen partial pressure and temperature and can, in principle, take any value between 0 and 0.5. From thermogravimetric measurements, Mizusaki et al. [16] were able to describe the defect chemistry for $x$=0-0.6 as a function of temperature and oxygen pressure, in the temperature range 873-1473 K and oxygen partial pressure range $10^{-20}$-1 bar, assuming a random distribution of oxygen vacancies. Adopting Kröger-Vink notation [17] the defect model consists of an oxidation reaction

$$2\,Fe_{Fe}^{x} + V_O^{\cdot\cdot} + \tfrac{1}{2}O_2 \rightleftharpoons 2\,Fe_{Fe}^{\cdot} + O_O^{x} \tag{2.2}$$

and a charge disproportionation reaction

$$2\,Fe_{Fe}^{x} \rightleftharpoons Fe_{Fe}^{'} + Fe_{Fe}^{\cdot}\ . \tag{2.3}$$

The corresponding equilibrium constants are independent of the level of nonstoichiometry, which might indicate that the defects in $La_{1-x}Sr_xFeO_{3-\delta}$ are randomly distributed on their lattice sites. Comparison of the experimental results and statistical thermodynamic calculations later confirmed that the defect chemistry of $La_{1-x}Sr_xFeO_{3-\delta}$ can be properly described by a random distribution approximation [18].

Since according to this model all oxygen vacancies exist as point defects, it implies that all oxygen vacancies can contribute to the transport of oxygen. However, the

coexistence of both mobile and immobile oxygen anions in $BaIn_{2/3}Zr_{1/3}O_y$ was demonstrated by Adler et al. using high temperature $^{17}$O-NMR [19]. Moreover, study of the local structure of several perovskite systems by electron diffraction, HR-TEM and Mössbauer spectroscopy has shown that, depending on the degree of nonstoichiometry, a variety of phases with the general formula $A_mM_mO_{3m-1}$ can exist [20]. These are structurally located between the brownmillerite structure ($AMO_{2.5}$, $m$=2) and the perovskite structure ($AMO_3$, $m$=∞). Such phases have also been discovered for $SrFeO_{3-\delta}$ [21] and for $La_{1/3}Sr_{2/3}FeO_{3-\delta}$ [22] and their general structure can be thought of as consisting of ($m$-1) layers in which Fe is octahedrally coordinated by oxygen, separated by a layer in which iron occupies tetrahedrally coordinated sites. In the latter layer, all the oxygen vacancies are ordered along one of the cubic <110> directions. Within a single phase, microdomains with vacancy ordering in different directions may be intergrown [23,24] and the simultaneous existence of microdomains with different $m$ values has also been observed [21,25]. In any case, these observations not only disagree with the point defect model described above, it is also generally believed that ordered oxygen vacancies are immobile and thus do not contribute to oxygen transport.

Alternative structural models have been proposed for $SrFeO_{2.75}$ [26,27] and for $La_{1/3}Sr_{2/3}FeO_{2.806}$ [22], in which layers of Fe in square pyramidal coordination are separated by two layers of Fe in octahedral coordination. In this structure, the oxygen vacancies would exist as point defects, though ordered. A similar model was proposed for $La_{0.5}Ba_{0.5}FeO_{2.75}$ [28] on the basis of electron diffraction experiments. However, in order to be consistent with the experimental results, it had to be assumed that the oxygen vacancies are disordered in the layers with 5-fold coordination.

Unfortunately, the structural studies are usually carried out at room temperature on quenched samples and more research is required to study the evolution of extended defects at high temperature.

Table 2.1. Estimated characteristic thickness $L_c$ for different $La_{1-x}Sr_xFeO_{3-\delta}$. $T$=1273 K, $p_{O_2}$ =0.065 bar. Data taken from Refs. [29,30].

| $x$ | $L_c$ (mm) |
|---|---|
| 0 | $3\cdot10^{-4}$ |
| 0.1 | 0.06 |
| 0.25 | 0.3 |
| 0.4 | 0.45 |

A study on the oxygen semipermeability of 0.5-2 mm thick $La_{1-x}Sr_xFeO_{3-\delta}$ membranes ($x$=0.1-0.4) in air/He gradients is reported in this chapter. To determine the nature of the rate-limiting step in oxygen transport, a comparison is made between fluxes calculated from Wagner theory, using data from literature, and the experimental

results. The characteristic thicknesses $L_c$ for compounds in the range $x$=0.1-0.4 can be estimated from data obtained by Ishigaki et al. from $^{18}O$-exchange experiments [29,30], as shown in Table 2.1. $L_c$ increases with increasing strontium concentration and it is seen that the transition from bulk to surface control occurs in the mm-range. In the next chapter [31] the permeation properties of $La_{1-x}Sr_xFeO_{3-\delta}$ membranes placed in a large gradient, i.e., air/$CO$,$CO_2$, are discussed.

## 2.2. Theory

### *2.2.1. Nonstoichiometry*

The equilibrium constants corresponding to reactions (2.2) and (2.3) are

$$K_{ox} = \frac{[O_O^x][Fe_{Fe}^{\cdot}]^2}{[V_O^{\cdot\cdot}][Fe_{Fe}^x]^2\, p_{O_2}^{1/2}} = e^{-\frac{(\Delta H_{ox} - T\Delta S_{ox})}{RT}} \tag{2.4}$$

and

$$K_i = \frac{[Fe_{Fe}^{'}][Fe_{Fe}^{\cdot}]}{[Fe_{Fe}^x]^2} = e^{-\frac{(\Delta H_i - T\Delta S_i)}{RT}} \quad . \tag{2.5}$$

From thermogravimetric experiments, the values of the thermodynamic quantities were determined by Mizusaki et al. [16] as given in Table 2.2. It was noted that these values, with the exception of $\Delta H_i$, were virtually independent of $x$ within experimental error [18].

Table 2.2. Thermodynamic quantities of oxidation and charge disproportionation reactions (2.2) and (2.3) versus composition. Data taken from Ref. [16].

| $x$ | $\Delta H_{ox}$ (kJ/mol) | $\Delta S_{ox}$ (J/mol K) | $\Delta H_i$ (kJ/mol) | $\Delta S_i$ (J/mol K) |
|---|---|---|---|---|
| 0.1 | -112 | -67 | 159 | 11 |
| 0.25 | -112 | -75 | 179 | 33 |
| 0.4 | -100 | -67 | 123 | -3 |

Taking into account the condition of charge neutrality

$$[Sr_{La}^{'}]+[Fe_{Fe}^{'}] = [Fe_{Fe}^{\cdot}]+2[V_O^{\cdot\cdot}], \tag{2.6}$$

and the constraints given due to the stoichiometry of the perovskite,

$$[Fe_{Fe}^x]+[Fe_{Fe}^{'}]+[Fe_{Fe}^{\cdot}] = 1 \ , \tag{2.7}$$

$$[O_O^x]+[V_O^{\cdot\cdot}] = 3 \ , \tag{2.8}$$

we finally have 5 equations. The Sr concentration $[Sr'_{La}]$ is given by the nominal A-site composition, thus $[Sr'_{La}]=x$. The degree of nonstoichiometry $[V_O^{\cdot\cdot}]$ is further referred to as δ. With Eqs. (2.4)-(2.8) and the data from Table 2.2, the concentrations of all species can be calculated analytically as a function of $p_{O_2}$ and $T$ for a given composition. If we set the nonstoichiometry to a certain value δ at a given temperature $T$, we can combine Eqs. (2.5)-(2.7) to obtain a second-order polynomal expression for $[Fe'_{Fe}]$:

$$[Fe'_{Fe}]^2(4K_i-1)+[Fe'_{Fe}](-4K_i+(x-2\delta)(1-4K_i))+K_i(1+2(x-2\delta)+(x-2\delta)^2)=0\,. \quad (2.9)$$

With the values of δ and $[Fe'_{Fe}]$, the calculation of the concentrations of the other charge-carrying species is trivial. Finally, the corresponding oxygen partial pressure $p_{O_2}$ can be calculated from Eq. (2.4). Figure 2.2 shows the calculated oxygen concentrations of these compounds as a function of $p_{O_2}$ at 1273 K. In Figure 2.3 the formation enthalpies for oxygen vacancies are shown as a function of the oxygen partial pressure. It can be seen that the formation enthalpy depends strongly on both the oxygen partial pressure and the strontium content.

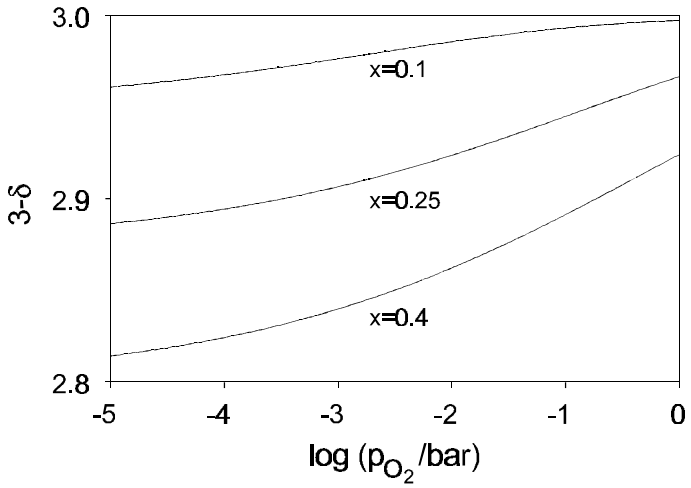


Figure 2.2. Calculated nonstoichiometries of $La_{1-x}Sr_xFeO_{3-\delta}$ for $x$=0.1-0.4 versus log $p_{O_2}$ at 1273 K.

### *2.1.2. Ionic conductivity*

In Sr-doped ferrite perovskites the ionic conductivity is due to diffusion of oxygen anions. If the mobile ions move independently an analytical expression is given by the Nernst-Einstein relation,

$$\sigma_{ion}=\sigma_{O^{2-}}=\frac{z_O^2 F^2 D_O c_O}{R T N_A}\,, \quad (2.10)$$

with $D_O$ and $c_O$ the diffusion coefficient and the concentration of oxygen anions. $z_O$ and $N_A$ are the ionic charge of lattice oxygen and Avogadro's constant, respectively.

Since the diffusion of oxygen anions is physically equal to the diffusion of oxygen vacancies in the opposite direction, the product $D_O c_O$ is related to the concentrations of oxygen vacancies $c_V$ via

$$D_O c_O = D_V c_V \ , \tag{2.11}$$

with $D_V$ the vacancy diffusion coefficient. In accordance with the point defect model described above, it is assumed here that singly- and non-ionized oxygen vacancies are not present. Furthermore, it is assumed that all oxygen vacancies are mobile, i.e., no clustering of vacancies occurs. Then

$$\sigma_{ion} = \frac{4 F^2 D_V c_V}{R T N_A} = \frac{4 F^2 D_V \delta}{R T V_m} \ , \tag{2.12}$$

where $V_m$ is the molar volume of the perovskite unit cell. $V_m$ depends on temperature and oxygen partial pressure. Since no data are available, it is assumed to be constant here.

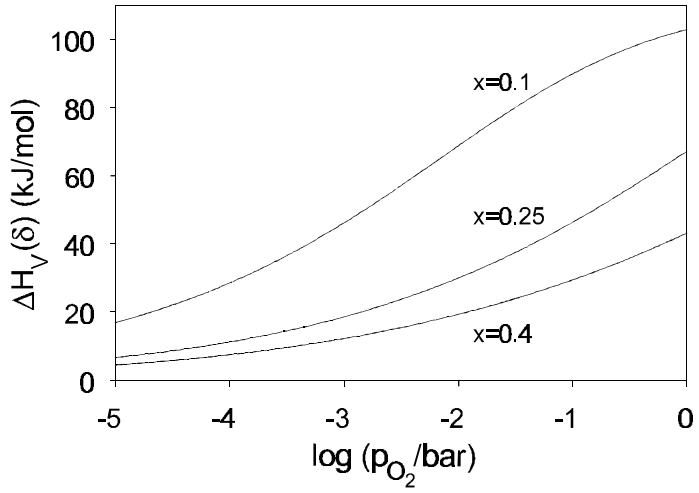


Figure 2.3. Calculated activation energies for oxygen vacancy formation at 1273 K.

In general, the vacancy diffusion coefficient is slightly dependent on the oxygen nonstoichiometry [32]. Due to the perovskite stoichiometry, the factor (1-δ/3) represents the fraction of sites in the oxygen sublattice to which an oxygen vacancy can jump. An expression for $D_V$ may thus be written as

$$D_V = D_V^0 \left(1 - \frac{\delta}{3}\right) \ . \tag{2.13}$$

Using nonstoichiometry data [16], Ishigaki et al. calculated oxygen vacancy diffusion coefficients $D_V$ from experimentally determined tracer diffusion coefficients for $x$=0, 0.1, 0.25 and 0.4, as well as the corresponding activation energies for $x$=0, 0.1 and 0.25 [29,30]. The latter values were found to be in the range of 75-114 kJ/mol. From the tracer diffusion coefficients reported by Kim et al. [33] for $x$=0.4 and $x$=0.6 a similar activation energy can be calculated. It was suggested that the activation energy is virtually independent of the Sr content [30]. The diffusion coefficients used in this study were calculated from the results of Ishigaki et al. and are listed in Table 2.3.

Table 2.3. Constants used in Eqs. (2.12)-(2.14). Data obtained from Refs. [16,29,30] ($D_V^0$), Ref. [36] ($V_m$) and Ref. [35] ($\mu_p$ and $\mu_e$).

| $x$ | $D_V^0$ ($10^{-6}$ cm$^2$ s$^{-1}$)$^\dagger$ | $V_m$ (cm$^3$ mol$^{-1}$) | $\mu_p$ (cm$^2$ V$^{-1}$ s$^{-1}$) | $\mu_e$ (cm$^2$ V$^{-1}$ s$^{-1}$) |
|---|---|---|---|---|
| 0.10 | 7.43 | 36.4 | 0.10 | 0.08 |
| 0.25 | 13.38 | 36.0 | 0.09 | 0.07 |
| 0.40 | 20.39 | 35.6 | - | - |

$^\dagger$at 1273 K.

### 2.1.3. Electronic conductivity

The electronic conductivity in $La_{1-x}Sr_xFeO_{3-\delta}$ is thought to occur via $Fe^{n+}$-O-$Fe^{(n+1)+}$ conduction pairs ($n$=2,3) [34]. Because of the simultaneous occurrence of $Fe^{2+}$, $Fe^{3+}$ and $Fe^{4+}$, n-type and p-type conductivity coexist. An analytical expression for the electronic conductivity was given by Mizusaki et al. [35]:

$$\sigma_{el} = \sigma_e + \sigma_p = [Fe'_{Fe}]\frac{N_A}{V_m}e(1-[Fe'_{Fe}])\mu_e + [Fe^{\cdot}_{Fe}]\frac{N_A}{V_m}e(1-[Fe^{\cdot}_{Fe}])\mu_p \ , \qquad (2.14)$$

where $\sigma_e$ and $\sigma_p$ are the electron and electron hole conductivity (S m$^{-1}$). $\mu_e$ and $\mu_p$ (m$^2$ V$^{-1}$ s$^{-1}$) are the mobilities of electrons and electron holes, respectively. $e$ refers to the electron charge (C). The mobilities for $x$=0.1 and $x$=0.25 were determined from electrical conductivity and Seebeck measurements [35] and are listed in Table 2.3. The activation energies for electron and electron hole hopping are neglected.

### 2.1.4. Bulk diffusion and ambipolar conductivity

When an oxygen partial pressure gradient is applied across a dense membrane made of $La_{1-x}Sr_xFeO_{3-\delta}$ oxygen diffuses from the high to the low partial pressure side. A joint flux of electrons or electron holes maintains local charge neutrality throughout the membrane. Assuming a bulk diffusion-controlled flux, the oxygen flux is expressed by [15]

$$j_{O_2} = \frac{RT}{4^2F^2L}\int_{p''_{O_2}}^{p'_{O_2}} \sigma_{amb}(p_{O_2})\, d\ln p_{O_2} \ . \qquad (2.15)$$

Here $j_{O_2}$ is the oxygen permeation flux in mol $m^{-2}$ $s^{-1}$, $p_{O_2}^{'}$ and $p_{O_2}^{''}$ are the oxygen partial pressures at opposite sides of the membrane and $L$ is the membrane thickness (m). The ambipolar conductivity $\sigma_{amb}$ (S $m^{-1}$) is defined by

$$\sigma_{amb} = \frac{\sigma_{ion}\sigma_{el}}{\sigma_{ion} + \sigma_{el}} \quad . \tag{2.16}$$

$\sigma_{ion}$ is the ionic conductivity (S $m^{-1}$) and $\sigma_{el}$ the electronic conductivity (S $m^{-1}$). The ambipolar conductivity can also be written in an empirical form:

$$\sigma_{amb} = \sigma_0 \, p_{O_2}^{n(p_{O_2})} \quad , \tag{2.17}$$

where $\sigma_0$ is a constant (S $m^{-1}$) and $n$ is called the order of the ambipolar conductivity. The validity of Eq. (2.15) is limited to cases where the overall transport is limited by bulk diffusion. With the model described above, the ambipolar conductivity can be calculated analytically. The total oxygen flux in a given partial pressure gradient can then be obtained by numerical integration. An analytical solution to the Wagner equation has also been described [37], assuming a constant $D_V$ and $\sigma_{amb}=\sigma_{ion}$. The former assumption may not hold when the level of strontium doping is considerable, while the latter does not hold at low oxygen partial pressures, typically in the range of $10^{-5}$-$10^{-15}$ bar in the temperature region of interest.

Since the ambipolar conductivity is a function of the oxygen partial pressure, its order with respect to the oxygen partial pressure can be calculated from

$$n(p_{O_2}^{'}) = \left( \frac{\partial \ln \sigma_{amb}(p_{O_2}^{'})}{\partial \ln p_{O_2}^{'}} \right) = \left( \frac{\partial}{\partial \ln p_{O_2}^{'}} \ln \left( \frac{\partial j_{O_2}}{\partial \ln p_{O_2}^{'}} \right)_{p_{O_2}^{''}} \right) . \tag{2.18}$$

If $\sigma_{el} \gg \sigma_{ion}$, then $\sigma_{amb} \approx \sigma_{ion}$. Substitution of Eq. (2.12) into Eq. (2.18) then yields

$$n(p_{O_2}^{'}) \approx \left( \frac{\partial \ln \sigma_{ion}(p_{O_2}^{'})}{\partial \ln p_{O_2}^{'}} \right) = \left( \frac{\partial \ln D_V \delta}{\partial \ln p_{O_2}^{'}} \right) \approx \left( \frac{\partial \ln \delta}{\partial \ln p_{O_2}^{'}} \right) . \tag{2.19}$$

Since $D_V$ does not change much in comparison with $\delta$, the value of $n(p_{O_2}^{'})$ is determined mainly by the change of oxygen nonstoichiometry $\delta$ with changing oxygen pressure. An average value of $n$ over a limited partial pressure range is then obtained from

$$\langle n \rangle = \int_{p_{O_2}^{''}}^{p_{O_2}^{'}} n(p_{O_2}) \, d \ln p_{O_2} \Big/ \int_{p_{O_2}^{''}}^{p_{O_2}^{'}} d \ln p_{O_2} \quad . \tag{2.20}$$

## 2.3. Experimental

### *2.3.1. Membrane synthesis*

Stoichiometric amounts of nitrate solutions of the constituent metals were mixed in $Q_2$ water. 1.5 mole of citric acid was added per mole of metal. The pH was kept below 2 using $HNO_3$. Water was evaporated until the liquid became viscous. The solution was then pyrolysed in an oven. The resulting powder was calcined at 1123-1150 K for 10 hours and subsequently ball-milled with YSZ milling balls in acetone for 3 hours. Disks of 20 mm diameter were obtained by uniaxial pressing at 1.5 bar and isostatic pressing at 4000 bar. The disks were sintered at 1473 K for 18-24 h in stagnant air. Membranes of 12.0 mm diameter and 0.5-2 mm thickness were cut from the sintered disks and polished with 1000 MESH SiC. All results reported here refer to 1.0 mm thick membranes unless stated otherwise. The membrane densities exceed 92% of theoretical in all cases.

### *2.1.2. Oxygen permeation measurements*

The measurements were performed in a quartz reactor with a reactor volume of approximately 3 ml, schematically shown in Figure 2.4. 1.0 mm thick Supremax glass rings (Schott Nederland B.V.) were used to seal the membrane into the quartz reactor at 1310-1330 K in stagnant air. Prior to sealing the cylindrical sides of the membrane were painted with Supremax-based paint. Before data were taken the permeate sides of the membranes were treated in a CO-containing atmosphere. The reader is referred to the next section for details.

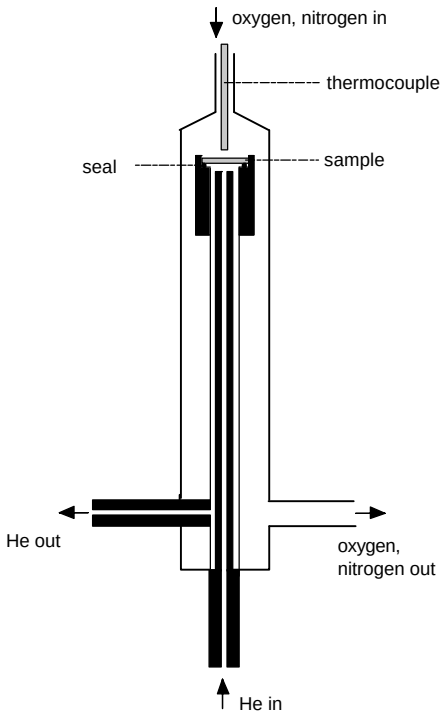

Figure 2.4. The permeation reactor.

He (4.6N) was supplied to the permeate side of the membrane and the oxygen partial pressure in this compartment was varied by adjusting the total flow rate, under the assumption of CISTR conditions. The oxygen partial pressure at the feed side could be varied between 0.01 and 1.0 bar by mixing of air, $N_2$ and $O_2$. Unless stated otherwise, all results reported here refer to measurements where air was supplied. The oxygen partial pressures of the retentate and permeate streams were continuously measured by YSZ-based oxygen sensors [38]. Analysis of the composition of the effluent stream was performed by a Varian 3300 gaschromatograph containing a molecular sieve 13X, which was coupled to a LDC/Milton Roy CL-10 integrator. All gas flows were controlled by Brooks 5800E mass flow controllers and the gas flow at the permeate side of the membrane was measured by a Brooks Volumeter. The oxygen flux was calculated from

$$j_{O_2} = \frac{1}{G} \cdot \frac{F\, c_{O_2}^{perm}}{A} \quad . \tag{2.21}$$

$F$ is the flow rate at the outlet of the reactor ($m^3\ s^{-1}$ (STP)), $c_{O_2}^{perm}$ the oxygen concentration in the effluent stream (mol $m^{-3}$) and $A$ the geometric surface area at the He-side of the membrane ($m^2$). $G$ is a dimensionless factor that corrects for the effect of non-axial diffusion, which occurs due to the fact that the surfaces exposed to air and He have different surface areas. See Appendix A for further details on the calculation of $G$. The gas tightness of membrane and seal was checked by GC detection of $N_2$ in the effluent stream. The contribution of molecular oxygen to the total oxygen flux through leakages was below 1% in all cases. All measured fluxes were corrected for this contribution.

## 2.4. Results and discussion

### *2.4.1. Pretreatment*

Upon sealing the gas phase on one of the membrane sides is changed from high (air) to low (He) oxygen partial pressure, which causes the membrane nonstoichiometry to adapt to the newly applied gradient by loosing oxygen. The observed time-dependent oxygen flux therefore consists of two contributions.

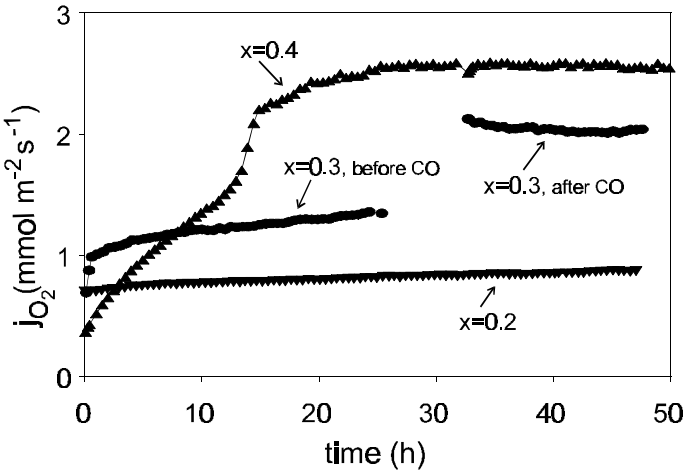


Figure 2.5. Oxygen flux versus time after sealing at 1273 K. $x$=0.2: $F_{He}$=46.8 ml/min (STP); $x$=0.3: $F_{He}$=69.3 ml/min (STP); $x$=0.4: $F_{He}$=30.1 ml/min (STP).

The first is the time-independent, steady-state contribution; the second is a time-dependent contribution due to the loss of lattice oxygen. The second contribution finally disappears, so that a steadily decreasing flux after sealing is expected. In contrast, it was observed that after the sealing procedure was performed and the flow rates were set to fixed values, the oxygen flux tended to increase for long periods of time at 1273 K, which indicates a surface effect. The stabilization of

the oxygen flux was also found to depend on the level of strontium doping. Lower strontium concentrations resulted in longer stabilization times.

An example is $La_{0.9}Sr_{0.1}FeO_{3-\delta}$, where the oxygen flux increased with 50% during the first week after sealing. Even then the flux had still only reached half of its final value. The stabilization times differed from sample to sample, even for those with equal strontium content. Some representative results are shown in Figure 2.5.

For $x$=0.4, steady state permeation is reached after 30 h. For $x$=0.2, only a 20% increase is seen during the same period of time. Figure 2.5 also shows the effect of a treatment of the He-side of the membrane in a 0.2 bar CO-containing atmosphere for $x$=0.3. After treatment, the oxygen flux has increased significantly and restores quickly to a steady-state value after evacuation of all CO. Similar results were obtained for all other compounds. Treatments of 1.5-3 h were in all cases sufficient for the oxygen flux to increase significantly and further treatment did not result in any further increase of the flux. It should be noted that only the side of the membrane that is normally exposed to He was exposed to the $CO,CO_2$,He mixture. This indicates that the oxygen flux is initially limited by a surface exchange process at the permeate side of the membrane. All further results reported here refer to measurements that were performed after treatment in a CO-containing atmosphere.

### *2.1.2. Thickness dependence*

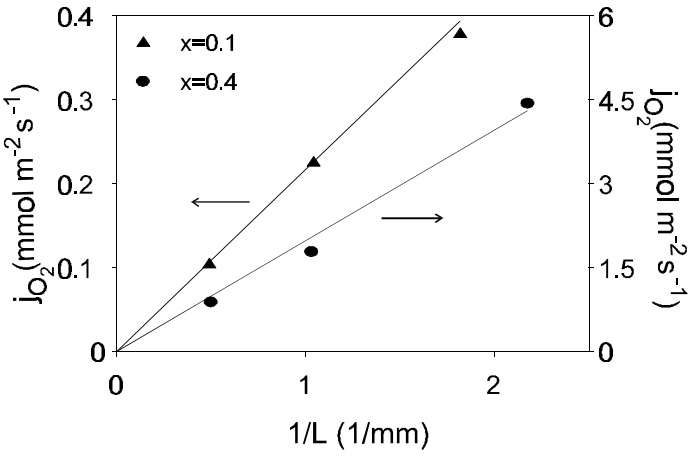


Figure 2.6. Membrane thickness dependence of oxygen fluxes for $x$=0.1 and $x$=0.4 at 1273 K. Oxygen partial pressures at permeate side are $p_{O_2}=10^{-3}$ bar ($x$=0.1) and $p_{O_2}=10^{-1.7}$ bar ($x$=0.4).

The results of thickness dependence measurements for $x$=0.1 and $x$=0.4 are given in Figure 2.6. It is clearly seen that the oxygen flux is inversely proportional to the membrane thickness for both compounds, in agreement with Eq. (2.15). These results strongly indicate an overall transport limitation by bulk diffusion.

The characteristic thicknesses $L_c$ shown in Table 2.1 suggest that in the membrane thickness range investigated here, an influence of the limiting role of surface exchange kinetics on oxygen permeation should be observed. In contrast, the

presented experiments show a purely bulk-controlled permeation rate. As was already stated in the introduction, the characteristic thickness is not an intrinsic material property.

However, changing conditions affects the characteristic thickness by much less than an order of magnitude. The deviation between the predicted values and the observed bulk behaviour may be explained if it is considered that the oxygen fluxes reported here were calculated by normalizing with respect to the geometric surface areas ($A_g$). The real surface area $A_r$ may be up to several orders of magnitude larger. This may mean that surface exchange can occur on a much larger area than the geometrical one. Hence the characteristic thickness for the membrane systems investigated here may be a factor of $A_g/A_r$ smaller than that determined from Eq. (2.1).

### *2.4.3. Oxygen partial pressure dependence*

Another indication for a bulk-controlled flux is obtained from the oxygen partial pressure dependence of the oxygen flux. Regardless of the nature of the rate-limiting transport process, the oxygen flux can be related to the oxygen partial pressure by the empirical equation

$$j_{O_2} = \alpha\, p_{O_2}^{n} + \beta \ . \tag{2.22}$$

$\alpha$, $\beta$ and $n$ are constants. Their values may be obtained by least-squares fitting of results of experiments in which the oxygen partial pressure is varied on one side of the membrane. In the case of a bulk diffusion-controlled flux the value of $n$ should be close to that of $\langle n \rangle$ in Eq. (2.20), if the limits of integration are set properly.

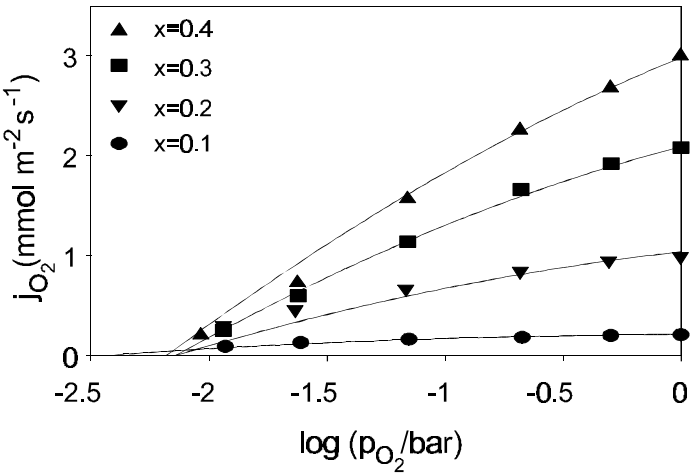


Figure 2.7. Fluxes with varying $p_{O_2}$ at the feed side at 1273 K. Permeate oxygen partial pressures are $3.8\cdot10^{-3}$ bar ($x$=0.1), $7.3\cdot10^{-3}$ bar ($x$=0.2, 0.3) and $6.8\cdot10^{-3}$ bar ($x$=0.4).

Table 2.4. Experimental $n_{expt}$ (Eq. (2.22)) and theoretical values $<n>$ (Eq. (2.20)) for the power dependence of the oxygen flux on the oxygen partial pressure at 1273 K.

| $x$ | $n_{expt}$ | $<n>$ |
|---|---|---|
| 0.1 | -0.39 | -0.42 |
| 0.2 | -0.24 | -0.20 |
| 0.3 | -0.17 | -0.16 |
| 0.4 | -0.09 | -0.12 |

Figure 2.7 shows fluxes from experiments in which the oxygen partial pressure at the feed side was varied between $10^{-2}$ and 1 bar at 1273 K. Least-squares fitting of the experimental values to Eq. (2.22) results in values of $n_{expt}$ as shown in Table 2.4. The corresponding theoretical values $<n>$ are also given. Since no data were available for $x$=0.2 and $x$=0.3 from literature, the data for $x$=0.25 were used for modeling in these two cases (except for the value of $x$).

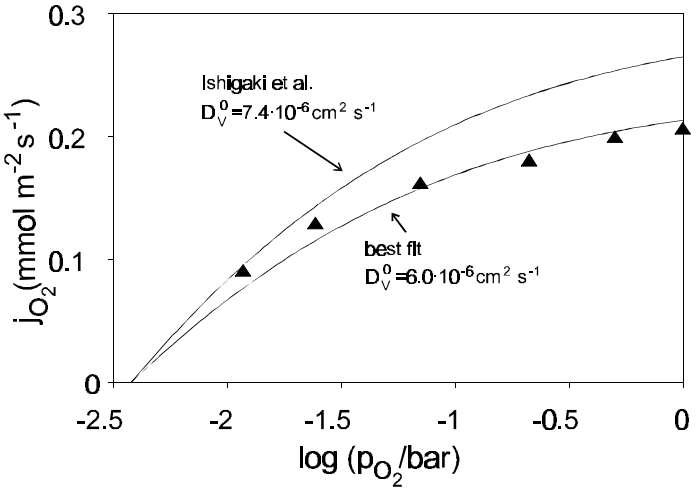


Figure 2.8. Comparison between experimental values of feed side dependence for $x$=0.1 and Wagner theory at 1273 K. Best fit to the experimental data and curve calculated from data from Ref. [30] are shown.

There is a fair agreement between the experimental and theoretical results. In the partial pressure range considered here, $\sigma_{el} \gg \sigma_{ion}$. Thus, taking Eq. (2.19) into account, the comparison between $n_{expt}$ and $<n>$ mainly shows that the experimental results are in agreement with the nonstoichiometry model of Mizusaki et al.

In Figure 2.8 the absolute values of the fluxes of $x$=0.1 are compared with a model calculation based on literature data. As can be seen the model calculation predicts higher fluxes than were determined experimentally. If we assume that the deviation between the model calculation and the experimental results is mainly caused by the error in the reported vacancy diffusion coefficient, the experimental results can be fitted by adjusting the value of $D_V^0$ only. This adjustment does not influence the calculated $<n>$-values.

Attributing the difference to the nonstoichiometry model is less likely, because fitting the fluxes by changing the thermodynamic quantities would involve very large adjustments. Moreover, such a procedure would not be justified on the basis of the observed agreement between $\langle n \rangle$ and $n_{expt}$. Least-squares refinement for all compounds leads to values for $D_V^0$ that are 20-60% lower than those reported by Ishigaki et al. [30]. Figure 2.7 shows the curves obtained with the best fits.

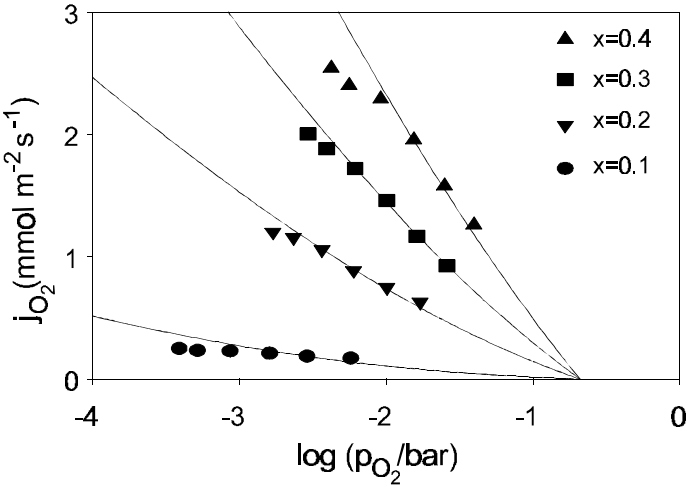


Figure 2.9. Fluxes with varying oxygen partial pressure at the permeate side at 1273 K. Drawn lines indicate best fits as described in the text.

The same procedure was applied to the permeate-side partial pressure dependence of the flux. The experimental values and the fitted curves are shown in Figure 2.9. The values of $D_V^0$, fitted independently from both sets of results, are in close agreement. The results for both types of fits are given in Table 2.5. The largest deviation is found for $x$=0.4, being equal to 20%.

Table 2.5. $D_V^0$ values at 1273 K determined from two least-squares fits of oxygen permeation experiments to Wagner model. Conditions are described in the text.

| $x$ | $D_V^0$ ($10^{-6}$ cm$^2$ s$^{-1}$) high $p_{O_2}$-side | $D_V^0$ ($10^{-6}$ cm$^2$ s$^{-1}$) low $p_{O_2}$-side |
|---|---|---|
| 0.1 | 5.98 | 5.32 |
| 0.2 | 7.84 | 7.58 |
| 0.3 | 8.16 | 7.96 |
| 0.4 | 7.77 | 9.34 |

### *2.4.4. Temperature dependence*

The activation energies were determined between 1123-1323 K. If we assume that $\sigma_{amb} \approx \sigma_{ion}$, then it can be seen from Eqs. (2.12) and (2.15) that the apparent activation energy of oxygen semipermeability is given by

$$E_{act}(j_{O_2}) = E_{act}(D_V) + \Delta H_V(\delta) \ . \qquad (2.23)$$

Since Figure 2.3 showed the enthalpy for oxygen vacancy formation to depend strongly on the oxygen partial pressure, the activation energy for oxygen permeation depends on the gradient. Therefore, oxygen permeation measurements were performed as a function of temperature with a fixed oxygen partial pressure gradient for each compound independently. The Arrhenius plots are shown in Figure 2.10. The corresponding activation energies and experimental conditions are given in Table 2.6.

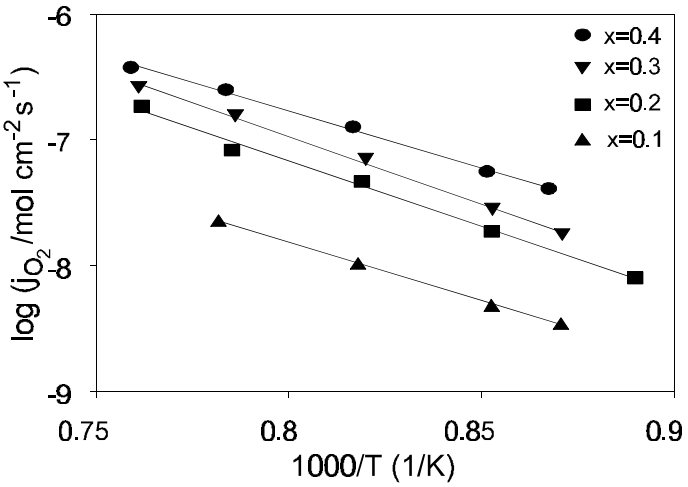


Figure 2.10. Arrhenius plots for $x$=0.1-0.4 in a fixed gradient (Table 2.6). The measurement for $x$=0.4 was performed on a 2.01 mm thick sample. Values shown for $x$=0.4 have an offset of $^{10}\log 2$ for reasons of consistency.

All values are in the range of 170-210 kJ/mol. Also shown in Table 2.6 are the enthalpies of oxygen vacancy formation in the same gradient, as calculated from the nonstoichiometry model. Accordingly, in view of Eq. (2.23), the activation energies of the vacancy diffusion coefficient lie in the range of 113-175 kJ/mol.

Table 2.6. Experimental activation energies of the oxygen flux in a fixed gradient in the temperature range 1123-1323 K. $p_{O_2}$ indicates the oxygen partial pressure at the permeate side. Calculated activation energies for oxygen vacancy formation in the corresponding gradient are also shown.

| $x$ | $p_{O_2}$ (bar) | $E_{act}(j_{O_2})$ (kJ/mol) | $\Delta H_V(\delta)$ (kJ/mol) |
|---|---|---|---|
| 0.1 | $1.0\cdot10^{-3}$ | 178±7 | 65 |
| 0.2 | $2.5\cdot10^{-3}$ | 199±18 | 38 |
| 0.3 | $5.0\cdot10^{-3}$ | 206±12 | 32 |
| 0.4‡ | $3.0\cdot10^{-3}$ | 173±11 | 21 |

‡Obtained on a 2.01 mm thick membrane.

Ishigaki et al. [30] reported activation energies for the vacancy diffusion coefficient in the region of 75-85 kJ/mol at an oxygen partial pressure of 0.065 bar. Since the vacancy diffusion coefficient can not be expected to depend strongly on the oxygen partial pressure (gradient), these results do not seem to be in agreement. Possibly, an explanation can be found in the fact that the aforementioned study of Ishigaki et al. was performed on single crystals, in contrast to the polycrystalline membranes used here.

## 2.5. Conclusions

It was shown that the oxygen semipermeability of $La_{1-x}Sr_xFeO_{3-\delta}$ ($x$=0.1-0.4) membranes can be increased significantly by treatment of the membrane's lower partial pressure side in CO. The oxygen fluxes through pretreated membranes of 0.5-2.0 mm thickness can be described properly in terms of diffusion-limited permeation behaviour. A point defect model was developed to describe the fluxes quantitatively. It was assumed that the difference between the measured fluxes and the calculated fluxes is mainly due to the lack of accuracy of the reported vacancy diffusion coefficient.

With respect to the differences found between the vacancy diffusion coefficients reported in this study and those reported by Ishigaki et al. [29,30], it may be concluded that the agreement is fair, since they do not differ by more than a factor of 2.5. A stronger deviation between both series of results is found in the trends upon changing the strontium concentration. Both series of diffusion coefficients are shown in Figure 2.11.

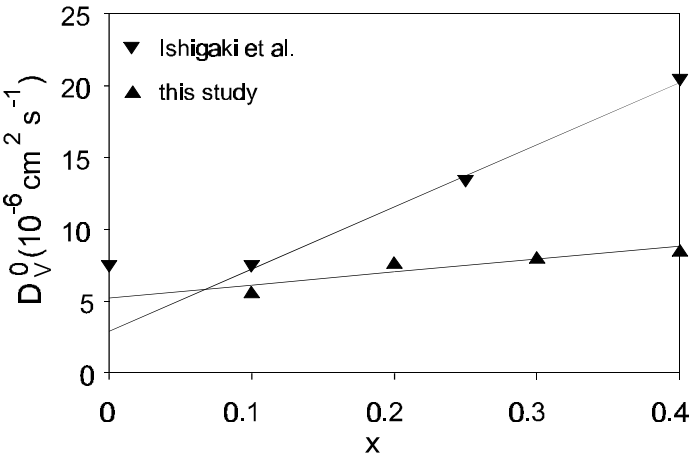


Figure 2.11. Comparison of oxygen vacancy diffusion coefficients at 1273 K.

The vacancy diffusion coefficients found in this study increase slightly with $x$. A larger dependence is found in Ishigaki's study. The activation energies of oxygen permeation were found to be in the range of 170-210 kJ/mol and were much larger than expected on the basis of literature data.

## References


1. H.U. Anderson, "Review of p-type perovskite materials for SOFC and other applications," *Solid State Ionics*, **52** (1992) 33-41.
2. P.J. Gellings and H.J.M. Bouwmeester, "Ion and mixed conducting oxides as catalysts," *Catal. Today*, **12** (1992) 1-106.
3. A.G. Dixon, W.R. Moser and Y.H. Ma, "Waste reduction and recovery using $O_2$-permeable membrane reactors," *Ind. Eng. Chem. Res.*, **33** (1994) 3015-3024.
4. S. Dou, C.R. Masson and P.D. Pacey, "Mechanism of oxygen permeation through lime-stabilized zirconia," *J. Electrochem. Soc.*, **132** (1985) 1843-1849.
5. Y. Nigara and B. Cales, "Production of carbon monoxide by direct thermal splitting of carbon dioxide at high temperature," *Bull. Chem. Soc. Jpn.*, **59** (1986) 1997-2002.
6. G.Z. Cao, X.Q. Liu, H.W. Brinkman, K.J. de Vries and A.J. Burggraaf, "Mixed conductivity and oxygen permeability of $ZrO_2$-$Tb_2O_{3.5}$-$Y_2O_3$ solid solutions" in: *Science and Technology of Zirconia V*, ed. S.P.S. Badwal, M.J. Bannister and R.J.H. Hannink, Technomic Publishing, Pennsylvania-Basel, 1993, p. 577-583.
7. H.J.M. Bouwmeester, H. Kruidhof, A.J. Burggraaf and P.J. Gellings, "Oxygen semipermeability of erbia-stabilized bismuth oxide," *Solid State Ionics*, **53-56** (1992) 460-468.
8. Y. Teraoka, T. Nobunaga and N. Yamazoe, "Effect of cation substitution on the oxygen semipermeability of perovskite-type oxides," *Chem. Lett.*, (1988) 503-506.
9. R.H.E. van Doorn, H. Kruidhof, H.J.M. Bouwmeester and A.J. Burggraaf, "Oxygen permeability of strontium-doped $LaCoO_{3-\delta}$," in: *Materials Research Society Symposium Proceedings, Vol. 369, Solid State Ionics IV*, ed. G.-A. Nazri, J.-M. Taracson and M.S. Schreiber, Materials Research Society, Pittsburgh, PA, 1995, p. 373-382.
10. N. Itoh, T. Kato, K. Uchida and K. Haraya, "Preparation of pore-free disks of $La_{1-x}Sr_xCoO_3$ mixed conductors and its oxygen permeability," *J. Membr. Sci.*, **92** (1994) 239-246.
11. Y. Teraoka, T. Nobunaga, K. Okamoto, N. Miura and N. Yamazoe, "Influence of constituent metal cations in substituted $LaCoO_3$ on mixed conductivity and oxygen permeability," *Solid State Ionics*, **48** (1991) 207-212.
12. T. Nakamura, G. Petzow and L.J. Gauckler, "Stability of the perovskite phase $LaBO_3$ (B=V, Cr, Mn, Fe, Co, Ni) in reducing atmospheres," *Mat. Res. Bull.*, **14** (1979) 649-659.
13. A.N. Petrov, V.A. Cherepanov, O.F. Kononchuk and L.Ya. Gavrilova, "Oxygen nonstoichiometry of $La_{1-x}Sr_xCoO_{3-\delta}$ ($0<x\leq0.6$)," *J. Solid State Chem.*, **87** (1990) 69-76.
14. H.J.M. Bouwmeester, H. Kruidhof and A.J. Burggraaf, "Influence of the surface exchange kinetics in rate limiting oxygen permeation through mixed-conducting oxides," *Solid State Ionics*, **72** (1994) 185-194.
15. H. Schmalzried, *Solid state reactions*, 2nd ed., Verlag Chemie, Weinheim, 1981.
16. J. Mizusaki, M. Yoshihiro, S. Yamauchi and K. Fueki, "Nonstoichiometry and defect structure of the perovskite-type oxide $La_{1-x}Sr_xFeO_{3-\delta}$," *J. Solid State Chem.*, **58** (1985) 257-266.
17. F.A. Kröger, *The Chemistry of Imperfect Crystals*, North-Holland, Amsterdam, 1964.
18. J. Mizusaki, M. Yoshihiro, S. Yamauchi and K. Fueki, "Thermodynamic quantities and defect equilibrium in the perovskite-type oxide solid solution $La_{1-x}Sr_xFeO_{3-\delta}$," *J. Solid State Chem.*, **67** (1987) 1-8.
19. S. Adler, S. Russek, J. Reimer, M. Fendorf, A. Stacy, Q. Huang, A. Santoro, J. Lynn, J. Baltisberger and U. Werner, "Local structure and oxide-ion motion in defective perovskites," *Solid State Ionics*, **68** (1994) 193-211.

20. C.N.R. Rao, J. Gopalakrishnan and K. Vidyasagar, "Superstructures, ordered defects & nonstoichiometry in metal oxides of perovskites & related structures," *Ind. J. Chem.*, **23A** (1984) 265-284.
21. Y. Takeda, K. Kanno, T. Takada, O. Yamamoto, M. Takano, N. Nakayama and Y. Bando, "Phase relation in the oxygen nonstoichiometric system, $SrFeO_x$ ($2.5<x<3$)," *J. Solid State Chem.*, **63** (1986) 237-249.
22. P.D. Battle, T.C. Gibb and S. Nixon, "A study of the ordering of oxygen vacancies in the nonstoichiometric perovskite $Sr_2LaFe_3O_{8+y}$ by Mössbauer spectroscopy and a comparison with $SrFeO_{3-y}$," *J. Solid State Chem.*, **79** (1989) 75-85.
23. J.-C. Grenier, N. Ea, M. Puchard and P. Hagenmuller, "Structural transitions at high temperatures in $Sr_2Fe_2O_{2.5}$," *J. Solid State Chem.*, **58** (1985) 243-252.
24. M.A. Alario-Franco, M.J.R. Henche, M. Vallet, J.M.G. Calbet, J.-C. Grenier, A. Wittiaux and P. Hagenmuller, "Microdomain texture and oxygen excess in the calcium-lanthanum ferrite: $Ca_2LaFe_3O_8$," *J. Solid State Chem.*, **46** (1983) 23-40.
25. J.M. González-Calbet, M. Vallet-Regí and M.A. Alario-Franco, "Structural intergrowth in the calcium-lanthanum ferrites: $Ca_xLa_{1-x}FeO_{3-y}$ ($2/3<x<1$)," *Mat. Res. Bull.*, **18** (1983) 285-292.
26. L. Fournès, Y. Potin, J.-C. Grenier, G. Demazeau and M. Pouchard, "High temperature Mössbauer spectroscopy of some $SrFeO_{3-y}$ phases," *Solid State Commun.*, **62** (1987) 239-244.
27. M. Takano, T. Okita, N. Nakayama, Y. Bando, Y. Takeda, O. Yamamoto and J.B. Goodenough, "Dependence of the structure and electronic state of $SrFeO_x$ ($2.5\leq x\leq 3$) on composition and temperature," *J. Solid State Chem.*, **73** (1988) 140-150.
28. J.M. González-Calbet, M. Parras, M. Vallet-Regí and J.C. Grenier, "Anionic vacancy distribution in reduced barium-lanthanum ferrites: $Ba_xLa_{1-x}FeO_{3-x/2}$ ($1/2\leq x\leq 2/3$)" *J. Solid State Chem.*, **92** (1991) 110-115.
29. T. Ishigaki, S. Yamauchi, J. Mizusaki, K. Fueki, H. Naito and T. Adachi, "Diffusion of oxide ion in $LaFeO_3$ single crystal," *J. Solid State Chem.*, **55** (1984) 50-53.
30. T. Ishigaki, S. Yamauchi, K. Kishio, J. Mizusaki and K. Fueki, "Diffusion of oxide ion vacancies in perovskite-type oxides," *J. Solid State Chem.*, **73** (1988) 179-187.
31. Chapter 3 of this thesis.
32. J.B. Goodenough, "Fast ionic conduction in solids," *Proc. R. Soc. Lond. A*, **393** (1984) 215-234.
33. M.C. Kim, S.J. Park, H. Haneda, J. Tanaka, T. Mitsuhasi and S. Shirasaki, "Self-diffusion of oxygen in $La_{1-x}Sr_xFeO_{3-\delta}$," *J. Mat. Sci. Let.*, **9** (1990) 102-104.
34. R.J.H. Voorhoeve, "Perovskite-related oxides as oxidation-reduction catalysts," in: *Advanced Materials in Catalysis*, ed. J.J. Burton and R.L. Garten, Academic Press, New York, 1977, p. 129-180.
35. J. Mizusaki, T. Sasamoto, W.R. Cannon and H.K. Bowen, "Electronic conductivity, Seebeck coefficient and defect structure of $La_{1-x}Sr_xFeO_3$ ($x$=0.1, 0.25)," *J. Am. Ceram. Soc.*, **66** (1983) 247-252.
36. S.E. Dann, D.B. Currie, M.T. Weller, M.F. Thomas and A.D. Al-Rawwas, "The effect of oxygen stoichiometry on phase relations and structure in the system $La_{1-x}Sr_xFeO_{3-\delta}$ ($0\leq x\leq 1$, $0\leq\delta\leq 0.5$)," *J. Solid State Chem.*, **109** (1994) 134-144.
37. B.A. van Hassel, T. Kawada, N. Sakai, H. Yokokawa, M. Dokiya and H.J.M. Bouwmeester, "Oxygen permeation modelling of perovskites," *Solid State Ionics*, **66** (1993) 295-305.
38. B.A. van Hassel, J.E. ten Elshof and H.J.M. Bouwmeester, "Oxygen permeation flux through $La_{1-x}Sr_xFeO_3$ limited by carbon monoxide oxidation rate," *Appl. Catal. A*, **119** (1994) 279-291.

# 3

# Oxygen transport through $La_{1-x}Sr_xFeO_{3-\delta}$ membranes

## Part II. Permeation in air/CO,$CO_2$ gradients


### Abstract

Oxygen permeation measurements were performed on dense $La_{1-x}Sr_xFeO_{3-\delta}$ ($x$=0.1-0.4) membranes in large oxygen activity gradients, i.e., air/CO,$CO_2$, in the temperature range 1173-1323 K, yielding fluxes up to 25 mmol $m^{-2}$ $s^{-1}$ at 1273 K. The oxygen semipermeability was linearly proportional to the CO partial pressure and the strontium content. It was concluded that the fluxes are limited by the surface exchange kinetics. Two simple models are proposed for the oxygen exchange reaction in the presence of CO. In both models oxygen vacancies at the phase boundary play a definite role in the exchange process. XPS and SEM analysis of the perovskite/CO,$CO_2$ interfaces indicated segregation of strontium, being present at the surface mostly in the form of $SrCO_3$ and/or SrO. The increased oxygen fluxes in air/He gradients as observed after exposure of the membrane surface to CO are probably (indirectly) related to the level of strontium segregation. Based on SEM analysis and surface profile measurements it is suggested that the segregation process is accompanied by an enlargement of the specific surface area, which may promote the rate of the overall permeation process under exchange-controlled conditions.

## 3.1. Introduction

The defect chemistry of $La_{1-x}Sr_xFeO_{3-\delta}$ ($x$=0-0.6) is well understood as a function of Sr content, oxygen partial pressure and temperature [1,2]. Properties such as the diffusion coefficient, electron and electron hole mobilities are also known [3-5]. In Part I [6] it was found that the oxygen semipermeable properties of $La_{1-x}Sr_xFeO_{3-\delta}$ membranes ($x$=0.1-0.4) in small partial pressure gradients, i.e., air/He, can be described by a diffusion-controlled mechanism. In the present chapter the oxygen permeation process through the same membranes is coupled to a simple chemical reaction, i.e., the oxidation of CO. The presence of CO,$CO_2$ mixtures results in large oxygen activity gradients across the membrane. Preliminary results showed a linear correlation between the oxygen flux and the CO partial pressure, indicating a surface exchange-controlled flux [7] under these circumstances.

Voorhoeve [8] divided oxidation catalysis by perovskite-type oxides $AMO_{3-\delta}$ into two types, suprafacial and intrafacial, depending on the predominant mechanism. CO oxidation at high temperature proceeds primarily through the partial removal of oxygen from the perovskite lattice and subsequent oxidation of the oxide bulk, and is an example of intrafacial catalysis. Thermodynamics, M-O bond strengths and oxygen diffusivity are the determining factors for this mechanism. An example of suprafacial catalysis is the oxidation of CO at relatively low temperatures, i.e., 400-650 K. It takes place by the reaction between adsorbed species and is therefore determined by the electronic configuration of localized sites on the surface. Most studies of CO oxidation on perovskite-type oxides were stimulated by the search for possible inexpensive substitutes of noble metals in automotive exhaust catalysts and were therefore performed in the range of 400-800 K at low concentrations and large space velocities [9-11]. Several relationships between the solid state chemistry and the catalytic activity of perovskites have been proposed. The catalytic activities of several $LaMO_{3-\delta}$ perovskite-type oxides (M=Cr, Mn, Fe, Co, Ni) at 500 K could be related to the crystal field stabilization energy [9] or Fermi level energy [8], revealing the suprafacial nature of the catalytic process under these conditions.

Nitadori et al. [12] observed that the catalytic activities of perovskites $LnMO_{3-\delta}$, with Ln and M being a trivalent rare-earth and a first-row transition metal cation, respectively, are determined by the nature of the transition metal cation. This implies that the activity may also be affected by the oxidation state of the transition metal. For the sake of experiment, its valency can be altered by (partial) substitution of trivalent Ln by di- or tetravalent cations. The effect of partial substitution of $La^{3+}$ by $Ca^{2+}$, $Sr^{2+}$, $Ba^{2+}$, $Ce^{4+}$ and $Th^{4+}$ has been studied. Doshi et al. [13] found a correlation between the p-type electrical conductivity and the rate of CO oxidation on $La_{1-x}Sr_xM_{1-y}M'_yO_{3-\delta}$ (M=Co, Cr, Fe, Mn; M'= Nb, Ti). However, it should be noted that even in unsubstituted $LaMO_3$, $M^{2+}$ and $M^{4+}$ cations co-exist with $M^{3+}$ in general, their relative concentrations depending on the oxygen partial pressure and temperature. Rao et al. [14] noticed a decrease in the catalytic activity of $LaCoO_{3-\delta}$ when the

catalyst was annealed in pure oxygen. It was suggested that this pretreatment lowers the oxygen deficiency and that the activity is reduced as a result. Nakamura et al. [15,16] determined the rates of reduction by CO and re-oxidation by $O_2$ of samples $La_{1-x}Sr_xCoO_{3-\delta}$ ($x$=0-0.6) as a function of the oxygen nonstoichiometry δ. The steady state catalytic activities were estimated from the intersection of the oxidation and reduction curves, and were found to agree well with the observed trend in activity, especially for large values of $x$. The catalytic process was explained in terms of a redoxlike (intrafacial) mechanism. The redox cycle involves a combined process of surface reaction and bulk diffusion of oxygen. To account for the discrepancies at small $x$, a suprafacial mechanism was suggested that was proposed earlier for $LaCoO_3$ by Tascón et al. [17]. The relationship between catalytic activity on one hand and oxygen vacancy concentration and electrical conductivity on the other has been observed also on the perovskite-related spinel-type oxide $La_{2-x}Sr_xCuO_{4-\delta}$ [18].

In this chapter the oxygen permeation properties of $La_{1-x}Sr_xFeO_{3-\delta}$ membranes ($x$=0.1-0.4) are studied when they are placed in an air/CO,$CO_2$ gradient. An attempt is made to relate the catalytic properties of $La_{1-x}Sr_xFeO_{3-\delta}$ to its oxygen vacancy concentration.

## 3.2. Theory

### *3.2.1. Bulk diffusion*

In small oxygen partial pressure gradients $p'_{O_2} / p''_{O_2}$ at relatively high oxygen partial pressures ($p'_{O_2} / p''_{O_2} > 10^{-4}$ bar), the permeation properties of $La_{1-x}Sr_xFeO_{3-\delta}$ membranes can be modeled by a diffusion mechanism [6]. The permeation flux can be expressed in terms of the Wagner equation:

$$j_{O_2} = \frac{RT}{16F^2L}\int_{p''_{O_2}}^{p'_{O_2}} \frac{\sigma_{ion}\sigma_{el}}{\sigma_{ion}+\sigma_{el}} d\ln p_{O_2} \quad . \tag{3.1}$$

Here $L$ is the membrane thickness (m); $\sigma_{ion}$ and $\sigma_{el}$ are the ionic and electronic conductivities (S $m^{-1}$), respectively; $p'_{O_2}$ and $p''_{O_2}$ are the oxygen partial pressures at opposite sides of the membrane.

At temperatures of 1000-1400 K and oxygen partial pressures $p_{O_2} > 10^{-5}$ bar, p-type electronic conductivity is predominant in $La_{1-x}Sr_xFeO_{3-\delta}$ and the electronic transference number is very close to unity. The electronic conductivity decreases with decreasing oxygen partial pressure, until a minimum is reached, where a transition from p-type to n-type conductivity occurs. The region of minimum electronic conductivity, typically $10^{-8}$-$10^{-13}$ bar $O_2$, coincides with a plateau region in the oxygen nonstoichiometry, where $\delta \approx x/2$, as shown in Figure 3.1.

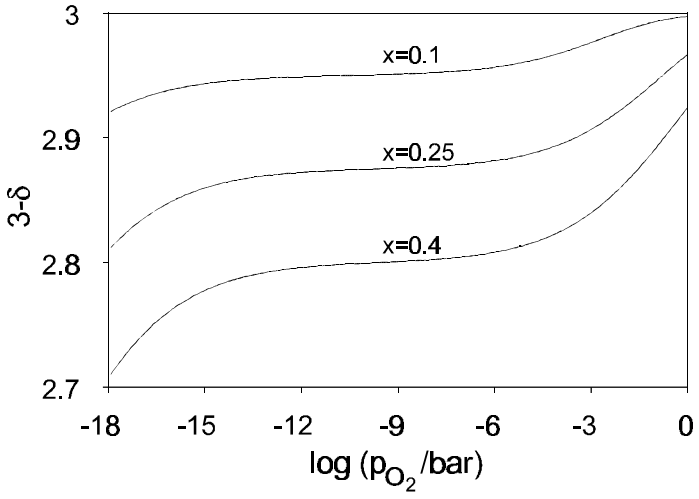


Figure 3.1. Calculated oxygen contents of $La_{1-x}Sr_xFeO_{3-\delta}$ for $x$=0.1-0.4 as function of log $p_{O_2}$ at 1273 K.

Figure 3.2 illustrates the calculated oxygen permeation fluxes. The partially limiting effect of the electronic conductivity on the oxygen permeation rate can be seen, especially for $x$=0.4, as a slight flattening of the curve at about $p_{O_2}=10^{-10}$ bar. Details of the calculations are described in the previous chapter.

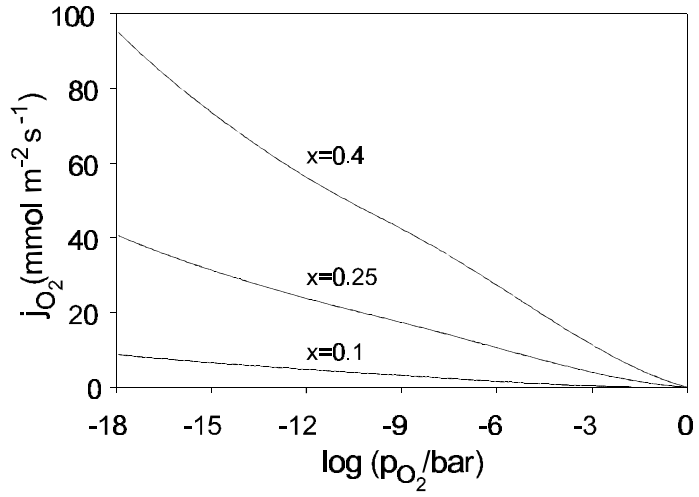


Figure 3.2. Calculated oxygen fluxes through 1.0 mm thick membranes at 1273 K as a function of the permeate side oxygen partial pressure when oxygen (1 bar) is supplied to the feed side. Model parameters are described in chapter 2.

### *3.2.2. Surface reaction*

Almost no details are known about the mechanism of oxygen exchange on perovskite-type oxides. In the absence of a chemical reaction occurring at one of the gas/solid interfaces, the overall process for the incorporation and release of oxygen can be written as

$$\tfrac{1}{2}O_2 + V_O^{\cdot\cdot} \rightleftharpoons O_O^x + 2h^{\cdot}, \tag{3.2}$$

using Kröger-Vink notation [19]. Based on $^{18}O/^{16}O$ exchange experiments, Boukamp et al. [20] proposed a two-step mechanism for the exchange on fluorite-type $Bi_{1.5}Er_{0.5}O_3$ in $O_2$-containing atmospheres, in which dissociative adsorption plus charge transfer appears to be rate-limiting at high $p_{O_2}$.

$$O_2 + 2e' \rightleftharpoons 2O_{ad}^{-}, \tag{3.3}$$

$$2O_{ad}^{-} + 2e' + 2V_O^{\cdot\cdot} \rightleftharpoons 2O_O^x. \tag{3.4}$$

Based on an observed interrelationship between the diffusion coefficients $D_O$ ($cm^2\ s^{-1}$) and the surface exchange coefficients $k_O$ ($cm\ s^{-1}$) of several oxides of the fluorite and perovskite types from $^{18}O/^{16}O$ exchange experiments, Kilner [21] suggested the possible involvement of surface oxygen vacancies in the exchange of oxygen. Since $D_O \approx \tfrac{1}{3} D_V \delta$ for perovskites, where the vacancy diffusion coefficient $D_V$ ($cm^2\ s^{-1}$) is approximately constant, the correlation between $D_O$ and $k_O$ suggests a correlation between $k_O$ and $\delta$ as well.

In the present study the effect of CO,$CO_2$ on the oxygen exchange reaction of perovskites $La_{1-x}Sr_xFeO_{3-\delta}$ is investigated. There is evidence that the mechanism of the surface reaction is changed drastically by their presence, e.g., from isotopic exchange on YSZ [22]. The overall reaction for the oxidation of CO can be written as

$$CO + O_O^x + 2h^{\bullet} \rightleftharpoons CO_2 + V_O^{\cdot\cdot}. \tag{3.5}$$

Yasuda and Hikita [23] found a linear correlation between the surface exchange constant and the nonstoichiometry of $La_{1-x}Ca_xCrO_{3-\delta}$ ($x$=0.1-0.3) in CO,$CO_2$ atmospheres from electrical conductivity relaxation experiments. This indicates that oxygen vacancies also play an essential role under these conditions.

## 3.3. Experimental

### *3.3.1. Permeation experiments*

The preparation of the $La_{1-x}Sr_xFeO_{3-\delta}$ membranes ($x$=0.1-0.4) and experimental procedure are described in Part I [6]. The density of the membranes was measured by means of an Archimedes method. Some samples of $La_{0.8}Sr_{0.2}FeO_{3-\delta}$ were sputtered with a 50 nm thick porous layer of Pt. The experimental setup is schematically depicted in Figure 3.3. Unless stated otherwise, air was supplied to the feed side of the membrane. Composition analysis of the permeate stream was performed by a Varian 3300 gaschromatograph coupled to a LDC/Milton Roy CL-10 integrator.

$O_2$, $N_2$ and CO were separated by a molecular sieve 13X. $CO_2$ was separated by a Porapak-N column. Measurements were performed only on leak-free membranes, in which case no nitrogen and oxygen were detected in the permeate stream. The oxygen fluxes were calculated from the mass balance of oxygen-containing species:

$$j_{O_2} = \frac{F}{A}(c^{out}_{CO_2} - c^{in}_{CO_2} + ½(c^{out}_{CO} - c^{in}_{CO})), \tag{3.6}$$

where $F$ is the flow rate at the permeate side ($m^3$ $s^{-1}$ (STP)), and $A$ the geometric surface area at the CO-side of the membrane ($m^2$). $c_i^{in}$ and $c_i^{out}$ are the inlet and outlet concentrations of species i.

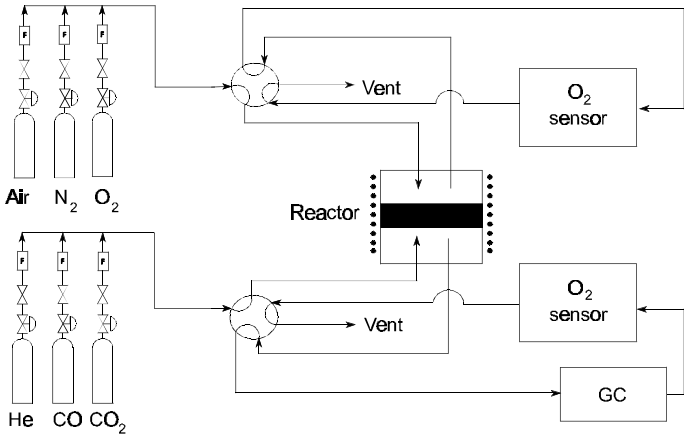


Figure 3.3. Schematic diagram of the experimental setup.

During the measurements, $F$ was kept at values between 7-25 ml/min (STP). In order to avoid deposition of carbon, the $CO/CO_2$ ratio was always kept above unity. Assuming ideal gas mixing behaviour, the oxygen pressure at the membrane/gas interface was calculated from the outlet partial pressures of CO and $CO_2$:

$$p_{O_2} = K\,(p_{CO_2}/p_{CO})^2. \tag{3.7}$$

The values of the equilibrium constant $K$ were obtained from a compilation of thermodynamic data given in Ref. [24].

### *3.3.2. Bulk analysis*

XRD spectra were taken on a Philips PW1710 with graphite-filtered CuKα radiation. $LaB_6$ was added as internal standard to powders obtained from crushed sintered membranes. The samples were measured with a 2θ scan from 20 to 130º with steps of 0.02º and the intensity was collected during 5-10 seconds. The $CuK\alpha_1$ (λ=1.5406 Å) component was used in the refinement procedure. The bulk concentrations of La, Sr

and Fe were determined by XRF (X-ray Fluorescence Spectroscopy) using a Philips PW 1480/10 X-ray spectrometer.

### *3.3.3. Surface analysis*

The membrane surface morphology was examined by HR-SEM (High Resolution Scanning Electron Microscopy) using a Hitachi S-800 Field Emission Microscope operating at 15 kV, which was coupled to a Kevex Delta Range EDX (Energy Dispersive X-ray analysis) system for surface element analysis. The surface profiles of the samples were measured using a Sloan DEKTAK 3030.

The XPS (X-ray Photoelectron Spectroscopy) experiments were carried out in a Kratos XSAM 800 system controlled by a PDP 11 microcomputer. For the excitation an AlKα radiation source (225 W) was used. The spectrometer was calibrated and its linearity checked by measuring the Ag $3d_{5/2}$, Cu $2p_{3/2}$ and Au $4f_{7/2}$ peaks on clean sputtered samples. The position of the C 1*s* peak, relative to its normal position at 284.8 eV, was used to correct the measured binding energies (BE) for electrostatic charging of the samples. The perovskite membrane surfaces were analyzed by measuring the La 3*d*, Fe 2*p* and Sr 3*d* spectra of clean sputtered samples. Analysis was performed using a DS 800 software package. 100% Gaussians were used for the synthesis of the Sr 3*d* peak. Internal consistency was maintained by constraining the spin-orbit coupling ΔBE(Sr $3d_{3/2}$-Sr $3d_{5/2}$) to 1.8 eV and the relative intensities and areas of the $3d_{5/2}$ and $3d_{3/2}$ components to a ratio of 3:2.

HR-TEM (High Resolution Transmission Electron Microscopy) and SAED (Selected Area Electron Diffraction) was performed with a Philips CM30 TWIN/(S)TEM operating at 300 keV, with an aperture of 0.1-0.2 mm (point resolution 2.3 Å), fitted with a double tilt goniometer stage (±45º). Measurements were performed on single-crystalline grains at the perovskite/CO interface at room temperature. The membranes were locally thinned with a Gatan dimple grinder, followed by ion milling.

## 3.4. Results and discussion

### *3.4.1. Crystal structure and bulk composition*

No second phases were detected in any sample. For $x$=0.1-0.3 all peaks could be indexed on the basis of an orthorhombic unit cell, whereas $x$=0.4 showed a rhombohedral symmetry. The refined unit cell parameters are given in Table 3.1.

The results are in good agreement with those obtained by others [5]. The bulk compositions determined by XRF are found to agree well with the corresponding nominal compositions. For the calculation of the cationic stoichiometries, listed in Table 3.2, it was assumed that the oxygen nonstoichiometries of the samples were negligible. The membrane densities were determined from an Archimedes type of method. The values, relative to theoretical, are also listed in Table 3.2.

Table 3.1. Unit cell data from XRD at room temperature for $x$=0.1-0.4.

| $x$ | Crystal system | $a$ (Å) | $b$ (Å) | $c$ (Å) |
|---|---|---|---|---|
| 0.1 | orthorhombic | 5.5403(1) | 5.5549(2) | 7.8351(2) |
| 0.2 | orthorhombic | 5.5254(6) | 5.5513(9) | 7.8267(2) |
| 0.3 | orthorhombic | 5.5210(8) | 5.5478(1) | 7.8054(3) |
| 0.4 | rhombohedral† | 5.5278(8) | | 13.4368(1) |

†Hexagonal setting.

### 3.4.2. Permeation experiments

Figure 3.4 shows the oxygen flux through $La_{0.9}Sr_{0.1}FeO_{3-\delta}$ at 1273 K versus the oxygen partial pressure. In the oxygen partial pressure range in which the measurements were performed, i.e., $p_{O_2}$ =$10^{-11}$-$10^{-15}$ bar, the nonstoichiometry $\delta \approx 0.05$. The model calculation is based on diffusion-limited permeation and would thus indicate an upper limit for the oxygen flux.

Table 3.2. Membrane densities and experimentally determined bulk composition of $La_pSr_qFe_rO_3$.

| $x$ | $\rho/\rho_{theor}$ (%) | $p$ | $q$ | $r$ |
|---|---|---|---|---|
| 0.1 | 96-97 | 0.90 | 0.10 | 0.99 |
| 0.2 | 95-96 | 0.80 | 0.20 | 0.99 |
| 0.3 | 94-95 | 0.70 | 0.29 | 1.00 |
| 0.4 | 91-92 | 0.60 | 0.40 | 1.00 |

Though the observed fluxes exceed this limit, the trends of theoretical and experimental behaviour differ substantially. Similar measurements for $x$=0.2 and $x$=0.3 showed no fluxes exceeding the theoretically predicted bulk diffusion limit, but the observed trends were similar to those seen for $La_{0.9}Sr_{0.1}FeO_{3-\delta}$. This suggests that application of the bulk diffusion model, used earlier to fit experimental data of oxygen permeation at relatively high oxygen pressures [6], is not valid when CO,$CO_2$ gas mixtures are present at the oxygen lean side of the membranes.

It is not clear why the diffusion limit is exceeded for $x$=0.1. Possibly, diffusion paths parallel to bulk diffusion contribute significantly to the overall diffusion process at low oxygen partial pressures, e.g., grain boundary diffusion. Furthermore, the vacancy diffusion coefficients $D_V$ used in the model calculations have only been determined at relatively high $p_{O_2}$, i.e., $10^{-3}$-1 bar. Although $D_V$ is generally considered to vary little with $\delta$, Yasuda and Hishinuma reported changes of $D_V$ of up to an order of magnitude at large $\delta$ in $La_{0.8}Sr_{0.2}Cr_{0.95}Ni_{0.05}O_{3-\delta}$ and $La_{0.65}Sr_{0.35}CrO_{3-\delta}$ [25], indicating that extrapolation to low oxygen partial pressures may not be allowed.

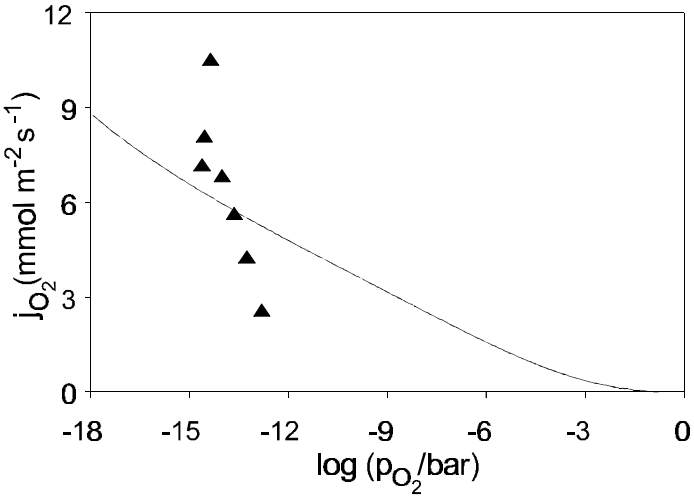


Figure 3.4. Experimental and calculated oxygen flux through a 1 mm thick membrane $La_{0.9}Sr_{0.1}FeO_{3-\delta}$ at 1273 K.

The oxygen flux is found to increase linearly with the CO partial pressure, as illustrated in Figure 3.5 for $x$=0.2. In view of Eq. (3.5), this clearly indicates the surface reaction of CO with lattice oxygen to be the rate-limiting step in the overall permeation process. Further evidence for a surface exchange-controlled flux is found from the observation that a sample sputtered with Pt shows a significantly increased flux. In comparison with the bare membrane, the slope ($dj_{O_2}/dp_{CO}$) is larger by a factor of 1.8±0.2 [7]. The absence of mass transfer limitations was verified by variation of the total flow rate between 7-25 ml/min (STP) at constant $p_{CO}$ at the outlet of the reactor. No significant change of the permeation was observed.

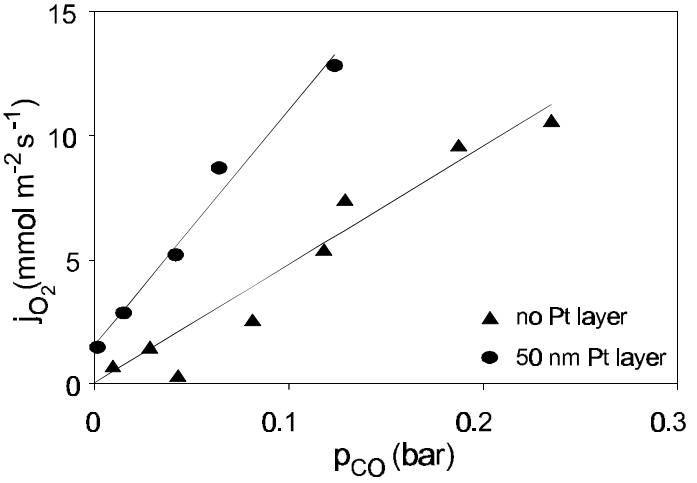


Figure 3.5. Oxygen flux through 1.0 mm thick $La_{0.8}Sr_{0.2}FeO_{3-\delta}$ membranes at 1273 K as function of the CO partial pressure.

Variation of the membrane thickness between 0.5 and 2.0 mm did not show any influence on the observed flux. Neither was an influence found from changing the

oxygen pressure at the higher partial pressure side. In the latter experiments, $p_{CO}$ was kept constant at a value of 0.12 bar, while the oxygen partial pressure at the feed side was varied between 0.02 and 1 bar. Thus, the surface reaction at the lower partial pressure side is fully limiting the oxygen flux.

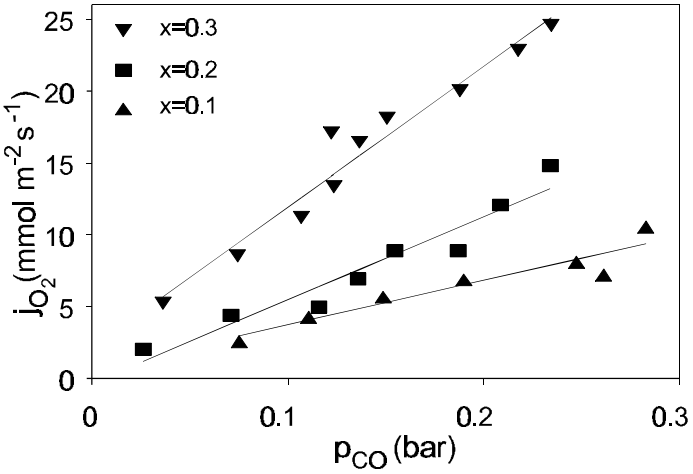


Figure 3.6. Oxygen fluxes through $La_{1-x}Sr_xFeO_{3-\delta}$ membranes at 1273 K as function of the CO partial pressure.

The effect of Sr doping on permeation at 1273 K is given in Figure 3.6. The oxygen flux clearly increases with increasing concentration of Sr. Due to instrumental limitations, the oxygen fluxes through $La_{0.6}Sr_{0.4}FeO_{3-\delta}$ were too large to be measured quantitatively, but the observed trends were comparable with those on other compounds. The slopes $k_{exp}$ ($dj_{O_2} / dp_{CO}$) of the plots of Figure 3.6 were determined by least-squares fitting. Figure 3.7 shows a linear relationship between $k_{exp}$ and $x$.

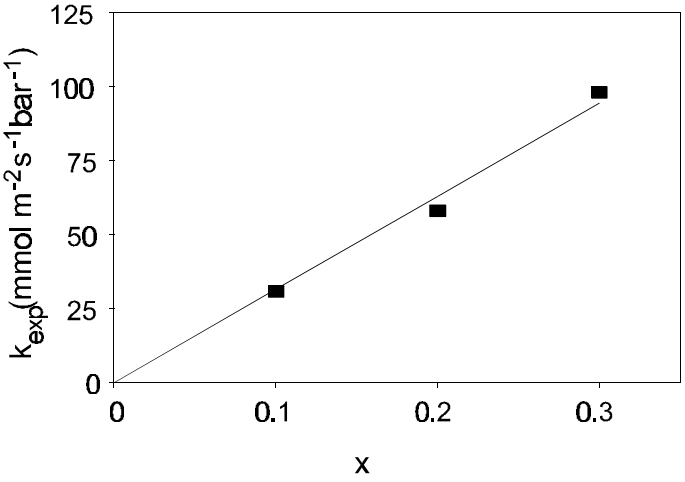


Figure 3.7. Slopes ($dj_{O_2}/dp_{CO}$) of $La_{1-x}Sr_xFeO_{3-\delta}$ ($x$=0.1-0.3) as shown in Figure 3.6.

By considering that the oxygen partial pressures in these experiments were in all cases in the range $10^{-10}$-$10^{-15}$ bar, in which region the oxygen nonstoichiometry of

$La_{1-x}Sr_xFeO_{3-\delta}$ is virtually constant, i.e., $\delta \approx x/2$, we may assume that oxygen vacancies play a role in the apparent exchange mechanism. It is unlikely that the proportionality is directly related to the strontium content, since catalytic studies on perovskites $AMO_3$ showed the activity not to be related to the nature of the A-site cation [12,26].

To account for the observed behaviour we may consider an Eley-Rideal mechanism [27] in which a surface oxygen anion can only be attacked by CO when it is residing next to a surface oxygen vacancy. When $\delta << 3-\delta$, the concentration of such vacancy-anion pairs is proportional to the vacancy concentration, leading to a proportionality between the flux and $\delta$. Since the oxygen vacancy concentrations do not exceed 5% of the total oxygen contents in the experiments presented here, $[V_O^{\bullet\bullet} - O_O^x] \approx [V_O^{\bullet\bullet}]$. Thus:

$$CO + V_O^{\bullet\bullet} - O_O^x \rightarrow CO_2 + V_O^{\bullet\bullet} - V_O^{\bullet\bullet} + 2e' . \tag{3.8}$$

A second explanation is that of a Langmuir-Hinshelwood type of mechanism in which CO adsorbs on a surface oxygen vacancy, before it reacts with a neighbouring oxygen ion:

$$CO + V_O^{\bullet\bullet} \rightarrow [V_O^{\bullet\bullet} \bullet\bullet\bullet CO]_s , \tag{3.9}$$

$$[V_O^{\bullet\bullet} \bullet\bullet\bullet CO]_s \rightarrow CO_2 + 2O_O^x + 2e' . \tag{3.10}$$

The first step is assumed to be rate-limiting. This model is in agreement with a suggestion done by Yasuda and Hikita for $La_{0.7}Ca_{0.3}CrO_{3-\delta}$ [23]. The authors speculated that gaseous species involved in the surface reaction (CO and $CO_2$) may form a temporary bond with vacant lattice sites present at the surface. It should be noted that due to the high temperatures, adsorption as assumed in this model is physically less likely. For both mechanisms described above, the kinetic expression for the oxygen flux is

$$j_{O_2} = \tfrac{1}{2} k_O^0 [V_O^{\bullet\bullet}] p_{CO} . \tag{3.11}$$

$[V_O^{\bullet\bullet}] = \delta$ by definition. When it is assumed that the value of $k_O^0$ does not vary with the strontium content, this gives

$$k_{exp} = \tfrac{1}{2} k_O^0 \delta . \tag{3.12}$$

From Figure 3.7, a value of 1.26±0.16 mol $m^{-2}$ $s^{-1}$ $bar^{-1}$ is found for $k_O^0$.

The positive intercepts in Figures 3.5 and 3.6 are due to the occurrence of a finite flux in the absence of CO [6], so that the overall expression for $j_{O_2}$ can be written as

$$j_{O_2} = j_0 + \tfrac{1}{2} k_O^0 \delta p_{CO} . \tag{3.13}$$

The activation energy for oxygen permeation was determined for $x$=0.3 in the temperature range 1173-1323 K from an experiment in which $p_{CO}$=0.08 bar and $p_{CO_2}$=0.32 bar were measured at the outlet. The Arrhenius plot is given in Figure 3.8. For the sake of comparison, the Arrhenius plot for the same compound (thickness 0.92 mm) in an air/He gradient is also shown. It is clear that under the conditions covered by the experiment, the oxygen flux is strongly increased by the presence of CO, and the activation energy has decreased. The calculated activation energy was found to be 31±19 kJ/mol. Using Eq. (3.11), we may interpret this activation energy as consisting of two contributions, namely the enthalpy of oxygen vacancy formation and the activation energy for $k_O^0$:

$$E_{act}(j_{O_2}) = E_{act}(k_O^0) + \Delta H_V(\delta). \tag{3.14}$$

Since the $CO/CO_2$ ratio was kept constant, the oxygen partial pressure changes considerably over the temperature interval ($10^{-12}$-$10^{-15}$ bar). The oxygen nonstoichiometry remains almost constant, varying from about 0.152 to 0.156 between 1173 and 1323 K. Thus, within experimental error, the apparent activation energy is almost completely determined by $k_O^0$.

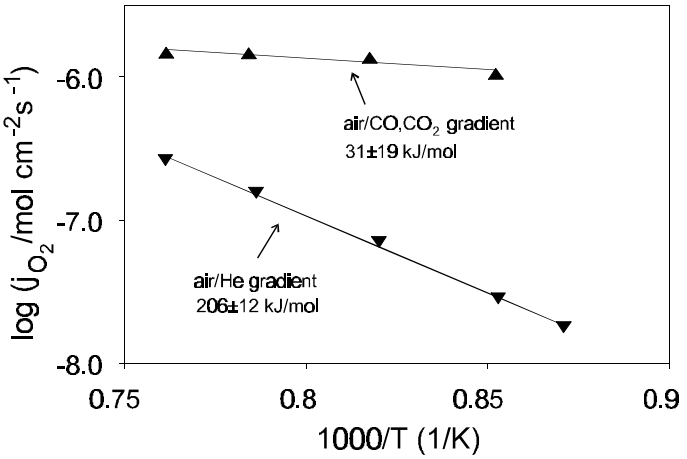


Figure 3.8. Apparent activation energies for oxygen permeation through $La_{0.7}Sr_{0.3}FeO_{3-\delta}$ in air/He [6] and air/$CO,CO_2$ gradients for 1.0 mm membranes.

### *3.4.3. Surface morphology and strontium segregation*

In the oxidation models proposed above, it is assumed that the surface composition is the same as that of the bulk. However, segregation of alkaline earth cations has been observed on several cobalt-based perovskites [28-30]. Furthermore, imposing an oxygen partial pressure gradient across the membrane appears to further increase the level of segregation [30]. Since the reaction model assumes $\delta=\frac{1}{2}[Sr_{La}^{'}]$, an increased strontium concentration in the near-surface layer may affect the local

concentration of oxygen vacancies. SEM, EDX and XPS analysis were performed to investigate segregation and surface morphology.

Several samples were quickly cooled down from reaction conditions to room temperature by quenching the quartz reactor in ice water. EDX analysis of the perovskite/CO,$CO_2$ interfaces did not show a significant deviation from the bulk composition. SEM analysis showed a second phase present at the surface, next to the perovskite phase. The morphology of this phase is very similar to that of $SrCO_3$ as found in a previous study on $La_{0.6}Sr_{0.4}Co_{0.8}Fe_{0.2}O_{3-\delta}$ and $La_{0.8}Ba_{0.2}Co_{0.8}Fe_{0.2}O_{3-\delta}$ membranes after exposure to air/methane gradients [29]. However, much higher levels of Sr and Ba segregation were observed in that case. The difference is most likely related to the large difference in chemical stability between cobalt- and iron-based perovskites [31].

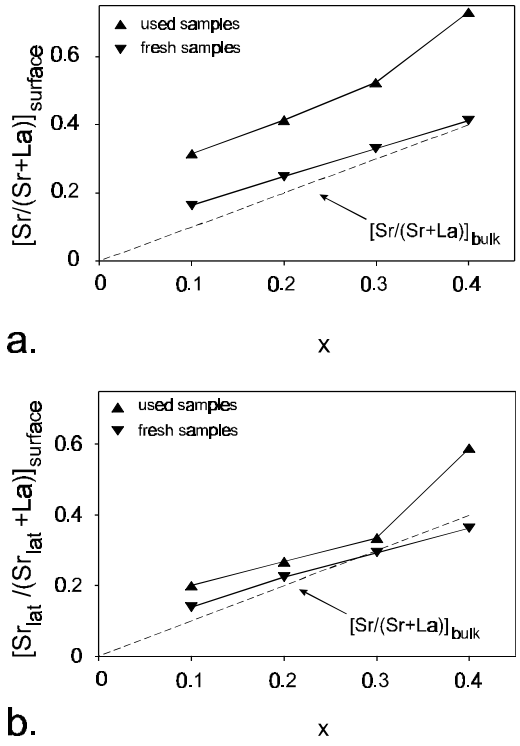


Figure 3.9. Normalized strontium concentration determined by XPS: a. Overall near-surface strontium concentration, b. Sr concentration in the near-surface perovskite lattice.

Semi-quantitative analysis of the level of Sr segregation was performed by XPS. Previous XPS work on related perovskites $La_{1-x}Sr_xCoO_{3-\delta}$ ($x$=0.4, 0.6) showed that the Sr 3*d* spectrum can be deconvoluted into a low (131.8 eV) and a high BE (133.8-134.2 eV) contribution [32]. The low BE has an anomalously low value and was attributed to strontium in the bulk of the perovskite. The high BE was considered to be due to the presence of minor second phases at the surface, such as $SrCO_3$ with a reported BE of 133.1-133.5 eV [33,34], and SrO with a BE of 135.1-

135.6 eV [33,35]. The strontium concentration at $La_{1-x}Sr_xFeO_{3-\delta}$ membrane surfaces is shown in Figure 3.9a.

Both fresh and used samples are enriched with Sr. The spectrum was deconvoluted into two components with $3d_{5/2}$ maxima at 131.4-131.8 eV and 133.2-133.9 eV. These peaks were attributed to strontium present in the form of $La_{1-x}Sr_xFeO_{3-\delta}$ and minor second phases, respectively. Their relative contributions to the total Sr 3*d* spectrum are given in Table 3.3. In each case these contributions are about 50% for the used samples, with the exception of the membrane that had only been exposed to He. The relative contributions of the high BE to the spectra of fresh samples are much smaller (12-19%). By using only the low BE contribution of the Sr 3*d* spectrum (denoted as $Sr_{lat}$), the Sr enrichment in the perovskite lattice near the surface can be estimated, as given in Figure 3.9b. Within experimental error, the fresh samples show little or no enrichment, whereas a slight enrichment is found for the used samples. The La/Fe ratios were also determined, and were found to be close to the bulk ratios for both the fresh and used membranes.

Table 3.3. Deconvolution of XPS-Sr 3*d* spectrum into high and low binding energy (BE) contributions for used and fresh membranes.

| *x* | Used | | Fresh | |
|---|---|---|---|---|
| | High BE (%) | Low BE (%) | High BE (%) | Low BE (%) |
| 0.1 | 46 | 54 | 17 | 83 |
| 0.2 | 48 | 52 | 12 | 88 |
| 0.3 | 54 | 46 | | |
| 0.4 | 47 | 53 | 19 | 81 |
| 0.4† | 31 | 69 | | |

†Sample exposed only to air/He gradient.

In Part I [6] it was reported that oxygen permeation through $La_{1-x}Sr_xFeO_{3-\delta}$ membranes in air/He gradients can be increased by treatment of the membrane's lower partial pressure side in a CO-containing atmosphere. XPS analysis of $La_{0.6}Sr_{0.4}FeO_{3-\delta}$ surfaces that had been exposed for 48 h to an air/He and an air/0.4 bar CO gradient, respectively, indicate a higher level of segregation for the latter sample. The [Sr/(Sr+La)] ratios at the surface are 0.61 and 0.73, respectively. The difference in strontium enrichment in the near-surface perovskite layers between the two samples is somewhat smaller, i.e., $[Sr_{lat}/(Sr_{lat}+La)]$ equals 0.52 and 0.59, respectively.

Thus it appears that strontium segregates to the surface where it forms $SrCO_3$ and/or SrO, and that this process is accelerated by the presence of $CO,CO_2$ mixtures. It is well possible that the level of segregation is correlated with the increased rate of oxygen exchange after treatment. For instance, it is conjectured that a larger specific area on which oxygen exchange can take place is directly or indirectly related to the level of segregation. The initial increase of the oxygen fluxes with time, as described

in Part I [6], may be indicative of the time scale on which the segregation process occurs.

Surface morphologies of a fresh and a used membrane (quenched from an air/CO gradient) of $La_{0.9}Sr_{0.1}FeO_{3-\delta}$ are shown in Figures 3.10 and 3.11. The membranes have a relative density of 96% and were taken from the same batch of material. The surface areas shown are representative for both types of surfaces. It appears that the surface roughness of the used membrane is larger, which indicates a larger specific surface area. Surface profile measurements also showed a small but reproducible increase of the surface roughness for the used membranes. In comparison with fresh samples, the surface profile lengths of used membranes were larger by a factor of 1.4-1.6. These results are in agreement with studies of Deng et al. [36,37], who showed theoretically that an enlargement of the specific surface area may have a very pronounced effect on the permeation fluxes through mixed conductors under conditions of surface exchange control.

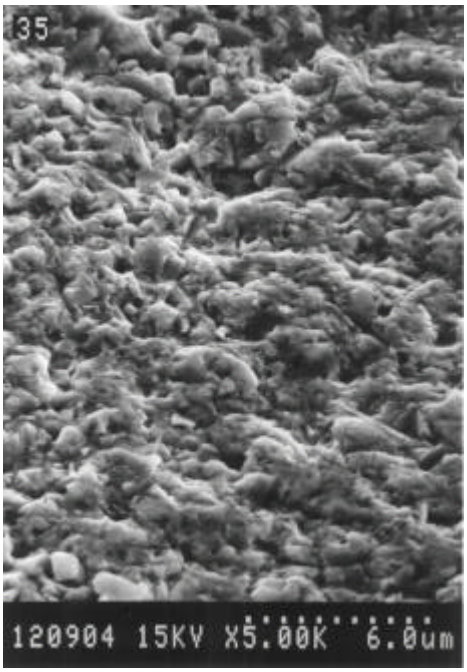


Figure 3.10. Surface morphology of $La_{0.9}Sr_{0.1}FeO_{3-\delta}$ before exposure to CO,$CO_2$.

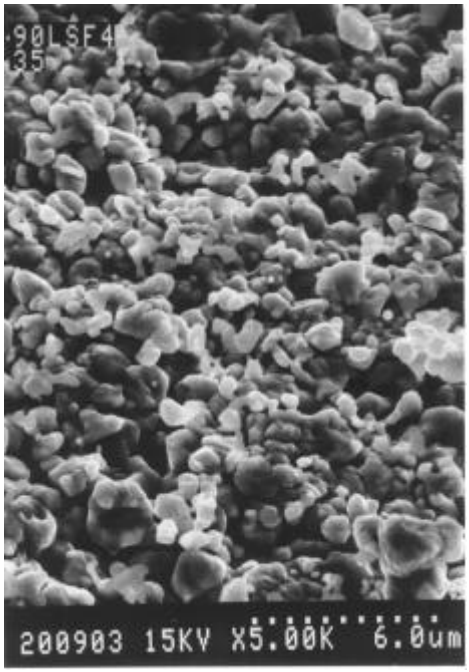


Figure 3.11. Surface morphology of $La_{0.9}Sr_{0.1}FeO_{3-\delta}$ after exposure to CO,$CO_2$.

Miura et al. [38] showed that the oxygen permeation rate through dense films of $La_{0.6}Sr_{0.4}Co_{0.8}Fe_{0.2}O_{3-\delta}$, prepared by slip casting, was increased significantly when the surface was treated with a solution containing 2 M $HNO_3$. The authors conclude that the acid treatment resulted in the removal of a surface layer containing impurities like SrO. Their XPS-Sr 3*d* spectrum of a freshly prepared surface showed maxima at 132 eV and 134 eV, with a shoulder at 135 eV. After the acid treatment, the low energy peak, assigned by the authors to SrO or $SrCO_3$, had disappeared completely,

while the intensity of the shoulder at 135 eV had increased. However, in contrast to their findings, XPS measurements in a study on perovskite-related superconductors $Bi_2Sr_2CaCu_2O_8$ and $Bi_2Sr_2CuO_6$ [39] indicate that the low energy peak is due to strontium from the perovskite lattice. XPS experiments on $SrCO_3$ powder performed in this laboratory showed the Sr $3d_{5/2}$ maximum at 133.2 eV. Furthermore, Table 3.3 shows that treatment of the membrane results in a strongly increased contribution of the high BE peak. It therefore appears that the acid treatment [38] decomposes the perovskite surface completely, forming SrO or $SrCO_3$, and is accompanied by an increased oxygen exchange rate. This result would be in agreement with the observations made here and in a methane coupling study on $La_{0.6}Sr_{0.4}Co_{0.8}Fe_{0.2}O_{3-\delta}$ membranes [30], where an increased oxygen flux was reported after reduction of the membrane surface by $CH_4$.

### *3.4.4. Crystal structure at the perovskite/CO interface*

Previous investigations on the relationship between crystal structure and oxygen content of the $La_{1-x}Sr_xFeO_{3-\delta}$ system [5] showed phase transitions to a cubic structure for $x$=0.3 and $x$=0.4 when the nonstoichiometry increased to a value of $x/2$. When the nonstoichiometry of these phases was small ($\delta \approx 0$), rhombohedral symmetry was found in $La_{0.6}Sr_{0.4}FeO_{3-\delta}$, and a mixture of rhombohedral and orthorhombic in $La_{0.7}Sr_{0.3}FeO_{3-\delta}$ [5].

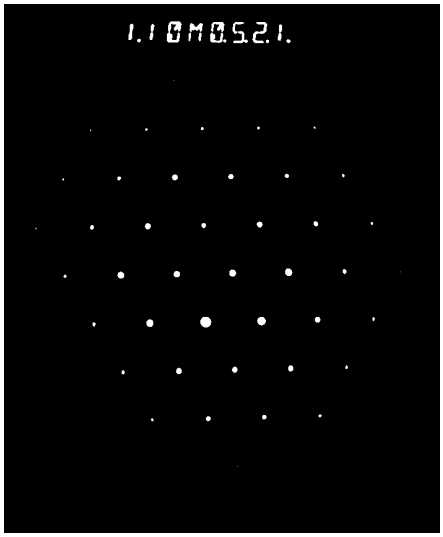

Figure 3.12. Electron diffraction pattern along the [$\bar{1}$11] zone axis of a cubic single-crystalline grain of $La_{0.6}Sr_{0.4}FeO_{3-\delta}$.

To verify the assumption of a strongly decreased oxygen concentration at the air/CO interface, SAED experiments were performed on single crystals at the interfaces of three $La_{0.6}Sr_{0.4}FeO_{3-\delta}$ membranes, either fresh or quenched from air/CO or air/He, respectively. In contrast to the rhombohedral symmetry found by XRD, only an

orthorhombic phase was found in the fresh sample, while both cubic ($a$=4.00±0.15 Å) and orthorhombic symmetries were observed in both used samples. A SAED pattern of a cubic crystal of $La_{0.6}Sr_{0.4}FeO_{3-\delta}$ is shown in Figure 3.12.

Measurements on $La_{0.7}Sr_{0.3}FeO_{3-\delta}$ samples gave similar results, with a unit cell parameter $a$=3.96±0.11 Å for the cubic grains. Although the presence of a cubic symmetry may indicate a high level of nonstoichiometry, care should be taken to attach great value to these results, since the simultaneous occurrence of more than one type of crystal symmetry, even in equilibrated samples, has been reported by Dann et al. [5]. Furthermore, the presence of an orthorhombic phase may indicate that part of the interface has been re-oxidized during the quench. Finally, cubic crystal symmetry does not necessarily prove a strongly decreased oxygen content, but may also be an intrinsic high temperature crystal structure, irrespective of the level of nonstoichiometry.

## 3.5. Conclusions

The oxygen semipermeability of dense mixed-conducting membranes with nominal composition $La_{1-x}Sr_xFeO_{3-\delta}$ ($x$=0.1-0.3) in air/CO,$CO_2$ gradients appeared to be limited by the rate of CO oxidation at the gas/solid interface. The activation energy found for $La_{0.7}Sr_{0.3}FeO_{3-\delta}$ was 31±19 kJ/mol, much lower than in air/He gradients. The oxygen fluxes were linearly proportional to the CO partial pressure and can be explained by simple models for the oxidation of CO. Essentially, these models yield the same kinetic expression for the flux and both are based on the assumption that the nonstoichiometry parameter $\delta$ is approximately equal to $\frac{1}{2}x$ at the perovskite/CO,$CO_2$ interface. Although segregation of strontium was found at the surface, the enrichment of Sr in the near-surface perovskite layer was found to be small. $SrCO_3$ and possibly SrO was found on the membrane surface, but no signs of complete decomposition of the perovskite surface were observed. SEM analysis and profile measurements of the membrane surfaces indicated an enlargement of the specific surface area after exposure to CO, which may explain the increased fluxes that were observed. SAED on single-crystalline grains at the interface of $La_{1-x}Sr_xFeO_{3-\delta}$ ($x$=0.3, 0.4) showed cubic symmetry to be present in several grains, while no cubic symmetry was observed in fresh membranes.

## References

1. J. Mizusaki, M. Yoshihiro, S. Yamauchi and K. Fueki, “Nonstoichiometry and defect structure of the perovskite-type oxides $La_{1-x}Sr_xFeO_{3-\delta}$,” *J. Solid State Chem.*, **58** (1985) 257-266.
2. J. Mizusaki, M. Yoshihiro, S. Yamauchi and K. Fueki, “Thermodynamic quantities and defect equilibrium in the perovskite-type oxide solid solution $La_{1-x}Sr_xFeO_{3-\delta}$,” *J. Solid State Chem.*, **67** (1987) 1-8.

3. T. Ishigaki, S. Yamauchi, K. Kishio, J. Mizusaki and K. Fueki, "Diffusion of oxide ion vacancies in perovskite-type oxides," *J. Solid State Chem.*, **73** (1988) 179-187.
4. J. Mizusaki, T. Sasamoto, W.R. Cannon and H.K. Bowen, "Electrical conductivity, Seebeck coefficient, and defect structure of $La_{1-x}Sr_xFeO_3$," *J. Am. Ceram. Soc.*, **66** (1983) 247-252.
5. S.E. Dann, D.B. Currie, M.T. Weller, M.F. Thomas and A.D. Al-Rawwas, "The effect of oxygen stoichiometry on phase relations and structure in the system $La_{1-x}Sr_xFeO_{3-\delta}$," *J. Solid State Chem.*, **109** (1994) 134-144.
6. Chapter 2 of this thesis.
7. B.A. van Hassel, J.E. ten Elshof and H.J.M. Bouwmeester, "Oxygen permeation flux through $La_{1-y}Sr_yFeO_3$ limited by carbon monoxide oxidation rate," *Appl. Catal. A*, **119** (1994) 279-291.
8. R.J.H. Voorhoeve, J.P. Remeika and L.E. Trimble, "Defect chemistry and catalysis in oxidation and reduction over perovskite-type oxides," *Ann. N.Y. Acad. Sci.*, **3** (1976) 3-20.
9. J.M.D. Tasc∴n, S. Mendioroz and L.G. Tejuca, "Preparation, characterization and catalytic properties of $LaMeO_3$ oxides," *Z. Phys. Chem.*, **124** (1981) 109-127.
10. L. Wachowski, "The activity of $LaMeO_3$ oxides obtained by various methods for the catalitic oxidation of CO and 1-butene," *Z. Phys. Chem.*, **269** (1988) 743-752.
11. G. Kremeni , J.M.L. Nieto, J.M.D. Tasc∴n and L.J. Tejuca, "Chemisorption and catalysis on $LaMO_3$ oxides," *J. Chem. Soc., Faraday Trans. 1*, **81** (1985) 939-949.
12. T. Nitadori, T. Ichiki and M. Misono, "Catalytic properties of perovskite-type oxides ($ABO_3$) consisting of rare earth and 3*d* transition metals. The roles of the A- and B-site ions," *Bull. Chem. Soc. Jpn.*, **61** (1988) 621-626.
13. R. Doshi, C.B. Alcock, N. Gunasekaran and J.J. Carberry, "Carbon monoxide and methane oxidation properties of oxide solid solution catalysis," *J. Catal.*, **140** (1993) 557-563.
14. D.Y. Rao and D.K. Chakrabarty, "Oxidation of carbon monoxide on perovskite cobaltites $Ln_{1-x}M_xCoO_3$ (Ln=La, Sm; M=Ba, Pb, Th)," *Ind. J. Chem.*, **23A** (1984) 375-378.
15. T. Nakamura, M. Misono and Y. Yoneda, "Catalytic properties op perovskite-type mixed oxides $La_{1-x}Sr_xCoO_3$," *Bull. Chem. Soc. Jpn.*, **55** (1982) 394-399.
16. T. Nakamura, M. Misono and Y. Yoneda, "Reduction-oxidation and catalytic properties of $La_{1-x}Sr_xCoO_3$," *J. Catal.*, **83** (1983) 151-159.
17. J.M.D. Tasc∴n, J.L.G. Fierro and L.G. Tejuca, "Kinetics and mechanism of CO oxidation on $LaCoO_3$," *Z. Phys. Chem.*, **124** (1981) 249-257.
18. S. Rajaduraj, J.J. Carberry, B. Li and C.B. Alcock, "Catalytic oxidation of carbon monoxide over superconducting $La_{2-x}Sr_xCuO_{4-\delta}$ systems between 373-523 K," *J. Catal.*, **131** (1986) 582-589.
19. F.A. Kröger, *The chemistry of imperfect crystals*, North-Holland, Amsterdam, 1964.
20. B.A. Boukamp, H.J.M. Bouwmeester and A.J. Burggraaf, "The surface oxygen exchange process in oxygen conducting materials," Proc. 2nd Intl. Symp. on *Ionic and Mixed Conducting Oxides*, ed. T.A. Ramanarayanan, W.L. Worrel and H.L. Tuller, Proc. vol. 94-12, The Electrochem. Soc, Pennington, NJ, 1994, p. 141-149.
21. J.A. Kilner, "Isotopic exchange in mixed and ionically conducting oxides," Proc. 2nd Intl. Symp. on *Ionic and mixed conducting oxides*, ed. T.A. Ramanarayanan, W.L. Worrell and H.L. Tuller, Proc. vol. 94-12, The Electrochemical Society, Pennington, NJ, 1994, p. 174-190.
22. E.Kh. Kurumchin and M.V. Perfiliev, "An isotope exchange study of the behaviour of electrochemical systems," *Solid State Ionics*, **42** (1990) 129-133.
23. I. Yasuda and T. Hikita, "Precise determination of the chemical diffusion coefficient of calcium-doped lanthanum chromites by means of electrical conductivity relaxation," *J. Electrochem. Soc.*, **141** (1994) 1268-1273.

24. I. Barin and O. Knacke, *Thermochemical properties of inorganic substances*, Springer, Berlin, Heidelberg, New York, 1973.
25. I. Yasuda and M. Hishinuma, "Electrical conductivity and chemical diffusion coefficient of Sr-doped lanthanum chromites," *Solid State Ionics*, **80** (1995) 141-150.
26. P.E. Marti and A. Baiker, "Influence of the A-site cation in $AMO_{3+x}$ and $AFeO_{3+x}$ (A=La, Pr, Nd, Gd) perovskite-type oxides on the catalytic activity for methane combustion," *Catal. Lett.*, **26** (1994) 71-84.
27. *Catalysis: an integrated approach to homogeneous, heterogeneous and industrial catalysis*, Studies in surface science and catalysis, vol.79, ed. J.A. Moulijn, P.W.N.M. van Leeuwen and R.A. van Santen. Elsevier, Amsterdam, 1993.
28. K. Tabata, I. Matsumoto and S. Kohiki, "Surface characterization and catalytic properties of $La_{1-x}Sr_xCoO_3$," *J. Mat. Sci.*, **22** (1987) 1882-1886.
29. J.E. ten Elshof, B.A. van Hassel and H.J.M. Bouwmeester, "Activation of methane using solid oxide membranes," *Catal. Today*, **25** (1995) 397-402.
30. Chapter 7 of this thesis.
31. T. Nakamura, G. Petzow and L.J. Gauckler, "Stability of the perovskite phase $LaBO_3$ (B=V, Cr, Mn, Fe, Co, Ni) in reducing atmospheres," Mat. Res. Bull., **14** (1979) 649-659.
32. A.E. Bocquet, P. Chalker, J.F. Dobson, P.C. Healy, S. Myhra and J.G. Thompson, "X-ray photoelectron spectra of perovskite-type cobalt oxides $La_{1-x}Sr_xCoO_{3-y}$ ($x$=0.4, 0.6)," *Physica C*, **160** (1989) 252-258.
33. J.F. Moulder, W.F. Stickle, P.E. Sobol and K.D. Bomben, *Handbook of X-ray photoelectron spectroscopy. A reference book of standard spectra for identification and interpretation of XPS data*, Ed. J. Chastain, Perkin-Elmer Corporation, Eden Prairie, USA, 1992.
34. A.B. Christie, J. Lee, I. Sutherland and J.M. Walls, "An XPS study of ion-induced compositional changes with group II and group IV compounds," *Appl. Surf. Sci.*, **15** (1983) 224-237.
35. H. van Doveren and J.A. Verhoeven, "XPS spectra of Ca, Sr, Ba and their oxides," *J. Electron Spectrosc. Relat. Phenom.*, **21** (1980) 265-273.
36. H. Deng, M. Zhou and B. Abeles, "Diffusion-reaction in mixed ionic-electronic solid oxide membranes with porous electrodes," *Solid State Ionics*, **74** (1994) 75-84.
37. H. Deng, M. Zhou and B. Abeles, "Transport in porous electrodes: effect of gas diffusion," *Solid State Ionics*, **80** (1995) 213-222.
38. N. Miura, Y. Okamoto, J. Tamaki, K. Morinaga and N. Yamazoe, "Oxygen semipermeability of mixed-conductive oxide thick-film prepared by slip casting," *Solid State Ionics*, **79** (1995) 195-200.
39. A.E. Bocquet, J.F. Dobson, P.C. Healy, S. Myhra and J.G. Thompson, "X-ray photoelectron spectra of High $T_c$ bismuth compounds," *Phys. Stat. Sol. B*, **152** (1989) 519-532.

# 4

# Oxygen exchange and diffusion coefficients of $La_{1-x}Sr_xFeO_{3-\delta}$ by conductivity relaxation


## Abstract

Electrical conductivity relaxation experiments were performed on thin specimens of $La_{1-x}Sr_xFeO_{3-\delta}$ ($x$=0.1, 0.4) at oxygen partial pressures $p_{O_2}$ =$10^{-5}$-1 bar in the temperature range 923-1223 K. The transient response of the electrical conductivity after a sudden change of the ambient oxygen partial pressure was analyzed in the frequency domain. The latter procedure allowed to distinguish between diffusion-limited and surface exchange-limited kinetics of re-equilibration. The response of specimens with thicknesses of 350-460 µm indicated diffusion-controlled kinetics at $p_{O_2}$ >0.03 bar. The chemical diffusion coefficients $\tilde{D}$ were found invariant with oxygen pressure. At 1073 K the absolute values were $\tilde{D}$ =6.5·$10^{-6}$ $cm^2$ $s^{-1}$ for $x$=0.1 and $\tilde{D}$ =1.1·$10^{-5}$ $cm^2$ $s^{-1}$ for $x$=0.4, with activation energies of about 80 kJ/mol. The equilibration process was governed by surface exchange at $p_{O_2}$ <0.01 bar. The surface exchange coefficient $k_O$ was proportional to $p_{O_2}^n$, where $n$=0.65-0.85. This pressure dependence was interpreted in terms of a slow surface process involving an oxygen molecule and a surface oxygen vacancy, and causes the observed sharp transition from diffusion- to exchange-controlled kinetics. The activation energy of $k_O$ was estimated to be 110-135 kJ/mol.

## 4.1. Introduction

Perovskite-type solid oxide solutions $La_{1-x}Sr_xFeO_{3-\delta}$ are candidate materials for use as high temperature electrodes and oxygen separation membranes. In two previous chapters [1,2] the oxygen permeation properties of dense $La_{1-x}Sr_xFeO_{3-\delta}$ membranes were investigated under variation of oxygen partial pressure gradients. It was demonstrated that the surface exchange kinetics of oxygen play a rate-determining role under steady state conditions in both air/He and air/CO,$CO_2$ gradients, in particular at the oxygen lean side of the membrane. By exposing this side to a CO-containing atmosphere at high temperature the surface exchange rate was significantly increased. Although the overall permeation rate remained exchange-limited in air/CO,$CO_2$ gradients, diffusion became rate-determining in $O_2$-containing atmospheres after exposure to CO. A mechanism in which oxygen vacancies play a definite role was proposed for the exchange process in the presence of CO [2].

Electrical conductivity relaxation experiments on cylindrical samples of $La_{1-x}Ca_xCrO_{3-\delta}$ ($x$=0.1-0.3) in CO,$CO_2$ atmospheres by Yasuda and Hikita [3] also indicated the involvement of oxygen vacancies in the exchange process. The same technique is applied to $La_{1-x}Sr_xFeO_{3-\delta}$ in the present chapter. In relaxation experiments, the time-dependent response of a physical property of the solid oxide is monitored, e.g., mass or electrical conductivity, after imposing a step-wise change of the chemical potential of molecular oxygen in the ambient atmosphere. Although the most direct way to obtain information about oxygen diffusion and surface exchange is to measure its mass change, the measurement of electrical conductivity has the advantage of being more sensitive to variations in oxygen pressure. This requires that the concentrations of ionic and electronic defects are correlated, e.g., via the charge neutrality requirement. According to thermogravimetric analyses by Mizusaki et al. [4], the defect chemistry of $La_{1-x}Sr_xFeO_{3-\delta}$ can be modeled quantitatively in terms of two point defect equilibria over a wide range of temperatures, oxygen partial pressures and strontium doping levels. In Kröger-Vink notation [5] these defect reactions read

$$\tfrac{1}{2}O_2 + V_O^{\cdot\cdot} + 2\,Fe_{Fe}^{x} \rightleftharpoons O_O^{x} + 2\,Fe_{Fe}^{\cdot}, \tag{4.1}$$

$$2\,Fe_{Fe}^{x} \rightleftharpoons Fe_{Fe}^{\cdot} + Fe_{Fe}^{\prime}. \tag{4.2}$$

Many studies employing the electrical conductivity relaxation technique have been reported, covering a wide range of oxides, e.g., Refs. [6-12]. Whether the overall kinetics of re-equilibration after a step change is governed by surface exchange or diffusion depends on the geometry of the specimen under investigation. For any given geometry, a typical length $L_c$, indicating the average distance across which transport of matter has to take place in order to equilibrate the entire specimen, can

be identified. Diffusion-limited re-equilibration occurs when $L_c \ll 1/h$ [13], with $h$ defined by

$$h = \frac{k_O}{D_O}. \tag{4.3}$$

$D_O$ and $k_O$ are the oxygen self-diffusion coefficient ($cm^2/s$) and surface exchange coefficient (cm/s), respectively. Surface controlled kinetics are encountered when the sample dimensions are decreased to such an extent that $L_c \gg 1/h$.

In studies reported to date, the geometry of the specimen is usually chosen such as to ensure an overall rate limitation by diffusion. Moreover it is generally assumed that the oxide interface equilibrates immediately with the newly imposed atmosphere, i.e., $k_O = \infty$. Several authors [14-17] have pointed out that large systematic errors may have been caused in some of these studies by neglecting the surface exchange process.

The chemical diffusion coefficient $\tilde{D}$ is usually determined by fitting the time-dependent theoretical curve to the experimental data. The disadvantage of this approach is that bulk diffusion and (linear) surface kinetics can not be distinguished easily, which may lead to misinterpretation of the nature of the re-equilibration process. In the frequency domain the two processes have quite different characteristics, and the analysis is not complicated if both are rate-limiting to more or less similar extents.

The aim of the present study is to determine the relevant transport parameters of the perovskite-type oxide $La_{1-x}Sr_xFeO_{3-\delta}$ (LSF) ($x$=0.1, 0.4), with emphasis on the investigation of the surface exchange kinetics. Thin dense specimens of perovskite material ($L_c \approx$175-230 μm) with large superficial surface areas are used to ensure one-dimensional diffusion. The chemical diffusion and surface exchange coefficients are determined from experimental data in the frequency domain, assuming linear kinetic behaviour for the surface exchange process.

## 4.2. Theoretical background

### *4.2.1. Transient response to a stepwise change of gas phase oxygen activity*

Consider a large plane sheet with sides $A$ and thickness $L$ ($A \gg L$) in chemical and thermal equilibrium with the surrounding atmosphere. The initial oxygen concentration in the solid is $c_s$.

At $t$=0, the oxygen activity in the ambient atmosphere is changed stepwise to a new value which corresponds with a new equilibrium concentration $c_g$ in the solid. Depending on the value of $c_g$ relative to $c_s$, oxygen starts to diffuse into or out of the solid via exchange with the gas phase. The oxygen concentration at a certain time $t$

and position $z$ (-½$L$#$z$#½$L$) in the solid is given by $c_O(z,t)$. The concentration $c(z,t)$ is defined as

$$c(z,t) = c_O(z,t) - c_s \,. \tag{4.4}$$

This concentration can be calculated by solving Fick's second law

$$\frac{\partial c(z,t)}{\partial t} = \tilde{D}\,\frac{\partial^2 c(z,t)}{\partial z^2}\,, \tag{4.5}$$

where $\tilde{D}$ is the chemical diffusion coefficient (cm$^2$ s$^{-1}$). Assuming linear interface kinetics, the boundary conditions are

$$-\tilde{D}\frac{\partial c(z,t)}{\partial z}\bigg|_{z=-½L} = K_{ex}(c_g - c_O(-½L,t)) = K_{ex}(\Delta c - c(-½L,t))\,, \tag{4.6}$$

$$-\tilde{D}\frac{\partial c(z,t)}{\partial z}\bigg|_{z=½L} = -K_{ex}(c_g - c_O(½L,t)) = -K_{ex}(\Delta c - c(½L,t))\,. \tag{4.7}$$

$K_{ex}$ (cm s$^{-1}$) is the apparent surface exchange coefficient, and $\Delta c \equiv c_g - c_s$. Fick's law is solved in the Laplace domain. The Laplace transform $\mathcal{L}(f(t)) = \overline{f(s)}$ of Eq. (4.5) reads

$$s \cdot \overline{c(z,s)} = \tilde{D}\,\frac{\partial^2 \overline{c(z,s)}}{\partial z^2}\,, \tag{4.8}$$

which has as a general solution

$$\overline{c(z,s)} = A\,\mathrm{e}^{kz} + B\,\mathrm{e}^{-kz}\,, \tag{4.9}$$

where $k = \sqrt{s/\tilde{D}}$. The Laplace transforms of the boundary conditions (4.6) and (4.7) are

$$-\tilde{D}\frac{\partial \overline{c(z,s)}}{\partial z}\bigg|_{z=-½L} = K_{ex}(\overline{\Delta c} - \overline{c(-½L,s)}) = K_{ex}\left(\frac{\Delta c}{s} - \overline{c(-½L,s)}\right), \tag{4.10}$$

$$-\tilde{D}\frac{\partial \overline{c(z,s)}}{\partial z}\bigg|_{z=½L} = -K_{ex}(\overline{\Delta c} - \overline{c(½L,s)}) = -K_{ex}\left(\frac{\Delta c}{s} - \overline{c(½L,s)}\right). \tag{4.11}$$

Inserting Eq. (4.9) into the above equations yields the values $A$ and $B$, and substitution results in

$$\overline{c(z,s)} = \overline{\Delta c}\left(1+\frac{k\tilde{D}}{K_{ex}}\tanh(½kL)\right)^{-1}\frac{\cosh(kz)}{\cosh(½kL)}. \tag{4.12}$$

In the time domain, the total mass change of the specimen is

$$m(t) = A^2 M_O \int_{-½L}^{½L} c(z,t)\,dz\ . \tag{4.13}$$

with $M_O$ the atomic mass of oxygen. The Laplace transform of the relative mass change $m(t)/m(\infty)$ is then expressed by

$$\frac{\overline{m(s)}}{m(\infty)} = \frac{1}{L\,\Delta c}\int_{-½L}^{½L}\overline{c(z,s)}\,dz = \left(1+\frac{k\tilde{D}}{K_{ex}}\tanh(½kL)\right)^{-1}\left(\frac{2}{skL}\right)\tanh(½kL). \tag{4.14}$$

### *4.2.2. Relationship between electrical conductivity and mass change*

The mass change of a $La_{1-x}Sr_xFeO_{3-\delta}$ specimen can be related to its electrical conductivity change via the charge neutrality requirement

$$[e'] + [Sr'_{La}] = [h^{\cdot}] + 2[V_O^{\cdot\cdot}], \tag{4.15}$$

where $[e']$ is the concentration of $Fe^{2+}$ ($Fe'_{Fe}$) and $[h^{\cdot}]$ the $Fe^{4+}$ concentration ($Fe^{\cdot}_{Fe}$). Under the conditions covered by the experiments described below, i.e., at sufficiently high values of $p_{O_2}$, it can be safely assumed that $[e'] \ll [Sr'_{La}], [h^{\cdot}], [V_O^{\cdot\cdot}]$. Since $[Sr'_{La}] = x$ is constant, any local change of the oxygen vacancy concentration is then linearly related to the accompanying electron hole concentration change:

$$\frac{[h^{\cdot}(z,t)]-[h^{\cdot}(z,0)]}{[h^{\cdot}(z,\infty)]-[h^{\cdot}(z,0)]} = \frac{[V_O^{\cdot\cdot}(z,t)]-[V_O^{\cdot\cdot}(z,0)]}{[V_O^{\cdot\cdot}(z,\infty)]-[V_O^{\cdot\cdot}(z,0)]}. \tag{4.16}$$

The local electron hole conductivity $\sigma_h(z,t)$ ($\Omega^{-1}\,m^{-1}$) is defined by $\sigma_h(z,t) = q_h \mu [h^{\cdot}(z,t)]$, with $q_h$ the hole charge (C) and $\mu$ the hole mobility ($cm^2\,V^{-1}\,s^{-1}$). The apparent conductivity $\sigma_{app}(t)$ on macroscopic scale is measured perpendicular to the direction in which the net oxygen transport occurs. It can be shown [3] that the following proportionality holds:

$$\sigma_{app}(t) = \frac{1}{L}\int_{-½L}^{½L}\sigma_h(z,t)\,dz\ . \tag{4.17}$$

The relative mass change $m(t)/m(\infty)$ of the specimen can be related to the relative average change of the oxygen vacancy concentration:

$$\frac{m(t)}{m(\infty)} = \frac{1}{L}\int_{-½L}^{½L} \frac{[V_O^{\cdot\cdot}](z,t)-[V_O^{\cdot\cdot}](z,0)}{[V_O^{\cdot\cdot}](z,\infty)-[V_O^{\cdot\cdot}](z,0)}\,dz\,. \tag{4.18}$$

Combination of Eqs. (4.16)-(4.18) and Laplace transformation leads to

$$\overline{\sigma_{app}^{rel}(s)} = \mathrm{L}\left(\frac{\sigma_{app}(t)-\sigma_{app}(0)}{\sigma_{app}(\infty)-\sigma_{app}(0)}\right) = \frac{\overline{m(s)}}{m(\infty)}\,. \tag{4.19}$$

### *4.2.3. Diffusion coefficients and surface exchange coefficients*

The oxygen self diffusion coefficient $D_O$ is related to the chemical diffusion coefficient $\tilde{D}$ via the thermodynamic factor $\gamma$ [18]:

$$\gamma = \frac{1}{RT}\left(\frac{\partial \mu_O}{\partial \ln c_O}\right) = \frac{\tilde{D}}{D_O}\,, \tag{4.20}$$

$\mu_O$ is the chemical potential of atomic oxygen, $\mu_O = \mu_O^0 + RT\ln\sqrt{p_{O_2}}$. Thus,

$$\gamma = \frac{1}{2}\left(\frac{\partial \ln p_{O_2}}{\partial \ln c_O}\right). \tag{4.21}$$

Since the diffusion of oxygen is physically equal to that of oxygen vacancies in the opposite direction, the vacancy diffusion coefficient $D_V$ can be calculated using the relationship $D_O c_O = D_V c_V$, where $c_V$ is the oxygen vacancy concentration.

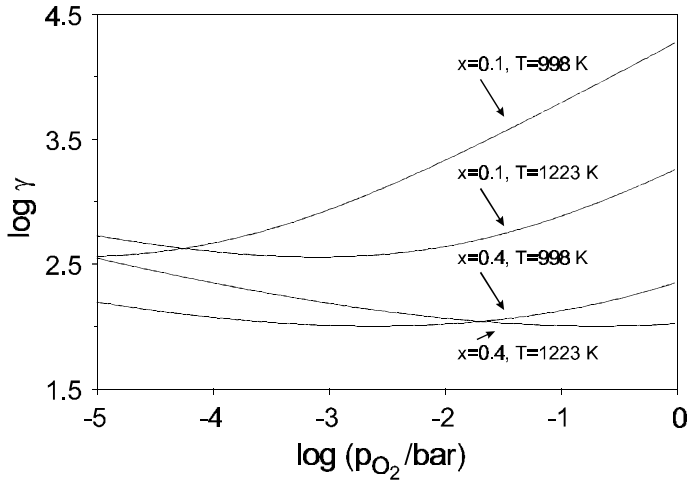


Figure 4.1. Thermodynamic enhancement factors of $La_{1-x}Sr_xFeO_{3-\delta}$ ($x$=0.1, 0.4) at 998 K and 1223 K.

$K_{ex}$ is defined in a purely empirical manner by Eqs. (4.6)-(4.7). Its value can not be related *a priori* to the thermodynamics of the system under investigation.

The oxygen flux expressed in terms of a small chemical potential difference $\Delta\mu_O = \mu_s - \mu_g$ between surface and gas phase reads [19]

$$j_O = -\frac{k_O c_O}{RT}\Delta\mu_O . \tag{4.22}$$

Here $k_O$ is the surface exchange coefficient as determined from measurements performed in thermodynamic equilibrium, e.g., $^{18}O/^{16}O$ isotopic exchange. Combination of Eq. (4.7) and Eq. (4.22) leads to

$$K_{ex} = \frac{k_O c_O}{RT}\frac{\Delta\mu_O}{\Delta c_O} \approx k_O\gamma . \tag{4.23}$$

The defect concentrations in LSF can be calculated from thermogravimetric measurements [4] as discussed in detail elsewhere [1]. The thermodynamic factors γ of $La_{1-x}Sr_xFeO_{3-\delta}$ at a few selected temperatures calculated from these results are illustrated in Figure 4.1.

## 4.3. Experimental

The experimental setup is shown in Figure 4.2. Oxygen ($O_2$ 5.0) diluted in nitrogen ($N_2$ 5.0) was used for re-equilibration of the sample in gas atmospheres with oxygen pressures of 0.01-1.0 bar. Remaining traces of water were stripped from the incoming gas streams to concentrations <0.5 ppm using molsieve 4A-based moisture filters. Two separate gas streams with flows of 100 ml/min (STP) were imposed by Brooks 5850E mass flow controllers. YSZ-based oxygen pumps were used for pumping small amounts of oxygen into either one of the nitrogen streams, yielding concentrations in the range of 3-2800 ppm $O_2$.

One of the gas flows was fed to a quartz sample tube which was placed inside a furnace, while the other flow was vented. With a fast electrical 4-way valve the flows leading to the sample furnace and the vent could be interchanged, thus making a stepwise change of the gas atmosphere in the sample tube. The oxygen concentrations in both gas streams were measured by an oxygen sensor (Systech ZR893/4). In Figure 4.3 the response of the oxygen sensor to a step change of 60 to 25 ppm $O_2$ is shown.

Oxygen pressure steps were performed in oxidizing or reducing direction in which the $p_{O_2}$ was varied with a factor of 5 (at high $p_{O_2}$) or smaller, typically below 3.3. To avoid mass transfer limitations, oxidation runs were only performed at a final oxygen concentration of 900 ppm or more.

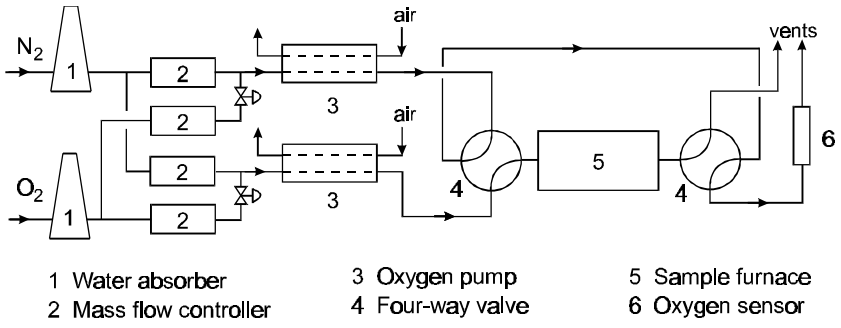


Figure 4.2. Schematic diagram of the experimental setup.

The method of preparation of the samples has been described extensively elsewhere [1]. The dimensions of the rectangular samples were 27x14x0.36-0.46 mm, with densities 93.5-94.5% for $La_{0.6}Sr_{0.4}FeO_{3-\delta}$ and 97.5-98.0% for $La_{0.9}Sr_{0.1}FeO_{3-\delta}$, relative to theoretical. The specimen surfaces were polished with 1000 MESH SiC, and ultrasonically cleaned in alcohol prior to use.

Electrical contacts were made by winding gold wire (0.1 mm diameter) around the outer ends of the samples. Gold paste (Blythe Colours B.V., Netherlands) was used to improve the contacts between wires and specimen. Gold was chosen since it is known to be rather inactive in the exchange of oxygen.

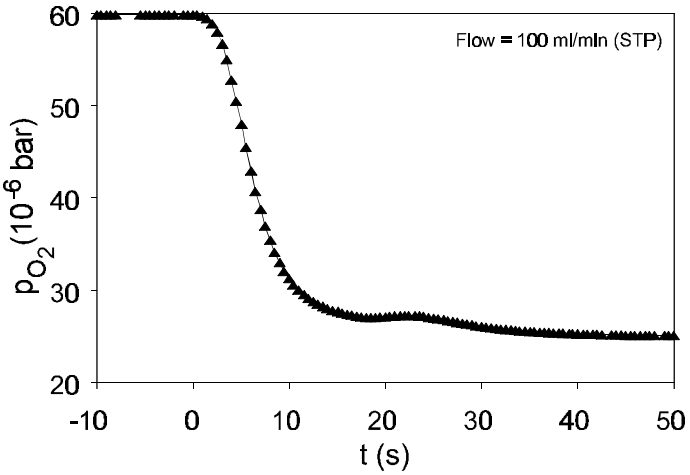


Figure 4.3. $O_2$ sensor response after stepwise change of the oxygen pressure in the specimen compartment.

The specimen resistance was measured in a Wheatstone bridge. A function generator was used to impose an AC voltage $V$ across the bridge. The outgoing signal was measured with reference to $V$ by a lock-in amplifier (Princeton Applied Research 129A), and logged with sampling rates of 0.01-1000 Hz. To determine $K_{ex}$ and/or $\tilde{D}$, the function $\overline{Z(s)}$, given by

$$\overline{Z(s)} = \frac{1}{s^2 \overline{\sigma_{app}^{rel}(s)}} = \frac{L}{2K_{ex}} + \sqrt{\frac{L^2}{4\tilde{D}s}} \coth(\tfrac{1}{2}kL) = R + T(s), \qquad (4.24)$$

was calculated from the data and analyzed using Equivalent Circuit software [20] by fitting $\overline{Z(j\omega)}$ to a serial electrical circuit consisting of a resistance $R$ (representing the surface reaction), and/or a cotangent-hyperbolic function $T$ (representing a finite length diffusion element).

## 4.4. Results and discussion

Impedance representations of some experimental data $\overline{Z(j\omega)} = -1/\omega^2 \overline{\sigma_{app}^{rel}(j\omega)}$ are shown in Figure 4.4. It was observed that the times necessary to re-equilibrate the samples were more or less the same in the oxygen partial pressure range of 0.03-1 bar $O_2$. Results from an oxygen partial pressure step from 0.03 to 0.0997 bar on $La_{0.9}Sr_{0.1}FeO_{3-\delta}$ at 998 K are given in Figure 4.4a.

Since the entire impedance spectrum is determined from a single relaxation curve, the scatter in the high frequency data is inherent to the method of measurement. More detailed analysis of this region is possible only upon direct application of complex impedance spectroscopy, i.e., by determining the response at each frequency individually. The high frequency behaviour can be attributed to the effect of diffusion. The finite diffusion element $T(j\omega)$ in Eq. (4.24) gives a fair description of the experimental response curve. The absence of a real axis offset in the high frequency limit of the data indicates the absence of the influence of a surface reaction (represented by the element $R$). Purely bulk-controlled kinetics are therefore assumed in the best fit of Eq. (4.24) to the data, indicated by the drawn line in Figure 4.4a. In general the re-equilibration kinetics above $10^{-2}$ bar $O_2$ were found to be fully determined by diffusion.

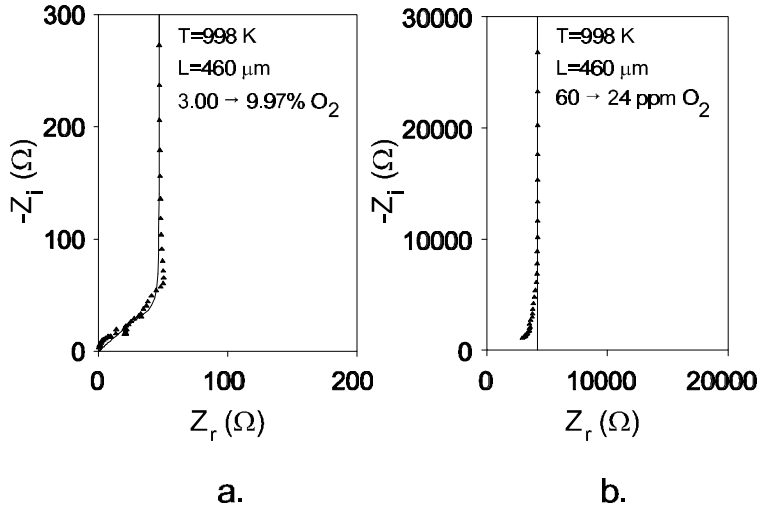


Figure 4.4. Impedance representations of transient conductivity of $La_{0.9}Sr_{0.1}FeO_{3-\delta}$. (a) diffusion-limited (b) exchange-limited. Best fits to Eq. (4.24) are indicated by drawn lines.

At oxygen partial pressures below about $10^{-2}$ bar, the re-equilibration times increased strongly with decreasing oxygen partial pressure. This observation can not

be ascribed to mass transfer limitations in the gas phase due to the thermally activated nature of the re-equilibration process under these conditions.

An impedance representation of data obtained in this pressure range is shown in Figure 4.4b. In comparison with the data in Figure 4.4a, the real part of $\overline{Z(j\omega)}$ has a much larger value. The deviation from a straight line at high frequency can not be explained in terms of finite diffusion behaviour, since the absolute value of the deviation is too large. The data are therefore interpreted in terms of a surface resistance $R$ only, as assumed in the best fit to the low frequency data, indicated by the drawn line in Figure 4.4b. The deviation from linearity at high frequency can be understood by considering that the re-equilibration times, attributed to $R$ in our explanation, increased strongly with decreasing oxygen pressure. This results in considerable changes of $R$ in the course of an equilibration run, in particular in the initial stages. The example illustrated in Figure 4.4b was typical for oxygen pressure steps in reducing direction. The observation that spectra from oxygen pressure steps in oxidizing direction showed the real part of the impedance to increase at higher frequencies further supports our interpretation. All re-equilibration experiments below $p_{O_2}=10^{-2}$ bar were interpreted in terms of exchange-controlled kinetics.

In the $p_{O_2}$ range of 0.01-0.10 bar, mixed diffusion/exchange-controlled kinetics were observed. It was difficult to separate these two processes properly, which is mainly due to the strong oxygen pressure dependence of $K_{ex}$. As this pressure dependence is reflected in nonlinear behaviour at high frequencies, the high frequency behaviour characterizing diffusion can not be distinguished easily.

Chemical diffusion coefficients $\tilde{D}$ and surface exchange coefficients $K_{ex}$ were determined from $T$ and $R$, respectively. No systematic differences were observed between the values of transport coefficients determined from oxidation and reduction runs when the results were assigned to the final oxygen pressure in the specimen compartment.

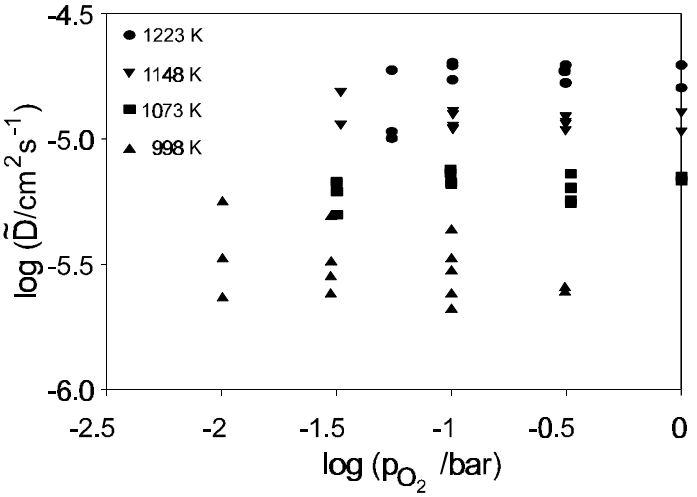


Figure 4.5. Chemical diffusion coefficient of $La_{0.9}Sr_{0.1}FeO_{3-\delta}$ versus $p_{O_2}$ at several temperatures.

### *4.4.1. Diffusion coefficients*

No pressure dependence of $\tilde{D}$ could be observed within experimental error, as illustrated in Figure 4.5 for $La_{0.9}Sr_{0.1}FeO_{3-\delta}$. The Arrhenius curves are shown in Figure 4.6. The calculated activation energies of $\tilde{D}$ are 82±7 kJ/mol for $La_{0.9}Sr_{0.1}FeO_{3-\delta}$ and 81±12 kJ/mol for $La_{0.6}Sr_{0.4}FeO_{3-\delta}$. Average values of $\tilde{D}$ obtained at various temperatures are listed in Table 4.1, where the corresponding oxygen vacancy diffusion coefficients $D_V$ are also given.

Table 4.1. Chemical diffusion coefficients and oxygen vacancy diffusion coefficients in the oxygen partial pressure range 0.03-1 bar at various temperatures.

| | $x$=0.1 | | $x$=0.4 | |
|---|---|---|---|---|
| $T$ (K) | log ( $\tilde{D}$ /cm$^2$ s$^{-1}$) | log ( $D_V$ /cm$^2$ s$^{-1}$) | log ( $\tilde{D}$ /cm$^2$ s$^{-1}$) | log ( $D_V$ /cm$^2$ s$^{-1}$) |
| 998 | -5.52±0.24 | -5.54±0.21 | -5.56±0.10 | -5.67±0.10 |
| 1073 | -5.19±0.10 | -5.21±0.10 | -4.95±0.06 | -5.22±0.15 |
| 1148 | -4.93±0.08 | -4.97±0.08 | -4.73±0.21 | -5.03±0.23 |
| 1223 | -4.74±0.07 | -4.83±0.17 | -4.46±0.17 | -4.89±0.07 |

Ishigaki et al. [21] obtained a value $D_V = 1.95 \cdot 10^{-5}$ cm$^2$ s$^{-1}$ from $^{18}O/^{16}O$ isotopic exchange on single crystals $La_{0.6}Sr_{0.4}FeO_{3-\delta}$ at 1273 K, and a vacancy diffusion coefficient of 0.8-0.9·10$^{-5}$ cm$^2$ s$^{-1}$ was calculated from oxygen fluxes through dense membranes at 1273 K [1]. Extrapolation of the present results to 1273 K yields $D_V = 1.7\text{-}2.0 \cdot 10^{-5}$ cm$^2$ s$^{-1}$, which is reasonably close.

There is also reasonable agreement with existing data in literature for $La_{0.9}Sr_{0.1}FeO_{3-\delta}$. A vacancy diffusion coefficient of 4.6·10$^{-6}$ cm$^2$ s$^{-1}$ was reported for single-crystalline material at 1223 K [21], and oxygen permeation measurements yielded 5.7·10$^{-6}$ cm$^2$ s$^{-1}$ for polycrystalline dense membranes at 1273 K [1]. The activation energies of $D_V$ calculated from Table 4.1 are 74±12 kJ/mol for $La_{0.9}Sr_{0.1}FeO_{3-\delta}$ and 80±25 kJ/mol for $La_{0.6}Sr_{0.4}FeO_{3-\delta}$, in agreement with oxygen exchange data [21].

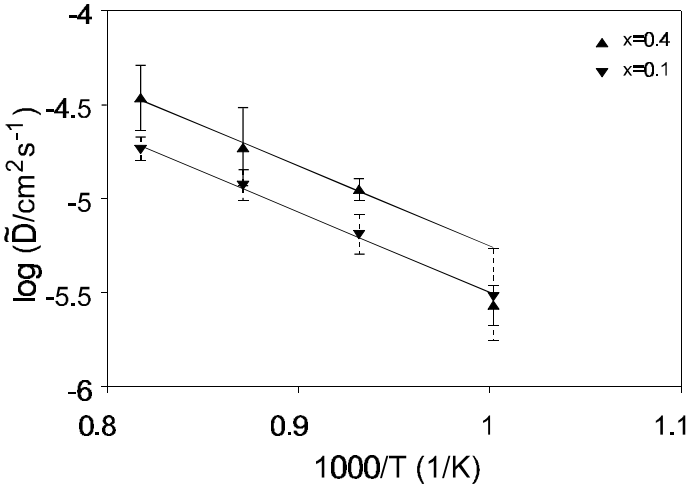


Figure 4.6. Arrhenius plots of chemical diffusion coefficients.

### 4.4.2. Surface exchange coefficients

In Figure 4.7 the surface exchange coefficient $K_{ex}$ of $La_{0.6}Sr_{0.4}FeO_{3-\delta}$ is shown versus oxygen partial pressure at several temperatures. Its value is proportional to $p_{O_2}^n$, with $n$=0.75-0.83. A similar dependence with $n$=0.82-0.95 was observed in the results of relaxation experiments on $La_{0.9}Sr_{0.1}FeO_{3-\delta}$.

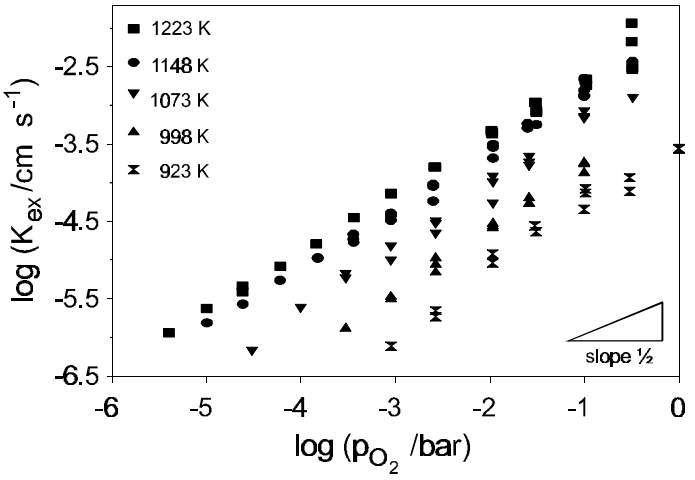


Figure 4.7. Apparent surface exchange coefficients $K_{ex}$ of $La_{0.6}Sr_{0.4}FeO_{3-\delta}$ versus $p_{O_2}$ at several temperatures.

In Figures 4.8 and 4.9 the surface exchange coefficients $k_O$ of both compounds, calculated with Eq. (4.23), are shown. At $p_{O_2}=10^{-3.04}$ bar the activation energies are approximately $E_{act}$=113±19 kJ/mol for $x$=0.1 and $E_{act}$=131±14 kJ/mol for $x$=0.4. The $p_{O_2}$ dependences are slightly lower than for $K_{ex}$, with powers $n$=0.75-0.86 and $n$=0.65-0.84 for $x$=0.1 and $x$=0.4, respectively.

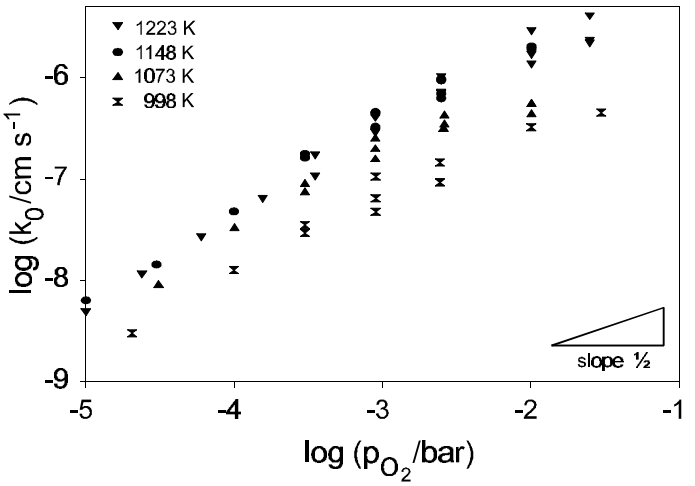


Figure 4.8. Surface exchange coefficients $k_O$ of $La_{0.9}Sr_{0.1}FeO_{3-\delta}$ versus $p_{O_2}$ at several temperatures.

The exchange coefficients $k_O$ reported for $x$=0.1 and $x$=0.4 at 0.065 bar $O_2$ in the aforementioned study by Ishigaki et al. [21] are systematically smaller than those from the present study, but are of the same order of magnitude. It should be noted that single crystals were used in the study by Ishigaki et al. The real surface area of an ideal single crystal is equal to its geometric surface area, which is the quantity used in calculation of the exchange coefficients. The real surface area of polycrystalline ceramics on a microscopic scale can be substantially larger.

The absolute values reported here are fairly close to isotopic exchange data reported by Carter et al. [22], i.e., at 1073 K, $k_O=2\cdot10^{-5}$ cm $s^{-1}$ for $La_{0.6}Ca_{0.4}Co_{0.8}Fe_{0.2}O_{3-\delta}$, and $k_O=5\cdot10^{-6}$ cm $s^{-1}$ for $La_{0.8}Sr_{0.2}CoO_{3-\delta}$. A $p_{O_2}$-dependence of $k_O$ can be observed in results from thermogravimetric transient measurements on polycrystalline $La_{0.7}Sr_{0.3}CoO_{3-\delta}$ [23]. Reported values vary from $k_O=8\cdot10^{-7}$ cm $s^{-1}$ at $p_{O_2}=10^{-3.5}$ bar and $T$=1093 K to $k_O=3\cdot10^{-5}$ cm $s^{-1}$ in air at 1393 K.

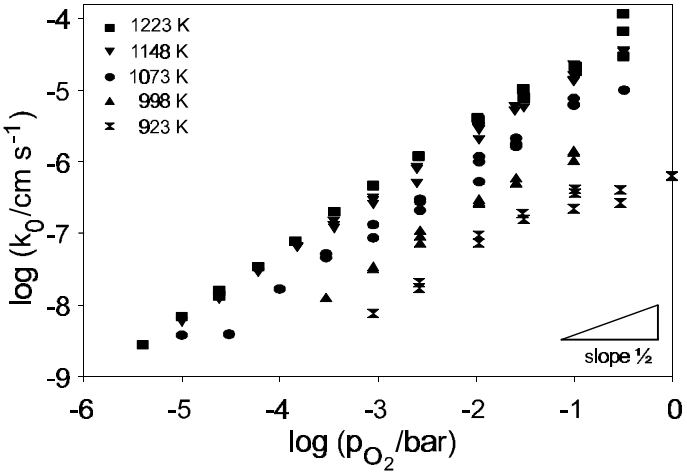


Figure 4.9. Surface exchange coefficients $k_O$ of $La_{0.6}Sr_{0.4}FeO_{3-\delta}$ versus $p_{O_2}$ at several temperatures.

The $p_{O_2}$ dependence of $k_O$ can be used to infer the nature of species involved in the rate-determining step of the surface reaction. The fact that $n\geq0.5$ is a strong indication for the involvement of molecular oxygen. Selected reaction mechanisms were considered to explain the experimental data, and the most probable ones are

Model 1: $O_2 + SW[S\cdots O_2]$, $k_O = k_1 p_{O_2}$, (4.25)

Model 2: $O_2 + V_O^{\cdot\cdot}W[V_O^{\cdot\cdot}\cdots O_2]$, $k_O = k_2 p_{O_2}[V_O^{\cdot\cdot}]$, (4.26)

Model 3: $O_2 + V_O^{\cdot\cdot} + e'W[V_O^{\cdot}\cdots O_2]W[V_O^{\cdot\cdot}\cdots O_2^-]$, $k_O = k_3 p_{O_2}[V_O^{\cdot\cdot}][e']$, (4.27)

Model 4: $O_2 + V_O^{\cdot\cdot} - V_O^{\cdot\cdot}W2[V_O^{\cdot\cdot}\cdots O]$, $k_O = k_4 p_{O_2}[V_O^{\cdot\cdot}]^2$. (4.28)

Since $k_O = r_O/c_O$, with $r_O$ the equilibrium oxygen exchange rate and $c_O$ the oxygen bulk concentration, possible expressions for $k_O$ for each model are also given.

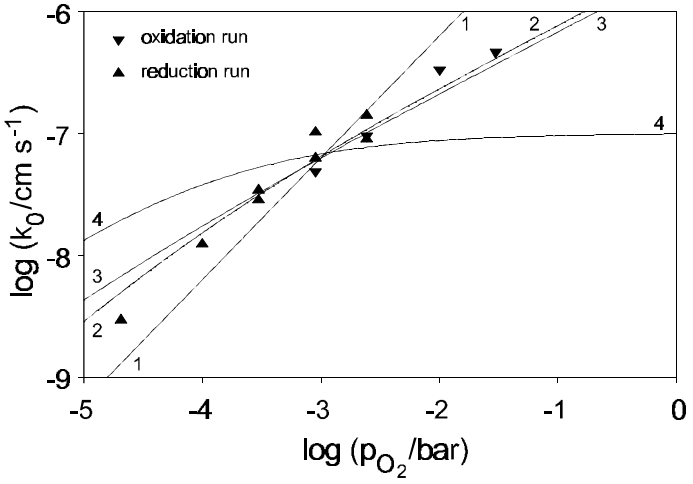


Figure 4.10. Experimental and theoretical surface exchange coefficients $k_O$ of $La_{0.9}Sr_{0.1}FeO_{3-\delta}$ at 998 K. Numbers refer to the mechanisms described in the text.

The concentration of adsorption sites S for oxygen is assumed to be large and independent of oxygen pressure in model 1. In model 2 a surface oxygen vacancy acts as an adsorption site for molecular oxygen. Since the concentration of oxygen vacancies either increases or remains constant with decreasing oxygen pressure under all conditions, its pressure dependence $[V_O^{\cdot\cdot}] \sim p_{O_2}^m$ has a power $m$ between -½ and 0 [24]. In model 3, oxygen may adsorb either in neutral form on an F-centre (a singly ionized surface oxygen vacancy), or in the form of $O_2^-$ [25] on a doubly ionized vacancy. In model 4 two neighbouring surface oxygen vacancies are involved.

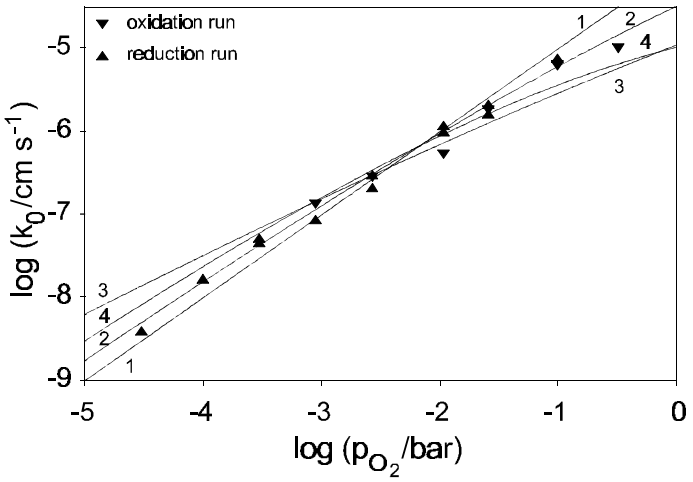


Figure 4.11. Experimental and theoretical surface exchange coefficients $k_O$ of $La_{0.6}Sr_{0.4}FeO_{3-\delta}$ at 1073 K. Numbers refer to the mechanisms described in the text.

Oxygen pressure dependences of surface defect concentrations $[V_O^{\cdot\cdot}]$ and [e'] were calculated as discussed elsewhere [1], assuming that the same reactions determine the defect concentrations in the bulk and at the surface [2]. Figures 4.10 and 4.11 show selected experimental data with the corresponding best fits derived from models 1-4. As is seen clearly in Figure 4.10, reasonable agreement with the experimental data is observed only for models 2 and 3 for $La_{0.9}Sr_{0.1}FeO_{3-\delta}$.

The curves obtained from model calculations on $La_{0.6}Sr_{0.4}FeO_{3-\delta}$, illustrated in Figure 4.11, are much more alike than those on $La_{0.9}Sr_{0.1}FeO_{3-\delta}$. Nevertheless, all models except 2 and 3 deviate systematically from the experimental trends at high and/or low oxygen partial pressures. These results suggest that the rate-determining step on both compounds can be described best by Eq. (4.26) or Eq. (4.27). In view of the small differences between the trends predicted by these two models, no conclusions can be drawn about the involvement of electronic species.

Mechanisms 2 and 3 both predict more or less linear relationships between the ratio $k_O/p_{O_2}$ and the oxygen vacancy parameter δ. This is illustrated by data of $La_{0.6}Sr_{0.4}FeO_{3-\delta}$ in Figure 4.12.

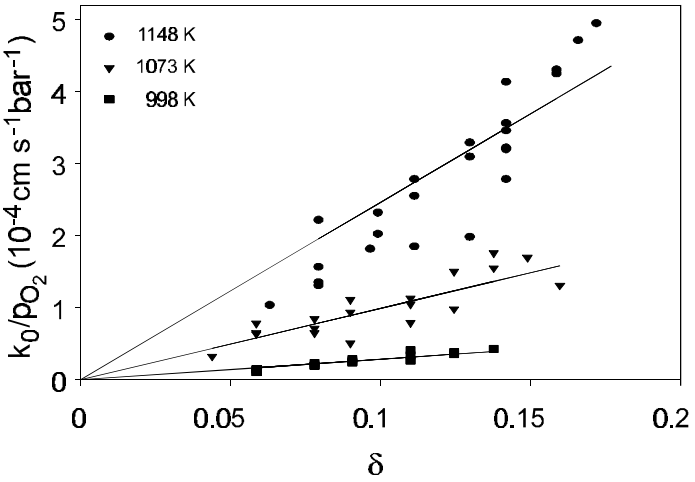


Figure 4.12. Ratio $k_O/p_{O_2}$ versus the oxygen vacancy concentration δ of $La_{0.6}Sr_{0.4}FeO_{3-\delta}$.

A linear-like correlation can be observed, which further supports the current interpretation. Similar trends were seen in the results of $La_{0.9}Sr_{0.1}FeO_{3-\delta}$. Table 4.2 lists the best fits of $k_2$ (Eq. (4.26)) to the experimental data. Remarkably, the value of $k_2$ does not vary strongly with temperature for $x$=0.1, whereas it does for $x$=0.4.

The involvement of oxygen vacancies has already been proposed for the oxygen exchange process on $La_{0.3}Sr_{0.7}CoO_{3-\delta}$ [26]. Utilizing isotopic exchange a $p_{O_2}^n$ dependence with $n$=0.41±0.02 was found for $k_O$, which was interpreted by assuming the rate determining step to involve an adsorbed oxygen atom ($[O_{ads}] \sim p_{O_2}^{1/2}$) and a surface oxygen vacancy ($[V_O^{\cdot\cdot}] \sim p_{O_2}^{-0.1}$).

Table 4.2. Best fits of $k_2$ (Eq. (4.26)) to the experimental data.

| | log ( $k_2$ /cm $s^{-1}$) | |
|---|---|---|
| $T$ (K) | $x$=0.1 | $x$=0.4 |
| 923 | | -3.82±0.06 |
| 998 | -1.80±0.10 | -3.55±0.08 |
| 1073 | -1.74±0.23 | -3.00±0.04 |
| 1148 | -1.62±0.07 | -2.61±0.03 |
| 1223 | -1.80±0.05 | -2.49±0.03 |

The indication of the direct involvement of oxygen vacancies in the surface exchange process agrees with a suggestion by Kilner [27] based on an observed relationship between $k_O$ and the oxygen tracer coefficient $D_O^*$ of different perovskite-type oxides. Since the value of $D_O^*$ is strongly correlated with the level of nonstoichiometry, $k_O$ must depend strongly on δ.

## 4.5. Conclusions

It has been shown that transformation of the time-dependent response of the electrical conductivity of thin specimens of $La_{1-x}Sr_xFeO_{3-\delta}$ ($x$=0.1, 0.4) to the frequency domain yields information regarding the nature of the rate-determining step in the re-equilibration process after an abrupt change of the oxygen partial pressure in the ambient atmosphere.

Diffusional control was observed at oxygen pressures of 0.03-1.0 bar $O_2$. The chemical diffusion coefficients $\tilde{D}$ were found to be independent of the oxygen pressure, and for both investigated compounds the activation energy was about 80-85 kJ/mol. The oxygen vacancy diffusion coefficients calculated from these data are in good agreement with values known from literature.

At pressures below 0.01 bar $O_2$ only exchange-controlled equilibration kinetics were seen. The absolute values of the apparent surface exchange coefficients $K_{ex}$ were strongly dependent on the oxygen partial pressure. In conjunction with nonstoichiometry data from literature, the surface exchange coefficients $k_O$ were calculated. The observed values agree reasonably well with values known from literature. The $p_{O_2}$ dependences of $k_O$ were interpreted in terms of an adsorption mechanism involving at least an oxygen molecule and a vacant oxygen site at the surface. The apparent activation energies of $k_O$ vary between 110-140 kJ/mol for both compositions.

## References

1. Chapter 2 of this thesis.
2. Chapter 3 of this thesis.

3. I. Yasuda and T. Hikita, "Precise determination of the chemical diffusion coefficient of calcium-doped lanthanum chromites by means of electrical conductivity relaxation," *J. Electrochem. Soc.*, **141** (1994) 1268-1274.
4. J. Mizusaki, M. Yoshihiro, S. Yamauchi and K. Fueki, "Nonstoichiometry and defect structure of the perovskite-type oxide $La_{1-x}Sr_xFeO_{3-\delta}$," *J. Solid State Chem.*, **58** (1985) 257-266.
5. F.A. Kröger, *The chemistry of imperfect crystals*, North-Holland, Amsterdam, 1964.
6. Y. Denos, F. Morin and G. Trudel, "Oxygen diffusivity in strontium-substituted lanthanum cobaltite," Proc. 2nd Intl. Symp. on *Ionic and mixed conducting oxides*, ed. T.A. Ramanarayanan, W.L. Worrell and H.L. Tuller, Proc. vol. 94-12, The Electrochemical Society, Pennington, NJ, 1994, p. 150-158.
7. I. Yasuda and M. Hishinuma, "Electrical conductivity and chemical diffusion coefficient of Sr-doped lanthanum chromites," *Solid State Ionics*, **80** (1995) 141-150.
8. C. J. Yu, D.M. Sparlin and H.U. Anderson, "Oxidation kinetics of polycrystalline $LaCrO_3$,"*J. Am. Ceram. Soc.*, **70** (1987) C189-C192.
9. B. Ma, U. Balachandran, J.-H. Park and C.U. Segre, "Determination of chemical diffusion coefficient of $SrFeCo_{0.5}O_x$ by the conductivity relaxation method," *Solid State Ionics*, **83** (1996) 65-71.
10. J. Nowotny and A. Sadowsky, "Chemical diffusion in nickel oxide," *J. Am. Ceram. Soc.*, **62** (1979) 24-28.
11. F. Morin and R. Dieckmann, "The determination of chemical diffusivity in cobaltous oxide by means of electrical conductivity," *Z. Phys. Chem. Neue Folge*, **129** (1982) 219-237.
12. J. Nowotny, J. Oblakowski, A. Sadowski and J.B. Wagner, jr., "Reequilibrium kinetics of $NiO$-$Cr_2O_3$ solid solutions," *Oxid. Met.*, **14** (1980) 437-448.
13. J. Crank, *The mathematics of diffusion*, 2nd Ed., Clarendon Press, Oxford, 1979.
14. V. Dovì, F. Gesmundo and F. Viani, "Kinetics of equilibration in relaxation-type measurements under partial rate control by a surface reaction following a general type of rate law. I: The direct problem," *Oxid. Met.*, **23** (1985) 35-51.
15. F. Gesmundo, F. Viani and V. Dovì, "Kinetics of oxide equilibration in relaxation experiments with a partial degree of surface control under a Wagner-type rate law for a surface reaction," *Oxid. Met.*, **23** (1985) 141-157.
16. F. Morin, "A mathematical assessment of chemical diffusion measurements in transition metal oxides," *J. Electrochem. Soc.*, **128** (1981) 2439-2446.
17. F. Morin, "Application of electrical conductivity for determining the chemical diffusivity in transition-metal compounds," *React. Solids*, **7** (1989) 307-323.
18. H. Schmalzried, *Solid state reactions*, 2nd ed., Verlag Chemie, Weinheim-Deerfield Beach-Basel, 1981.
19. H. Deng, M. Zhou and B. Abeles, "Diffusion-reaction in mixed ionic-electronic solid oxide membranes with porous electrodes," *Solid State Ionics*, **74** (1994) 75-84.
20. B.A. Boukamp, *Equivalent Circuit*, 2nd ed., University of Twente, Enschede, the Netherlands, 1989.
21. T. Ishigaki, S. Yamauchi, K. Kishio, J. Mizusaki and K. Fueki, "Diffusion of oxide ion vacancies in perovskite-type oxides," *J. Solid State Chem.*, **73** (1988) 179-187.
22. S. Carter, A. Selcuk, R.J. Chater, J. Kajda, J.A. Kilner and B.C.H. Steele, "Oxygen transport in selected nonstoichiometric perovskite-type oxides," *Solid State Ionics*, **53-56** (1992) 597-605.
23. O.F. Kononchuk, D.P. Sutija, T. Norby and P. Kofstad, "Transient thermogravimetric measurement of chemical diffusion in $La_{0.7}Sr_{0.3}CoO_{3-\delta}$," Proc. 4th Intl. Symp. on *Solid Oxide*

*Fuel Cells*, ed. M. Dokiya, O. Yamamoto, H. Tagawa and S.C. Singhai, Proc. vol. 95-1, The Electrochemical Society, Pennington, NJ, 1995, p. 395-403.

24. Chapter 7 of this thesis.
25. M. Che and A.J. Tench, "Characterization and reactivity of molecular oxygen species on oxide surfaces," in: *Advances in Catalysis*, vol. 32, Academic Press, New York, 1983, p. 1-148.
26. R.H.E. van Doorn, "Surface oxygen exchange of $La_{0.3}Sr_{0.7}CoO_{3-\delta}$," Chapter 8 in: *Oxygen separation with mixed conducting perovskite membranes*, Thesis, University of Twente, Enschede, the Netherlands, 1996.
27. J.A. Kilner, "Isotopic exchange in mixed and ionically conducting oxides," Proc. 2nd Intl. Symp. on *Ionic and mixed conducting oxides*, ed. T.A. Ramanarayanan, W.L. Worrell and H.L. Tuller, Proc. vol. 94-12, The Electrochemical Society, Pennington, NJ, 1994, p. 174-190.

# 5

# Thermodynamic quantities and defect structure of $La_{0.6}Sr_{0.4}Co_{1-y}Fe_yO_{3-\delta}$[†]


## Abstract

The partial energies and entropies of $O_2$ in perovskite-type oxides $La_{0.6}Sr_{0.4}Co_{1-y}Fe_yO_{3-\delta}$ ($y$=0, 0.1, 0.25, 0.4, 0.6) were determined as a function of nonstoichiometry $\delta$ by coulometric titration of oxygen in the temperature range 650-950°C. An absolute reference value of $\delta$ was obtained from thermogravimetry in air. The nonstoichiometry at a given oxygen pressure and temperature decreases with iron content $y$. At low nonstoichiometries the oxygen chemical potential decreases with $\delta$. The observed behaviour can be interpreted by assuming random distribution of oxygen vacancies, and an electronic structure with both localized states on Fe, and a partially filled itinerant electron band, of which the density of states at the Fermi level scales with the Co content. The energy of the Fe states is close to the energy at the Fermi level in the conduction band. The observed trends of the thermodynamic quantities can be interpreted in terms of the itinerant electron model only when the iron content is small. At high values of $\delta$ the chemical potential of $O_2$ becomes constant, indicating partial decomposition of the perovskite phase. The maximum value of $\delta$ at which the compounds are single-phase increases with temperature.


[†] This chapter was published in nearly identical form in M.H.R. Lankhorst, *Thermodynamic and transport properties of mixed ionic-electronic conducting perovskite-type oxides*, Chapter 7: "Thermodynamic quantities and defect structure of $La_{0.6}Sr_{0.4}Co_{1-y}Fe_yO_{3-\delta}$ ($y$=0.0-0.6)," Thesis, University of Twente, Enschede, the Netherlands, 1997.

## 5.1. Introduction

The $La_{1-x}Sr_xMO_{3-\delta}$ perovskite-type oxides, in which M is a first row transition metal cation, are well-known for their ability to exhibit significant electronic and oxygen ionic conductivity. It is generally accepted that the high ionic conductivity at elevated temperatures is caused by a relatively high concentration ($\delta$) of vacant crystallographic sites in the oxygen sublattice, in conjunction with a high mobility of the regular oxygen ions. The formation of these lattice oxygen vacancies, which have an electrical charge of +2 with respect to the surrounding oxygen sublattice, is charge-compensated by a change of the average valency of the transition metal cations M. Gas separation membranes [1-3], oxidation catalysts [4,5] and electrodes in solid oxide fuel cells and oxygen sensors [6] are possible applications for these materials.

The present chapter is intended to provide insight into the oxygen nonstoichiometry characteristics of the $La_{0.6}Sr_{0.4}Co_{1-y}Fe_yO_{3-\delta}$ (LSCF) system ($y$=0-0.6) at elevated temperatures. For this purpose, changes of $\delta$ are measured as a function of oxygen partial pressure and temperature using the method of oxygen coulometric titration. Thermodynamic quantities such as partial molar energy and entropy of oxygen incorporation are determined with this method, whereas thermogravimetry is used to provide an absolute reference value of $\delta$.

The oxygen nonstoichiometry of the end member $La_{0.6}Sr_{0.4}CoO_{3-\delta}$, has been measured as a function of temperature and oxygen partial pressure by coulometric titration [7,8]. The observed trends were in close agreement with results of thermogravimetric [9] and coulometric titration [10] studies on other compounds $La_{1-x}Sr_xCoO_{3-\delta}$. Within the homogeneity region of the perovskite phase, the value of $\delta$ at elevated temperatures is seen to increase almost linearly with decreasing $\log p_{O_2}$ [10,11]. This feature has been explained by assuming the conduction electrons to be delocalized, occupying energy levels in a partially filled conduction band [7].

In terms of the ZSA framework [12] this band is thought to have mixed O 2*p*-Co 3*d* character [13], which accounts also for the high metallic-like conductivity and low Seebeck coefficient exhibited by $La_{0.6}Sr_{0.4}CoO_{3-\delta}$ [13-16]. With decreasing level of strontium doping in $La_{1-x}Sr_xCoO_{3-\delta}$ a small band gap appears which results in semi-conducting properties at room temperature when $x$<0.25-0.3 [13,15]. However, metallic-like conductivity is still encountered at higher temperatures [15].

Thermogravimetric experiments in a wide range of temperatures and oxygen partial pressures on the other end member $La_{0.6}Sr_{0.4}FeO_{3-\delta}$ [17] indicated that the increase of the nonstoichiometry with decreasing oxygen partial pressure was substantially smaller than in $La_{0.6}Sr_{0.4}CoO_{3-\delta}$ under the same conditions. Moreover, in contrast to $La_{0.6}Sr_{0.4}CoO_{3-\delta}$ an intermediate region was observed in which $\delta$ remains almost constant at a level fixed by the dopant concentration, i.e., $\delta \approx \frac{1}{2}[Sr'_{La}]$. For compounds $La_{0.75}Sr_{0.25}FeO_{3-\delta}$ and $La_{0.9}Sr_{0.1}FeO_{3-\delta}$ [18] this region was

shown to coincide with a minimum in electrical conductivity. To interpret the observed behaviour a Mott-Hubbard type of charge disproportionation is thought to occur: $2Fe^{3+} \text{W} Fe^{4+} + Fe^{2+}$. Thus, both the conduction electrons and holes are localized, giving rise to hopping-type electrical conductivity. The region of constant nonstoichiometry is caused by a change of the dominant charge carrier from $Fe^{4+}$ to $Fe^{2+}$ upon decreasing $p_{O_2}$ which changes the conductivity from p-type to n-type. On the other hand, data from X-ray absorption spectrometry on $La_{1-x}Sr_xFeO_{3-\delta}$ ($x$=0-1) [19] suggest that the holes induced by Sr doping are in states of mixed Fe 3*d*-O 2*p* character, in particular for low concentrations of Sr. In both end members $La_{0.6}Sr_{0.4}CoO_{3-\delta}$ and $La_{0.6}Sr_{0.4}FeO_{3-\delta}$ the oxygen vacancies are assumed to be distributed randomly among energetically equivalent oxygen sites, although there are indications of microdomain formation with ordered oxygen vacancies at high values of $\delta$ for $La_{0.6}Sr_{0.4}CoO_{3-\delta}$ [7].

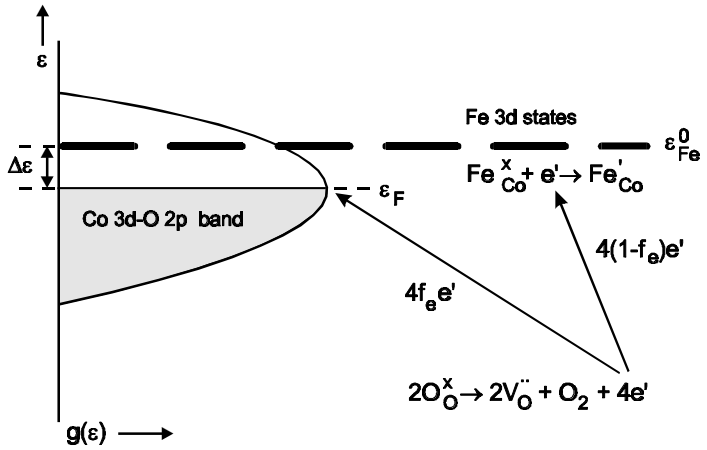


Figure 5.1. Schematic representation of the proposed electronic structure of $La_{0.6}Sr_{0.4}Co_{1-y}Fe_yO_{3-\delta}$ and the distribution of electrons created in the oxygen vacancy formation among the band and states.

A study of the electrical properties and Seebeck coefficients of the system $La_{0.8}Sr_{0.2}Co_{1-y}Fe_yO_{3-\delta}$ ($y$=0-1) in air [20] showed a maximum (with respect to temperature) in the electrical conductivity of all compositions. The conduction mechanism assumed is that of adiabatic hopping of small polarons. Since the conductivity decreases with increasing iron content, the iron centres are assumed to represent energetically lower small polaron sites than the cobalt centres, although the energy difference is too small to lead to clear trapping of holes on iron at high temperatures.

There is lack of data about the nonstoichiometry of $La_{0.6}Sr_{0.4}Co_{1-y}Fe_yO_{3-\delta}$. The oxygen deficiency of $La_{0.6}Sr_{0.4}Co_{0.2}Fe_{0.8}O_{3-\delta}$ in air was measured by thermogravimetry using constant heating and cooling rates of 5°C/min and 2°C/min, respectively [21]. From the absence of hysteresis it was concluded that the material was close to its

equilibrium oxygen content during the entire measurement. The oxygen content at room temperature, determined by wet-chemical analysis, was found to be essentially stoichiometric. Significant weight loss was observed only above 600°C, up to a relative mass change of about 1.0% at 1200°C, which corresponds with $\delta \approx 0.14$.

The energy band scheme of $La_{0.6}Sr_{0.4}Co_{1-y}Fe_yO_{3-\delta}$ assumed in the present study for the analysis of experimental data is shown schematically in Figure 5.1. It essentially features the characteristics of both end members in the sense that a band model, which takes into account the delocalized behaviour of electrons as seen in $La_{0.6}Sr_{0.4}CoO_{3-\delta}$, is combined with the presence of localized electronic states due to partial substitution of cobalt with iron. A rigid band approach to the properties of $La_{0.6}Sr_{0.4}Co_{1-y}Fe_yO_{3-\delta}$ is assumed, whereas it is further assumed that the density of states at the Fermi level and the concentration of localized electronic defects are proportional to the concentrations of cobalt and iron, respectively.

## 5.2. Theory

### *5.1.1. Oxygen coulometric titration*

The principle of oxygen coulometric titration has been described extensively in Refs. [7,8]. It is performed by placing an oxide sample into a sealed electrochemical cell. In chemical equilibrium the oxygen chemical potential of the oxide sample $\mu_{O_2}^{oxide}$ is equal to that of the surrounding atmosphere inside the cell. Its value is determined by measuring the EMF $E$ across a solid electrolyte wall, onto which two identical metal electrodes are attached on opposite sides, in contact with a reference gas and the atmosphere inside the cell, respectively:

$$\mu_{O_2}^{oxide} = \mu_{O_2}^{ref} - 4FE = \mu_{O_2}^{ref} + RT \ln(p_{O_2} / p_{O_2}^{ref}). \tag{5.1}$$

Here $\mu_{O_2}^{ref}$ is the oxygen chemical potential of the reference gas. Its value can be found in thermodynamic tables [22]. $F$ is Faraday's constant, $R$ the gas constant and $T$ the temperature. $p_{O_2}$ and $p_{O_2}^{ref}$ are the oxygen partial pressures of the inner atmosphere and the reference gas, respectively.

A second auxiliary electrolyte wall in contact with the two gases is used for electrochemical pumping of oxygen into or out of the cell. In potentiostatic coulometric titration experiments the EMF across the electrolyte is changed stepwise from one to another constant value, thus perturbing the equilibrium between the oxide inside the cell and the surrounding atmosphere. The electrical pumping current decays over the time needed for re-equilibration. The change in oxygen nonstoichiometry $\Delta\delta$ of the sample follows from integrating the current $I$ over time $t$:

$$\Delta\delta = \frac{M}{m_s} \int_0^\infty \frac{I(t) - I(\infty)}{2F} dt. \tag{5.2}$$

Here $I(\infty)$ is the current at $t=\infty$, which is due to unavoidable leakage of oxygen [7]. $M$ is the molar mass of perovskite and $m_s$ the sample mass.

The coulometric titration technique also permits easy determination of the entropy of oxygen $s_{O_2}^{oxide}$ defined as the change of the chemical potential with temperature at constant nonstoichiometry $\delta$ [7]:

$$s_{O_2}^{oxide} = -\left(\frac{\partial \mu_{O_2}^{oxide}}{\partial T}\right)_{\delta}. \tag{5.3}$$

The energy of oxygen $\varepsilon_{O_2}^{oxide}$ may be calculated from $\varepsilon_{O_2}^{oxide} = \mu_{O_2}^{oxide} + Ts_{O_2}^{oxide}$.

### *5.2.2. Solid state defect model for $La_{0.6}Sr_{0.4}Co_{1-y}Fe_yO_{3-\delta}$*

The creation of oxygen vacancies in $La_{0.6}Sr_{0.4}Co_{1-y}Fe_yO_{3-\delta}$ is assumed to take place in a similar way as in $La_{0.6}Sr_{0.4}CoO_{3-\delta}$ [9] and $La_{0.6}Sr_{0.4}FeO_{3-\delta}$ [17]. But in contrast to these compounds it is conjectured that the electrons created during vacancy formation are neither donated exclusively to a partially filled conduction band like in $La_{0.6}Sr_{0.4}CoO_{3-\delta}$ [7], nor distributed solely among localized electronic states, like in $La_{0.6}Sr_{0.4}FeO_{3-\delta}$. Instead, both processes occur to some extent: a fraction $f_e$ of the electrons formed is donated to the conduction band, while the remaining fraction $1-f_e$ is distributed among localized states on iron centres. This is illustrated in Figure 5.1. It is also assumed that the energy level of $Fe^{2+}$ is too high to be occupied at the oxygen pressures and temperatures covered by our experiments, which leaves $Fe^{3+}$ and $Fe^{4+}$ as the only possible oxidation states. Representing the latter defects in Kröger-Vink notation [23] by $Fe_{Co}^{'}$ and $Fe_{Co}^{x}$, respectively‡, the oxidation reaction for a given compound $La_{0.6}Sr_{0.4}Co_{1-y}Fe_yO_{3-\delta}$ can be written as

$$2O_O^x + 4(1-f_e)Fe_{Co}^x WO_2^{gas} + 2V_O^{\cdot\cdot} + 4f_e e' + 4(1-f_e)Fe_{Co}^{'}. \tag{5.4}$$

$O_O^x$ denotes a regular lattice oxygen ion, $V_O^{\cdot\cdot}$ an oxygen vacancy, and e' a conduction electron. The exchange of electronic charge carriers between the band and the localized iron states is described by

$$Fe_{Co}^x + e' W Fe_{Co}^{'}. \tag{5.5}$$

It follows from these reactions that at chemical equilibrium, where $\mu_{O_2}^{oxide} = \mu_{O_2}^{gas}$,

‡ The notation chosen here allows to describe the electronic behaviour in terms of electrons only. $Fe^{3+}$ and $Fe^{4+}$ would normally be defined in Kröger-Vink notation as $Fe_{Co}^x$ and $Fe_{Co}^{\cdot}$, respectively.

$$\mu_{O_2}^{oxide} + 2(\mu_{V_O^{\cdot\cdot}} - \mu_{O_O^x}) + 4f_e\mu_{e'} + 4(1-f_e)(\mu_{Fe_{Co}^{'}} - \mu_{Fe_{Co}^{x}}) = 0\,, \tag{5.6}$$

$$(\mu_{Fe_{Co}^{'}} - \mu_{Fe_{Co}^{x}}) - \mu_{e'} = 0\,, \tag{5.7}$$

where $\mu_i$ is the chemical potential of species i. The oxygen vacancies and regular lattice ions are assumed to be non-interacting and randomly distributed among equivalent oxygen sites. A similar assumption is made for the electrons on iron centres. This allows their respective structure elements to be described as

$$\mu_{V_O^{\cdot\cdot}} - \mu_{O_O^x} = \mu_V = \mu_V^0 + RT\ln\left(\frac{\delta}{3-\delta}\right), \tag{5.8}$$

$$\mu_{Fe_{Co}^{'}} - \mu_{Fe_{Co}^{x}} = \mu_{Fe} = \mu_{Fe}^0 + RT\ln\left(\frac{[Fe_{Co}^{'}]}{y-[Fe_{Co}^{'}]}\right). \tag{5.9}$$

By definition, the concentrations of defect species are expressed per unit cell. $[V_O^{\cdot\cdot}] = \delta$ is the oxygen vacancy concentration. $\mu_i = \varepsilon_i - Ts_i$ is the chemical potential of species i, with $\varepsilon_i$ and $s_i$ its energy and entropy parts, respectively. $\mu_i^0 = \varepsilon_i^0 - Ts_i^0$ is the standard chemical potential of species i.

Under the assumption that the electron band is rigid upon filling with electrons, an expression has been derived for $La_{1-x}Sr_xCoO_{3-\delta}$ [7] which relates $\mu_{e'}$ to the electron occupancy [e'] and the density of states at the Fermi level $g(\varepsilon_F)$. The entropy of electrons can be neglected in the description since the electron band is assumed to be relatively wide. Assuming that the density of states at the Fermi level is proportional to the concentration 1-*y* of cobalt in the compound, an expression similar to the one derived in Ref. [7] can be used for the electron chemical potential in the conduction band in $La_{0.6}Sr_{0.4}Co_{1-y}Fe_yO_{3-\delta}$ :

$$\mu_{e'} = \mu_{e'}^0 + \frac{[e'] - [e']^0}{g(\varepsilon_F)(1-y)}\,. \tag{5.10}$$

$\mu_{e'}^0$ is the chemical potential of electrons when $\delta$=0, *y*=0 and $[Sr_{La}^{'}]$=*x*=0, i.e., the chemical potential of electrons in stoichiometric $LaCoO_3$. $[e']^0$ is the electron occupancy under these standard conditions, and corresponds with an average valency of 3+ for Co. The charge neutrality requirement for this system may now be written as $2\delta+y=x+n+[Fe_{Co}^{'}]$, with $n=[e']-[e']^0$. The value of $f_e$ can be determined by considering that Eq. (5.7) must still be valid after addition and distribution of the electrons created during oxygen vacancy formation, from which it follows that

$$\left(\frac{\partial \mu_{e'}}{\partial n}\right)_T f_e = \left(\frac{\partial \mu_{Fe}}{\partial [Fe'_{Co}]}\right)_T (1-f_e). \tag{5.11}$$

Combining the above equation with Eqs. (5.9)-(5.10), $f_e$ can be derived to be

$$f_e = \left(1+\frac{[Fe'_{Co}](y-[Fe'_{Co}])}{g(\varepsilon_F)(1-y)RTy}\right)^{-1}. \tag{5.12}$$

The energy of oxygen $\varepsilon_{O_2}^{oxide}$ may be written as $\varepsilon_{O_2}^{oxide} = -2\varepsilon_V - 4f_e\varepsilon_{e'} - 4(1-f_e)\varepsilon_{Fe}$, in view of Eq. (5.6). Using Eqs. (5.8)-(5.10) it then follows that

$$\begin{aligned}\varepsilon_{O_2}^{oxide} &= -2\varepsilon_V^0 - 4f_e\left(\varepsilon_{e'}^0 + \frac{n}{g(\varepsilon_F)(1-y)}\right) - 4(1-f_e)\varepsilon_{Fe}^0 \\ &= \varepsilon_{ox} - 4f_e\left(\frac{n}{g(\varepsilon_F)(1-y)}\right) - 4(1-f_e)\Delta\varepsilon_i^0 ,\end{aligned} \tag{5.13}$$

where $\varepsilon_{ox} = 2\varepsilon_V^0 - 4\varepsilon_{e'}^0$ is constant for a given iron concentration $y$. $\Delta\varepsilon_i^0 = \varepsilon_{Fe}^0 - \varepsilon_{e'}^0$ is constant independent of composition, because $\varepsilon_{Fe}^0$ indicates the energy of the $3d$ state of iron, which can be assumed constant, and $\varepsilon_{e'}^0$ is the energy at the Fermi level in stoichiometric $LaCoO_3$. Note, however, that the energy difference $\varepsilon_{Fe}^0 - \varepsilon_{e'}$ scales with the electron occupancy $n$.

Following the same procedure as above the entropy of oxygen $s_{O_2}^{oxide}$ may be evaluated from Eq. (5.6): $s_{O_2}^{oxide} = -2s_V - 4f_e s_{e'} - 4(1-f_e)s_{Fe}$. Making the appropriate substitutions for $s_V$, $s_{e'}$ and $s_{Fe}$, it is found that

$$\begin{aligned}s_{O_2}^{oxide} &= -2\left(s_V^0 - R\ln\left(\frac{\delta}{3-\delta}\right)\right) - 4f_e s_{e'}^0 - 4(1-f_e)\left(s_{Fe}^0 - R\ln\left(\frac{[Fe'_{Co}]}{y-[Fe'_{Co}]}\right)\right) \\ &= s_{ox} + 2R\ln\left(\frac{\delta}{3-\delta}\right) - 4(1-f_e)\left(\Delta s_i^0 - R\ln\left(\frac{[Fe'_{Co}]}{y-[Fe'_{Co}]}\right)\right),\end{aligned} \tag{5.14}$$

where $s_{ox} = 2s_V^0 - 4s_{e'}^0$ and $\Delta s_i^0 = s_{Fe}^0 - s_{e'}^0$ are constants. The latter value can be roughly estimated if possible vibrational contributions to the entropy are neglected. The entropy of electrons in the wide band can be assumed negligible, i.e., $s_{e'}^0 \approx 0$ [24]. $s_{Fe}^0$ represents the difference in entropy between the $3d^5$ ($Fe^{3+}$) and $3d^4$ ($Fe^{4+}$) states due to differences in degeneracy $\nu$ of the magnetic state. This difference may be evaluated using a procedure analogous to that used by Korotin et al. [25]. The total spin in the high spin configuration of $3d^5$ and $3d^4$ states are $S$=5/2 and $S$=2,

respectively. Thus, their corresponding spin multiplicities ($2S+1$) are 6 and 5, respectively. As the configuration in $3d^4$ is $t_{2g}^3 e_g$, either one of the $e_g$ orbitals remains empty, which increases the total number of possible microstates for $Fe^{4+}$ by another factor of 2. Thus, $\nu=6$ for $Fe^{3+}$ ($t_{2g}^3 e_g^2$) and $\nu=10$ for $Fe^{4+}$. Hence $\Delta s_i^0 = s_{Fe}^0 = R\ln(\frac{6}{10}) =$ -4.25 J/mol K.

It should be noted that the defect model presented here incorporates the itinerant electron model proposed for $La_{1-x}Sr_xCoO_{3-\delta}$ as a limiting case. If $y=0$ and $f_e=1$ are substituted into Eqs. (5.13) and (5.14), the result is the same as described previously [7,8]. That is, when the concentration $y$ of iron reaches zero, all electrons formed necessarily go into the conduction band.

## 5.3. Experimental

### *5.3.1. Sample preparation*

All powders were prepared by thermal decomposition of metal nitrate solutions containing a complexing agent. The EDTA method [6] was applied for making compounds with iron dopant levels $y=0$, 0.1, 0.25 and 0.4, and the citrate synthesis [4] was used for the compound with $y=0.6$. After calcination in stagnant air at 925°C for 8 h and thorough milling, the powders were pressed uniaxially into cylindrical pellets, followed by isostatic pressing at 4000 bar. The pellets were then sintered in air at 1200°C for 12-18 h.

The densities of the resulting disks, expressed relative to theoretical, were 96-98% for all compositions. XRD phase analysis revealed single-phase perovskite-type oxides (see Appendix B). Cylindrical samples 7.75 mm in diameter and 3 mm thick were cut from the disks for the experiments. The samples with $y=0.4$ and $y=0.6$ were pretreated for 3 h in 2 M $HNO_3$ to enhance the surface exchange kinetics [26].

### *5.3.2. Coulometric titration experiments*

The electrochemical cell in which the measurements were performed has been described in detail elsewhere [7,8]. The experimental setup is schematically shown in Figure 5.2.

A $La_{0.6}Sr_{0.4}Co_{1-y}Fe_yO_{3-\delta}$ disk was enclosed in an electrochemical cell with a volume of approximately 250 $mm^3$. $Zr_{0.87}Y_{0.13}O_{1.935}$ solid electrolytes were used for pumping oxygen into or out of the cell, and for the EMF measurements. The reference gas used was air ($p_{O_2}$=0.209 bar) and the temperature range in which experiments were performed was 650-950°C. Two types of experiments were performed. In the first type, further on referred to as voltage step measurements, the equilibrium between oxide and ambient atmosphere in the cell was perturbed by a stepwise change of the imposed EMF across the electrolyte, after which the decay current $I(t)$ was monitored. After a new equilibrium was reached, i.e., $I(t)=I(\infty)$, the oxygen chemical

potential $\mu_{O_2}^{oxide}$ and the nonstoichiometry change $\Delta\delta$ were calculated using Eqs. (5.1) and (5.2), respectively.

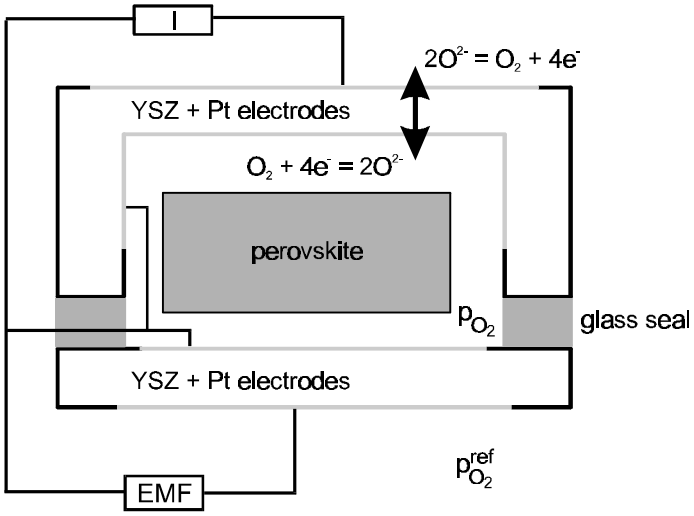


Figure 5.2. Schematic diagram of the experimental setup.

In the second type of experiments, referred to as temperature step measurements, the open cell EMF was measured at different temperatures at a fixed value of $\delta$. From the temperature variation of $\mu_{O_2}^{oxide}$ its entropy and energy parts were determined using Eq. (5.3). Both heating and cooling steps were applied and the results were averaged. A temperature step measurement was also performed between two isothermal series of voltage step measurements in order to relate their respective $\delta - p_{O_2}$ curves.

### *5.3.3. Thermogravimetric and wet-chemical analysis*

The nonstoichiometry of $La_{0.6}Sr_{0.4}CoO_{3-\delta}$ at room temperature ($\delta_{RT}$) was determined using the oxidizing power method [27] described in more detail by Stevenson et al. [21]. Prior to analysis the $La_{0.6}Sr_{0.4}CoO_{3-\delta}$ powder was heated to 1000°C and slowly cooled in air (144°C/day) to room temperature.

Perovskite powder was dissolved in concentrated HCl. Irrespective of the original oxidation state, all Fe and Co is reduced by the available $Cl^-$ to their 3+ and 2+ oxidation states, respectively. The amount of $Cl_2$ which developed in the reduction process was transported to a KI solution, where it oxidized $I^-$ to $I_2$. The amount of iodine was determined by titration with $Na_2S_2O_3$, from which the average valency of the transition metal cations was calculated.

For the thermogravimetric (TG) analyses about 200 mg of $La_{0.6}Sr_{0.4}Co_{1-y}Fe_yO_{3-\delta}$ powder was weighed and placed in a platinum cup in a Setaram Microbalance MTB 10-8. Before measurements were made, the powder was heated in air to 900°C to remove traces of impurities, followed by slow cooling to room temperature (0.5-1°C/min) to ensure chemical equilibrium with the ambient oxygen pressure. The

powder was then heated with 5-10°C/min in air to several temperatures in the range where coulometric titration experiments had been performed. After equilibration of the sample the weight loss from room temperature was measured, from which the nonstoichiometry change was calculated. Finally the sample was slowly cooled (2-3°C/min) to room temperature. No significant weight change was observed between room temperature and 900°C in a reference measurement on $\alpha$-$Al_2O_3$ under the same conditions.

## 5.4. Results and discussion

### *5.4.1. Nonstoichiometry in air*

The chemical analysis of $La_{0.6}Sr_{0.4}CoO_{3-\delta}$ was complicated by the presence of a small amount of carbon (0.13±0.03 mass%) in the powder. $Cl_2$ formed in the redox reaction may possibly react with it, forming chlorinated hydrocarbons, and thus remain undetected in the iodometric titration. This reduces the accuracy of the experiments. Still, the result indicated an oxygen concentration close to stoichiometric, i.e., $\delta_{RT}$=0.00±0.02.

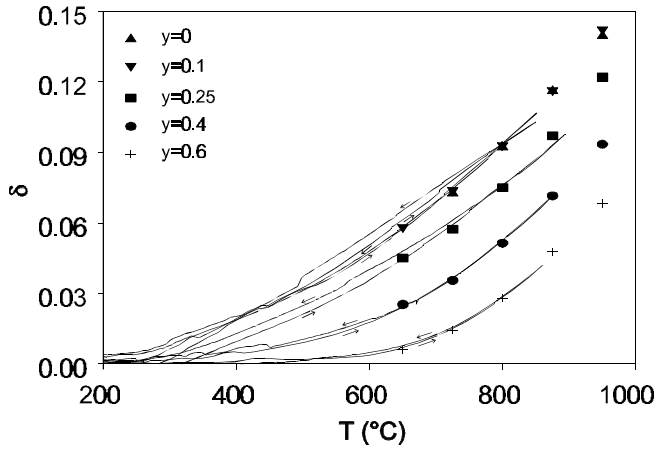


Figure 5.3. Nonstoichiometry of $La_{0.6}Sr_{0.4}Co_{1-y}Fe_yO_{3-\delta}$ in air.

This is consistent with the results of Mizusaki et al. [9], who determined the oxygen contents of $La_{0.5}Sr_{0.5}CoO_{3-\delta}$ and $La_{0.7}Sr_{0.3}CoO_{3-\delta}$ at room temperature to be stoichiometric or very close to it. As it may be assumed safely that $\delta$ decreases with increasing iron content at a given oxygen pressure and temperature, the other compositions are also close to stoichiometric.

The results of the thermogravimetric analyses in air are indicated in Figure 5.3 by the drawn lines. Depending on composition, the onset of weight loss was observed at temperatures of 150-400°C. All weight changes were reversible and independent of cooling rate in the range of 0.5-2.5°C/min.

Table 5.1. Nonstoichiometries of $La_{0.6}Sr_{0.4}Co_{1-y}Fe_yO_{3-\delta}$ at 800°C in air determined by TGA. Error $\Delta\delta=\pm0.003$.

| $y$ | $\delta$ (800°C, air) |
|---|---|
| 0 | 0.093 |
| 0.1 | 0.093 |
| 0.25 | 0.075 |
| 0.4 | 0.052 |
| 0.6 | 0.028 |

Based on these observations and the iodometric titration result, it is concluded that all investigated compounds are stoichiometric at room temperature within experimental error. For all compounds, the data from coulometric titration experiments at $p_{O_2}$=0.21 bar were fitted to the TG curves by varying the absolute value of the nonstoichiometry at 800°C. The best fits are indicated by the symbols in Figure 5.3. The values for $\delta$ obtained from fitting are listed in Table 5.1. A value $\delta\approx0.023$ has been determined for $La_{0.6}Sr_{0.4}Co_{0.2}Fe_{0.8}O_{3-\delta}$ under the same conditions [21], which agrees reasonably with that obtained from extrapolation of the present results.

### *5.4.2. Thermodynamic stability of the $La_{0.6}Sr_{0.4}Co_{0.75}Fe_{0.25}O_{3-\delta}$ phase*

The partial thermodynamic quantities $\varepsilon_{O_2}^{oxide}$ and $s_{O_2}^{oxide}$ of $La_{0.6}Sr_{0.4}Co_{0.75}Fe_{0.25}O_{3-\delta}$ obtained from temperature step measurements in the range 650-950°C are shown in Figure 5.4a.

The range of nonstoichiometries covered by the experiments is $\delta$=0.066-0.364. Two different regions can be distinguished within this range. In the region where $\delta<0.20$ the general trends are more or less similar to those observed previously on $La_{0.8}Sr_{0.2}CoO_{3-\delta}$ [8]. This range of nonstoichiometries is discussed in more detail below. The region $\delta>0.20$ is characterized by an increasing partial energy $\varepsilon_{O_2}^{oxide}$ with $\delta$, while the entropy of oxygen $s_{O_2}^{oxide}$ increases much more strongly than in the region $\delta<0.20$. At very high values of $\delta$ both quantities tend to become constant. The change in slope of $\varepsilon_{O_2}^{oxide}$ at $\delta$=0.20-0.25 can not be explained in terms of randomly distributed, non-interacting defects. The chemical potential of oxygen $\mu_{O_2}^{oxide} = \varepsilon_{O_2}^{oxide} - Ts_{O_2}^{oxide}$ is shown in Figure 5.4b. The deviation from linear behaviour is observed clearly at values $\delta>0.25$. In the region $\delta$=0.20-0.25 the change of slope of $\varepsilon_{O_2}^{oxide}$ can still be compensated by the increasing slope of $s_{O_2}^{oxide}$. At higher values of $\delta$ the oxygen chemical potential appears to reach a constant value, which indicates a chemical equilibrium between two or more phases.

Petrov et al. [10,16] showed by combined coulometric titration and XRD experiments that $La_{0.7}Sr_{0.3}CoO_{3-\delta}$ decomposes into $La_{1.4}Sr_{0.6}CoO_{4\pm\nu}$, $Co_{1-\gamma}O$ and $O_2$ at sufficiently high value of $\delta$. A similar kind of decomposition reaction may occur in

$La_{0.6}Sr_{0.4}Co_{0.75}Fe_{0.25}O_{3-\delta}$. The limit of thermodynamic stability in $La_{0.7}Sr_{0.3}CoO_{3-\delta}$ moves to higher values of δ upon increasing temperature [10]. This is consistent with the results in Figure 5.4b, where the $O_2$ chemical potential becomes constant at a slightly higher value of δ with increasing temperature.

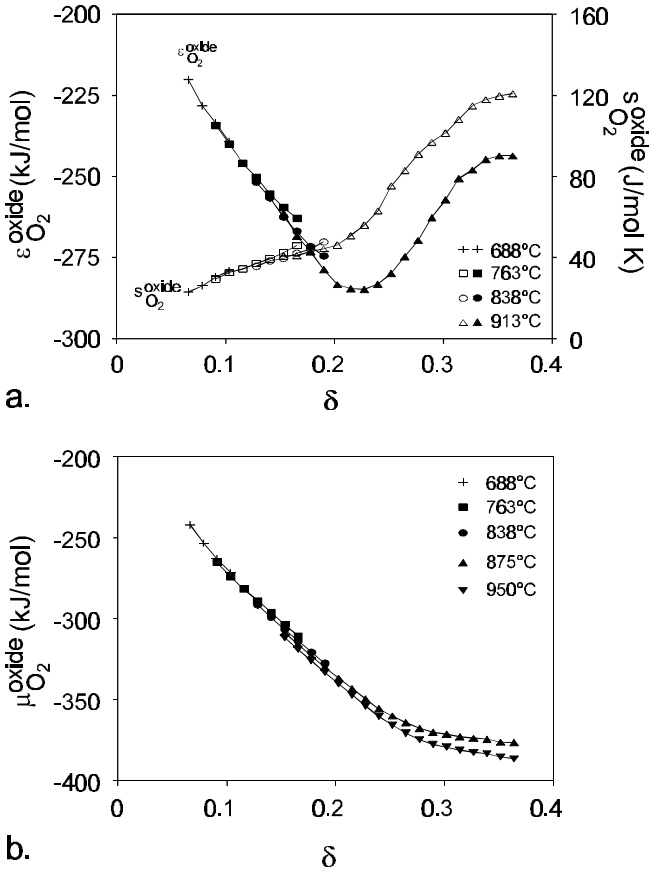


Figure 5.4. (a) Experimental energy $\varepsilon^{oxide}_{O_2}$ and entropy $s^{oxide}_{O_2}$ of oxygen in $La_{0.6}Sr_{0.4}Co_{0.75}Fe_{0.25}O_{3-\delta}$. (b) Chemical potential $\mu^{oxide}_{O_2}$ of oxygen.

It should be noted that the onset of decomposition occurs at a value near $\delta \approx \frac{1}{2}[Sr'_{La}]$, the nonstoichiometry at which the average valency of all transition metals cations is exactly 3+. Similar features were observed in the same region of nonstoichiometries on all other compounds containing iron. Attention is focused on the region δ<0.20 in the remainder of this study.

### *5.4.3. Partial thermodynamic quantities of $La_{0.6}Sr_{0.4}Co_{1-y}Fe_yO_{3-\delta}$*

As was stated already the overall features observed in Figure 5.4a in the region δ<0.2 are similar to those observed on $La_{0.8}Sr_{0.2}CoO_{3-\delta}$ [7,8]. $\varepsilon^{oxide}_{O_2}$ is seen to decrease almost linearly with δ, while $s^{oxide}_{O_2}$ is logarithmically dependent on δ to a first order of approximation. Both features can be understood in terms of the itinerant electron

model, which has been applied successfully to describe $La_{0.8}Sr_{0.2}CoO_{3-\delta}$, as well as $La_{0.6}Sr_{0.4}CoO_{3-\delta}$ and $La_{0.3}Sr_{0.7}CoO_{3-\delta}$ at high temperature and small $\delta$ [7,8]. According to this model, the decrease of $\varepsilon_{O_2}^{oxide}$ is linear due to the filling of the conduction band with electrons upon creation of oxygen vacancies, while $s_{O_2}^{oxide}$ increases with $\delta$ because of the increasing configurational entropy of oxygen $s_{conf} = R\ln(\delta/(3-\delta))$. The same contributions also emerge in the defect model proposed for LSCF in Section 5.2.2.

The argument of discussion given below is that for small values of *y* the itinerant electron model gives a fair description of the nonstoichiometry behaviour of LSCF, but this model no longer holds at high iron substitution levels. This agreement at small value of *y* can be clearly illustrated by the thermodynamic quantities of $La_{0.6}Sr_{0.4}Co_{0.9}Fe_{0.1}O_{3-\delta}$, shown in Figure 5.5.

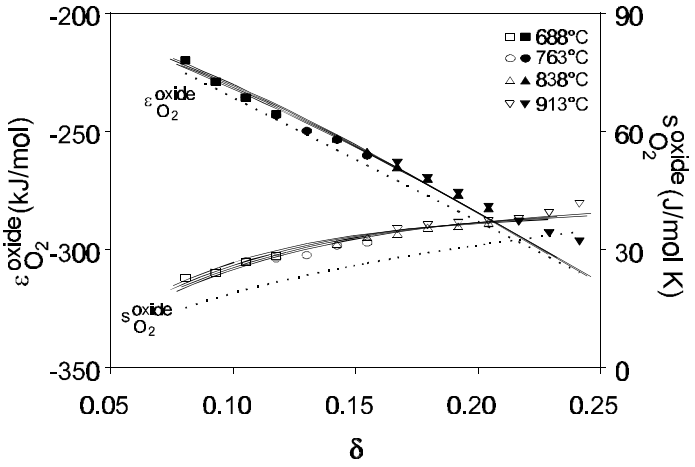


Figure 5.5. Energy $\varepsilon_{O_2}^{oxide}$ and entropy $s_{O_2}^{oxide}$ of oxygen in $La_{0.6}Sr_{0.4}Co_{0.9}Fe_{0.1}O_{3-\delta}$. Experimental results are indicated by symbols; best fits of LSCF model indicated by drawn lines; trends according to itinerant electron model indicated by dotted lines.

Note that these data exhibit the same trends as observed on $La_{0.6}Sr_{0.4}Co_{0.75}Fe_{0.25}O_{3-\delta}$ as shown in Figure 5.4. The drawn lines in Figure 5.5 are the best fits of Eqs. (5.13) and (5.14) to the experimental data. The corresponding values of $\varepsilon_{ox}$, $s_{ox}$ and $\Delta\varepsilon_i^0$ are listed in Table 5.2. It should be noted that since $\Delta\varepsilon_i^0$ is assumed to be independent of iron content, its value was determined by optimization of curve fits to data of other compounds as well. The value $g(\varepsilon_F)$=1.47 $eV^{-1}$, determined from the best fit of Eq. (5.13) to the data of $La_{0.6}Sr_{0.4}CoO_{3-\delta}$, was adopted for all compositions. This value is close to $g(\varepsilon_F)$=1.53 $eV^{-1}$ reported previously for $La_{0.6}Sr_{0.4}CoO_{3-\delta}$ [7].

Table 5.2. Thermodynamic quantities $\varepsilon_{ox}$. $\Delta\varepsilon_i^0$, $s_{ox}$, $\Delta s_i^0$ and $g(\varepsilon_F)$ determined from fitting Eqs. (5.13) and (5.14) to the experimental data.

| $y$ | $\varepsilon_{ox}$ (kJ/mol) | $\Delta\varepsilon_i^0$ (kJ/mol) | $s_{ox}$ (J/mol K) | $\Delta s_i^0$ (J/mol K) | $g(e_F)$((kJ/mol)$^{-1}$) |
|---|---|---|---|---|---|
| 0 | -281 | -25 | 86 | -4.25 | 0.0153 |
| 0.1 | -288 | -25 | 75 | -4.25 | 0.0153 |
| 0.25 | -297 | -25 | 73 | -4.25 | 0.0153 |
| 0.4 | -305 | -25 | 79 | -4.25 | 0.0153 |
| 0.6 | -314 | -25 | 83 | -4.25 | 0.0153 |

For the sake of clarity, the values of $\varepsilon_{ox}$ and $s_{ox}$ from Table 5.2 were used to draw the dotted lines in Figure 5.5, which indicate the predictions according to the itinerant electron model. Very close agreement is obtained if the values are adjusted to $\varepsilon_{ox}$=-281 kJ mol$^{-1}$ and $s_{ox}$=82 J mol$^{-1}$ K$^{-1}$.

Hence, it is concluded that the thermodynamics of $La_{0.6}Sr_{0.4}Co_{0.9}Fe_{0.1}O_{3-\delta}$ can be understood both within the framework of the itinerant electron model and the proposed defect model for LSCF. Next to the small iron content the close agreement between the models is also due to the small energy difference between the 3*d* states of iron and the energy at the Fermi level.

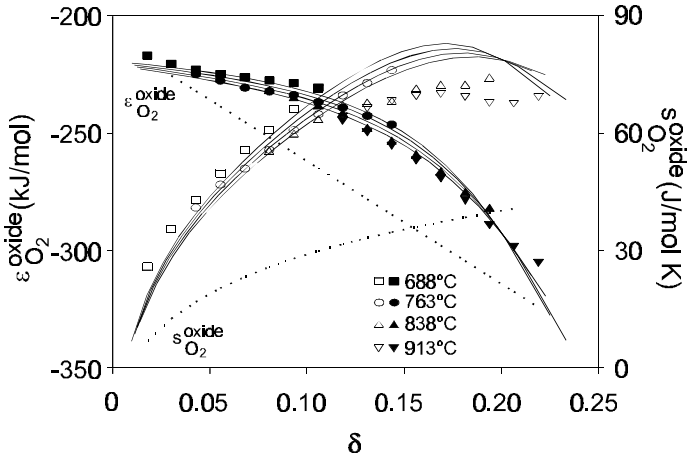


Figure 5.6. Energy $\varepsilon_{O_2}^{oxide}$ and entropy $s_{O_2}^{oxide}$ of oxygen in $La_{0.6}Sr_{0.4}Co_{0.4}Fe_{0.6}O_{3-\delta}$. Experimental results are indicated by symbols; best fits of LSCF model indicated by drawn lines; trends according to itinerant electron model indicated by dotted lines.

The value $\Delta\varepsilon_i^0$=-25 kJ mol$^{-1}$ indicates a small energy difference of about 0.25 eV between the Fermi level of $LaCoO_3$ and the $e_g$ state of iron. The difference becomes even smaller upon doping $LaCoO_3$ with strontium, due to the downward shift of the Fermi level. This implies that trapping of electron holes by Fe 3*d* states does not occur. These results are essentially in agreement with the findings of Tai et al. [20]. Large differences between the predictions of both models will occur only at large concentrations of iron, as discussed in more detail below.

It is interesting to note that deviations from the behaviour predicted by the itinerant electron model occur at much lower values of δ in $La_{0.6}Sr_{0.4}CoO_{3-\delta}$ [7] than in $La_{0.6}Sr_{0.4}Co_{0.9}Fe_{0.1}O_{3-\delta}$. In $La_{0.6}Sr_{0.4}CoO_{3-\delta}$ this has been attributed to additional ionic contributions to the partial energy and entropy of oxygen, possibly caused by the formation of microdomains with ordered oxygen vacancies. In contrast, such additional ionic contributions are not apparent in $La_{0.6}Sr_{0.4}Co_{0.9}Fe_{0.1}O_{3-\delta}$ up to large δ. This suggests that substitution of a small amount of Co by Fe may stabilize the random distribution of oxygen vacancies to much higher concentrations.

Figure 5.6 shows the thermodynamic quantities of $La_{0.6}Sr_{0.4}Co_{0.4}Fe_{0.6}O_{3-\delta}$. Symbols and lines have the same meaning as in the previous figure. Reasonable agreement is obtained between experimental data and best fits of Eqs. (5.13) and (5.14), but the itinerant electron model predicts strongly deviating trends, with best fits for $\varepsilon_{ox} \approx -290$ kJ mol$^{-1}$ and $s_{ox}=120$ J mol$^{-1}$ K$^{-1}$. Note that the values of $s_{ox}$ remain constant within experimental error for the LSCF model.

### *5.4.4. Nonstoichiometry of $La_{0.6}Sr_{0.4}Co_{1-y}Fe_yO_{3-\delta}$*

The experimental data for the nonstoichiometry of $La_{0.6}Sr_{0.4}Co_{0.9}Fe_{0.1}O_{3-\delta}$ and $La_{0.6}Sr_{0.4}Co_{0.4}Fe_{0.6}O_{3-\delta}$ obtained from voltage step measurements are shown in Figures 5.7 and 5.8.

The drawn lines are the theoretical curves according to the LSCF model with the values of $\varepsilon_{ox}$, $s_{ox}$ and $\Delta\varepsilon_i^0$ determined from the temperature step measurements inserted. The good agreement supports the correctness of the energy band scheme proposed in Figure 5.1 for modeling the data of oxygen nonstoichiometry of compounds $La_{0.6}Sr_{0.4}Co_{1-y}Fe_yO_{3-\delta}$. For $La_{0.6}Sr_{0.4}Co_{0.9}Fe_{0.1}O_{3-\delta}$ deviations from the theoretical curves are observed when $\delta > 0.20$, which is attributed to a limited phase stability as discussed above for $La_{0.6}Sr_{0.4}Co_{0.75}Fe_{0.25}O_{3-\delta}$. Deviations are also observed at 650°C at high oxygen pressure, which is not understood at present.

Excellent agreement is seen between experimental and theoretical curves for $La_{0.6}Sr_{0.4}Co_{0.4}Fe_{0.6}O_{3-\delta}$ in Figure 5.8 in the whole temperature and pressure range. It appears from this figure as well as from other data that the LSCF model performs better in representing the defect chemistry of the $La_{0.6}Sr_{0.4}Co_{1-y}Fe_yO_{3-\delta}$ system at higher iron contents.

The observed decrease of δ with $y$ in $La_{0.6}Sr_{0.4}Co_{1-y}Fe_yO_{3-\delta}$ at a given temperature and oxygen pressure can be explained in terms of the defect model by considering that $\varepsilon_{ox}$ can be regarded as a measure of the binding strength of $O^{2-}$ in the oxide. Thus, the increase of its absolute magnitude with iron concentration reflects an increasing binding strength, which suppresses oxygen vacancy formation. Furthermore, it can be shown that the average valency of the iron atoms is higher than the average valency of cobalt under all conditions. This indicates that strontium doping is charge-compensated more readily by hole formation on iron than on cobalt.

Considering that the hole concentration is negatively proportional to the oxygen vacancy concentration, the presence of iron lowers the nonstoichiometry.

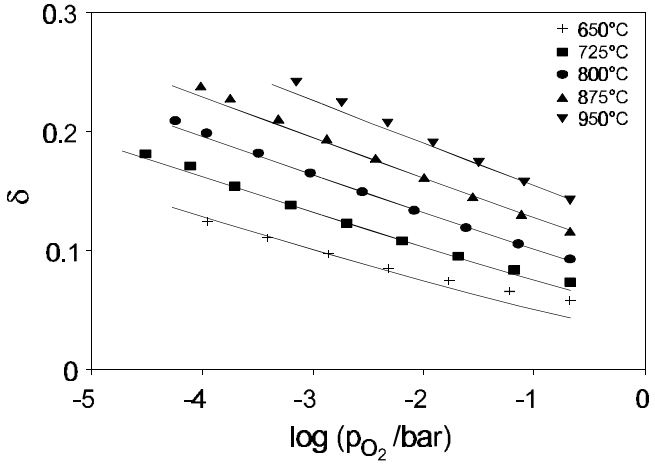


Figure 5.7. Nonstoichiometry of $La_{0.6}Sr_{0.4}Co_{0.9}Fe_{0.1}O_{3-\delta}$ versus oxygen partial pressure. Drawn lines indicate best fits of the LSCF model to the experimental data.

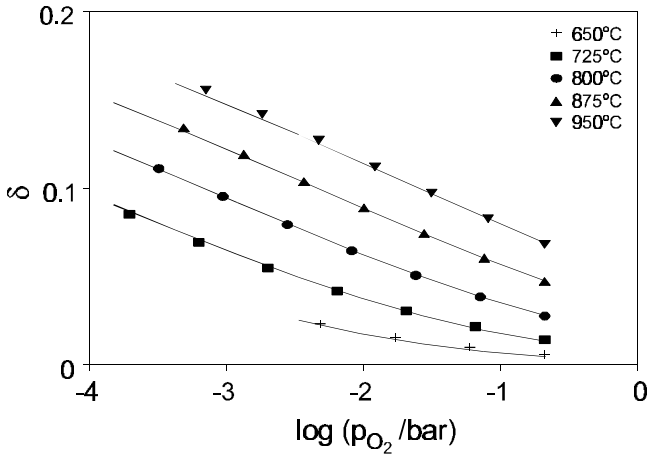


Figure 5.8. Nonstoichiometry of $La_{0.6}Sr_{0.4}Co_{0.4}Fe_{0.6}O_{3-\delta}$ versus oxygen partial pressure. Drawn lines indicate best fits of the LSCF model to the experimental data.

## 5.5. Conclusions

The level of nonstoichiometry δ in perovskites $La_{0.6}Sr_{0.4}Co_{1-y}Fe_yO_{3-\delta}$ decreases with iron content, which is attributed to an increasing binding energy of oxygen $O^{2-}$ in the lattice and a larger tendency of iron to form holes rather than oxygen vacancies. At relatively small values of δ, the energy and entropy of $O_2$ in the oxide can be interpreted in terms of a new model proposed to describe the defect structure. The oxygen vacancies are thought to be distributed randomly, while the electrons created during oxygen vacancy formation are partly donated to a partially filled electron

band, of which the density of states at the Fermi level is proportional to the Co content, and partly to Fe donor centres. The energy of the latter states is close to the Fermi level energy.

The observed trends can only be described satisfactorily in terms of the itinerant electron model at small values of *y*. The substitution of small amounts of Co by Fe appears to suppress features observed previously on $La_{0.6}Sr_{0.4}CoO_{3-\delta}$ at relatively high δ, attributed to clustering of oxygen vacancies in microdomains. The perovskite phase decomposes partly at high values of δ, but the value of δ at which the onset of decomposition occurs increases with temperature.

## References


1. Y. Teraoka, H.-M. Zhang, S. Furukawa and N. Yamazoe, "Oxygen permeation through perovskite-type oxides," *Chem. Let.*, (1985) 1743-1746.
2. L. Qiu, T.H. Lee, L.-M. Liu, Y.L. Yang and A.J. Jacobsen, "Oxygen permeation studies of $SrCo_{0.8}Fe_{0.2}O_{3-\delta}$," *Solid State Ionics*, **76** (1995) 321-329.
3. Chapter 2 of this thesis.
4. H.M. Zhang, Y. Shimizu, Y. Teraoka, N. Miura and N. Yamazoe, "Oxygen sorption and catalytic properties of $La_{1-x}Sr_xCo_{1-y}Fe_yO_3$ perovskite-type oxides," *J. Catal.*, **121** (1990) 432-440.
5. Chapter 7 of this thesis.
6. H.J.M. Bouwmeester, "Dense ceramic membranes for oxygen separation," in: *CRC Handbook Solid State Chemistry*, ed. P.J. Gellings and H.J.M. Bouwmeester, CRC Press, Boca Raton, 1996, p. 481-553.
7. M.H.R. Lankhorst, "Oxygen nonstoichiometry behavior in $La_{1-x}Sr_xCoO_{3-\delta}$," Chapter 5 in: *Thermodynamic and transport properties of mixed ionic-electronic conducting perovskite-type oxides*, Thesis, University of Twente, Enschede, the Netherlands, 1997.
8. M.H.R. Lankhorst, H.J.M. Bouwmeester and H. Verweij, "Use of the rigid band formalism to interpret the relationship between O chemical potential and electron concentration in $La_{1-x}Sr_xCoO_{3-\delta}$," *Phys. Rev. Let.*, **77** (1996) 2989-2992.
9. J. Mizusaki, Y. Mima, S. Yamauchi, K. Fueki and H. Tagawa, "Nonstoichiometry of the perovskite-type oxides $La_{1-x}Sr_xCoO_{3-\delta}$," *J. Solid State Chem.*, **80** (1989) 102-111.
10. A.N. Petrov, V.A. Cherepanov, O.F. Kononchuk and L.Ya. Gavrilova, "Oxygen nonstoichiometry of $La_{1-x}Sr_xCoO_{3-\delta}$ ($0<x\leq0.6$)," *J. Solid State Chem.*, **87** (1990) 69-76.
11. V.A. Cherepanov, L.Yu. Barkhatova, A.N. Petrov and V.I. Voronin, "Phase equilibria in the La-Sr-Co-O system and thermodynamic stability of the single phases," Proc. 4th Intl. Symp. on *Solid Oxide Fuel Cells*, ed. M. Dokiya, O. Yamamoto, H. Tagawa and S.C. Singhal, Proc. vol. 95-1, The Electrochemical Society, Pennington, NJ, 1995, p. 434-443.
12. J. Zaanen, G.A. Sawatzky and J.W. Allen, "Band gaps and electronic structure of transition-metal compounds," *Phys. Rev. Let.*, **55** (1985) 418-421.
13. A. Mineshige, M. Inaba, T. Yao, Z. Ogumi, K. Kikuchi and M. Kasawe, "Crystal structure and metal-insulator transition of $La_{1-x}Sr_xCoO_{3-\delta}$," *J. Solid State Chem.*, **121** (1996) 423-429.
14. M.H.R. Lankhorst, "Electrical transport properties of $La_{1-x}Sr_xCoO_{3-\delta}$," Chapter 3 in: *Thermodynamic and transport properties of mixed ionic-electronic conducting perovskite-type oxides*, Thesis, University of Twente, Enschede, the Netherlands, 1997.

15. J. Mizusaki, J. Tabuchi, T. Matsuura, S. Yamauchi and K. Fueki, “Electrical conductivity and Seebeck coefficient of $La_{1-x}Sr_xCoO_{3-\delta}$,” *J. Electrochem. Soc.*, **136** (1989) 2082-2088.
16. A.N. Petrov, O.F. Kononchuk, A.V. Andreev, V.A. Cherepanov and P. Kofstad, “Crystal structure, electrical and magnetic properties of $La_{1-x}Sr_xCoO_{3-y}$,” *Solid State Ionics*, **80** (1995) 189-199.
17. J. Mizusaki, M. Yoshihiro, S. Yamauchi and K. Fueki, “Nonstoichiometry and defect structure of the perovskite-type oxides $La_{1-x}Sr_xFeO_{3-\delta}$,” *J. Solid State Chem.* **58** (1985) 257-266.
18. J. Mizusaki, T. Sasamoto, W.R. Cannon and H.K. Bowen, “Electronic conductivity, Seebeck coefficient, and defect structure of $La_{1-x}Sr_xFeO_{3-\delta}$ ($x$=0.1, 0.25),” *J. Am. Ceram. Soc.*, **66** (1983) 247-252.
19. M. Abbate, F.M.F. de Groot, J.C. Fuggle, A. Fujimori, O. Strebel, F. Lopez, M. Domke, G. Kaindl, G.A. Sawatzky, M. Takano, Y. Takeda, H. Eisaki and S. Uchida, “Controlled-valence properties of $La_{1-x}Sr_xFeO_3$ and $La_{1-x}Sr_xMnO_3$ studied by soft x-ray absorption spectroscopy,” *Phys. Rev. B*, **46** (1992) 4511-4519.
20. L.-W. Tai, M.M. Nasrallah, H.U. Anderson, D.M. Sparlin and S.R. Sehlin, “Structure and electrical properties of $La_{1-x}Sr_xCo_{1-y}Fe_yO_3$. Part 1. The system $La_{0.8}Sr_{0.2}Co_{1-y}Fe_yO_3$,” *Solid State Ionics*, **76** (1995) 259-271.
21. J.W. Stevenson, T.R. Armstrong, R.D. Carneim, L.R. Pederson and W.J. Weber, “Electrochemical properties of mixed conducting perovskites $La_{1-x}M_xCo_{1-y}Fe_yO_3$ (M=Sr, Ba, Ca),” *J. Electrochem. Soc.*, **143** (1996) 2722-2729.
22. IUPAC, Commission on Thermodynamics; *Oxygen, International thermodynamic tables of the fluid state-9*, Blackwell Scientific Publications, (1987).
23. F.A. Kröger, *The chemistry of imperfect crystals*, North-Holland, Amsterdam, (1964).
24. M.H.R. Lankhorst, “Thermodynamics and transport of ionic and electronic defects in crystalline oxides,” Chapter 2 in: *Thermodynamic and transport properties of mixed ionic-electronic conducting perovskite-type oxides*, Thesis, University of Twente, Enschede, the Netherlands, 1997.
25. M.A. Korotin, S.Yu. Ezhov, I.V. Solovyev, V.I. Anisimov, D.I. Khomskii and G.A. Sawatzky, “Intermediate-spin state and properties of $LaCoO_3$,” *Phys. Rev. B*, **54** (1996) 5309-5316.
26. N. Miura, Y. Okamoto, J. Tamaki, K. Morinaga and N. Yamazoe, “Oxygen semipermeability of mixed-conductive oxide thick-film prepared by slip casting,” *Solid State Ionics*, **79** (1995) 195-200.
27. R.J. Nadalin and W. Brozda, “Chemical methods for the determination of the "oxidizing (or reducing) power" of certain materials containing a multivalent element in several oxidation states,” *Anal. Chim. Acta*, **28** (1963) 282-293.

# 6

# Chemical diffusion and oxygen exchange of $La_{0.6}Sr_{0.4}Co_{0.6}Fe_{0.4}O_{3-\delta}$


## Abstract

The transport parameters of $La_{0.6}Sr_{0.4}Co_{0.6}Fe_{0.4}O_{3-\delta}$ were determined by electrical conductivity relaxation and high temperature coulometric titration experiments. The experimental response curves were analyzed in the frequency domain. The results obtained by both methods were in good agreement. The chemical diffusion coefficients measured at temperatures of 923-1255 K and oxygen partial pressures of 0.03-1 bar $O_2$ vary between $10^{-6}$-$5 \cdot 10^{-5}$ $cm^2$ $s^{-1}$. The experimental activation energies are in the range 95-117 kJ/mol. At oxygen partial pressures below 0.03 bar $O_2$ the re-equilibration process is completely governed by the rate of oxygen exchange at the interface. The surface exchange coefficients were determined by conductivity relaxation experiments at temperatures of 1000-1285 K and oxygen pressures of $10^{-4}$-0.1 bar $O_2$. The activation energy is about 60-70 kJ/mol. The exchange coefficients are almost proportional to the oxygen pressure. Treatment of the surface in a nitric acid solution for several hours increases the surface exchange rates by factors of 3-5.

## 6.1. Introduction

Knowledge of the relevant transport parameters of solid oxides is of fundamental importance in the development of high temperature solid state electrochemical devices. Several experimental techniques have already been employed in the study of oxygen transport through perovskite-type oxides, such as isotopic exchange analysis [1-3], transient thermogravimetry [4], oxygen coulometric titration [5-7] and electrical conductivity relaxation [8-10].

Transient methods are based on the principle of subjecting an oxide sample to a sudden change of the oxygen chemical potential of the ambient atmosphere and monitoring the rate at which the specimen proceeds to equilibrium. The transient response is commonly analyzed in the time domain under the assumption that chemical diffusion is the only rate-determining factor in the re-equilibration process [5,11]. In general, however, the rate of re-equilibration may also be affected by slow interfacial exchange, gas phase diffusion and, in the case of oxygen coulometric titration, polarization losses over electrical wiring and contacts.

These contributions can be discriminated from chemical diffusion by analyzing the experimental data in the frequency domain. This approach has been followed in recent studies on chemical diffusion in $La_{0.8}Sr_{0.2}CoO_{3-\delta}$ [7] and $La_{1-x}Sr_xFeO_{3-\delta}$ ($x$=0.1, 0.4) [12]. In the present paper the chemical diffusion and surface exchange coefficients of $La_{0.6}Sr_{0.4}Co_{0.6}Fe_{0.4}O_{3-\delta}$ are determined. Both electrical conductivity relaxation and oxygen coulometric titration are applied. The analysis of transient data is performed in the frequency domain and the results obtained with the two techniques are compared.

## 6.2. Theory

A solid oxide body in chemical and thermal equilibrium with the surrounding atmosphere has a uniform bulk concentration of oxygen $c_b(x,y,z,t)$ equal to $c_0$. At $t$=0, the oxygen activity in the ambient atmosphere is changed stepwise to a value corresponding to a new equilibrium concentration $c_\infty$ in the solid. Chemical diffusion allows the sample to adapt its stoichiometry to $c_\infty$. The concentration at any point $(x,y,z)$ in the bulk at time $t$>0 can be calculated from the solution of Fick's second law

$$\frac{\partial c(x,y,z,t)}{\partial t} = \tilde{D}\nabla^2 c(x,y,z,t). \qquad (6.1)$$

The bulk concentration is expressed relative to its initial concentration: $c(x,y,z,t) = c_b(x,y,z,t) - c_0$. $\tilde{D}$ is the chemical diffusion coefficient. A boundary condition appropriate for both types of measurements performed here is $c(x,y,z,0) = 0$. Their respective cases are discussed below.

### *6.2.1. Electrical conductivity relaxation*

The electrical conductivity relaxation technique is based on the principle that a change of the nonstoichiometry δ of a specimen is reflected in a change of the apparent macroscopic conductivity $\sigma_{app}$. The relative change of conductivity $\sigma_{app}^{rel}$ after a stepwise change of the ambient oxygen pressure is related to the mass change $m$ of the specimen via [13]

$$\sigma_{app}^{rel}(t) = \frac{\sigma_{app}(t) - \sigma_{app}(0)}{\sigma_{app}(\infty) - \sigma_{app}(0)} = \frac{m(t)}{m(\infty)}, \tag{6.2}$$

provided that the conductivity is measured in a direction perpendicular to the direction in which oxygen diffusion in the sample occurs. Even when electrical conductivity and departure from stoichiometry are not linearly related, this relationship can still be applied as long as there is no extremum in the electrical conductivity within the re-equilibration step [11].

The geometry and dimensions of the oxide samples used in the present electrical relaxation experiments were selected such that diffusion occurs in one direction ($z$) only. Considering diffusion in a sheet of thickness $L$ (-½$L$#$z$#½$L$), the boundary conditions for the interfaces are $-\tilde{D}(\partial c(z,t)/\partial z)_{z=\pm L/2} = \mp K_{ex}(\Delta c - c(\pm ½ L,t))$, where $K_{ex}$ is the apparent surface exchange coefficient and $\Delta c = c_\infty - c_0$. That is, the oxide surface is assumed not to equilibrate immediately with the newly imposed ambient atmosphere, but equilibration is described by a linear rate law. Eq. (6.1) is readily solved in the Laplace domain [12], yielding

$$\overline{c(z,s)} = \frac{\Delta c}{s}\left(1 + \frac{k\tilde{D}}{K_{ex}}\tanh(½kL)\right)^{-1} \frac{\cosh(kz)}{\cosh(½kL)}, \tag{6.3}$$

with $\overline{c(z,s)}$ the Laplace transform of $c(z,t)$, and $k = \sqrt{s/\tilde{D}}$. The total mass change $\overline{m(s)}$ in the frequency domain is obtained by integration of Eq. (6.3) over the specimen volume. An impedance representation $\overline{Z(s)}$ of the theoretical solution can be given [12]

$$\overline{Z(s)} = \frac{1}{s^2}\frac{m(\infty)}{\overline{m(s)}} = \frac{L}{2K_{ex}} + \sqrt{\frac{L^2}{4\tilde{D}s}}\coth(½kL) = R_s + T(s). \tag{6.4}$$

Hence, the impedance can be described by a serial arrangement of a resistance $R_s$, associated with the limited oxygen exchange rate at the interface and an element $T(s)$, describing the finite length diffusion in the sample.

### 6.2.2. Oxygen coulometric titration

In coulometric titration measurements the sample is enclosed in an isolated compartment. Two of the compartment walls are oxygen-conducting solid electrolytes with identical metallic electrodes attached to both sides, and in contact on opposite sides with the atmosphere inside the cell and a reference gas, respectively. The oxygen pressure inside the cell is controlled by imposing an EMF across one of the electrolytes. After a sudden potentiostatic change by a value ΔEMF, the gas/solid system inside the cell re-equilibrates by electrochemical pumping of oxygen through the second electrolyte wall. The electrical decay current $I(t)$ through this electrolyte is monitored. Upon neglecting the gas phase capacity for oxygen, this current is equal to the electrical current through the sample interfaces.

The samples used in the present experiments are disk-shaped (radius $R$, thickness $L$). Due to the complicated mathematics involved, the diffusion equation is solved under the simplifying assumption that the surface reaction is very fast. Using cylindrical coordinates ($-½L \# z \# ½L$; $0 \# r \# R$), the boundary conditions are $c(\pm ½ L, r, t) = c(z, R, t) = \Delta c$ and $(\partial c(z,r,t)/\partial r)_{r=0} = 0$. The solution to Fick's second law is [14]

$$\overline{c(z,r,s)} = \frac{\Delta c}{s}\left(1 - \sum_{i=1}^{\infty}\sum_{n=1}^{\infty}\left(\frac{2J_0(\alpha_i r/R)}{\alpha_i J_1(\alpha_i)}\right)\left(\frac{-4\cos((2n-1)\pi z/L)}{(-1)^n(2n-1)\pi}\right)\frac{s\tau}{s\tau + \alpha_i^2/\alpha + (2n-1)^2\pi^2/\beta}\right), \quad (6.5)$$

where $\alpha = R^2/(R^2+L^2)$, $\beta = L^2/(R^2+L^2)$, and $\tau = (R^2+L^2)/\tilde{D}$. $J_0$ and $J_1$ are $0^{th}$ and $1^{st}$ order Bessel functions, respectively, and $\alpha_i$ is the $i^{th}$ value for which $J_0(\alpha_i) = 0$. The frequency transform of the electrical current, $\overline{I(s)}$, associated with transport of $O^{2-}$ through the sample interfaces, can be calculated from Fick's first law using Eq. (6.5). The impedance of the sample due to diffusion, defined by $\overline{T(s)} = \overline{\Delta EMF}/\overline{I(s)}$, is [14]

$$\overline{T(s)} = \left(\frac{\Delta EMF}{\Delta Q}\right)\left(\frac{\alpha\beta\tau}{32}\right)\left(\sum_{i=1}^{\infty}\sum_{n=1}^{\infty}\left(\frac{\alpha}{\alpha_i^2} + \frac{\beta}{(2n-1)^2\pi^2}\right)\left(\frac{s\tau}{s\tau + \alpha_i^2/\alpha + (2n-1)^2\pi^2/\beta}\right)\right)^{-1}, \quad (6.6)$$

where $\Delta Q = -2eR^2L\Delta c$ ($e$ is the elementary electron charge) is the total electrical charge pumped through the electrolyte in the course of re-equilibration.

## 6.3. Experimental

### 6.3.1. Sample preparation

The method of preparation of the samples has been described extensively elsewhere [15]. XRD analysis indicated a single-phase perovskite-type oxide [16]. The sample surfaces were polished with 1000 MESH SiC. The final samples had densities of 95-98% relative to theoretical. The sample for the coulometric titration experiment

was disk-shaped ($R$=7.75 mm, $L$=2.5 mm). Rectangular samples of 27x14x0.51 mm were used for the conductivity relaxation experiments. Some of the samples were given a treatment in a 2.5-5 M $HNO_3$ solution for 2-18 h [17], followed by ultrasonic cleaning in water and alcohol.

### *6.3.2. Electrical conductivity relaxation*

Gold wires of 0.1 mm diameter were wound around the outer ends of the samples. The contact between wires and sample was provided by gold electrodes. The sample was placed in a quartz tube. A thermocouple to measure the temperature was positioned 3 mm above the sample. The quartz tube was flushed with oxygen diluted in nitrogen at atmospheric pressure. A second gas stream was vented. The oxygen concentrations in both streams, each with a flow of 100 ml/min (STP), were varied between 100 ppm and 100% and could be measured with an oxygen sensor. The flows leading to the sample and vent could be interchanged with a fast electrical four-way valve.

Oxygen pressure steps were performed in oxidizing and reducing direction, in which the oxygen partial pressure changed with a factor of 10 (at low temperature and high pressure) or less, typically a factor of about 3. The absence of mass transfer limitations in the gas phase was verified by variation of the total gas flow and the magnitude of the oxygen pressure step. Measurements were performed in the temperature range 1000-1285 K. To avoid mass transfer limitations oxidation runs were only performed at a final oxygen concentration of 1% or more. Further details can be found elsewhere [12].

The specimen resistance was measured in a Wheatstone bridge using a lock-in amplifier. The experimental data $\sigma_{app}^{rel}(t)$ were transformed to an impedance representation $\overline{Z(j\omega)} = -(\omega^2 \overline{\sigma_{app}^{rel}(j\omega)})^{-1}$ and analyzed using Equivalent Circuit software [18] by fitting to a serial circuit consisting of a cotangent-hyperbolic function ($T$), representing a finite length diffusion element, and a resistance ($R$).

### *6.3.3. Oxygen coulometric titration*

Details regarding the equipment and experimental procedure can be found elsewhere [7,14]. The cell consisted of a YSZ crucible onto which a YSZ disk was sealed using a Pyrex glass ring. The internal volume of the cell was approximately 250 $mm^3$. Crucible and disk served as electrolytes and Pt-based electrodes were painted on opposite sides of both. The sealed cell containing the sample was placed in a quartz tube which was flushed with air.

Potentiostatic steps $\Delta$EMF=25 mV were applied at temperatures between 923-1223 K in a cell-voltage range corresponding to the oxygen pressure range 0.01-0.209 bar $O_2$. The data were analyzed by a modified version of Equivalent Circuit software [18].

## 6.4. Results and discussion

### *6.4.1. Diffusion coefficients*

Complex impedance representations of experimental data from both methods obtained at high oxygen partial pressures are shown in Figure 6.1. Note that the data represent physically different cases. In the conductivity relaxation experiments only changes of conductivity are monitored, so that the resistance of external wiring, assumed constant, is filtered from the data. The impedance data shown can therefore be related directly to finite length diffusion and surface exchange processes of the oxide sample, represented by the circuit elements $T$ and $R_s$, respectively. In the example shown in Figure 6.1a, the resistance $R_s$ is negligible. A chemical diffusion coefficient $\tilde{D}$ =2.8·10$^{-6}$ cm$^2$ s$^{-1}$ at 1000 K was calculated using Eq. (6.4) from the best fit.

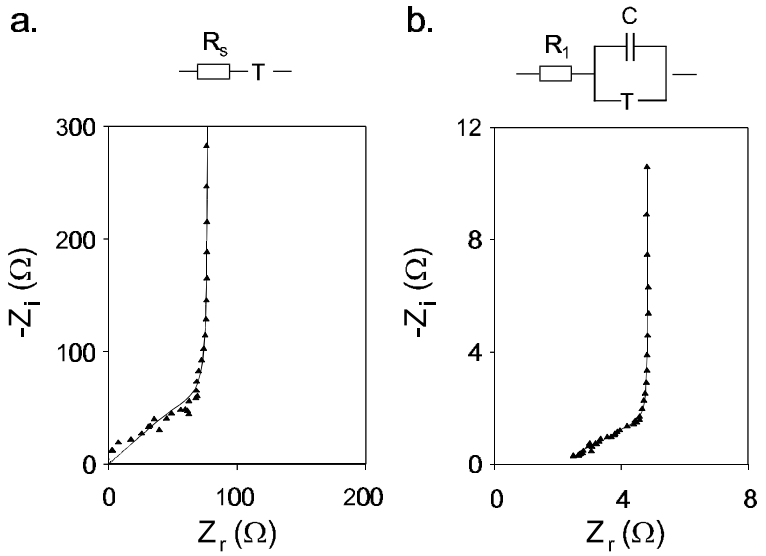


Figure 6.1. Impedance representations of experimental data. (a) Conductivity relaxation, T=1000 K, 0.104→0.316 bar $O_2$; (b) Coulometric titration, T=1073 K, 0.209→0.071 bar $O_2$. Drawn lines indicate best fits to equivalent circuits shown above.

In the coulometric titration experiments the impedance of the entire cell is measured. Hence, the impedance contains a series resistance associated with external electrical wiring and (possibly) internal gas phase diffusion. Moreover, the gas phase in the cell acts as a capacitance parallel to the impedance of the oxide sample. The corresponding circuit to which the data were fitted is shown in Figure 6.1b. $R_1$ represents the resistance effects such as gas phase diffusion in the bulk and resistance of external wiring. The capacitance $C$ represents the capacitative effect of the gas phase and $T$ is the impedance associated with diffusion in the oxide sample, given by Eq. (6.6). Best fits to various data indicated that $C$ was proportional to the oxygen pressure, as is expected on theoretical grounds for the gas phase capacitance [14]. In the experiment illustrated in Figure 6.1b, $C$ was about 3.2 F. In

the same experiment $R_1$ was about 2.2 Ω, and from the value of $T$ a chemical diffusion coefficient $\tilde{D}$ =8.1·10$^{-6}$ cm$^2$ s$^{-1}$ at 1073 K was calculated using Eq. (6.6).

Diffusion coefficients were determined with both methods, covering the oxygen partial pressure range 0.03-1 bar $O_2$. The Arrhenius representations of the diffusion coefficients obtained by both methods are shown in Figure 6.2. The indicated data points are the average values obtained at that temperature. No oxygen pressure dependence was observed within the oxygen partial pressure range in which the chemical diffusion coefficients were determined. The agreement between the two series of data is fairly good. From the results of the conductivity relaxation experiments an activation energy of 95±4 kJ/mol was calculated for chemical diffusion, while the coulometric titration results yielded 117±5 kJ/mol. At 1150 K, $\tilde{D}$ =10$^{-5}$ cm$^2$ s$^{-1}$ was reported for $La_{0.8}Sr_{0.2}CoO_{3-\delta}$ [10].

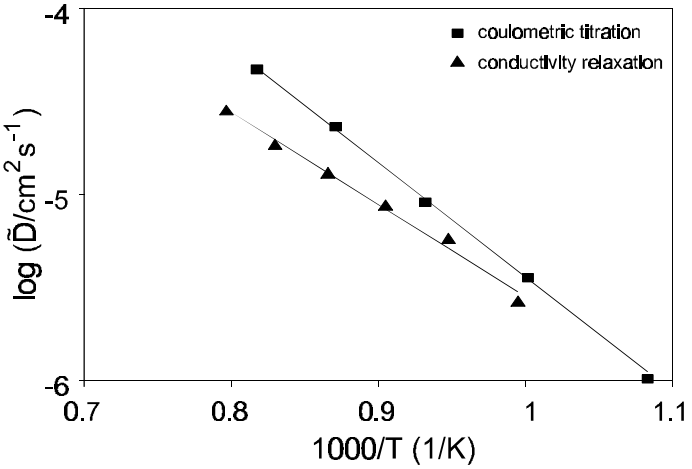


Figure 6.2. Chemical diffusion coefficient of oxygen in $La_{0.6}Sr_{0.4}Co_{0.6}Fe_{0.4}O_{3-\delta}$ at 0.1-1 bar $O_2$ from different relaxation experiments.

The oxygen deficiency δ, oxygen content $c_O$ (=3-δ) and thermodynamic factor $\gamma = \frac{1}{2}(\partial \ln p_{O_2} / \partial \ln c_O)$ of $La_{0.6}Sr_{0.4}Co_{0.6}Fe_{0.4}O_{3-\delta}$ were calculated at selected temperatures and pressures from oxygen coulometric titration data reported previously [19]. The oxygen self-diffusion coefficient $D_O$ and vacancy diffusion coefficient $D_V$ were determined using the relationships $\tilde{D} = D_O\gamma$ and $D_O c_O = D_V\delta$ under the assumption that the value of $\tilde{D}$ could be assigned to the oxygen partial pressures at the end of the experiment. The resulting values are listed in Table 6.1. The corresponding activation energies for $D_O$ were 140±15 kJ/mol and 165±12 kJ/mol derived from conductivity relaxation and coulometric titration results, respectively, and calculation of the activation energy of $D_V$ yielded 69±11 kJ/mol and 94±6 kJ/mol, respectively.

### 6.4.2. Surface exchange coefficients

In the coulometric titration experiments the value of $R_1$ was seen to increase strongly with decreasing oxygen partial pressure. At oxygen pressures below 0.05-0.10 bar the diffusion coefficient could no longer be determined due to the high value of $R_1$. Similar features observed in potentiostatic step experiments on compounds $La_{0.8}Sr_{0.2}CoO_{3-\delta}$ [14] could be explained by the increased contribution from surface exchange in re-equilibration at lower oxygen partial pressures. The surface exchange process was explicitly taken into account in fitting the impedance spectra by placing an extra resistance $R_2$ in series with the diffusion element $T$ in the circuit shown in Figure 6.1b. The value of $R_1$ appeared to be independent of oxygen pressure, while $R_2$ increased strongly with decreasing $p_{O_2}$, i.e., $R_2 \sim p_{O_2}^n$, where $n$=0.5-1. The absence of mass transfer limitation in the gas phase was concluded from the constancy of $R_1$. No further attempts were made in this paper to derive values of $K_{ex}$ from data of coulometric titration experiments.

Table 6.1. Self-diffusion coefficient ($D_O$) and vacancy diffusion coefficient ($D_V$) of oxygen. δ and γ were calculated from Ref. [19].

| $T$ (K) | δ | log γ | log ($D_O$ /cm$^2$ s$^{-1}$) | log ($D_V$ /cm$^2$ s$^{-1}$) |
|---|---|---|---|---|
| conductivity relaxation ($p_{O_2}$ =1 bar) | | | | |
| 1005 | 0.010 | 2.51 | -8.08 | -5.68 |
| 1055 | 0.017 | 2.35 | -7.58 | -5.39 |
| 1105 | 0.027 | 2.24 | -7.30 | -5.28 |
| 1155 | 0.037 | 2.15 | -7.03 | -5.15 |
| 1205 | 0.049 | 2.04 | -6.81 | -5.06 |
| 1255 | 0.062 | 2.00 | -6.59 | -4.92 |
| coulometric titration ($p_{O_2}$ =0.209 bar) | | | | |
| 923 | 0.007 | 2.65 | -8.64 | -6.07 |
| 998 | 0.017 | 2.37 | -7.82 | -5.60 |
| 1073 | 0.033 | 2.19 | -7.23 | -5.29 |
| 1148 | 0.053 | 2.08 | -6.72 | -4.98 |
| 1223 | 0.074 | 2.02 | -6.35 | -4.76 |

In the conductivity relaxation experiments the times needed to re-equilibrate the samples were also seen to increase strongly at lower oxygen partial pressures. The impedance spectra indicated pure resistive behaviour. Since mass transfer limitation in the gas phase is absent, the re-equilibration process under these conditions can be attributed to slow interfacial exchange of oxygen. At partial pressures below 0.03-0.10 bar $O_2$ the effect of diffusion could no longer be observed in the experimental impedance spectra. The value of $R_s$ was determined from the low frequency part of the impedance spectra at low oxygen pressures. The surface

exchange coefficient $K_{ex}$ was calculated from $R_s$ using Eq. (6.4). No systematic differences could be observed between the values of $K_{ex}$ obtained from oxidation and reduction runs.

It has been observed that the oxygen permeation rate through $La_{0.6}Sr_{0.4}Co_{0.8}Fe_{0.2}O_{3-\delta}$ membranes [17] was increased significantly upon treatment of the membrane surfaces for several hours in a 2 M nitric acid solution. The XPS spectra [17] indicated that the acid had decomposed the perovskite phase at the surface into the constituent oxides [20]. The effect on the surface exchange rate is shown in Figure 6.3. A small but significant increase of the surface exchange coefficients by a factor of 3-5 can be observed with decreasing pH and increasing duration of the treatment. It should be noted that values of $\tilde{D}$ were not influenced by the treatment.

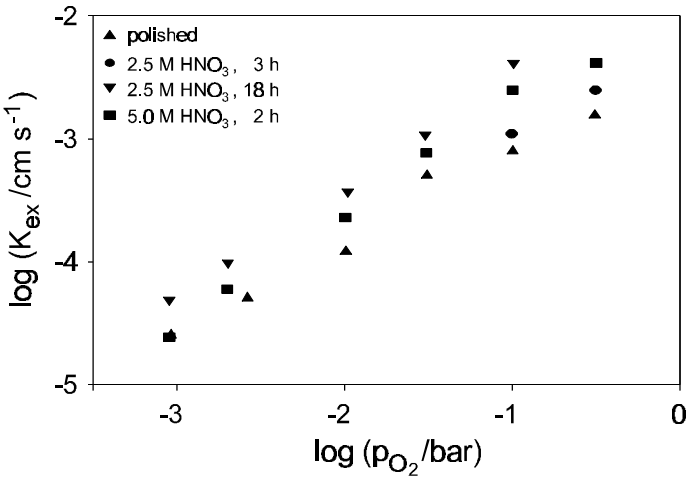


Figure 6.3. Influence of acid treatment on the magnitude of the apparent exchange coefficients $K_{ex}$ at 1225 K.

The oxygen pressure dependence of $K_{ex}$ for the different samples does not vary significantly. $K_{ex}$ is roughly proportional to the oxygen partial pressure. This may indicate that the predominant mechanism of exchange does not change upon treatment, although the rate of exchange may be increased by the presence of basic oxides at the surface. It is possible that the main effect of the acid treatment is an increase of the effective surface area on which exchange of oxygen may occur. SEM analysis indicated that the porosity of the surface increased with duration of the treatment. Etching by $HNO_3$ was seen to take place primarily via the grain boundaries. The sample treated for 18 h showed the surface region to have a large internal porosity of over 30 μm depth.

Arrhenius plots of $K_{ex}$ are shown in Figure 6.4. Data were obtained on the sample treated for 18 h in a 2.5 M $HNO_3$ solution. The activation energy is about 60-70 kJ/mol and this value is independent of oxygen partial pressure, which is

taken as a further indication that the predominant mechanism of oxygen exchange does not change with pressure.

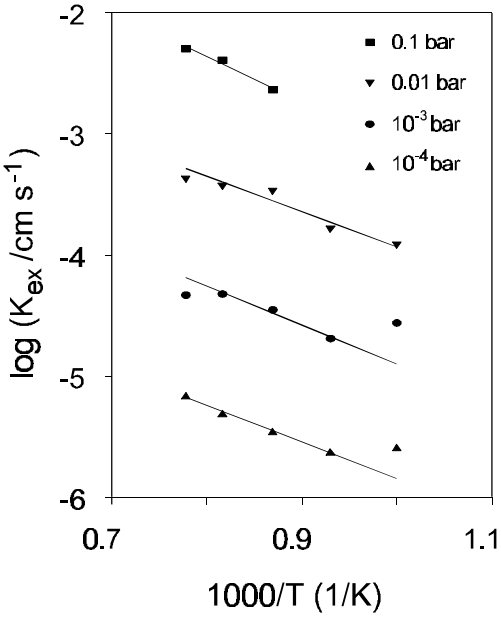


Figure 6.4. Arrhenius representations of apparent surface exchange coefficients $K_{ex}$ at different oxygen partial pressures of a sample treated for 18 h in a 2.5 M nitric acid solution.

The surface exchange coefficient $k_O$ determined from experiments performed in chemical equilibrium, e.g., isotopic exchange experiments, can be calculated from the present data via $k_O = K_{ex} / \gamma$ [12]. The calculated values are given in Figure 6.5. Under the conditions covered by the experiments, the value of the thermodynamic enhancement factor $\gamma$ varies slightly between 90-150. Therefore $k_O$ and $K_{ex}$ have the same activation energy within experimental error. The general trends are similar to those observed previously on $La_{1-x}Sr_xFeO_{3-\delta}$ [12].

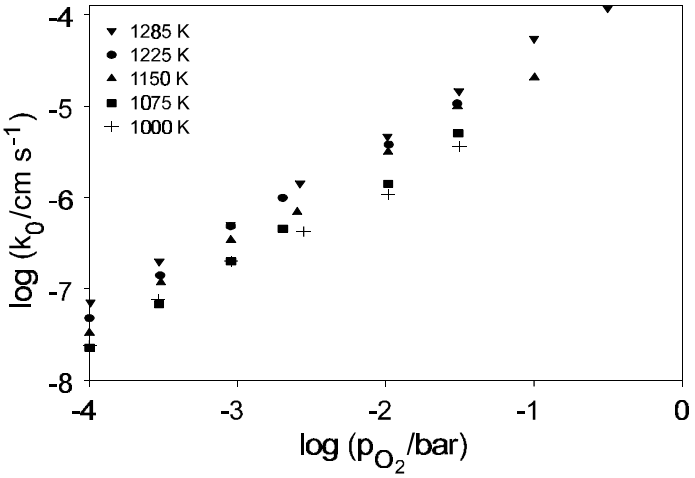


Figure 6.5. Surface exchange coefficients $k_O$ of a sample treated for 18 h in a 2.5 M nitric acid solution.

The obtained values are close to those of isotopic exchange data reported [1], i.e., $k_O = 2 \cdot 10^{-5}$ cm s$^{-1}$ for $La_{0.6}Ca_{0.4}Co_{0.8}Fe_{0.2}O_{3-\delta}$, and $k_O = 5 \cdot 10^{-6}$ cm s$^{-1}$ for $La_{0.8}Sr_{0.2}CoO_{3-\delta}$ at 1073 K at high oxygen pressure. The strong oxygen pressure dependence of $k_O$ may indicate that the rate-determining step in the exchange process involves molecular oxygen. In recent conductivity relaxation studies on $La_{1-x}Sr_xFeO_{3-\delta}$ [12] and $La_{1-x}Ca_xCrO_{3-\delta}$ [13] it was possible to correlate the surface exchange coefficients with the concentration of oxygen vacancies in the bulk of the material. In contrast, such a relationship could not be found for the compound under investigation here. It should be noted that the former compounds are p-type semiconductors, while $La_{0.6}Sr_{0.4}Co_{0.6}Fe_{0.4}O_{3-\delta}$ exhibits metallic-like features [19]. It is therefore possible that the rate-determining step is dependent on the electronic structure of the compound.

## 6.5. Conclusions

The magnitude of the chemical diffusion coefficients $\tilde{D}$ and its activation energy determined from both conductivity relaxation and potentiostatic step experiments on samples of 0.5-2.5 mm thickness are found to be in reasonable agreement. In the range 923-1255 K the chemical diffusion coefficient varies between $10^{-6}$-$5 \cdot 10^{-5}$ cm$^2$ s$^{-1}$, corresponding to an activation energy of 90-120 kJ/mol. The re-equilibration processes at oxygen pressures of 0.1-1 bar is governed by diffusion. At oxygen pressures below 0.01-0.03 bar the re-equilibration process is governed by slow kinetics of interfacial exchange. The surface exchange coefficient $K_{ex}$ is almost proportional to the oxygen partial pressure. The activation energy for $K_{ex}$ is about 60-70 kJ/mol and is found to be independent of oxygen pressure. Treatment of the oxide surface in a nitric acid solution for several hours does not alter the oxygen pressure dependence, but increases the surface exchange rate with a factor 3-5. The oxygen pressure dependence of the surface exchange coefficient $k_O$ suggests the involvement of molecular oxygen in the rate-determining step of the surface reaction.

## References

1. S. Carter, A. Selcuk, R.J. Chater, J. Kajda, J.A. Kilner and B.C.H. Steele, "Oxygen transport in selected nonstoichiometric perovskite-type oxides," *Solid State Ionics*, **53-56** (1992) 597-605.
2. I. Yasuda, K. Ogasawara and M. Hishinuma, "Oxygen tracer diffusion in (La,Ca)$CrO_{3-\delta}$," Proc. 2nd Intl. Symp. on *Ionic and mixed conducting oxides*, ed. T.A. Ramanarayanan, W.L. Worrell and H.L. Tuller, Proc. vol. 94-12, The Electrochemical Society, Pennington, NJ, 1994, p. 164-173.
3. Ch. Ftikos, S. Carter and B.C.H. Steele, "Mixed electronic/ionic conductivity of the solid solution $La_{(1-x)}Sr_xCo_{(1-y)}Ni_yO_{3-\delta}$ ($x$: 0.4, 0.5, 0.6 and $y$: 0.2, 0.4, 0.6)," *J. Eur. Ceram. Soc.*, **12** (1993) 79-86.
4. O.F. Kononchuk, D.P. Sutija, T. Norby and P. Kofstad, "Transient thermogravimetric measurement of chemical diffusion in $La_{0.7}Sr_{0.3}CoO_{3-\delta}$," Proc. 4th Intl. Symp. on *Solid oxide*

*fuel cells*, ed. M. Dokiya, O. Yamamoto, H. Tagawa and S.C. Singhal, Proc. vol. 95-1, The Electrochemical Society, Pennington, NJ, 1995, p. 395-403.

5. T.M. Gür, A. Belzner and R.A. Huggins, "A new class of oxygen selective chemically driven nonporous ceramic membranes. Part I. A-site doped perovskites," *J. Membr. Sci.*, **75** (1992) 151-162.
6. K. Nisancioglu and T.M. Gür, "Potentiostatic step technique to study ionic transport in mixed conductors," *Solid State Ionics*, **72** (1994) 199-203.
7. M.H.R. Lankhorst and H.J.M. Bouwmeester, "Determination of oxygen nonstoichiometry and diffusivity in mixed conducting oxides by oxygen coulometric titration, Part I: Chemical diffusion in $La_{0.8}Sr_{0.2}CoO_{3-\delta}$," *J. Electrochem. Soc.*, in press (1997).
8. I. Yasuda and M. Hishinuma, "Chemical diffusion in polycrystalline calcium-doped lanthanum chromites," *J. Solid State Chem.*, **115** (1995) 152-157.
9. I. Yasuda and M. Hishinuma, "Electrical conductivity and chemical diffusion coefficient of Sr-doped lanthanum chromites," *Solid State Ionics*, **80** (1995) 141-150.
10. Y. Denos, F. Morin and G. Trudel, "Oxygen diffusivity in strontium-substituted lanthanum cobaltite," Proc. 2nd Intl. Symp. on *Ionic and mixed conducting oxides*, ed. T.A. Ramanarayanan, W.L. Worrell and H.L. Tuller, Proc. vol. 94-12, The Electrochemical Society, Pennington, NJ, 1994, p. 150-158.
11. F. Morin, "Application of electrical conductivity for determining the chemical diffusivity in transition-metal compounds," *React. Solids*, **7** (1989) 307-323.
12. Chapter 4 of this thesis.
13. I. Yasuda and T. Hikita, "Precise determination of the chemical diffusion coefficient of calcium-doped lanthanum chromites by means of electrical conductivity relaxation," *J. Electrochem. Soc.*, **141** (1994) 1268-1274.
14. M.H.R. Lankhorst, "Coulometric titration experiments," Chapter 4 in: *Thermodynamic and transport properties of mixed ionic-electronic conducting perovskite-type oxides*, Thesis, University of Twente, Enschede, the Netherlands, 1997.
15. Chapter 7 of this thesis.
16. Appendix B of this thesis.
17. N. Miura, Y. Okamoto, J. Tamaki, K. Morinaga and N. Yamazoe, "Oxygen semipermeability of mixed-conductive thick-film prepared by slip casting," *Solid State Ionics*, **79** (1995) 195-200.
18. B.A. Boukamp, *Equivalent Circuit*, 2nd ed., University of Twente, Enschede, the Netherlands, (1989).
19. Chapter 5 of this thesis.
20. Chapter 3 of this thesis.

# 7

# Oxidative coupling of methane on dense $La_{0.6}Sr_{0.4}Co_{0.8}Fe_{0.2}O_{3-\delta}$ membranes


## Abstract

The ionic-electronic mixed-conducting perovskite-type oxide $La_{0.6}Sr_{0.4}Co_{0.8}Fe_{0.2}O_{3-\delta}$ was applied as a dense membrane for oxygen supply in a reactor for methane coupling. The oxygen permeation properties were studied in the $p_{O_2}$-range of $10^{-3}$-1 bar at 1073-1273 K, using He as a sweeping gas at the permeate side of the membrane. The oxygen semipermeability has a value close to 0.8 mmol $m^{-2}$ $s^{-1}$ at 1173 K with a corresponding activation energy of 130-140 kJ/mol. The oxygen flux is limited by a surface process at the permeate side of the membrane. It was found that the oxygen flux is only slightly increased if methane is admixed with helium. Methane is converted to ethane/ethene with selectivities up to 70%, albeit that conversions are low, typically 1-3% at 1073-1173 K. When oxygen was admixed with methane rather than supplied through the membrane, selectivities obtained were found to be in the range 30-35%. Segregation of strontium was found at both sides of the membrane, being seriously affected by the presence of an oxygen pressure gradient across it. The importance of a surface limited oxygen flux for application of perovskite membranes for methane coupling is emphasized.

## 7.1. Introduction

Many mixed oxides of the perovskite-type ($AMO_3$) show catalytic activity in oxidation reactions. The catalytic properties are closely related to the nature of the M-cation, as was shown for propane oxidation [1]. The A-site cation is in general catalytically inactive, but the partial substitution of the A-site cation by aliovalent ions has been used by several authors to control both the valency of the M-element and the oxygen vacancy concentration in the bulk [2,3]. By this substitution the M-O bond strength and the mobility of the oxygen anions are affected. Since the oxygen ion conductivity is generally increased by the partial substitution of A-site cations by lower valent cations [4], oxygen ions in subsurface layers may be able to take part in the catalytic process.

The intrafacial mechanism suggested by Voorhoeve for oxidation reactions on perovskites [5] may be promoted by this, as it is generally believed that there is a connection between this mechanism and the ease of oxygen ion migration [6]. In addition to their high ionic conductivity some A-site substituted perovskite-type oxides with transition metal ions at the M-site show electronic conductivity [7]. As an example, the partial substitution of trivalent lanthanum in $LaMO_3$ (M is a transition metal cation) by divalent strontium, resulting in the solid solution $La_{1-x}Sr_xMO_{3-\delta}$, is given by

$$SrMO_3 \xrightarrow[LaMO_3]{} Sr'_{La} + M^{\cdot}_{M} + 3O^{x}_{O} \quad , \tag{7.1}$$

where the notation for defects is from Kröger and Vink [8]. Due to the above substitution the concentration of oxygen vacancies is increased according to the defect reaction

$$2M^{\cdot}_{M} + O^{x}_{O} \rightleftharpoons 2M^{x}_{M} + V^{\cdot\cdot}_{O} + \tfrac{1}{2}O_2 \quad . \tag{7.2}$$

Furthermore, M-site transition metal cations can show charge disproportionation:

$$2M^{x}_{M} \rightleftharpoons M^{\cdot}_{M} + M'_{M} \quad . \tag{7.3}$$

Ionic conduction can take place by hopping of oxygen ions to neighbouring vacant sites, whereas electronic conduction is thought to occur via $M^{n+}$-O-$M^{(n+1)+}$ conduction pairs [9].

Several perovskite-type oxides were already investigated as catalysts for the methane coupling reaction [10-15]. Some $LaCoO_3$-based perovskites, partially substituted with barium and iron on the A- and M-sites, respectively, were found to be active in the oxidative coupling reaction when the reaction was performed by the TPR method and cyclic operation [10]. A study of perovskites of the formula $Ca_{1-x}Sr_xTi_{1-y}M_yO_{3-\delta}$ (M=Fe or Co; $x$=0-1; $y$=0-0.6) indicated that these catalysts showing both ionic and p-type electronic conductivity give a high selectivity to the

desired products [11]. A combined Mössbauer and catalytic study of $ACo_{0.8}Fe_{0.2}O_{3-\delta}$ (A=Ba, Sr, Ca) showed that the barium and strontium perovskites, which gave a high selectivity towards $C_2$ products ($C_2$ indicates the sum of ethane and ethene), have a disordered oxygen vacancy structure [12]. In contrast, the calcium-containing sample adopted the brownmillerite structure, which is known to have an ordered arrangement of oxygen vacancies. The performance of this composition was considerably worse. Ca-doped $Ba_{0.95}Ca_{0.05}Co_yFe_{1-y}O_{3-\delta}$ ($y \geq 0.8$) showed even better catalytic properties than the above-mentioned $BaCo_yFe_{1-y}O_{3-\delta}$ [13]. It was considered by the authors that the oxygen deficiency of $BaCo_yFe_{1-y}O_{3-\delta}$ was small and that it tended to contain mixed oxides of different structures. By adding a small amount of Ca the perovskite structure was stabilized and its nonstoichiometry increased, which was thought to contribute to the improved $C_2$ selectivity.

The simultaneous occurrence of ionic and electronic conductivity makes these materials suitable for application as oxygen semipermeable membranes in membrane reactors. Teraoka et al. were the first to measure steady state oxygen permeation through $La_{1-x}A_xCo_{1-y}M_yO_{3-\delta}$ membranes (A=Sr, Ca; M=Fe, Co, Cu, Ni) directly [16,17]. Higher oxygen fluxes were observed with increasing level of A-site substitution and reducibility of the perovskites [18]. Since these initial studies, compounds with compositions $La_{1-x}Sr_xCo_{1-y}Fe_yO_{3-\delta}$ have been claimed in patents for use as oxygen separation membrane, e.g., for the production of oxygen [19].

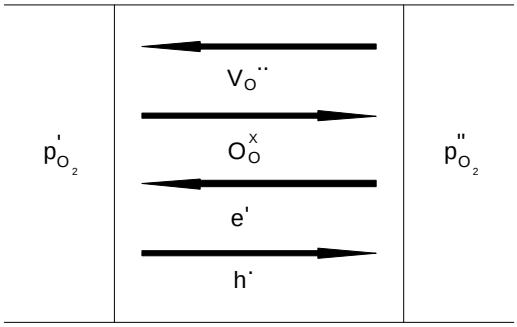


Figure 7.1. Fluxes in mixed conducting membrane under the influence of a partial pressure gradient. $p'_{O_2}$ and $p''_{O_2}$ denote higher and lower oxygen partial pressure, respectively.

The principle of a membrane, semipermeable to oxygen, is shown in Figure 7.1. By applying an oxygen partial pressure gradient across the membrane, oxygen is driven from the high to the low partial pressure side. Local charge neutrality is maintained by the joint diffusion of oxygen vacancies and electrons or electron holes. The net flux is determined by the species with the smallest conductivity. Wagner's theory of oxide film growth [20,21] on metals is generally used to describe the oxygen flux across a membrane.

$$j_{O_2} = \frac{RT}{4^2 F^2 L} \int_{p'_{O_2}}^{p''_{O_2}} t_i t_{el} \sigma_{total} \, d \ln p_{O_2} \quad . \tag{7.4}$$

Here $j_{O_2}$ is the oxygen permeation flux in mol cm$^{-2}$ s$^{-1}$, $t_i$ and $t_{el}$ are the ionic and electronic transference numbers, $\sigma_{total}$ ($=\sigma_{ion}+\sigma_{el}$) is the total conductivity ($\Omega^{-1}$ cm$^{-1}$), $p'_{O_2}$ and $p''_{O_2}$ are the oxygen partial pressures at the high and the low partial pressure side of the membrane, respectively; $L$ is the membrane thickness (cm). $R$, $F$ and $T$ refer to the gas constant (J mol$^{-1}$ K$^{-1}$), Faraday's constant (C mol$^{-1}$) and the temperature (K), respectively.

The oxygen permeability of $La_{0.6}Sr_{0.4}CoO_{3-\delta}$ was found to be roughly proportional to its ionic conductivity [22], which is in agreement with the fact that its electronic conductivity is several orders of magnitude larger. For several other $La_{1-x}Sr_xCo_{1-y}Fe_yO_{3-\delta}$ perovskites the electronic conductivity was also found to control the total conductivity [4,23]. This implies that $t_{el} \approx 1$ so that the product $t_i t_{el} \sigma_{total}$ reduces to $\sigma_{ion}$ and the oxygen flux becomes proportional to the ionic conductivity. On the assumption that all oxygen vacancies are fully ionized, an expression for ionic conduction can be given on the basis of the Nernst-Einstein relation:

$$\sigma_{ion} = \frac{4F^2 [V_O^{\cdot\cdot}] D_V}{RTV_m} \quad . \tag{7.5}$$

$[V_O^{\cdot\cdot}]$ is the oxygen vacancy concentration per unit cell volume, $D_V$ the oxygen vacancy diffusion coefficient (cm$^2$ s$^{-1}$) and $V_m$ the molar volume of the perovskite (cm$^3$ mol$^{-1}$).

Equation (7.4) is valid only if the oxygen flux through the membrane is controlled by bulk diffusion through the oxide lattice. Reduction of the membrane thickness $L$ will in that case lead to higher oxygen fluxes. Teraoka mentioned the influence of sintering temperature on oxygen semipermeability [16], which may indicate that grain boundary diffusion plays a significant role.

In addition, the oxygen flux may be influenced or limited by surface exchange kinetics [24]. A characteristic thickness $L_c$ has been identified, i.e., the membrane thickness at which the oxygen flux is equally determined by surface exchange kinetics and bulk transport. The value of $L_c$ can be calculated provided that the surface oxygen exchange rate and the oxygen diffusivity are known, e.g., from $^{18}O/^{16}O$ isotopic exchange techniques. In a previous paper [25] we reported on the use of $La_{1-x}Sr_xFeO_{3-\delta}$ membranes in the high temperature oxidation of carbon monoxide. It was shown that the oxygen permeation rate is limited by the reduction process at the surface in the lower partial pressure compartment.

From the above it is clear that mixed-conducting perovskite membranes may be used as oxygen supplying membrane and methane coupling catalyst at the same

time. Otsuka was the first to use separate feeds of air and methane in a study in which oxygen was electrochemically pumped into the methane stream by using an yttria-stabilized zirconia (YSZ) electrolyte cell [26]. This approach has been attempted by several others later and was reviewed recently [27]. It was shown that electrochemically pumped oxygen coupled more selectively than gaseous oxygen. Since the measured activation energies for $C_2$ and $CO_2$ formation differed when oxygen was supplied by electrochemical pumping rather than by premixing of molecular oxygen in the feed stream [28], it has been suggested that the active species is different in these two cases. Besides that lattice oxygen may couple methane more selectively than gaseous oxygen, air may be used as the oxidant instead of more expensive oxygen.

The observations that were made in the CO oxidation study on $La_{1-x}Sr_xFeO_{3-\delta}$ membranes [25] are of importance from a technological point of view, since they suggest that under actual operating conditions the depth of reduction of the oxide membrane surface can be kept limited. It implies that constraints regarding the structural integrity and chemical stability in reducing environments of potential membrane candidates can be relaxed. Therefore, $La_{0.6}Sr_{0.4}Co_{0.8}Fe_{0.2}O_{3-\delta}$ membranes are used as an oxygen separation membrane and methane coupling catalyst in the present study. Cobalt was partially substituted by iron to increase the chemical stability of the perovskite in reducing atmospheres. The results are compared with those observed when the membrane is placed in a single-chamber reactor and oxygen is admixed with the methane feed stream.

## 7.2. Experimental

### *7.2.1. Membrane preparation*

Nitrates of the constituent metals (Merck, p.a. quality) were dissolved separately in $Q_2$ water and their concentrations were determined by titration with EDTA. Stoichiometric amounts of the solutions were taken and mixed. A solution of ammonia/EDTA was added to the mixed metal solution, the final concentration of EDTA being 1.5 times the total metal cation concentration. The pH of the solution was adjusted to 8-9 by using ammonia. The solution was mixed for several hours under moderate heating to complete complexation and then pyrolysed in a stove at 500 K. The resulting powder was milled for several hours in a planetary mill in acetone and after drying calcined at 1200 K in stagnant air for 12 hours. Calcination at lower temperatures also resulted in perovskite formation but in these cases XRD revealed traces of $SrCO_3$. After repeating the milling procedure disks of 25 mm diameter were obtained by uniaxial pressing at 1.5 bar, followed by isostatic pressing at 4000 bar. The disks were sintered in Pt-lined boats at 1450-1500 K for 24 h in a pure oxygen atmosphere. Membranes of 15.2 mm diameter and 0.5-2 mm thickness were cut from the sintered disks. Prior to use the membranes were polished with

1000 MESH SiC and ultrasonically cleaned in ethanol. An Archimedes method was used to determine the density of the membranes.

### 7.2.2. Experimental setup

Oxygen permeation measurements were performed in a quartz reactor [25] with a reactor volume of approximately 3 ml. Catalytic experiments were performed in a quartz reactor depicted in Figure 7.2. Supremax glass rings (Schott Nederland B.V.) were used to seal the membrane into the quartz reactor at 1310-1330 K in stagnant air, thus creating two isolated chambers.

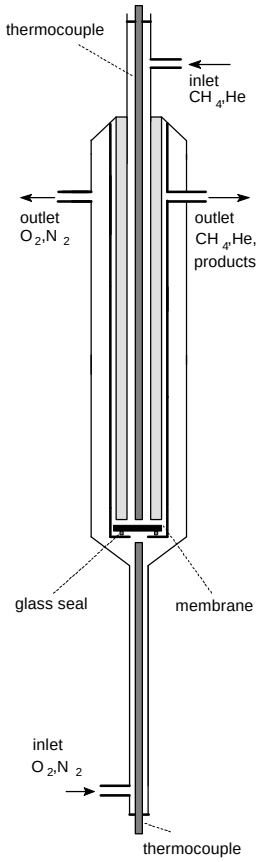


Figure 7.2. Schematic diagram of the catalytic reactor.

The experimental setup is shown in Figure 7.3. In the higher oxygen partial pressure compartment the oxygen partial pressure was monitored with an YSZ-based oxygen sensor. The oxygen partial pressure in this compartment could be adjusted in the range $10^{-2}$-1 bar by admixing $N_2$, air and $O_2$. The total flow rate in this compartment was kept high (100-180 ml/min (STP)) to prevent mass transfer limitations in the gas phase. Brooks 5800 mass flow controllers were used to control the gas flow rates through both compartments. A Varian 3300 gas chromatograph and a LDC/Milton Roy CL-10 integrator were used for analysis of the compositions at both the inlet and outlet of the lower oxygen partial pressure compartment of the reactor. A molecular sieve 13X was used for separation of $H_2$, $O_2$, $N_2$, $CH_4$ and CO. A Porapak-N column was used for separation of $CO_2$, hydrocarbons and $H_2O$. The total gas flows at the inlet and outlet of the reactor were measured separately with a Brooks Volumeter.

### 7.2.3. Permeation and catalytic measurements

In the oxygen permeation measurements the oxygen partial pressure at the lean side of the membrane was varied by adjusting the He (4.6N) flow rate in the range 5-70 ml/min (STP). The gas tightness of membrane and seal was checked by GC detection of nitrogen in the effluent stream, since in case of a leak free membrane no $N_2$ is present there. The contribution of leakage to the total oxygen flux could be calculated from the measured nitrogen concentration and was found to be less than 3% in all cases, and typically well below 1%. Calculated oxygen permeation fluxes were corrected for this contribution.

In the catalytic measurements the feed consisted of He and $CH_4$. The permeation was calculated from the outlet flow rate and the concentrations of all oxygen containing species ($O_2$, CO, $CO_2$ and $H_2O$). Selectivities were calculated from the total amounts of products formed. The carbon balance was in all cases in the range 99±2%. Oxygen fluxes and reaction rates were normalized with respect to the

geometric surface area exposed to the methane(helium) atmosphere. To compare the results with the effect of cofed oxygen, measurements were also performed in a single-chamber reactor with similar geometry and dimensions. An amount of oxygen was admixed with methane that was equal to the amount of permeated oxygen measured under similar conditions. These experiments will be referred to as 'cofeed mode', as distinct from the 'membrane mode' described above.

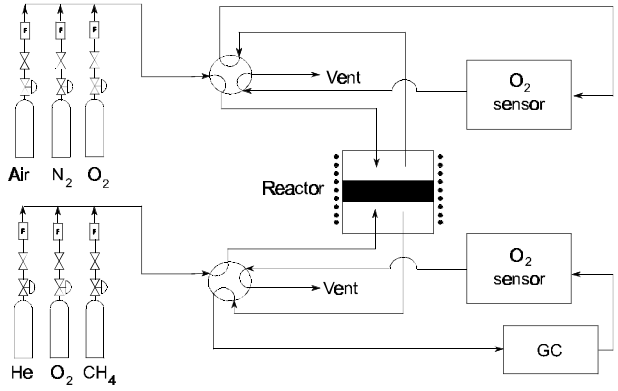


Figure 7.3. Schematic diagram of the experimental setup.

### *7.2.4. XRD, SEM, EDX and AES*

Sample characterization was performed by taking XRD spectra (Philips PW1710) from crushed sintered membranes using graphite-filtered $CuK\alpha_1$ (1.5406 Å) radiation. $LaB_6$ was added as an internal standard and the samples were measured with a 2θ scan from 20º to 140º with steps of 0.018º. The intensity was measured during 5-10 seconds. The membrane surface morphology was examined by HR-SEM (Hitachi S-800 field emission microscope). Phases present at the surface were determined by XRD. Surface element analysis was performed by EDX (Kevex Delta Range) and by AES (Perkin Elmer PHI 600). An Auger depth profile was obtained by sputtering with a 1 $mm^2$ 3.5 keV $Ar^+$ beam on 30º tilted samples with a sputter rate of 32.5 Å $min^{-1}$ (±10%). The incident angle between the beam and the sample was 45° and the surface area analyzed was 150x120 $\mu m^2$.

## 7.3. Results and discussion

### *7.3.1. XRD*

The XRD spectra of powders obtained from crushed freshly prepared membranes showed a single-phase perovskite. All peaks could be indexed on the basis of a rhombohedrally distorted cubic cell with lattice parameters $a$=5.4450(9) Å and $c$=13.2553(3) Å (hexagonal setting) [29]. These data are in close agreement with crystallographic data of $La_{0.6}Sr_{0.4}CoO_3$ [30]. On the basis of the unit cell volume, the densities of membranes used in this study were calculated to be in the range of 96.5-98.0% of theoretical.

### 7.3.2. Oxygen permeation measurements

The Arrhenius curves of the oxygen flux in an air/helium gradient are shown in Figure 7.4 for two samples of different thickness. After sealing the samples were cooled to temperatures between 1223-1273 K and kept at this temperature until the permeation had become stable (10-15 h). At the helium side an oxygen partial pressure of 0.017 bar was maintained. As can be seen from the figure the two curves coincide well in absolute magnitude.

In contrast, the stabilization times of membranes which were immediately cooled from the temperature at which sealing was performed to 1100-1200 K were considerably longer and their final permeability was a factor of 3-4 lower than is expected on the basis of the results shown in Figure 7.4. Upon increasing the temperature to 1200-1300 K the fluxes through these membranes increased irreversibly and their performances became similar to those of the high-temperature stabilized samples.

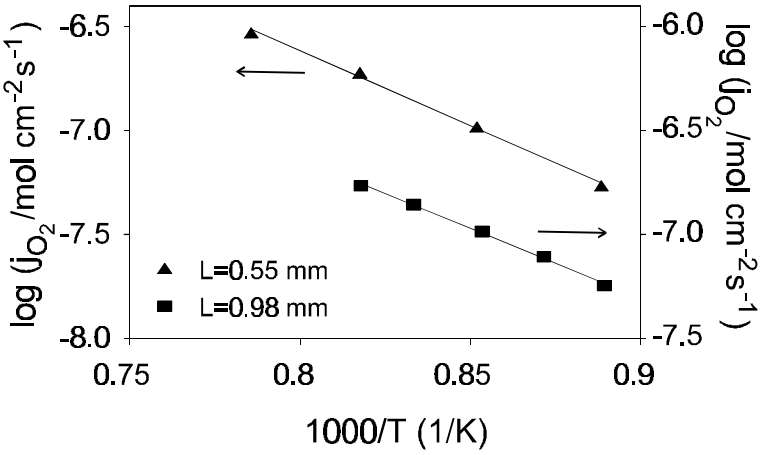


Figure 7.4. Temperature dependence of oxygen permeation flux in air/He (0.017 bar $O_2$) gradient for samples of different thicknesses.

The activation energies obtained from the Arrhenius plots in Figure 7.4 are given in Table 7.1. Itoh et al. calculated an activation energy of 117 kJ/mol for the ionic conductivity from oxygen permeation data of $La_{0.6}Sr_{0.4}CoO_{3-\delta}$ [31]. The authors used a simple logarithmic dependence for the oxygen flux, which can be derived from Eq. (7.4) assuming a constant ionic conductivity. It is plausible that the activation energy for $La_{0.6}Sr_{0.4}Co_{0.8}Fe_{0.2}O_{3-\delta}$ is slightly higher due to the presence of iron.

Table 7.1. Activation energies of oxygen permeability of $La_{0.6}Sr_{0.4}Co_{0.8}Fe_{0.2}O_{3-\delta}$ in an air/He gradient.

| $L$ (mm) | $T$ (K) | $E_{act}$ (kJ/mol) |
|---|---|---|
| 0.55 | 1123-1273 | 138±10 |
| 0.98 | 1123-1223 | 128±8 |

Figure 7.5 shows the oxygen permeation flux in an air/helium gradient as a function of the oxygen partial pressure in the lower partial pressure compartment. All measurements were performed on two different samples of 1.0 mm thickness at different temperatures. Stabilization was performed at the temperature of measurement. The difference in permeation rates correspond well with the observed activation energy. A strong indication for a surface-controlled flux emerges from the dependence of the oxygen flux on the partial pressure.

For all membranes measured, the oxygen flux can be related to the oxygen partial pressure in the helium-containing chamber via

$$j_{O_2} \propto -p_{O_2}^{n} \ , \tag{7.6}$$

where $n$=0.22±0.01. When a mass action type relation is applied to Eq. (7.2), taking into account that the oxygen concentration is defined by $[O_O^x]=3-[V_O^{\cdot\cdot}]$, the following relation holds for the oxygen vacancy concentration:

$$[V_O^{\cdot\cdot}] = \frac{3[M_M^{\cdot}]^2}{[M_M^{\cdot}]^2 + K_2[M_M^x]^2 p_{O_2}^{1/2}} \ , \tag{7.7}$$

with $K_2$ the equilibrium constant. The power dependence of the oxygen vacancy concentration on oxygen partial pressure thus varies between -½ and 0, depending on oxygen partial pressure and temperature. From Eqs. (7.4), (7.5) and (7.7) the same power dependence is expected for the oxygen flux.

A positive value of $n$ as is experimentally found here may indicate that a process other than bulk diffusion limits the oxygen flux. Combined with the data presented in Figure 7.4, as discussed above, we take this as evidence of a surface-exchange controlled flux.

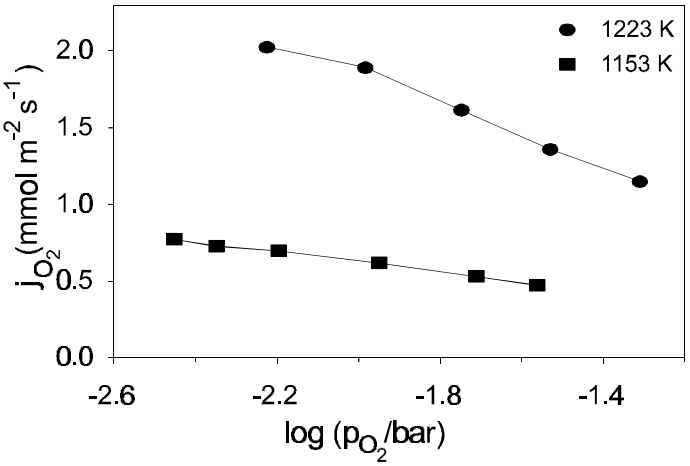


Figure 7.5. Dependence of oxygen flux on partial pressure in lower partial pressure compartment at different temperatures.

Measurements at 1153 K were performed in which the partial pressure in the higher partial pressure compartment was varied (0.01-0.21 bar), while the oxygen concentration at the permeate (He) side was kept at a constant value of 0.52%. In these cases the value of *n* is close to zero. The experimental oxygen fluxes can be represented by

$$j_{O_2} = 1.054 + 0.506 \log p'_{O_2} \quad . \tag{7.8}$$

It has been shown [32] that the applied gradient has a great influence on the $p_{O_2}$ dependence. This is also clear when considering Eq. (7.7). The oxygen vacancy concentration is different on both sides of the membrane. Thus, the differences in dependences as found here do not necessarily indicate a difference in the nature of the rate-determining step of the permeation process.

### *7.3.3. Catalytic measurements*

The temperature dependence of the catalytic activity and $C_2$ selectivity was determined by feeding 0.25 bar methane at a total flow of 16.4 ml/min (STP) (2.79 μmol $s^{-1}$ $CH_4$). Air was supplied at the high oxygen partial pressure side of the membrane. The results are shown in Figure 7.6.

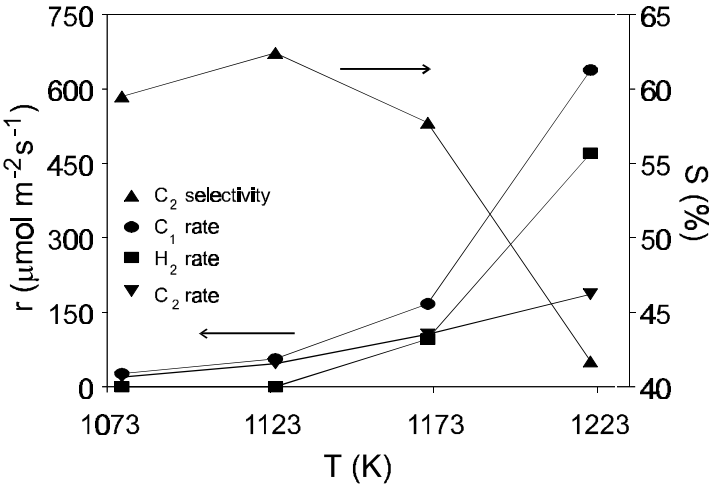


Figure 7.6. Reaction rates and selectivity to ethane/ethene versus temperature. $p_{CH_4}$ =0.25 bar. Total flow rate is 16.4 ml/min (STP).

After an initial increase of the selectivity between 1073-1123 K to 62%, a slight decrease is observed between 1123-1173 K, followed by a steep decrease above 1173 K to finally reach 41% at 1223 K. The selectivity drop can be attributed to a strong increase of the production rate of $CO_2$. Since this rate increase is accompanied by a strong increase of the $H_2$ production rate it is likely that above 1173 K carbon deposition occurs by thermal decomposition of methane, followed by oxidation with unreacted permeated oxygen.

The activation energy for oxygen permeation was determined to be 169±6 kJ/mol. Although this value is about 35 kJ/mol higher than determined from the permeation measurements, the difference is likely due to the fact that stabilization was performed at 1073 K only.

The activation energy for methane conversion was 217±12 kJ/mol, while that of $C_2$ formation was calculated to be 175±10 kJ/mol. In the aforementioned temperature range the $C_2$ yield varied between 0.25% and 3.1%. From these results 1153 K was selected as standard temperature for further experiments, since both reasonable selectivities and oxygen fluxes are found here.

The methane partial pressure dependence at a total flow rate of 20.5 ml/min (STP) is shown in Figure 7.7. Air was again supplied in the high partial pressure chamber. The oxygen flux was found to be 0.84±0.05 mmol $m^{-2}$ $s^{-1}$ and was not influenced by changing the methane partial pressure. Production of $H_2$ is seen at methane pressures above 0.5 bar, probably due to thermal decomposition of methane. The rate of carbon monoxide formation was virtually independent of the methane partial pressure, while the rates of formation of ethane, ethene and carbon dioxide increased steadily. The methane conversion ranges between 2.6 and 1.1%, to be compared with 0.45-0.35% from blank experiments.

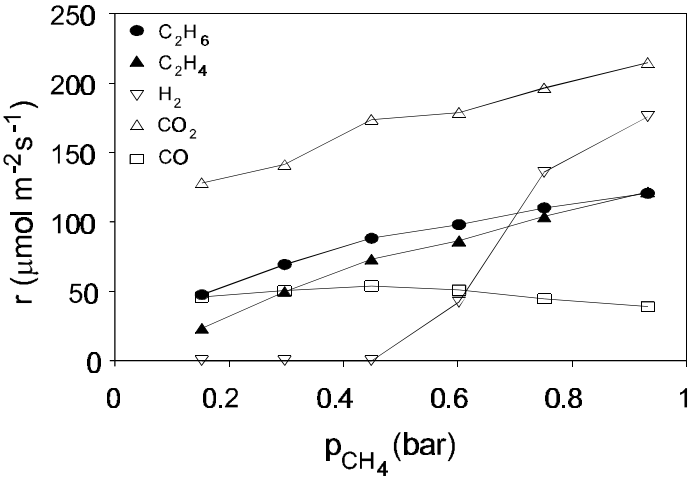


Figure 7.7. Reaction rates at 1153 K versus methane partial pressure at a total flow rate of 20.5 ml/min (STP).

Methane conversion, selectivities and relative oxygen consumption are given in Table 7.2. The oxygen consumption $X_{O_2}$ (defined as the total amount of oxygen consumed by reaction divided by the total amount of oxygen permeated) increases from 44% to 75% upon increasing the methane partial pressure from 0.15 bar to 0.93 bar. Thus, gaseous oxygen is observed in the methane containing compartment, and $p_{O_2}$ varies there between $10^{-2.21}$ and $10^{-2.55}$ bar. Comparing the observed oxygen flux with the results shown in Figure 7.5 shows that the oxygen flux is not or only slightly increased by the presence of methane.

Figure 7.8 shows the ratios of the production rates of $C_2$ products and $CO_2$ as a function of $p_{CH_4}$ when operating in the membrane mode and cofeed mode. No production of carbon monoxide was observed in the cofeed mode. It is seen that the selectivity to ethane/ethene is much higher in the membrane mode. Not only is the production rate of carbon dioxide 40-50% of that in the cofeed mode, the rates of ethane and ethene formation are considerably higher. At $p_{CH_4}$ =0.93 bar the rates of ethane and ethene formation equal 1.4 and 3.2 times those in the cofeed mode, respectively. The production rates obtained using membrane and cofeed mode, as well as those from blank experiments (without catalyst), are given in Table 7.3.

Table 7.2. Methane conversion, selectivities and relative oxygen consumption versus $p_{CH_4}$ . $T$=1153 K. Flow rate is 20.5 ml/min (STP).

| $p_{CH_4}$ (bar) | $X_{CH_4}$ (%) | $S_{CO}$ (%) | $S_{CO_2}$ (%) | $S_{C_2H_6}$ (%) | $S_{C_2H_4}$ (%) | $X_{O_2}$ (%) |
|---|---|---|---|---|---|---|
| 0.15 | 2.6 | 14.5 | 40.5 | 30.1 | 14.8 | 43.8 |
| 0.30 | 1.9 | 11.6 | 32.3 | 31.6 | 22.8 | 49.9 |
| 0.60 | 1.3 | 8.3 | 29.1 | 31.9 | 28.0 | 66.6 |
| 0.93 | 1.1 | 5.0 | 27.8 | 31.2 | 31.4 | 74.7 |

The presence of the catalyst leads to a large increase in the production rate of $CO_2$. At low methane partial pressures the production rates of ethane and ethene are substantially higher in the cofeed mode than in the blank experiments, but at 0.93 bar this difference is almost negligible. Although the rate of $CO_2$ production is also high in membrane mode, the rate of $C_2$ production becomes higher than in the other two cases at high $p_{CH_4}$ .

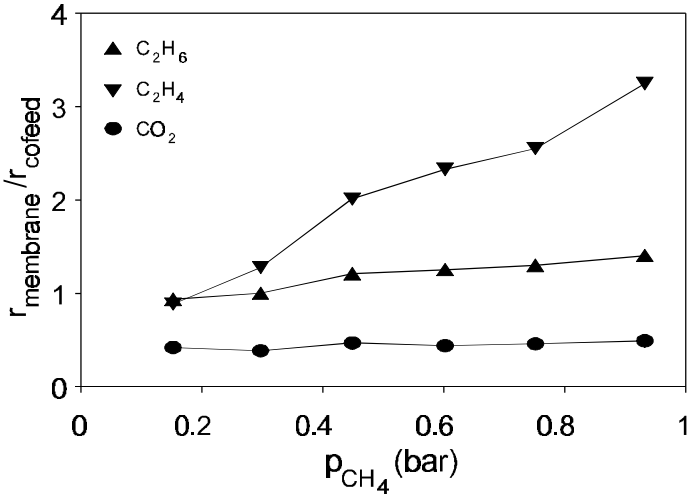


Figure 7.8. Ratios of reaction rates in membrane mode and cofeed mode at 1153 K versus methane partial pressure. Flow rate is 20.5 ml/min (STP).

To compare the $C_2$ selectivity as a function of the methane conversion in both modes of operation, methane was fed to the reactor with a partial pressure of 0.40 bar, while the conversion was varied by changing the total flow rate. The results are shown in Figure 7.9. The selectivity of the membrane process is considerably higher than that of the cofeed process.

Table 7.3. Production rates at different methane partial pressures in membrane mode (MM) and cofeed mode (CM). 'BL' refers to cofeed mode measurements with a polished quartz membrane. Flow rate is 20.5 ml/min (STP).

| $p_{CH_4}$ | $CO_2$ (μmol $m^{-2}$ $s^{-1}$) | | | $C_2H_6$ (μmol $m^{-2}$ $s^{-1}$) | | | $C_2H_4$ (μmol $m^{-2}$ $s^{-1}$) | | |
|---|---|---|---|---|---|---|---|---|---|
| (bar) | MM | CM | BL | MM | CM | BL | MM | CM | BL |
| 0.15 | 128 | 305 | 8 | 48 | 51 | 19 | 23 | 27 | 0 |
| 0.45 | 174 | 370 | 12 | 88 | 73 | 44 | 73 | 36 | 16 |
| 0.93 | 215 | 437 | 17 | 121 | 86 | 77 | 122 | 37 | 38 |

These results may indicate that the nature of the catalyst is different in the two cases. However, due to the high temperatures applied in these experiments, the role of the gas phase reactions can not be underestimated. Therefore, the results may also be attributed to a simple mass transport effect. Since the concentration profile of oxygen throughout the reactor is different in the two modes of operation, it could be suggested that the difference in selectivity results from a different $CH_4/O_2$ ratio in the vicinity of the surface. In the membrane mode the concentration of methane may be very low close to the surface, due to the continuous feeding of molecular oxygen from the surface, whereas it would remain high in the cofeed mode.

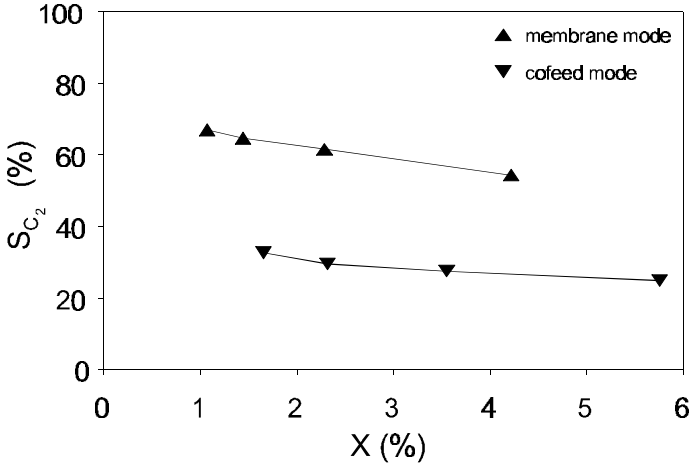


Figure 7.9. $C_2$ selectivities versus methane conversion at 1153 K for membrane mode and cofeed mode. $p_{CH_4}$ at inlet is 0.40 bar.

The dependence of the oxygen partial pressure in the oxygen supplying compartment on the oxygen flux and reaction rates in the lower partial pressure chamber, when operating in membrane mode, is shown in Figure 7.10. Roughly a linear relation

between $j_{O_2}$ and log $p_{O_2}$ is seen, in agreement with the results obtained from the permeation experiments. Increasing the oxygen partial pressure in the high partial pressure chamber mainly contributes to the conversion of methane to CO and $CO_2$. The rate of $C_2$ formation remains nearly constant.

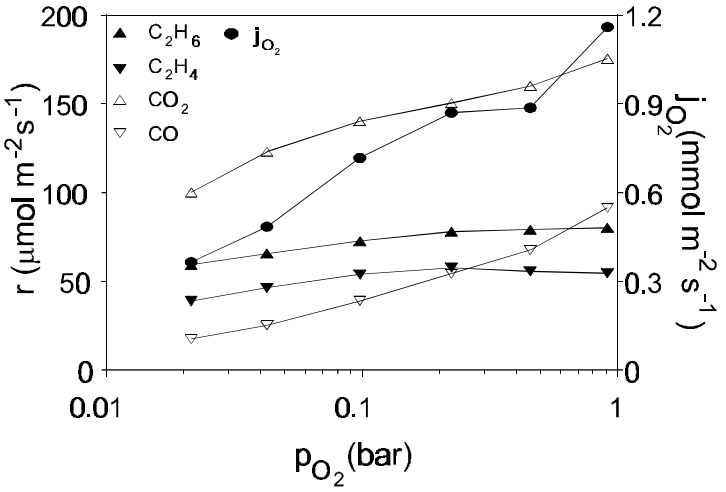


Figure 7.10. Reaction rates and oxygen flux as function of the oxygen partial pressure in the oxygen-supplying compartment. Flow rate is 20.5 ml/min (STP). $p_{CH_4}$ =0.40 bar.

The importance of a surface-exchange limited oxygen flux can be illustrated by an experiment in which a membrane was first equilibrated at 1153 K in a 1% $O_2$(He) atmosphere and subsequently reduced in 15% $CH_4$(He) (20 ml/min (STP); 2.0 μmol $s^{-1}$ $CH_4$). The experiment was performed in a single-chamber reactor as used in the cofeed mode experiments, but with no additional oxygen supplied after equilibration. The results are shown in Figure 7.11.

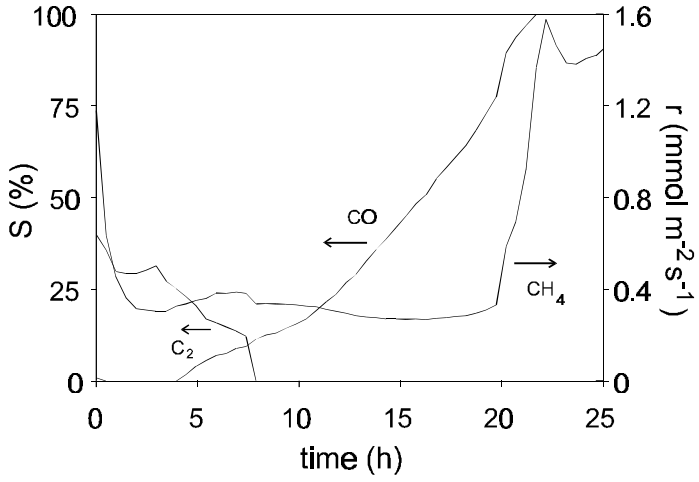


Figure 7.11. Selectivities to $C_2$ and CO and conversion rate of methane at 1153 K versus time in a reduction experiment. Flow rate is 20.5 ml/min (STP). $p_{CH_4}$ =0.15 bar.

Initially, a $C_2$ selectivity of over 30% and a high methane conversion rate are reached. In the course of the experiment the production of $C_2$ stops. CO production is seen after 4 h, accompanied by formation of hydrogen (not shown in the figure). After 20 h the selectivities to carbon monoxide and $H_2$ reach 100% and 93%, respectively. At the same moment the methane conversion rate increases steeply. These results indicate that reduction of the perovskite to either basic oxides or metallic Co and/or Fe leads to an active catalyst for syngas production. Thus, in case of a diffusion-controlled oxygen flux the surface would become reduced by methane, until the membrane thickness has decreased to such an extent that the increase of the oxygen flux, due to the decreased membrane thickness, counterbalances the consumption of oxygen by methane.

The catalytic permeation experiments that were described in this chapter were performed on samples that showed no deactivation, even after several weeks of continuous operation under varying conditions. Taking the results of the reduction experiment described above into account, this confirms that a surface exchange process limits the oxygen permeation process. Moreover, the reduction experiment shows that it may be possible to fine-tune the catalytic properties of the membrane by treatment of the membrane surface in a reducing atmosphere [33] or by adjustment of the amount of oxygen that is fed to the catalyst surface, either by cofeeding or by permeation.

### *7.3.4. Strontium segregation*

EDX analysis of samples after treatment in an air/He and/or air/He,$CH_4$ gradient showed an enrichment in strontium at both high and low partial pressure sides of the membrane. XRD analysis of the sample surfaces indicated the presence of $SrCO_3$ and $SrSO_4$. The origin of sulfur is not immediately clear, but it may be noted that the catalytic activity of $SrSO_4$ is known to be small [34].

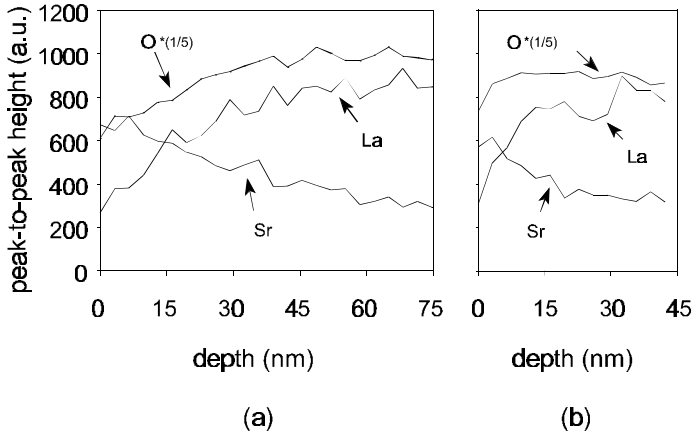


Figure 7.12. Auger depth profiles of samples after 48 h treatment at 1153 K. $p_{CH_4}$ =0.25 bar. (a) Membrane mode, $p'_{O_2}$ =0.21 bar. (b) Cofeed mode, $p_{O_2}$ =0.01 bar at inlet.

To investigate the segregation in more detail, two samples were treated for 48 h at 1153 K in 0.25 bar $CH_4$ at a total flow of 20.5 ml/min (STP) and rapidly cooled to room temperature. One sample was obtained after operation in the membrane mode, the other after operation in the cofeed mode under comparable conditions. Figure 7.12 shows depth profiles made by Auger analysis on the membrane sides that had been exposed to methane. The profiles of Fe and Co are not shown in this figure, but their behaviour is similar to that observed for La.

Surface enrichment of strontium occurs in both cases. The segregation depth is about 15-30 nm for the sample obtained from the cofeed mode, while it extends over 60-80 nm in that from the membrane mode. No segregation was observed on a fresh membrane. This shows that not only segregation occurs in both modes of operation, but also that segregation might be affected by the presence of an oxygen potential gradient across the material as occurs during operation in the membrane mode. The influence of the oxygen partial pressure gradient on segregation can possibly be described in terms of kinetic demixing [35], but the precise mechanism is unclear.

A SEM picture of a cross section of a sample exposed over 200 h to $CH_4$(He) at 1153 K after various catalytic experiments in the membrane mode is shown in Figure 7.13. As can be seen the perovskite structure is preserved. However, the presence of molecular oxygen is required. In experiments in which $O_2$ was absent, thermal decomposition of methane occurred easily. At the temperatures used here, strontium reacts with the deposited carbon to form $SrCO_3$. This reaction probably induces further segregation of strontium.

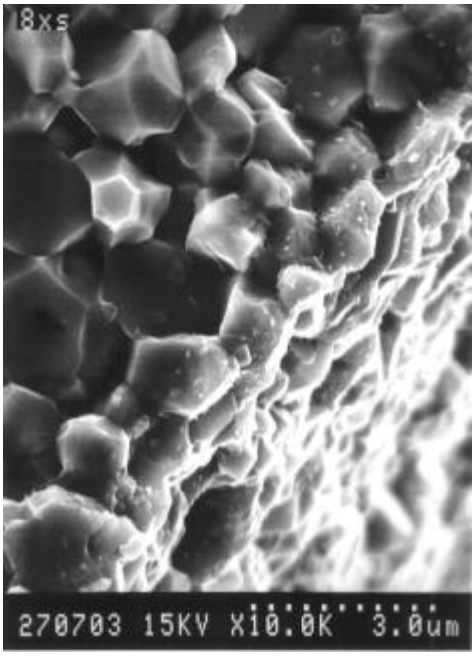


Figure 7.13. SEM photograph of cross section of membrane after treatment at 1153 K under varying conditions.

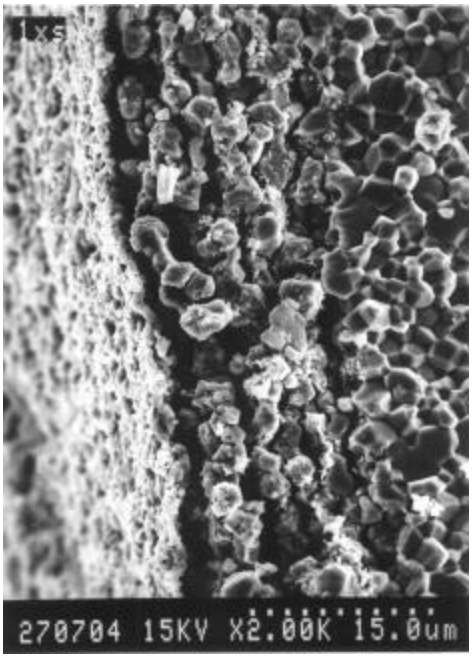


Figure 7.14. SEM photograph of cross section of membrane after treatment at 1100 K in an air/1 bar $CH_4$ gradient for 3 days.

A SEM picture of a sample treated for 3 days in pure $CH_4$ under permeation conditions at 1100 K is shown in Figure 7.14. At this temperature $SrCO_3$ is stable even in a $CO_2$-free atmosphere [36]. At the surface exposed to the ambient atmosphere, a thin, highly porous $SrCO_3$ layer is present. Below this layer a porous, decomposed layer of about 10 μm consisting mostly of La, Co and Fe, is found. At a depth of about 10 μm, the bulk structure appears. Furthermore, the observation that this sample showed a much higher flux than expected on the basis of the results shown in this chapter suggests that the permeation flux increases with increasing surface area at the methane side.

## 7.4. Conclusions

Dense $La_{0.6}Sr_{0.4}Co_{0.8}Fe_{0.2}O_{3-\delta}$ membranes, free of microcracks, were prepared by making powders by thermal decomposition of metal nitrate solutions and subsequent sintering of the pressed powders. The densities were 96.5-98.0% of theoretical. Permeation fluxes are typically 0.8 mmol $m^{-2}$ $s^{-1}$ at 1173 K with an activation energy in the range of 130-140 kJ/mol. Since the oxygen flux remained constant with decreasing membrane thickness and increased with increasing surface area at the He-side of the membrane, it is concluded that the oxygen flux is limited by the release of oxygen at the permeate side of the membrane.

When the membrane was applied as an oxygen supplier and methane coupling catalyst, no increase of the oxygen flux could be observed in comparison with the fluxes observed in air/He gradients. For methane coupling purposes it is important that the oxygen flux is limited by surface exchange kinetics, since a diffusion-controlled flux would lead to reduction of the membrane surface, lowering the overall selectivity towards $C_2$ products.

At temperatures above 1170 K substantial production of hydrogen was seen, probably due to thermal decomposition of methane. The $C_2$ selectivity decreased strongly above this temperature. At 1153 K $C_2$ selectivities increased with increasing methane partial pressure, up to 67% at $p_{CH_4}$ =0.93 bar. Increasing the oxygen partial pressure in the oxygen supplying chamber was shown to contribute mainly to the formation of CO and $CO_2$.

When molecular oxygen was cofed with methane rather than supplied via the membrane, the $C_2$ selectivities were considerably lower (25-35%), due to an increased rate of $CO_2$ formation and lower rates of ethane and ethene formation. This may indicate that the nature of the catalyst is different in the membrane mode and cofeed mode of operation, possibly due to the presence of different types of active oxygen species at the surface. Segregation of strontium was found by EDX and AES. The depth of segregation is a factor of 2-3 larger in the membrane mode.

Substantial improvements of the methane conversion and selectivity may be expected from surface modification, e.g., the application of thin porous layers of

well-known methane coupling catalysts such as Li/MgO or $Sr/La_2O_3$. The total supply of oxygen to the methane stream may be increased by enlargement of the surface area of the membrane. For industrial applications the use of ceramic tubes instead of planar membranes will be advantageous, since large active surface areas per unit volume can be achieved in such geometries. Hazbun [37] proposed several multi-tube configurations, both with cross flows and counter flows of the methane and air streams.

## References


1. T. Nitadori, T. Ichiki and M. Misono, "Catalytic properties of perovskite-type mixed oxides ($ABO_3$) consisting of rare earth and 3d transition metals. The roles of the A- and B-site ions," *Bull. Chem. Soc. Jpn.*, **61** (1988) 621-626.
2. T. Nakamura, M. Misono and Y. Yoneda, "Reduction-oxidation and catalytic properties of $La_{1-x}Sr_xCoO_3$," *J. Catal.*, **83** (1983) 151-159.
3. T. Nitadori and M. Misono, "Catalytic properties of $La_{1-x}A_xFeO_3$ and $La_{1-x}Ce_xCoO_3$," *J. Catal.*, **93** (1985) 459-466.
4. S. Sekido, H. Tachibana, Y. Yamamura and T. Kambara, "Electronic-ionic conductivity in perovskite-type oxides, $Sr_xLa_{1-x}Co_{1-y}Fe_yO_{3-\delta}$," *Solid State Ionics*, **37** (1990) 253-259.
5. R.J.H. Voorhoeve, J.P. Remeika and L.E. Trimble, "Defect chemistry and catalysis in oxidation and reduction over perovskite-type oxides," *Ann. N.Y. Acad. Sci.*, **3** (1976) 3-20.
6. N. Yamazoe and Y. Teraoka, "Oxidation of perovskites - relationships to bulk structure and composition (valency, defect, etc.)," *Catal. Today*, **8** (1990) 175-200.
7. W.L. Worrell, "Electrical properties of mixed-conducting oxides having high oxygen-ion conductivity," *Solid State Ionics*, **52** (1992) 147-151.
8. F.A. Kröger, *The chemistry of imperfect crystals*, North-Holland, Amsterdam, 1964.
9. R.J.H. Voorhoeve, "Perovskite-related oxides as oxidation-reduction catalysts," in: *Advanced materials in catalysis*, ed. J.J. Burton and R.L. Garten, Academic Press, New York, 1977, p. 129-180.
10. T. Hayakawa, H. Orita, M. Shimizu, K. Takehira, A.G. Andersen, K. Nomura and Y. Ujihira, "Oxidative coupling of methane over $LaCoO_{3-\delta}$-based mixed oxides," *Catal. Lett.*, **16** (1992) 359-371.
11. A.G. Andersen, T. Hayakawa, M. Shimizu, K. Suzuki and K. Takehira, "Oxidative coupling of methane over some titanate based perovskite oxides," *Catal. Lett.*, **23** (1994) 59-68.
12. K. Nomura, T. Goda, Y. Ujihira, T. Hayakawa and K. Takehira, "Mössbauer spectrometric study of nonstoichiometric perovskite, $ACo_{0.8}Fe_{0.2}O_{3-\delta}$ (A=Ba, Sr, Ca) for oxidative coupling of methane," *Hyperfine Interactions*, **69** (1991) 835-838.
13. K. Nomura, T. Hayakawa, K. Takehira and Y. Ujihira, "Oxidative coupling of methane on perovskite oxides $(Ba,Ca)(Co,Fe)O_{3-\delta}$," *Appl. Catal. A: General*, **101** (1993) 63-72.
14. K. Omata, O. Yamazaki, K. Tomita and K. Fujimoto, "Oxidative coupling of methane on an $ABO_3$ type mixed oxide with mixed conductivity," *J. Chem. Soc., Chem. Commun.*, (1994) 1647-1648.
15. D. Dissanayake, K.C.C. Kharas, J.H. Lunsford and M.P. Rosynek, "Catalytic partial oxidation of methane over Ba-Pb, Ba-Bi and Ba-Sn perovskites," *J. Catal.*, **139** (1993) 652-663.

16. Y. Teraoka, T. Nobunaga and N. Yamazoe, "Effect of cation substitution on the oxygen semipermeability of perovskite-type oxides," *Chem. Lett.*, (1988) 503-506.
17. Y. Teraoka, T. Nobunaga, N. Miura and N. Yamazoe, "Influence of constituent metal cations in substituted $LaCoO_3$ on mixed conductivity and oxygen permeability," *Solid State Ionics*, **48** (1991) 207-212.
18. T. Nakamura, G. Petzow and, L.J. Gauckler, "Stability of the perovskite phases $LaBO_3$ (B=V, Cr, Mn, Fe, Co, Ni) in reducing atmospheres," *Mat. Res. Bull.*, **14** (1979) 649-659.
19. R.M. Thorogood, R. Srinivasan, T.F. Yee and M.P. Drake, "Composite mixed conductor membranes for producing oxygen," *U.S. Patent 5,240,480* (1993).
20. C. Wagner, "Beitrag zur Theorie des Anlaufvorgangs," *Z. Phys. Chem.*, **21** (1933) 25-41.
21. M.H.R. Lankhorst, H.J.M. Bouwmeester and H. Verweij, "Theory of oxygen transport through mixed conducting membranes," Proc. 4th Intl. Conf. on *Electronic Ceramics & Applications*, Sept. 5-7, 1994, Aachen, Germany, p. 697-702.
22. Y. Teraoka, H.-M. Zhang, K. Okamoto and N. Yamazoe, "Mixed ionic-electronic conductivity of $La_{1-x}Sr_xCo_{1-y}Fe_yO_{3-\delta}$," *Mat. Res. Bull.*, **23** (1988) 51-58.
23. T. Inoue, J. Kamimae, M. Ueda, K. Eguchi and H. Arai, "Ionic and electronic conductivities of $LaMnO_3$-based perovskite-type oxides measured by the A.C. impedance method with electron-blocking electrodes," *J. Mater. Chem.*, **3** (1993) 751-754.
24. H.J.M. Bouwmeester, H. Kruidhof and A.J. Burggraaf, "Importance of the surface exchange kinetics in rate limiting oxygen permeation through mixed-conducting oxides," *Solid State Ionics*, **72** (1994) 185-194.
25. B.A. van Hassel, J.E. ten Elshof and H.J.M. Bouwmeester, "Oxygen permeation flux through $La_{1-x}Sr_xFeO_3$ limited by carbon monoxide oxidation rate," *Appl. Catal. A: General*, **119** (1994) 279-291.
26. K. Otsuka, S. Yokoyama and A. Morikawa, "Catalytic activity- and selectivity-control for oxidative coupling of methane by oxygen-pumping through yttria stabilized zirconia," *Chem. Lett.*, (1985) 319-322.
27. D. Eng and M. Stoukides, "Catalytic and electrocatalytic methane oxidation with solid oxide membranes," *Catal. Rev.-Sci. Eng.*, **33** (1991) 375-412.
28. H. Nagamoto, K. Hayashi and H. Inoue, "Methane oxidation by oxygen transported through solid electrolyte," *J. Catal.*, **126** (1990) 671-673.
29. J.E. ten Elshof and J. Boeijsma, "Influence of iron content on cell parameters of rhombohedral $La_{0.6}Sr_{0.4}Co_{1-x}Fe_xO_3$," *Powder Diff.*, **11** (1996) 240-245.
30. Powder Diffraction File, JCPDS-International Centre for Diffraction Data, no. 36-1393.
31. N. Itoh, T. Kato, K. Uchida and K. Haraya, "Preparation of pore-free disks of $La_{1-x}Sr_xCoO_3$ mixed conductor and its oxygen permeability," *J. Membr. Sci.*, **92** (1994) 239-246.
32. Chapter 2 of this thesis.
33. J.O. Petunchi and E.A. Lombardero, "The effect of bulk and surface reduction upon the catalytic behaviour of perovskite oxides", *Catal. Today*, **8** (1990) 201-220.
34. A.M. Maitra, I. Campbell and R.J. Tyler, "Influence of basicity on the catalytic activity for oxidative coupling of methane," *Appl. Catal. A: General*, **85** (1992) 27-46.
35. H. Schmalzried, *Solid State Reactions*, Verlag Chemie, Weinheim, 1981.
36. M.J. Scholten, J. Schoonman, J.C. van Miltenburg and H.A.J. Oonk, "Synthesis of strontium and barium cerate and their reaction with carbon dioxide," *Solid State Ionics*, **61** (1993) 83-91.
37. E.A. Hazbun, "Ceramic membrane for hydrocarbon conversion," *U.S. Patent 4,791,079* (1988).

# 8

# Oxygen permeation properties of dense $Bi_{1.5}Er_{0.5}O_3$-Ag cermet membranes


## Abstract

Oxygen permeation experiments were performed on dense mixed-conducting ceramic-metal composite membranes (thickness 0.2-2 mm) $Bi_{1.5}Er_{0.5}O_3$-Ag with 10.0, 27.8 and 40.0 vol% silver, respectively, in the temperature range 873-993 K and oxygen partial pressure range $10^{-3.5}$-1 bar $O_2$. The oxygen fluxes increased with increasing silver content. In the cermets with a nonpercolative silver phase (10.0 and 27.8 vol%), the increased oxygen flux relative to that of pure $Bi_{1.5}Er_{0.5}O_3$ was attributed to faster surface oxygen exchange in the presence of silver. The existence of a percolative silver network in the 40 vol% Ag-containing compound increases the ambipolar diffusion of oxygen ions and electrons. High oxygen fluxes (.0.25 mmol $m^{-2}$ $s^{-1}$ at 873 K) were observed for this compound. They were shown to be fully limited by the surface exchange kinetics. The activation energy for oxygen permeation in the temperature range 848-1003 K is about 85-95 kJ/mol for the compounds without a percolative silver phase, and 115 kJ/mol for the composite with 40 vol% Ag. The difference reflects a change of the rate-limiting step upon passing the percolation threshold. Results from both permeation and isotopic exchange measurements on the compound with a percolative silver phase indicated the kinetic order in oxygen of the surface process to be ¼, which indicates a process fundamentally different from that on pure $Bi_{1.5}Er_{0.5}O_3$.

## 8.1. Introduction

The high-temperature fcc δ-phase of the defect fluorite-type $Bi_2O_3$ is the best oxygen ion conductor known. Its anomalously high ionic conductivity is related to the cubic crystal structure, the nature of the bismuth ion and the intrinsically large concentration of vacant sites in the oxygen sublattice, which is 25% of the total number of available crystallographic sites. The temperature range in which the δ-phase is stable is rather narrow (1002-1097 K) and the transition from the δ-phase to the low temperature α-phase is accompanied by a conductivity decrease of 2-3 orders of magnitude.

The more conductive cubic phase can be stabilized down to room temperature by partial doping with rare earth elements or yttria [1-3], although the conductivity decreases with increasing dopant concentration. The maximum conductivity below the transition temperature of δ-$Bi_2O_3$ is therefore obtained at the minimum doping level necessary to stabilize the fcc phase [1]. Doping with erbia or yttria have been shown to preserve the ionic conductivity best [2].

The conductivity of compounds $Bi_{2-x}(Y,Er)_xO_3$ have been investigated extensively [1-7]. In the $Bi_{2-x}Er_xO_3$ system maximum conductivity is reached at 20-25 mol% Er ($x$=0.4-0.5) [4]. The ionic conductivity of $Bi_{1.5}Er_{0.5}O_3$ (denoted as BE25) has an activation energy of 72±4 kJ/mol above 873 K, and reaches an absolute value of 25 $\Omega^{-1}$ $m^{-1}$ at 973 K. The ionic conductivities of several compounds $Bi_{2-x}Y_xO_3$ have been shown [5,6] to be independent of oxygen pressure.

The partial electronic conductivity of $Bi_{1.46}Y_{0.54}O_3$ at elevated temperatures has been investigated by Takahashi et al. [7]. The electronic conductivity $\sigma_e$ is predominantly p-type at high oxygen pressures, and has an activation energy $E_{act}$ of 106 kJ/mol. In Kröger-Vink notation [8], the oxygen incorporation reaction under these conditions can be written as

$$\tfrac{1}{2}O_2 + V_O^{\cdot\cdot} + O_O^x \rightleftharpoons 2h^{\cdot} \,. \qquad (8.1)$$

Since the concentrations of oxygen anions $O_O^x$ and oxygen vacancies $V_O^{\cdot\cdot}$ are virtually constant, it follows that

$$\sigma_e \propto [h^{\cdot}] \propto p_{O_2}^{1/4} \,. \qquad (8.2)$$

At low oxygen partial pressures ($p_{O_2}$ <$10^{-6}$-$10^{-8}$ bar), n-type conductivity with a -1/4 dependence on the oxygen pressure is predominant ($E_{act}$=213 kJ/mol). The literature on $Bi_2O_3$-based electrolytes has been reviewed recently [9]. The surface exchange kinetics of BE25 has been investigated by Boukamp et al. [10,11] by means of $^{18}O/^{16}O$ isotopic exchange. The following mechanism was proposed for the dissociative

adsorption of oxygen in order to account for the $p_{O_2}^{1/2}$ dependence of the exchange rate that was observed experimentally:

$$O_2 + e'WO_{2,ads}^- , \tag{8.3}$$

$$O_{2,ads}^- + e'W2O_{ads}^- , \tag{8.4}$$

$$2O_{ads}^- + 2V_O^{\cdot\cdot} + 2e'W2O_O^x . \tag{8.5}$$

The second step in the above scheme is proposed to be rate-determining.

The simultaneous occurrence of ionic and electronic conductivity makes it possible to utilise these materials as oxygen separation membranes in oxygen pressure gradients. The oxygen semipermeability of 0.2-2.85 mm thick dense BE25 membranes has been studied by Bouwmeester et al. [12], who found that the permeability in the temperature range 883-1083 K in air/He gradients is determined partly by bulk diffusion of electron holes and partly by the oxygen exchange process at the gas/solid interfaces. In modelling the data, a 5/8 power dependence of the oxygen exchange rate on oxygen partial pressure was assumed. Experimentally observed fluxes were in the range $10^{-3}$-0.1 mmol $m^{-2}$ $s^{-1}$.

Enhancement of both the electronic conductivity and the surface exchange of oxygen are therefore required to make practical application of $Bi_{2-x}(Y,Er)_xO_3$-based membranes possible. The electronic conductivity can be increased to some extent by partial substitution of bismuth by terbium [13]. An alternative approach is to disperse a percolative second phase with high electrical conductivity [14], e.g., Au or Ag, beyond a critical volume fraction (percolation threshold) in the oxide matrix. Preliminary measurements on both 40 vol% gold- and 40 vol% silver-doped $Bi_2O_3$-based cermets by Chen et al. [15] indicated much higher fluxes through the latter.

Shen et al. [16] found that 33 vol% of silver needs to be introduced in $Bi_{1.5}Y_{0.5}O_3$ in order to obtain percolative networks of both phases. In membrane applications a particular advantage of the use of silver as the electronically conducting phase is its high activity in the dissociation of molecular oxygen $O_2 \rightarrow 2O_{ads}^-$ [17]. Silver is also known to be permeable to oxygen [18], but this is negligible compared to that of $Bi_{2-x}(Y,Er)_xO_3$. Oxygen fluxes up to 8 mmol $m^{-2}$ $s^{-1}$ at 1023 K were reported through dense membranes $(Bi_{1.5}Y_{0.5}O_3)_{65vol\%}(Ag)_{35vol\%}$ of 0.2-2 mm thickness. Although the fluxes tended to increase with decreasing thickness, the authors showed from the thickness dependence of the permeation flux that the rate was partially controlled by the surface exchange process for the thinnest specimens used in their study.

In the present study oxygen permeation characteristics of $Bi_{1.5}Er_{0.5}O_3$-Ag cermet membranes with different silver contents are investigated. The attention is mainly focused on the compound with 40.0 vol% in which the silver phase is percolative.

## 8.2. Modeling of oxygen permeation

### 8.2.1. Bulk diffusion

Consider a cermet membrane with percolative ionic and electronic conducting phases. If both interfaces are in equilibrium with the imposed atmospheres having oxygen partial pressures $p_{ox}$ and $p_{red}$, respectively, then the magnitude of the driving force for permeation is the negative of the Nernst potential $E$. To maintain overall charge neutrality, the ionic flux through the oxide phase is counterbalanced by that of electrons through the electronic conducting phase in the opposite direction. The ambipolar conductivity $\sigma_{amb}$ is the effective conductivity originating from this charge-coupled diffusion of ions and electrons and is defined by

$$\frac{1}{\sigma_{amb}} = \frac{\tau_i}{\nu_i \sigma_i} + \frac{\tau_e}{\nu_e \sigma_e}, \tag{8.6}$$

in which $\sigma_i$ and $\sigma_e$ are the ionic and electronic conductivity of the oxide and metal phase, respectively. $\nu_i$ and $\nu_e$ are the respective volume fractions of the ionic and electronically conducting phases in the composite, and $\tau_i$ and $\tau_e$ are dimensionless factors to include the effect of geometry on the partial conductivities.

As seen from Eq. (8.6) the value of the ambipolar conductivity is determined by the phase with the smallest effective conductivity. For a percolative metal/ceramic composite, the ionic conductivity of the oxide phase is generally much smaller than the electronic conductivity of the metal phase, in which case $\sigma_{amb} = \nu_i \sigma_i / \tau_i$. In steady state, the flux of $O_2$ through the membrane bulk can be calculated with [19]

$$j_{O_2} = \frac{\sigma_{amb}}{4FL} E = \frac{\sigma_{amb}}{4FL} \left( \frac{RT}{4F} \ln \frac{p_{ox}}{p_{red}} \right), \tag{8.7}$$

where $L$ is the membrane thickness, $F$ the Faraday constant and $T$ the temperature.

### 8.2.2. Surface exchange

In the absence of an oxygen chemical potential difference the surface exchange of oxygen will be in a dynamic equilibrium. The net rate of reaction at each interface is zero. The exchange flux $j_{ex}^0$ generally found under these conditions [20] can be expressed by the empirical relationship

$$j_{ex}^0 = j_{ex}^* \, p_{O_2}^n, \tag{8.8}$$

where $n$ is the apparent kinetic order of the surface reaction and $j_{ex}^*$ the oxygen exchange rate at 1 bar $O_2$. Both parameters can be obtained from $^{18}O/^{16}O$ isotopic exchange experiments.

Under non-equilibrium steady state conditions, there is an oxygen chemical potential difference between the gas phase and the surface layer. The resulting net transport of oxygen through an interface can be approximated by $j_{O_2} = j_{ex}^{*} \Delta p_{O_2}^{n}$, yielding for the feed side interface of the membrane

$$j_{O_2} = j_{ex}^{*}(p'_{O_2}{}^{n} - p_{ox}{}^{n}), \tag{8.9}$$

and for the permeate side interface of the membrane

$$j_{O_2} = j_{ex}^{*}(p_{red}{}^{n} - p''_{O_2}{}^{n}). \tag{8.10}$$

In the above equations $p'_{O_2}$ and $p''_{O_2}$ are the oxygen partial pressures at the membrane feed and permeate side, respectively. $p_{ox}$ and $p_{red}$ are 'virtual' oxygen pressures in the surface layers at feed and permeate side, corresponding to certain local oxygen chemical potentials.

If diffusion is sufficiently fast in steady state, then the oxygen flux is determined only by the exchange process. Thus, $p_{ox} = p_{red}$. It then follows from combination of Eqs. (8.9)-(8.10) that

$$j_{O_2} = \tfrac{1}{2} j_{ex}^{*}(p'_{O_2}{}^{n} - p''_{O_2}{}^{n}). \tag{8.11}$$

To calculate the overall flux through a membrane in which partial rate limitations are exerted by diffusion and exchange the equations (8.7), (8.9) and (8.10) have to be solved simultaneously.

## 8.3. Experimental

### *8.3.1. Membrane preparation*

$Bi_{1.5}Er_{0.5}O_3$ (BE25) powders were prepared by both the conventional ceramic route and the coprecipitation technique reported by Kruidhof et al. [21]. The mixtures of $Bi_2O_3$ and $Er_2O_3$ were calcined at 1010 K for 8 h, yielding phase-pure BE25. Calcined BE25 and $Ag_2O$ were mixed and milled in the appropriate ratio in acetone in a planetary mill for several hours to obtain a physical mixture with a median agglomerate size smaller than 5 μm. Compounds containing 10.0, 27.8 and 40.0 vol% Ag were prepared. These compounds are referred to as BE25Ag10, BE25Ag278 and BE25Ag40, respectively.

The powders were pressed uniaxially into pellets with a diameter of 25 mm, followed by isostatic pressing at 4000 bar. The pellets were sintered at 1113-1123 K for 14-16 h (heating/cooling rate 0.5 K/min) and cut into membranes with a diameter of 14.83 mm and thicknesses varying between 0.2-2.0 mm. The membranes were polished on both sides with 1000 MESH SiC.

### 8.3.2. Permeation experiments

The experimental setup and methods for the oxygen permeation experiments have been described in detail elsewhere [22]. The membranes were sealed into the reactor using low-melting glass rings (AR glass) of 1 mm thickness. The reactor was heated with 3 K/min to 980-1000 K, at which temperature it was kept for 1 h to let the glass ring seal the membrane. No reaction was observed between the glass and the membranes. The reactor was then cooled to its lowest operating temperature with 1 K/min. Air or an $O_2$,$N_2$ mixture with oxygen partial pressures of $10^{-2}$-1 bar was supplied to the feed side of the membrane. Helium was supplied to the permeate side. The concentrations of $O_2$ and $N_2$ were measured by a Varian 3300 GC containing a molecular sieve 13X. The oxygen flux was calculated from

$$j_{O_2} = \frac{1}{G} \cdot \frac{F c_{O_2}}{A_{He}}. \qquad (8.12)$$

$F$ is the flow rate at the outlet of the reactor ($m^3$ $s^{-1}$ (STP)), $c_{O_2}$ the oxygen concentration in the effluent stream (mol $m^{-3}$) and $A_{He}$ the geometric surface area at the helium side of the membrane (1.13 $cm^2$).

The dimensionless factor $G$ corrects for the effect of non-radial diffusion, since the applied method of sealing results in different membrane surface areas at opposite sides of the membrane [23]. In case of surface-controlled permeation, $G$ will be equal to 1 when the limitation occurs at the permeate side, whereas $G=A_{air}/A_{He}$ ($A_{air}$ is the geometric surface area at the $O_2$,$N_2$ side of the membrane, 1.77 $cm^2$) upon limitation at the feed side. Details of the calculation of $G$ in case of a diffusion-controlled flux can be found elsewhere [23]. In the present study, the value of $G$ is taken to be unity.

### 8.3.3. Isotopic exchange analysis

The experimental setup for the $^{18}O/^{16}O$ isotopic exchange experiments has been described in detail elsewhere [24]. Measurements were performed at 873 K at several oxygen pressures in the range 0.15-0.88 bar. The samples with geometric surface areas $A$=1.36-1.60 $cm^2$ (mass 327-358 mg) were made from disks with a diameter of 13.7-14.0 mm that were cut in half. After mechanical polishing to submicron size and ultrasonic cleaning, the samples were placed in a quartz tube with a volume of 54.9 $cm^3$ and heated up to 973 K, where the samples were preannealed for 1 h in dry natural oxygen at a pressure of 0.2 bar. The quartz tube was then quenched to room temperature and evacuated. After repeated flushing with argon and evacuating the chamber, an amount of natural oxygen necessary to establish the desired pressure at 873 K was introduced into the tube. The tube was heated up quickly to 873 K, at which temperature it was kept for 1 h. Again the tube was rapidly cooled to room temperature, flushed with argon and evacuated several times. Precisely the same amount of gas as in the previous equilibration step, but now from a reservoir with

97.5% $^{18}$O-enriched gas, was entered into the tube. The tube was heated quickly to 873 K. The exchange was monitored by measuring the mass 32 ($^{16}O_2$), 34 ($^{16}O^{18}O$) and 36 ($^{18}O_2$) quadrupole signals. The atomic fraction of $^{18}$O in the gas phase at time $t$ was calculated from

$$x_{18}(t) = \frac{p_{^{18}O_2}(t) + \frac{1}{2} p_{^{18}O^{16}O}(t)}{p_{^{18}O_2}(t) + p_{^{18}O^{16}O}(t) + p_{^{16}O_2}(t)} \,, \tag{8.13}$$

with $p_{^{16}O_2}$, $p_{^{18}O^{16}O}$ and $p_{^{18}O_2}$ the oxygen pressures of the respective isotopic fractions.

### *8.3.4. Phase analysis and microstructure*

XRD spectra were taken on a Philips PW1710 with graphite-filtered CuKα radiation. The bulk mass concentrations of bismuth and erbium were determined by X-ray Fluorescence Spectroscopy (XRF) using a Philips PW 1480/10 X-ray spectrometer. The silver content was determined by Atomic Adsorption Spectroscopy (AAS) using a Varian SpectrAA-10. The membrane surface morphology was examined by High Resolution Scanning Electron Microscopy (HR-SEM) using a Hitachi S-800 Field Emission Microscope operating at 15 kV, which was coupled to a Kevex Delta Range EDX (Energy Dispersive X-ray analysis) system for surface element analysis.

## 8.4. Results and discussion

### *8.4.1. Phase analysis and microstructure*

The densities of the membranes were in the range of 96-98% of theoretical. XRD spectra of all investigated compounds indicated the presence of two separate phases which were identified as $Bi_{1.5}Er_{0.5}O_3$ and Ag. No other diffraction peaks were observed. The experimental mass fractions of bismuth and erbium in both freshly prepared and used BE25Ag40 membranes varied between 39.3-39.6% and 10.5-10.6%, respectively, close to the theoretical values of 39.5% and 10.5%, respectively. The silver fractions found by AAS were 43.9-44.2 mass%, in agreement with the theoretical value of 43.9 mass%.

A SEM picture of the surface structure of a polished BE25Ag40 membrane before use is shown in Figure 8.1. EDX analysis indicated the dark parts to be the silver phase, and the white areas to be the oxide phase. Figure 8.2 shows the surface of a membrane exposed to a temperature of 993 K for 2 h. Severe agglomeration of silver on the membrane surface can be observed clearly. When the maximum temperature was kept below 973 K, a much smaller degree of agglomeration was found. The agglomeration is due to the large diffusivity of silver at these temperatures, and may be suppressed by using PdAg alloys instead of pure Ag. The use of these alloys in cermet membranes was demonstrated by Shen et al. [16].

### 8.4.2. Variation of silver content on flux

The existence of a percolative silver network was checked for by measuring the DC electrical resistance at room temperature. BE25Ag40 was found to have a resistance of about 0.5-3 Ω, while the resistances of the other compounds were in the range of 0.1-1 MΩ. An electronic short-circuit was therefore concluded to exist only in BE25Ag40, which is expected based on the results of Shen et al. [16].


Figure 8.1. SEM picture of polished fresh BE25Ag40 membrane surface.

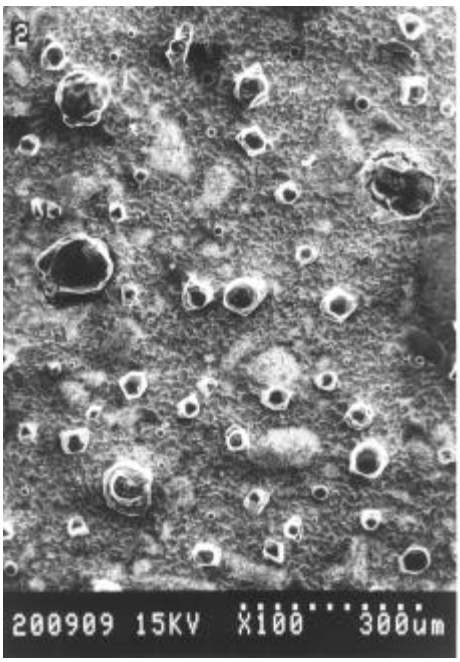


Figure 8.2. SEM picture of BE25Ag40 surface after thermal treatment at 993 K.

Arrhenius curves of the fluxes through 0.7-0.8 mm thick membranes are given in Figure 8.3. All measurements were performed in fixed oxygen partial pressure gradients. The Arrhenius curve obtained by Bouwmeester et al. [12] on a 0.7 mm thick BE25 membrane in a 0.15 bar $O_2$/He gradient is shown for comparison.

Compared with phase-pure BE25, the substitution of 10.0 vol% of ceramic by silver increases the permeation rate by more than half an order of magnitude. Upon increasing the silver content from 27.8 vol% to 40.0 vol% the permeation rate increases by almost an order of magnitude. This can be understood by considering that the silver phase becomes continuous upon passing the percolation threshold at 33-35 vol% Ag [16], thus creating a continuous path for transport of electronic species parallel to that in the BE25 phase, but with a much larger conductivity. Under these conditions, it can be assumed safely that $\sigma_{amb} = \nu_i \sigma_i / \tau_i$, i.e., the rate-limiting effect due to a limited electron hole conduction in the oxide phase is eliminated.

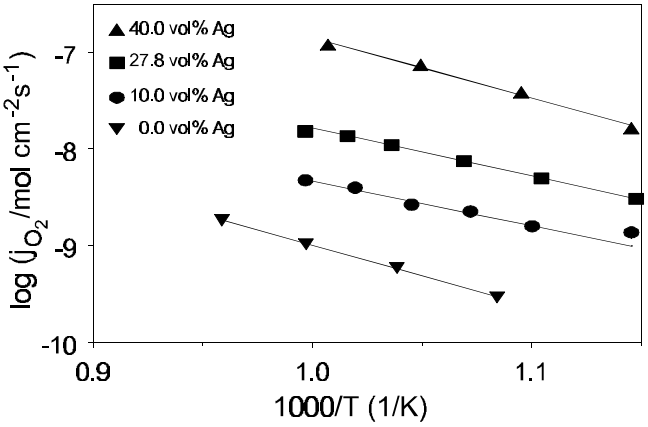


Figure 8.3. Arrhenius curves of 0.7-0.8 mm membranes of varying silver content in air/He fixed gradients. Details can be found in Table 8.1.

Calculated activation energies and experimental conditions are listed in Table 8.1. Based on these results, a distinction can be made between phase-pure BE25, the non-percolative Ag-doped compounds and percolative BE25Ag40. Doping with small amounts of silver (below the percolation threshold) will cause a fundamentally different exchange mechanism than on pure BE25, which is reflected in a decrease of the apparent activation energy. Upon passing the percolation threshold, the ambipolar diffusion process is accelerated considerably as an electronic short-circuit now exists in the bulk. The ambipolar diffusion process changes from being governed by the electronic conductivity to being governed by the ionic conductivity, which is reflected in an increase of the activation energy to 116 kJ/mol.

Table 8.1. Activation energies of oxygen semipermeability of 0.7-0.8 mm thick membranes with varying silver contents.

| $V_{Ag}$ (%) | $L$ (mm) | - log ( $p''_{O_2}$ /bar) | $E_{act}$ (kJ/mol) |
|---|---|---|---|
| 0.0 | 0.70 | | 121±4 |
| 10.0 | 0.77 | 2.70-2.80 | 88±10 |
| 27.8 | 0.79 | 2.80 | 95±1 |
| 40.0 | 0.75 | 2.25 | 116±9 |

It follows from Eq. (8.7) that for a diffusion-controlled flux the activation energy of $j_{O_2}$ is the same as that of the ambipolar conductivity, i.e., the ionic conductivity in the case of BE25Ag40. Verkerk et al. [4] reported an activation energy of 72 kJ/mol for the ionic conductivity of BE25. As the value derived from oxygen permeation measurements through BE25Ag40 is much higher, this implies the involvement of a process other than diffusion to (partially) control the flux.

### *8.4.3. Influence of thickness on flux*

Oxygen fluxes through BE25Ag40 membranes at 873 K are shown versus the reciprocal thickness in Figure 8.4. The gradient was fixed at 0.21(air)/0.003 bar $O_2$.

The flux of 0.24±0.04 mmol $m^{-2}$ $s^{-1}$ remains constant with decreasing thickness, indicating a surface exchange-limited flux within experimental error. The permeance, defined as the ratio of flux and driving force $j_{O_2}/E$, is 2.9±0.5 mmol $m^{-2}$ $s^{-1}$ $V^{-1}$ at this temperature., much smaller than the value of 22.1 mmol $m^{-2}$ $s^{-1}$ $V^{-1}$ that can be calculated from the data of Shen et al. [16] for 0.2 mm thick $(Bi_{1.5}Y_{0.5}O_3)_{65vol\%}(Ag)_{35vol\%}$ under similar conditions. The reason for this large discrepancy is not clear.

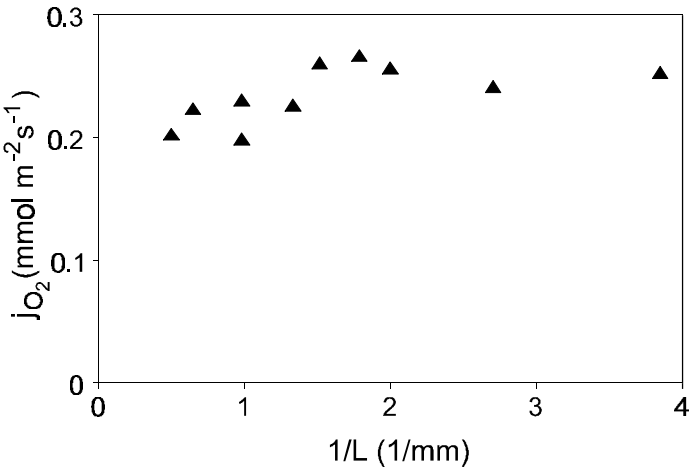


Figure 8.4. Thickness dependence of oxygen flux through BE25Ag40 membranes at 873 K in fixed air/0.003 bar $O_2$ gradient.

### *8.4.4. Effect of oxygen pressure on flux*

The effect of variation of the feed side pressure on the flux (the permeate side pressure was kept constant) through BE25Ag40 is shown in Figure 8.5a. Assuming the permeation rate to be controlled by the surface exchange process only, the experimental data were fitted to Eq. (8.11).

The best fits yielded values $n$=0.26, 0.27 and 0.23, at 873 K, 913 K and 953 K, respectively, suggesting that $n$=¼. Subsequently the data were fitted to the equation $j_{O_2} = \frac{1}{2} j_{ex}^{*}((p_{O_2}^{'})^{1/4} - (p_{O_2}^{''})^{1/4})$, as shown graphically in Figure 8.5b. The same pressure dependence was found for other membrane thicknesses.

Table 8.2. Oxygen exchange rates $j_{ex}^{*}$ (mmol $m^{-2}$ $s^{-1}$) on BE25Ag40 at 1 bar $O_2$ determined from oxygen permeation and isotopic exchange experiments.

| | permeation | | isotopic exchange |
|---|---|---|---|
| $T$ (K) | feed | permeate | |
| 873 | 0.55±0.03 | 0.54±0.12 | 0.56±0.08 |
| 913 | 1.43±0.05 | 1.20±0.12 | |
| 953 | 2.43±0.06 | 2.37±0.16 | |
| 993 | 3.69±0.30 | | |

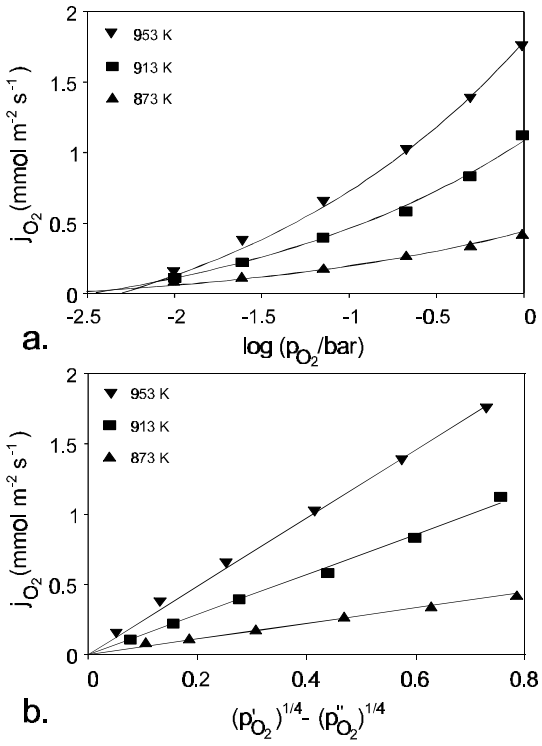


Figure 8.5. Feed side pressure dependence of oxygen flux of 1.02 mm BE25Ag40 membrane.

In Figure 8.6 the permeate side dependence of BE25Ag40 is shown when air was supplied to the feed side. The drawn lines indicate the best fits of Eq. (8.11) with $n$=¼ to the experimental data. Oxygen exchange rates $j_{ex}^{*}$ determined from pressure variation experiments are listed in Table 8.2.

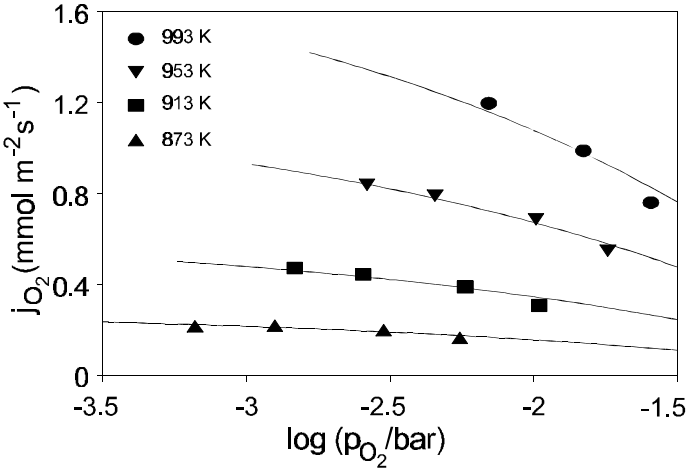


Figure 8.6. Permeate side pressure dependence of oxygen flux through 1.03 mm BE25Ag40 membrane.

Results of feed side pressure variation experiments on nonpercolative BE25Ag278 at 953 K are shown in Figure 8.7. The best fits to Eq. (8.11) with $n$=¼ are indicated by drawn lines in the figure.

As was demonstrated earlier, it is plausible that ambipolar diffusion in the oxide phase exerts a partial control of the permeation rate through the nonpercolative Ag-containing compounds. Taking into account that in the oxide phase $\sigma_e \ll \sigma_i$ and $\sigma_e \propto p_{O_2}^{1/4}$, the rate of diffusion is governed by electron hole conductivity, and thus proportional to $p_{O_2}^{1/4}$ [12]. Furthermore, under the assumption that the surface process is essentially the same as on BE25Ag40, a ¼ power dependence on oxygen pressure is expected for the surface reaction rate as well. No conclusion can therefore be drawn about the nature of the rate-determining step for BE25Ag278 based on oxygen pressure variation.

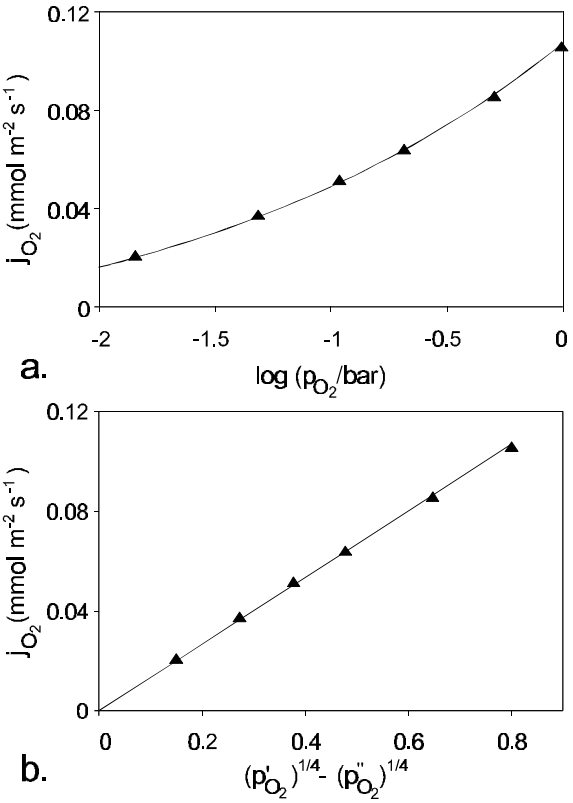


Figure 8.7. Feed side pressure dependence of oxygen flux of 0.79 mm BE25Ag278 membrane at 953 K.

### *8.4.5. Isotopic exchange*

Oxygen isotopic exchange analysis was performed on percolative BE25Ag40 to verify the indications of an exchange-controlled flux described above. An equilibration of isotopic fractions between the gas and solid phase that is completely rate-determined by the surface exchange reaction follows first order kinetics. For the atomic fraction of $^{18}O$ in the gas phase it can be shown [24] that

$$x_{18}(t) = x_{18}(\infty) + [x_{18}(0) - x_{18}(\infty)]\exp[-A r_s (n_{ox}^{-1} + n_{gas}^{-1})t], \qquad (8.14)$$

where $n_{ox}$ is half the total number of moles $O^{2-}$ in the bulk, and $n_{gas}$ the total number of moles $O_2$ in the surrounding gas phase. $r_s$ is the equilibrium exchange rate and $A$ the sample surface area.

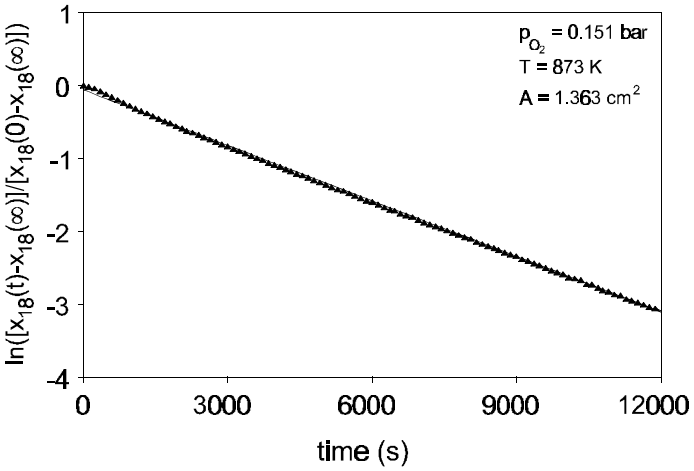


Figure 8.8. Decay curve of $^{18}O$ gas phase atomic fraction $x_{18}(t)$ in isotopic equilibration of BE25Ag40 at 873 K.

Figure 8.8 displays an exchange curve of BE25Ag40 in the form $\ln[(x_{18}(t)-x_{18}(\infty))/(x_{18}(0)-x_{18}(\infty))]$ versus $t$. The absence of a deviation from linearity indicates that diffusion does not exert a partial rate limitation. Calculated values of $r_s$ at 873 K at selected oxygen pressures are given in Figure 8.9. The best fit to the data, indicated by the drawn line, has a slope $n$=0.30±0.08, reasonably close to ¼. The exchange rate $j^*_{ex}$ =0.56±0.08 mmol m$^{-2}$ s$^{-1}$ at 873 K is in very close agreement with the exchange rates determined from permeation data listed in Table 8.2.

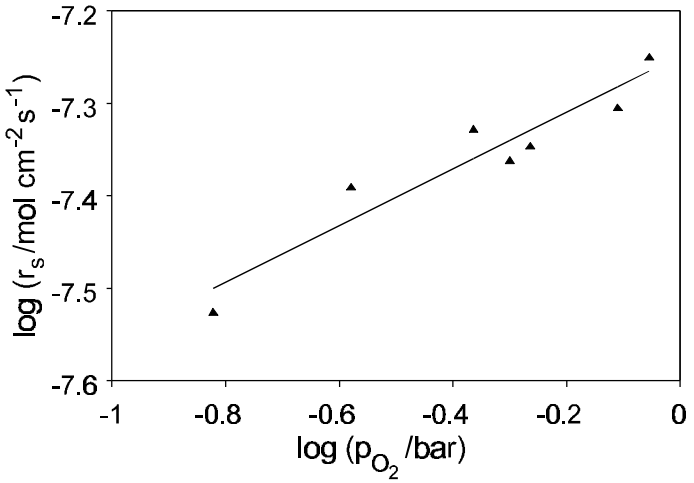


Figure 8.9. Oxygen exchange rates obtained from $^{18}O/^{16}O$ isotopic exchange at 873 K and various pressures. The best fit to the data, indicated by a drawn line, has a slope $n$=0.30±0.08.

One may speculate about the nature of the rate-determining step in the exchange mechanism. For instance, the ¼ power dependence can be explained by assuming the rate-determining step to involve surface diffusion of electron holes on the BE25 surface. The observed activation energy of 116±9 kJ/mol is close to the value of 106 kJ/mol reported for electron hole conduction in $Bi_{1.5}Y_{0.5}O_3$ [7]. However, surface diffusion of adsorbed $O^-$ species would also be in agreement with the observed kinetic order. Additional work is required to gain more insight into the mechanism of the surface oxygen exchange mechanism.

## 8.5. Conclusions

Oxygen permeation experiments were conducted on BE25Ag10, BE25Ag278 and BE25Ag40 membranes, with a relative density of 97-98%, thickness in the range of 0.2 to 2.0 mm, under various $p_{O_2}$ gradients. The observed fluxes increased with increasing fraction of silver. The oxygen flux through BE25Ag10 and BE25Ag278 is at least partly determined by diffusion of electron holes through the BE25 oxide phase. The activation energies for oxygen permeation for these compounds is in the range of 80-100 kJ/mol.

The flux through BE25Ag40 membranes is entirely limited by the surface kinetics. At 873 K the permeance is 2.9±0.5 mmol $m^{-2}$ $s^{-1}$ $V^{-1}$. The ambipolar diffusion in BE25Ag40 is high due to the fact that the silver phase is percolative, which allows fast transport of electrons. The activation energy for the surface exchange process is 116±9 kJ/mol. Both oxygen permeation and isotopic exchange experiments on BE25Ag40 indicate an oxygen pressure dependence of $n$=¼ for the oxygen exchange rate, which means that the surface process is different from that observed on pure BE25, where $n$=½.

## References

1. H. Iwahara, T. Esaka, T. Sato and T. Takahashi, “Formation of high oxide ion conductive phases in the sintered oxides of the system $Bi_2O_3$-$Ln_2O_3$ (Ln=La-Yb),” *J. Solid State Chem.*, **39** (1981) 173-180.
2. M.J. Verkerk and A.J. Burggraaf, “High oxygen ion conduction in sintered oxides of the $Bi_2O_3$-$Ln_2O_3$ system,” *Solid State Ionics*, **3-4** (1981) 463-467.
3. T. Takahashi, H. Iwahara and T. Esaka, “High oxide ion conduction in sintered oxide of the system $Bi_2O_3$-$M_2O_3$,” *J. Electrochem. Soc.*, **124** (1977) 1563-1569.
4. M.J. Verkerk, K. Keizer and A.J. Burggraaf, “High oxygen ion conduction in sintered oxides of the $Bi_2O_3$-$Er_2O_3$ system,” *J. Appl. Electrochem.*, **10** (1980) 81-90.
5. T. Takahashi, H. Iwahara and T. Arao, “High oxide ion conduction in sintered oxides of the system $Bi_2O_3$-$Y_2O_3$,” *J. Appl. Electrochem.*, **5** (1975) 187-195.
6. C. Wang, X. Xu and B. Li, “Ionic and electronic conduction of oxygen ion conductors in the $Bi_2O_3$-$Y_2O_3$ system,” *Solid State Ionics*, **13** (1984) 135-140.

7. T. Takahashi, T. Esaka and H. Iwahara, "Conduction in $Bi_2O_3$-based oxide ion conductor under low oxygen pressure. II. Determination of the partial electronic conductivity," *J. Appl. Electrochem.*, **7** (1977) 303-308.
8. F.A. Kröger, The chemistry of imperfect crystals, North-Holland, Amsterdam, (1964).
9. P. Shuk, H.-D. Wiemhöfer, U. Guth, W. Göpel and M. Greenblatt, "Oxide ion conducting solid electrolytes based on $Bi_2O_3$," *Solid State Ionics*, **89** (1996) 179-196.
10. B.A. Boukamp, H.J.M. Bouwmeester and A.J. Burggraaf, "The surface oxygen exchange process in oxygen ion conducting materials," Proc. 2nd Intl. Symp. on *Ionic and mixed conducting ceramics*, ed. T.A. Ramanarayanan, W.L. Worrell and H.L. Tuller, Proc. vol. 94-12, The Electrochemical Society, Pennington, NJ, 1994, p. 141-150.
11. B.A. Boukamp, I.C. Vinke, K.J. de Vries and A.J. Burggraaf, "Surface oxygen exchange kinetics of solid oxide ion conductors," in NATO ASI series: *Fast Ion Transport in Solids*, ed. B. Scrosati, A. Magistris, C.M. Mari and G. Mariotto, Kluwer Academic Publishers, series E: Applied Science, 250 (1993) 167-180.
12. H.J.M. Bouwmeester, H. Kruidhof, A.J. Burggraaf and P.J. Gellings, "Oxygen semipermeability of erbia-stabilized bismuth oxide, *Solid State Ionics*," **53-56** (1992) 460-468.
13. I.C. Vinke, B.A. Boukamp, K.J. de Vries and A.J. Burggraaf, "Mixed conductivity in terbia stabilized bismuth oxide," *Solid State Ionics*, **57** (1992) 91-98.
14. T.J. Mazanec, T.L. Cable and J.G. Frye, jr., "Electrocatalytic cells for chemical reaction," *Solid State Ionics*, **53-56** (1992) 111-118.
15. C.S. Chen, H. Kruidhof, H.J.M. Bouwmeester, H. Verweij and A.J. Burggraaf, "Oxygen permeation fluxes through oxygen ion oxide-noble metal dual phase composites," *Solid State Ionics*, **86-88** (1996) 569-572.
16. Y. Shen, M. Liu, D. Taylor, S. Bolagopal, A. Joshi and K. Krist, "Mixed ionic-electronic conductors based on Bi-Y-O-Ag metal-ceramic system," Proc. 2nd Intl. Symp. on *Ionic and mixed conducting ceramics*, ed. T.A. Ramanarayanan, W.L. Worrell and H.L. Tuller, Proc. vol. 94-12, The Electrochemical Society, Pennington, NJ, 1994, p. 574-597.
17. V.M. Gryaznov, S.G. Gul'yanova and Yu.M. Serov, "The role of the adsorbed forms of hydrogen and oxygen in the reaction of oxygen-containing one-carbon molecules on membrane catalysts," *Russ. Chem. Rev.*, **58** (1989) 35-40.
18. G. Saracco and V. Specchia, "Catalytic inorganic-membrane reactors: Present experience and future opportunities," *Catal. Rev. - Sci. Eng.*, **36** (1994) 305-384.
19. C.S. Chen, Chapter 2 in: *Fine grained zirconia-metal dual phase composites*, Thesis, University of Twente, Enschede, the Netherlands, 1994.
20. G. Parravano, "Equilibrium oxygen transfer at metal oxide surfaces," *Catal. Rev.*, **4** (1970) 53-76.
21. H. Kruidhof, K. Seshan, B.C. Lippens jr., P.J. Gellings and A.J. Burggraaf, "Bismuth oxide based ceramics with improved electrical and mechanical properties. Part I. Preparation and characterisation," *Mat. Res. Bull.*, **22** (1987) 1635-1643.
22. Chapter 7 of this thesis.
23. Chapter 2 of this thesis.
24. B.A. Boukamp, I.C. Vinke, K.J. de Vries and A.J. Burggraaf, "Surface oxygen exchange properties of bismuth oxide based solid electrolytes and electrode materials," *Solid State Ionics*, **32-33** (1989) 918-923.

# 9

# Evaluation


## Abstract

To establish high rates of oxygen diffusion through dense perovskite-type membranes placed in an oxygen partial pressure gradient, a large oxygen vacancy diffusion coefficient and a high oxygen vacancy concentration over the entire pressure interval are needed. For membrane reactor applications a high chemical stability is required as well. Among the compounds studied in this thesis, the combination of these demands is met best by iron-rich perovskites. The rate of oxygen exchange on $La_{1-x}Sr_xFeO_{3-\delta}$ appears to be promoted by a large concentration of oxygen vacancies at the perovskite interface. For several types of membranes described in this thesis the steady state oxygen fluxes are rate-limited by the exchange process at the low partial pressure side. A significant enlargement of the specific surface area may therefore lead to considerable improvements. The possibility of performing oxidative methane coupling with membrane reactors has been demonstrated, but higher operating temperatures than used for this reaction are preferred for the present generation of perovskite-type membranes. Consequently, the production of syngas appears to be the most promising application at present. For the application of dense membranes at significantly lower temperatures, bismuth oxide-based composites are promising compounds, e.g., for the combined separation of oxygen and oxidative dehydrodimerization of olefins.

## 9.1. Introduction

In this chapter the main results of this thesis are evaluated briefly. The demands on membranes for oxygen separation and use in membrane reactors are discussed. Some recommendations for further research are given.

## 9.2. Defect chemistry, oxygen diffusion and chemical stability

It is commonly assumed that the transport of oxygen is facilitated by a defect structure with a high concentration of randomly distributed oxygen vacancies. Clustering of these vacancies, as has been observed in a wide range of mixed-conducting perovskites [1,2], has been shown to immobilize them, thus inhibiting oxygen transport [3,4]. For the perovskites under investigation here, i.e., $La_{1-x}Sr_xFeO_{3-\delta}$ ($x$=0.1-0.4) and $La_{0.6}Sr_{0.4}Co_{1-y}Fe_yO_{3-\delta}$ ($y$=0.1-0.6), no indications for vacancy ordering were found (Chapters 2 and 5).

It was observed in Chapter 5 that a 10% substitution of Co by Fe in $La_{0.6}Sr_{0.4}CoO_{3-\delta}$ may possibly stabilise the random distribution of vacancies up to higher concentrations, although the absolute level of oxygen deficiency is hardly affected. Hence, it seems that the tendency to clustering in the perovskites is influenced not only by the concentration of anionic defects, but also by the nature of the transition metal cation. In general, vacancy clustering phenomena have been reported more often in perovskite-type oxides and related compounds with high concentrations of cobalt, nickel or copper than with other first-row transition metals like chromium, manganese or iron. However, an alternative explanation for the effect of the substituted iron may be that it creates disorder in the cation sublattice which prevents the formation of microdomains.

Some other trends can also be observed in the series of compounds $La_{1-x}Sr_xMO_{3-\delta}$, with M=Cr, Mn, Fe, Co, Ni, Cu. The level of nonstoichiometry at a given temperature and oxygen partial pressure increases with atomic number of M [5-10]. The self-diffusion of oxygen also increases significantly on going from chromium to cobalt [11-14]. On the other hand, the chemical stability of $LaMO_3$ is seen to decrease in the given direction [15]. At 1000°C where $LaNiO_3$ already decomposes at a partial pressure of $10^{-1}$ bar $O_2$, $LaCrO_3$ remains stable to below $10^{-20}$ bar. All these trends are most likely related closely to the nature and strength of the M-O bond.

The qualifications for an appropriate material for long term application in a membrane reactor for high temperature oxidation reactions, e.g., the production of syngas, are high oxygen semipermeability in a large oxygen partial pressure range, and high chemical stability. In view of the above, these demands are in conflict. Among the first-row transition metals, acceptor-doped perovskites based on iron appear to meet the combination of characteristics best.

The study in Chapter 3 showed that $La_{1-x}Sr_xFeO_{3-\delta}$ membranes remain stable for at least several hundreds of hours at 1000°C with oxygen partial pressures down to

$10^{-15}$ bar in the reaction compartment. It should be noted that the long term effect of strontium segregation on mechanical stability and permeation rate still remains to be investigated. Although the oxygen permeation properties of cobalt-rich compounds have received considerable attention due to their possible applicability in oxygen separation processes [4,16-18], the thermal and chemical stabilities of these materials are probably not sufficient for membrane reactor applications involving high temperatures and low oxygen partial pressure. Since all lanthanum in $La_{1-x}Sr_xFeO_{3-\delta}$ can be replaced by strontium without loosing the perovskite structure (at high oxygen partial pressures) [19,20], candidate materials for membrane reactor applications are iron-rich perovskites with high concentrations of alkaline earth dopants, e.g., $La_{1-x}Sr_xFe_{1-y-y,}Cr_yMn_{y,}O_{3-\delta}$.

With respect to oxygen diffusion in $La_{1-x}Sr_xFeO_{3-\delta}$, the vacancy diffusion coefficient of $La_{0.6}Sr_{0.4}FeO_{3-\delta}$ (reported in Chapters 2 and 4) differs only slightly from that of $La_{0.6}Sr_{0.4}Co_{0.6}Fe_{0.4}O_{3-\delta}$ (Chapter 6). It therefore appears that the main reason for the lower oxygen permeation rates through $La_{1-x}Sr_xFeO_{3-\delta}$, in comparison with their cobalt-containing equivalents, is the difference in nonstoichiometry behaviour. Under the assumption that all vacancies are equally mobile, the diffusional flux in an oxygen partial pressure gradient $p'_{O_2} / p''_{O_2}$ is proportional to $\int_{p''_{O_2}}^{p'_{O_2}} \delta \, d\ln p_{O_2}$. Hence, the permeation process is facilitated by a high oxygen vacancy concentration over the entire pressure interval. In the oxygen pressure range where $La_{1-x}Sr_xCoO_{3-\delta}$ is stable its oxygen deficiency is significantly larger than that of $La_{1-x}Sr_xFeO_{3-\delta}$. However, regarding the assumption of mobile points defects, there are indications that microdomain formation may already occur at relatively low vacancy concentrations in $La_{1-x}Sr_xCoO_{3-\delta}$ at lower temperatures [21]. The aforementioned stabilisation by partial substitution of cobalt by iron may therefore be important for further development of oxygen separation membranes.

## 9.3. Surface exchange of oxygen

Application of the electrical conductivity method to thin specimens (Chapters 4 and 6) is a useful tool in the investigation of the surface exchange kinetics of oxides. Although $^{18}O/^{16}O$ isotopic exchange analysis may provide more detailed information regarding the possible exchange mechanism, the electrical conductivity relaxation technique can be applied over a much wider range of partial pressures. A combination of both techniques is recommended.

In both the oxygen exchange reaction $2O^{2-} \rightleftharpoons O_2+4e^-$ (Chapter 4) and the partial oxidation of CO (Chapter 3) the oxygen exchange rates of dense $La_{1-x}Sr_xFeO_{3-\delta}$ samples appear to be promoted by a the presence of a large concentration of oxygen vacancies at the interface. From the results described in Chapters 2, 3, 7 and 8 of this thesis the importance of oxygen exchange kinetics on the overall permeation

rate becomes clear. In all cases the rate-determining step was found to occur at the low oxygen partial pressure side of the membrane. For membrane reactor applications an exchange-limited permeation process may be beneficial, since it assures that the oxide membrane does not become reduced. However, for the development of new membranes with higher permeation rates considerable attention should not only be paid to the preparation of thin dense layers on porous substrates in order to maximize the diffusional flux [22], but also to the composition and morphology of the lower pressure side surface.

Several methods of surface modification for exchange rate enhancement have been discussed in this thesis. *In situ* treatment of the lower partial pressure side of $La_{1-x}Sr_xFeO_{3-\delta}$ with a CO-containing gas mixture (Chapter 2) was shown to increase the surface exchange rate considerably. A similar effect was noticed upon *in situ* reduction of the lower partial pressure side of a $La_{0.6}Sr_{0.4}Co_{0.8}Fe_{0.2}O_{3-\delta}$ membrane in a $CH_4$ atmosphere (Chapter 7). The exchange rates of $La_{0.6}Sr_{0.4}Co_{0.8}Fe_{0.2}O_{3-\delta}$ were increased considerably upon treatment of the surface in an acid solution for several hours (Chapter 6). It was also shown that the oxidation rate of CO on $La_{1-x}Sr_xFeO_{3-\delta}$ was increased by a factor of two upon deposition of a porous Pt layer on the lower partial pressure side (Chapter 3).

Probably the most effective way to enhance the rate of surface exchange is to enlarge the effective surface area on which the exchange of oxygen can occur. Based on theoretical grounds Deng et al. [23,24] showed that deposition of a porous layer on the perovskite surface may increase the permeation rates by a few orders of magnitude.

## 9.4. Catalytic properties

The oxidative methane coupling study on $La_{0.6}Sr_{0.4}Co_{0.8}Fe_{0.2}O_{3-\delta}$ illustrates the possibility of performing a selective oxidation reaction in a membrane reactor. The major drawback is the high temperature needed to obtain a sufficient flux of oxygen. At the preferred temperatures for membrane operation the combination of high methane partial pressure and low oxygen concentration may easily give rise to deposition of carbon. This increases the rate of $CO_2$ formation and may cause significant decomposition of the perovskite structure at the surface due to the reaction between strontium and carbon, forming $SrCO_3$. As a result, the catalytic activity of the membrane for methane dimerization is easily lost.

At present the primary advantage of the membrane reactor approach is not the possible increase of selectivity, but the combination of air separation and chemical reaction in a single high temperature unit. For the present generation of dense membranes syngas production appears to be the most promising application [25,26], since it is performed preferably at a much higher temperature than methane coupling. The reaction compartment can be packed with a catalyst bed for carbon dioxide and steam reforming, while a large oxygen partial pressure gradient can be

achieved by taking benefit from the considerable catalytic activity for total combustion already reported for several perovskite-type dense membranes (Chapter 7) [25,26].

Since most partial oxidation reactions take place at temperatures of 200-600°C, the design of future classes of materials should be focused on application in that temperature range. Perovskite-type oxides are not very promising in this respect. At present the $Bi_{1.5}Er_{0.5}O_3$-Ag cermet membranes (Chapter 8) are the most appropriate materials known for operation at lower temperatures. Substantial improvements with respect to the oxygen flux may be achieved by optimisation of the microstructure and enlargement of the specific surface area. $Bi_2O_3$-based membranes may be promising materials for application in selective oxidation reactions [27], in particular in the oxidative dehydrodimerization of olefins [28].

## References


1. C.N.R. Rao, J. Gopalakrishnan and K. Vidyasagar, "Superstructures, ordered defects & nonstoichiometry in metal oxides of perovskites & related structures," *Ind. J. Chem.*, **23A** (1984) 265-284.
2. M.T. Anderson, J.T. Vaughey and K.R. Poeppelmeier, "Structural similarities among oxygen-deficient perovskites," *Chem. Mater.*, **5** (1993) 151-165.
3. S. Adler, S. Russek, J. Reimer, M. Fendorf, A. Stacy, Q. Huang, A. Santoro, J. Lynn, J. Baltisberger and U. Werner, "Local structure and oxide-ion motion in defective perovskites," *Solid State Ionics*, **68** (1994) 193-211.
4. L. Qiu, T.H. Lee, L.-M. Liu, Y.L. Yang and A.J. Jacobson, "Oxygen permeation studies of $SrCo_{0.8}Fe_{0.2}O_{3-\delta}$," *Solid State Ionics*, **76** (1995) 321-329.
5. J. Mizusaki, S. Yamauchi, K. Fueki and A. Ishikawa, "Nonstoichiometry of the perovskite-type oxide $La_{1-x}Sr_xCrO_{3-\delta}$," *Solid State Ionics*, **12** (1984) 119-124.
6. J.H. Kuo, H.U. Anderson and D.M. Sparlin, "Oxidation-reduction behavior of undoped and Sr-doped $LaMnO_3$ Nonstoichiometry and defect structure," *J. Solid State Chem.*, **83** (1989) 52-60.
7. J. Mizusaki, H. Tagawa, K. Naraya and T. Sasamoto, "Nonstoichiometry and thermochemical stability of the perovskite-type $La_{1-x}Sr_xMnO_{3-\delta}$," *Solid State Ionics*, **49** (1991) 111-118.
8. J. Mizusaki, M. Yoshihiro, S. Yamauchi and K. Fueki, "Nonstoichiometry and defect structure of the perovskite-type oxides $La_{1-x}Sr_xFeO_{3-\delta}$," *J. Solid State Chem.*, **58** (1985) 257-266.
9. J. Mizusaki, Y. Mima, S. Yamauchi, K. Fueki and H. Tagawa, "Nonstoichiometry of the perovskite-type oxides $La_{1-x}Sr_xCoO_{3-\delta}$," *J. Solid State Chem.*, **80** (1989) 102-111.
10. A.N. Petrov, V.A. Cherepanov, O.F. Kononchuk and L.Ya. Gavrilova, "Oxygen nonstoichiometry of $La_{1-x}Sr_xCoO_{3-\delta}$," *J. Solid State Chem.*, **87** (1990) 69-76.
11. C.J. Yu, D.M. Sparlin and H.U. Anderson, "Oxidation kinetics of $LaCrO_3$," *J. Am. Ceram. Soc.*, **70** (1987) C189-C192.
12. T.M. Gür, A. Belzner and R.A. Huggins, "A new class of oxygen selective chemically driven nonporous ceramic membranes. Part I. A-site doped perovskites," *J. Membr. Sci.*, **75** (1992) 151-162.
13. T. Ishigaki, S. Yamauchi, K. Kishio, J. Mizusaki and K. Fueki, "Diffusion of oxide ion vacancies in perovskite-type oxides," *J. Solid State Chem.*, **73** (1988) 179-187.

14. O.F. Kononchuk, D.P. Sutija, T. Norby and P. Kofstad, “Transient thermogravimetric measurement of chemical diffusion in $La_{0.7}Sr_{0.3}CoO_{3-\delta}$,” Proc. 4th Intl. Symp. on *Solid Oxide Fuel Cells*, ed. M. Dokiya, O. Yamamoto, H. Tagawa and S.C. Singhai, Proc. vol. 95-1, The Electrochemical Society, Pennington, NJ, 1995, p. 395-403.
15. T. Nakamura, G. Petzow and L.J. Gauckler, “Stability of the perovskite phase $LaBO_3$ (B=V, Cr, Mn, Fe, Co, Ni) in reducing atmosphere,” *Mat. Res. Bull.*, **14** (1979) 649-659.
16. Y. Teraoka, T. Nobunaga, K. Okamoto, N. Miura and N. Yamazoe, “Influence of constituent metal cations in substituted $LaCoO_3$ on mixed conductivity and oxygen permeability,” *Solid State Ionics*, **48** (1991) 207-212.
17. H. Kruidhof, H.J.M. Bouwmeester, R.H.E. van Doorn and A.J. Burggraaf, “Influence of order-disorder transitions on oxygen permeability through selected nonstoichiometric perovskite-type oxides,” *Solid State Ionics*, **63-65** (1993) 816-822.
18. N. Itoh, T. Kato, K. Uchida and K. Haraya, “Preparation of pore-free disk of $La_{1-x}Sr_xCoO_3$ mixed conductor and its oxygen permeability,” *J. Membr. Sci.*, **92** (1994) 239-246.
19. Y. Takeda, K. Kanno, T. Takada, O. Yamamoto, M. Takano, N. Nakayama and Y. Bando, “Phase relation in the oxygen nonstoichiometric system, $SrFeO_x$ ($2.5<x<3$),” *J. Solid State Chem.*, **63** (1986) 237-249.
20. M. Takano, T. Okita, N. Nakayama, Y. Bando, Y. Takeda, O. Yamamoto and J.B. Goodenough, “Dependence of the structure and electronic state of $SrFeO_x$ ($2.5\leq x\leq 3$) on composition and temperature,” *J. Solid State Chem.*, **73** (1988) 140-150.
21. M.H.R. Lankhorst, “Chemical diffusion in $La_{1-x}Sr_xCoO_{3-\delta}$,” Chapter 6 in: *Thermodynamic and transport properties of mixed ionic-electronic conducting perovskite-type oxides*, Thesis, University of Twente, Enschede, the Netherlands (1997).
22. C.S. Chen, H.J.M. Bouwmeester, H. Kruidhof, J.E. ten Elshof and A.J. Burggraaf, “Fabrication of $La_{1-x}Sr_xCoO_{3-\delta}$ thin layers on porous supports by a polymeric sol-gel process”, *J. Mater. Chem.*, **6** (1996) 815-819.
23. H. Deng, M. Zhou and B. Abeles, “Diffusion-reaction in mixed ionic-electronic solid oxide membranes with porous electrodes,” *Solid State Ionics*, **74** (1994) 75-84.
24. H. Deng, M. Zhou and B. Abeles, “Transport in porous electrodes: effect of gas diffusion,” *Solid State Ionics*, **80** (1995) 213-222.
25. U. Balachandran, J.T. Dusek, S.M. Sweeney, R.B. Poeppel, R.L. Mieville, P.S. Maiya, M.S. Kleefisch, S. Pei, T.P. Kobylinski, C. Udovich and A.C. Bose, "Methane to syngas via ceramic membranes," *Am. Cer. Soc. Bull.*, **74** (1995) 71-75.
26. U. Balachandran, J.T. Dusek, R.L. Mieville, R.B. Poeppel, M.S. Kleefisch, S. Pei, T.P. Kobylinski, C.A. Udovich and A.C. Bose, “Dense ceramic membranes for partial oxidation of methane to syngas,” *Appl. Cat. A*, **133** (1995) 19-30.
27. E.A. Mamedov, “Bismuth-containing oxides as catalysts for oxidative coupling of hydrocarbons,” *Catal. Rev.-Sci. Eng.*, **36** (1994) 1-23.
28. R. Di Cosimo, J.D. Burrington and R.K. Graselli, “Oxidative dehydrodimerization of propylene over a $Bi_2O_3$-$La_2O_3$ oxide ion-conductive catalyst,” *J. Catal.*, **102** (1986) 234-239.

# Appendix A - The geometric correction factor

Due to the applied method of sealing, the membrane side exposed to helium has a smaller surface area than the side exposed to $O_2$,$N_2$ in oxygen permeation measurements. This sealing effect is schematically depicted in Figure A.1. As a result, the oxygen flux has a non-zero radial component. Since the measured oxygen flux is normalized with respect to the He-side surface area, the axial flux is overestimated. A factor *G* can be calculated to correct for this effect in order to obtain the one-dimensional, axial oxygen flux.

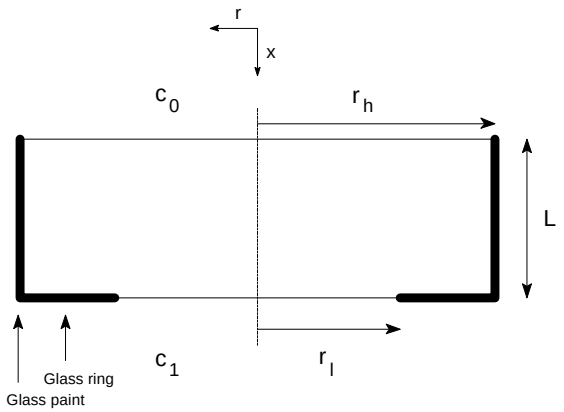


Figure A.1. Schematic diagram of membrane geometry. Thick lines indicate insulating boundaries. Gas phase oxygen activities are indicated as $c_0$ and $c_1$.

The basic equation to be solved is the steady-state diffusion equation in cylindrical coordinates

$$\tilde{D}\left(\frac{\partial^2 c}{\partial x^2}+\frac{\partial^2 c}{\partial y^2}+\frac{\partial^2 c}{\partial z^2}\right)=0\,, \tag{A.1}$$

where $\tilde{D}$ ($cm^2\ s^{-1}$) is the chemical diffusion coefficient (assumed isotropically) and *c* the oxygen concentration (mol $m^{-3}$). The boundary conditions are

$$c(x=0)=c_0\ , \tag{A.2}$$

$$c(x=L, r\le r_l)=c_1\ , \tag{A.3}$$

for the gas/solid interfaces,

$$(\partial c/\partial r)_{r=r_h}=0\ , \tag{A.4}$$

$$(\partial c/\partial x)_{x=L,r>r_l} = 0 \ , \tag{A.5}$$

for the insulating boundaries and

$$(\partial c/\partial r)_{r=0} = 0 \tag{A.6}$$

for the central axis. This set of equations can be solved numerically or analytically [1] under certain assumptions. This finally results in an oxygen flux $j_r$. Dividing this flux by the calculated one-dimensional flux $j_a$ yields $G$. For the membranes used in this study, $r_l$=4.5 mm and $r_h$=6 mm. The correction factors used here were calculated by a numerical procedure and were found to be equal to 1.12, 1.21 and 1.38 for membranes of 0.5, 1.0 and 2.0 mm thickness, respectively.

## Reference

1. K.H. Keller and T.R. Stein, “A two-dimensional analysis of porous membrane transport,” *Math. Biosci.*, **1** (1967) 421-437.

# Appendix B - The cell parameters of $La_{0.6}Sr_{0.4}Co_{1-y}Fe_yO_{3-\delta}$

The cell parameters of $La_{0.6}Sr_{0.4}Co_{1-y}Fe_yO_{3-\delta}$ ($y$=0.1, 0.25, 0.4, 0.6, 0.8) at room temperature were determined from powder XRD spectra taken on a Philips PW 1710 diffractometer (instrument power 40 kV, 30 mA) with graphite-filtered CuKα radiation. Prior to analysis the powders were treated at 1000°C in air and slowly cooled (<0.3°C/min). $LaB_6$ ($a$=4.1569 Å) [1] was added to the perovskite powders as an internal standard. The samples were measured with a 2θ scan from 20 to 137º with steps of 0.02º and the intensity was collected during 5-10 seconds. The line patterns were indexed by the TREOR90 program [2] and refinement was done using the PIRUM program. The $CuK\alpha_1$ ($\lambda$=1.5406 Å) component was used in the refinement procedure. Further details can be found elsewhere [3].

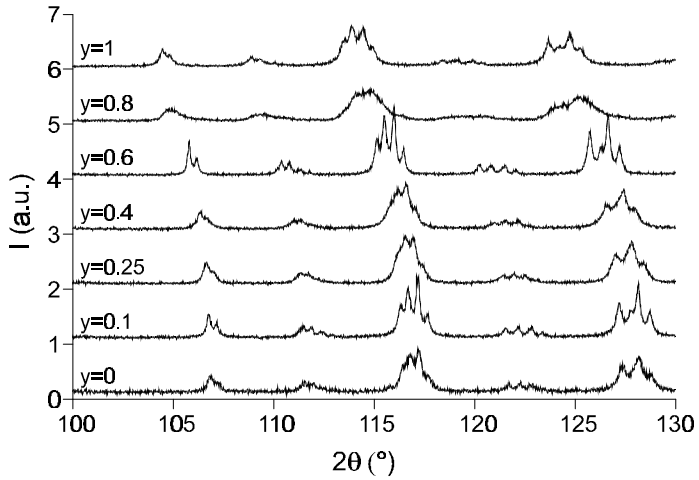


Figure B.1. X-ray diffractograms of $La_{0.6}Sr_{0.4}Co_{1-y}Fe_yO_{3-\delta}$ ($y$=0, 0.1, 0.25, 0.4, 0.6, 0.8, 1.0) in the region 2θ 100-130°. Diffractogram of $La_{0.6}Sr_{0.4}CoO_3$ taken from Ref. [5].

All compounds showed similar diffraction patterns. The patterns are pseudo-cubic ($a$ . 3.8-3.9 Å) and are related to the perovskite structure. The region 2θ 100-130° of all compounds, including $La_{0.6}Sr_{0.4}FeO_{3-\delta}$ [4], is shown in Figure B.1. The corresponding powder data can be found elsewhere [3]. All patterns were indexed on the basis of a rhombohedral unit cell. The space group is probably $R\bar{3}c$ (167) for all compositions. Table B.1 shows the refined unit cell parameters. Both the values of $a$ and $c$ increase with increasing iron content. In Figure B.2, the pseudo-cubic cell parameter $a_c$, defined by

$$a_c = \sqrt[3]{\frac{a^2 c}{4\sqrt{3}}}\,, \qquad \text{(B.1)}$$

is shown versus the iron content. Two regions can be distinguished in which the value of $a_c$ increases linearly with the iron content. This change of slope can be understood by considering the charge neutrality condition. Since the perovskites are nearly stoichiometric at room temperature ($\delta \approx 0$), 60% of the transition metal cations must be in the 3+ oxidation state, while the remaining 40% are in the 4+ oxidation state.

Table B.1. Diffraction data for $La_{0.6}Sr_{0.4}Co_{1-y}Fe_yO_{3-\delta}$ ($y$=0.1, 0.25, 0.4, 0.6, 0.8) The data for $y$=1.0 [4] are shown for comparison.

| $y$ | 0.1 | 0.25 | 0.4 | 0.6 | 0.8 | 1.0 |
|---|---|---|---|---|---|---|
| hexagonal setting | | | | | | |
| $a$ (Å) | 5.4388(1) | 5.4427(2) | 5.4530(1) | 5.4769(2) | 5.5047(4) | 5.5278(2) |
| $c$ (Å) | 13.2355(2) | 13.2542(5) | 13.2838(5) | 13.3175(6) | 13.3918(12) | 13.4368(7) |
| rhombohedral cell | | | | | | |
| $a$ (Å) | 5.4152 | 5.4216 | 5.4331 | 5.4502 | 5.4810 | 5.4997 |
| $\alpha$ (°) | 60.29 | 60.26 | 60.24 | 60.32 | 60.35 | 60.34 |

Furthermore, the results presented in this chapter show that $Fe^{4+}$ is more stable than $Co^{4+}$ [8]. Replacing cobalt by iron at low doping levels ($y$<0.4) is effectively a substitution of $Co^{4+}$ by $Fe^{4+}$. When all $Co^{4+}$ has been replaced (at $y$=0.4), further substitution by iron results in substituting $Co^{3+}$ by $Fe^{3+}$. The effect of $Co^{4+}/Fe^{4+}$ substitution on $a_c$ is different from the effect of $Co^{3+}/Fe^{3+}$ substitution, as observed clearly in Figure B.2.

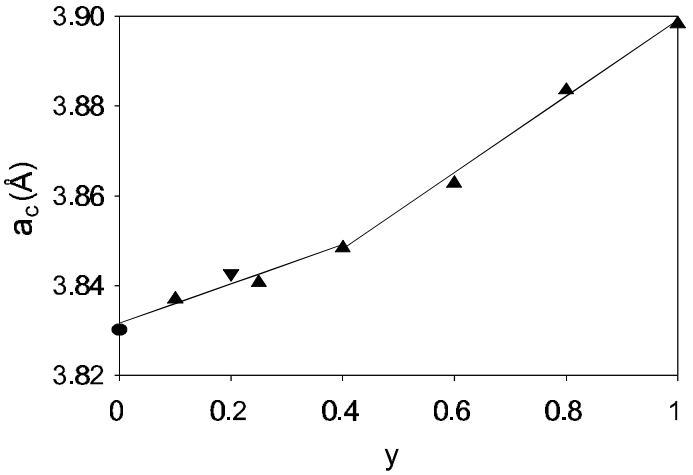


Figure B.2. Pseudo-cubic cell parameter $a_c$ of $La_{0.6}Sr_{0.4}Co_{1-y}Fe_yO_{3-\delta}$. Data of $y$=0 and $y$=0.2 were taken from Refs. [6,7].

## References

1. Powder Diffraction File database. 34-427 (JCPDS-ICDD).

2. P.-E. Werner, L. Eriksson and M. Westdahl, "TREOR, a semi-exhaustive trial-and-error powder indexing program for all symmetries," *J. Appl. Crystallogr.*, **18** (1985) 367-370.
3. J.E. ten Elshof and J. Boeijsma, "Influence of iron content on cell parameters of rhombohedral $La_{0.6}Sr_{0.4}Co_{1-y}Fe_yO_3$," *Powder Diff.*, **11** (1996) 240-245.
4. Chapter 3 of this thesis.
5. N.M.L.N.P. Closset, R.H.E. van Doorn, H. Kruidhof and J. Boeijsma, "About the crystal structure of $La_{1-x}Sr_xCoO_{3-\delta}$ (0#*x*#0.6)," *Powder Diff.*, **11** (1996) 31-34.
6. Powder Diffraction File database. 36-1392, 36-1393 (JCPDS-ICDD).
7. J.E. ten Elshof and J. Boeijsma, "Powder diffraction of $La_{1-x}A_xCo_{0.8}Fe_{0.2}O_3$ (A=Sr, Ba)," *Powder Diff.*, **11** (1996) 28-30.
8. L.-W. Tai, M.M. Nasrallah, H.U. Anderson, D.M. Sparlin and S.R. Sehlin, "Structure and properties of $La_{1-x}Sr_xCo_{1-y}Fe_yO_3$. Part 1. The system $La_{0.8}Sr_{0.2}Co_{1-y}Fe_yO_3$," *Solid State Ionics*, **76** (1995) 259-271.

# Dankwoord

Hoewel u, geachte lezer, al bijna tot het eind van dit boekje gevorderd bent, denkt u misschien nog steeds dat dit het resultaat van het werk van slechts één persoon is. Maar ofschoon het doel van een promotieopdracht het zelfstandig verrichten van onderzoek is, is het niet de bedoeling, zelfs niet mogelijk, om het alleen te doen. Toen ik vier jaar geleden met mijn promotieonderzoek begon wist ik vrijwel niets over anorganische materiaalkunde. Dat het desondanks toch nog wat met dit proefschrift is geworden, heb ik dan ook voor een groot deel te danken aan de welwillende medewerking van anderen. Ik wil hier graag de volgende mensen bedanken voor hun - directe of indirecte - bijdragen:

- Henk Verweij voor het bieden van de mogelijkheid om in dit laboratorium te werken en voor alle kansen die hij me daarna heeft gegeven om me in alle aspecten van het vak te bekwamen.
- Henny Bouwmeester voor het corrigeren van manuscripten en voor de vele prettige gesprekken over perovskieten, permeatie en alle andere dingen die ertoe doen in het leven. Ook dank ik hem voor zijn gezelschap tijdens onze reizen naar Griekenland en Bulgarije.
- Mijn (ex-)kamergenoten Zeger Vroon, René van Doorn, Sven van der Gijp, Bas Kerkwijk en Han Saeijs voor de vele prettige uren die ik met hen op een (meestal rumoerige maar juist daarom gezellige) kamer heb doorgebracht. René wil ik speciaal bedanken voor de onvergetelijke reis door de VS en voor alle moeite die hij gedaan heeft om mij in te werken. Mijn 'voorgangers' Zeger en René ben ik zeer dankbaar voor alle prettige contacten. Tenslotte wil ik Bas speciaal bedanken voor zijn lekkere koffie op de vroege ochtend.
- Martijn Lankhorst voor de samenwerking in de afgelopen vier jaar. Afgezien van ons gezamenlijke onderzoek dat beschreven staat in hoofdstuk 5, zijn zijn grote en minder grote bijdragen aan dit proefschrift te talrijk om op te noemen. Ook hem dank ik hartelijk voor die gedenkwaardige tijd in de VS.
- Danny Nguyen, die zijn afstudeeropdracht bij mij vervulde, voor de permeatiemetingen van hoofdstuk 8. Zonder zijn inzet en enthousiasme zou het werk aan de composietmembranen niet zover zijn gekomen.
- Henk Kruidhof, die voor mij altijd een aanspreekpunt is geweest op het gebied van de synthese van anorganische materialen. Ook dank zij zijn 'lab-management' heb ik steeds probleemloos kunnen werken.
- José Rietmann voor veelvuldige (computer)technische ondersteuning, en in het bijzonder voor het razendsnel gebruiksklaar maken van de TG-balans.

- De vakgroeptechnici Karin Schildkamp en Attila Csaki die altijd klaarstonden om te helpen bij grote of kleine technische problemen.
- Matthijs den Otter voor het uitvoeren van de isotoopuitwisselingsmetingen van hoofdstuk 8.
- Nicole, Arian, Eddy, Balu, Baukje, Renate, Bernard, Claudia, Cis en alle andere vakgroepleden die niet met name genoemd zijn voor de prettige sfeer in het lab in de afgelopen vier jaar.
- Ron Pathuis voor het schrijven van enkele zeer nuttig gebleken spreadsheet-macro's.
- Jaap Boeijsma voor het opnemen en interpreteren van XRD-spectra. Aan deze samenwerking, die tot twee publikaties heeft geleid, heb ik veel plezier beleefd.
- Mark Smithers, Rico Keim en Albert van den Berg van het Centrum voor Materialenonderzoek (CMO) voor hun analyses (SEM, EDX, SAED, HR-TEM, XPS, SAM) van vele van mijn preparaten.
- Alle medewerkers van de glasinstrumentmakerij voor het vele werk dat ze verzet hebben. In het bijzonder wil ik Gerrit Mollenhorst bedanken voor alle adviezen en zijn hulp bij het ontwerpen van nieuwe kwartsreactoren.
- Michael Stoukides, Panagiotis Tsiakaras, Athanasios Koungolos, Giorgos Marnellos and Kostas Athanasiou (Chemical Process Research Engineering Institute, Thessaloniki), who made my stay in Greece a very pleasant event. I want to thank Panos especially for his help and unforgettable hospitality.
- Jeffry Stevenson (Pacific Northwest Laboratory, Richland, WA) for kindly providing me with a detailed description of the 'chlorine method' of chapter 5.
- Professor P.J. Gellings voor het nauwkeurig corrigeren van het manuscript van dit proefschrift.
- Mijn huisgenoot Herman voor zijn vriendschap en de prettige sfeer thuis.
- Mijn ouders, Gré, verdere familie en vrienden voor de steun die ik in de afgelopen jaren van hen heb gekregen. Bovenal wil ik mijn ouders bedanken, die me steeds gestimuleerd hebben me verder te ontwikkelen en zonder wie ik dit nooit bereikt zou hebben.
- Tenslotte ... Alice voor alle dagen met sterretje!

André ten Elshof

# Levensloop

De schrijver van dit proefschrift werd op 13 november 1968 geboren in Groenlo. In 1987 behaalde hij aan de Rijksscholengemeenschap te Lochem het VWO-diploma, waarna hij in datzelfde jaar aan de Universiteit Twente de studie Chemische Technologie begon. De doctoraal praktijkstage verrichte hij in 1991 bij het Department of Physics aan het Mendeleev Institute of Chemical Technology in Moskou. Onder begeleiding van dr. A.A. Varnek voerde hij een theoretische studie uit naar de complexering van alkali-kationen door organofosforzure verbindingen. De afstudeer-opdracht werd uitgevoerd bij de vakgroep Chemische Fysica (prof. dr. D. Feil) onder begeleiding van dr. W.J. Briels. Het betrof een onderzoek door middel van computersimulaties naar de invloed van waterstofbindingen op de structuur en dynamica van methanol. In 1993 werd het doctoraaldiploma behaald (met lof). In datzelfde jaar was hij medewinnaar van de Unilever Researchprijs. Van 1 april 1993 tot 1 april 1997 was hij als Assistent in Opleiding werkzaam bij de vakgroep Anorganische Materiaalkunde binnen de faculteit Chemische Technologie aan de Universiteit Twente. Het in dit proefschrift beschreven onderzoek werd uitgevoerd onder begeleiding van prof. dr. ir. H. Verweij en dr. H.J.M. Bouwmeester.